University of Warsaw
Faculty of Physics
Institute of Experimental Physics

Measurements of Hadronic Cross Section for Precise Determination of Neutrino Beam Properties in T2K Oscillation Experiment

Magdalena Zofia Posiadała

Ph.D. thesis written under supervision of prof. dr hab. Danuta Kiełczewska

Warsaw, 2011

Abstract
Differential cross sections and mean multiplicities in production processes for low momentum charged pion mesons and protons in p+C interactions at 31 GeV/c measured with the large acceptance NA61/SHINE spectrometer at the CERN SPS are presented. A set of data collected during the first NA61/SHINE run in 2007 with a thin graphite target was used for the analysis. The results are presented as a function of laboratory momentum in 10 intervals of the laboratory polar angle covering the range from 0 up to 420 mrad. The spectra are compared with predictions of several hadron production models. Measurements for π^+ and π^- mesons are used by the T2K experiment to tune neutrino beam simulations and reduce uncertainties on charged pion production.

Contents

List of Figures

List of Tables

Acknowledgments

At the very beginning I would like to thank my supervisor prof. Danuta Kiełczewska for her guidance, many inspiring remarks and lots of patience and work during my Ph.D. studies. I am also very grateful to prof. Ewa Rondio for her encouragement and support while working with me on this thesis. Both Danka and Ewa helped me in numerous ways and taught me a lot which I will never forget. Without them this thesis would not be written. Thank you!

I want to express also my gratitude to members of the NA61/SHINE collaboration for friendly atmosphere of the work. In particular, I would like to thank Joanna Stepaniak, Marek Gaździcki, Alberto Marchionni, Boris Popov, Zoltan Fodor and Alain Blondel for many fruitful discussions with important comments and suggestions towards the analysis presented in this thesis.

I would like to thank Paweł Przewłocki, Piotr Mijakowski, Anna Korbecka, Claudia Strabel, Nicolas Abgrall, Tomasz Palczewski, Justyna Łagoda, Robert Sulej and Katarzyna Grebieszkow for having fun during Ph.D. studies. Big cheers to all of you.

My special thanks go to Beata Brzozowska. I could always count on her friendly advice.

Finally, I would like to thank my family for their endless support and encouragement while preparing this thesis. I am happy to have you.

This work was supported by the Polish Ministry of Science and Higher Education, grant N N202 126736.

Introduction

The T2K (Tokai-to-Kamioka) is a second generation long baseline neutrino oscillation experiment which aims at precise measurements of the neutrino masses and mixing angles. The most significant search concerns examination of still unknown θ_{13} which will be carried out by detection of $\nu_\mu \to \nu_e$ *appearance*. Moreover, T2K will be able to achieve an order of magnitude better precision in the measurements of θ_{23} as well as Δm_{23} in the ν_μ *disappearance* channel. In order to accomplish it, high intensity narrow band neutrino beam is produced at Japan Proton Accelerator Research Complex (J-PARC) in Japan from secondary pions and kaons created by interactions of 30 GeV (kinetic energy) protons on 90 cm long carbon target. The neutrino beam is tuned to the oscillation maximum at ~ 0.6 GeV and is directed at 2.5^0 off-axis towards near station, placed at 280 m from the target, named ND280 and far station located 295 km away - the world largest water Cherenkov detector Super-Kamiokande (SK). It is designed to study neutrino oscillations by comparing measured with predicted neutrino flux at SK. The latter one is obtained using measured flux in ND280 which is later on extrapolated to the SK with the help of Monte Carlo simulations of neutrino beam. These neutrino beam predictions require knowledge of the hadron productions which is strongly model dependent. In order to diminish uncertainty on the knowledge of pion and kaon production mechanism off the carbon target, precise hadron production measurements are crucial. Unfortunately, in the history of the hadron production experiments no one carried out needed measurements. In this scenario the NA61/SHINE comes into importance as in the first stage of data taking (2007-2010) it aimed to deliver data needed for the T2K.

The NA61/SHINE (SHINE = SPS Heavy Ion and Neutrino Experiment) experiment is a large acceptance hadron spectrometer located in the North Area H2 beam line of the European Organization for Nuclear Research (CERN) in Geneva. The experiment uses beams from the Super Proton Synchrotron. The NA61/SHINE apparatus offers the unique possibility of accurate measurement of hadron production, including good particle identification. The main tracking devices are four large volume Time Projection Chambers (TPCs) inherited from NA49 experiment. In 2007 the detector has been upgraded with a new forward time-of-flight detector (ToF-F) in order to extend the acceptance for pion and kaon identification as required for T2K measurements.

The author of this thesis is a member of NA61/SHINE and T2K collaborations. The analysis presented in this dissertation is based on a set of data collected during the first NA61/SHINE run in 2007 with thin graphite target. Total sample of registered and reconstructed thin target events consists of around 669 thousands.

In this dissertation we concentrate on the low momentum region. The procedure of particle identification was developed by author especially for this area of phase space. For momenta $p \leq 1$ GeV/c an information on the particle type can be obtained only with the dE/dx measurements as the time-of-flight (tof) method is not available since the particles do not reach the ToF-F detectors. Among all low momentum particles pion mesons are of major interest, as they are the main source of neutrino production. Above 1 GeV/c a reliable identification π^+ mesons was not possible without tof measurements at momenta where the

Bethe-Bloch curves for pions, kaons and protons cross each other. On the other hand, for π^- mesons, where the contribution of K^- and antiprotons is almost negligible, the *dE/dx* analysis could be extended in momentum up to 3 GeV/c allowing consistency checks with the other analysis methods in the region of overlap. For pions of both charges the analysis was performed starting from tracks with $p > 0.2$ GeV/c as below this momentum range the Bethe-Bloch curve for pions crosses with that for electrons (positrons). In addition, we were able to extract low momentum proton yields which are also included in this thesis. The identification procedure was performed in bins of particle momentum p and polar angle θ. Narrow momentum intervals of 0.1 GeV/c for $0.2 < p \leq 1$ GeV/c and 0.2 GeV/c for $1 < p \leq 3$ GeV/c were chosen to account for the strong dependence of *dE/dx* on momentum. For the final results of identified charged pion mesons and protons spectra ten polar angle intervals covering the range from 0 up to 420 mrad were chosen.

The analysis of charged pion and proton spectra carried out by the author consists of several consecutive steps. They are as follows.

1. Preparation of samples for data and Monte Carlo. We need to apply the same event and track selection criteria in order to clean both samples.

2. Identification of π^+, π^- mesons and protons. This procedure requires a special approach which has to account for the fast change of energy loss with momentum.

3. Evaluation of corresponding *global* Monte Carlo corrections separately for given particle species and calculation of corrected particle spectra.

4. Normalization of corrected spectra. As a result we obtain differential inclusive cross sections and mean particle multiplicity in production processes for π^+, π^- mesons and protons.

5. Evaluation of the systematic uncertainties for given particle type.

6. Comparison of obtained mean particle multiplicities with different model predictions.

The results on interaction cross sections and charged pion spectra for p+C interactions at 30 GeV (kinetic energy) have already been published in Ref. [1]. These measurements were also used by the T2K in order to tune the existing neutrino beam simulations to the NA61 results. This approach allowed to reduce uncertainty on π^+ production from 50% to 5-10%. Improved neutrino flux was used in the analysis in which an indication of ν_e *appearance* from off-axis muon neutrino beam was reported by the T2K experiment [2].

Beside the analysis, the author of this thesis was also involved in the technical work for NA61/SHINE. This task included controlling the performance of the NA61 detector during each data taking, years 2007-2010 (of around two weeks per year at CERN). In addition, author was participating in preparation of the light guides which are used in the ToF-F detector. This elements were produced in Soltan Institute for Nuclear Studies, Warsaw, Poland (July 2007). Apart from the NA61 experiment, author was also taking part in tests performed to control the work of second horn used in the T2K target station in Tokai, Japan (November 2007).

The thesis starts with introduction to the neutrino oscillation phenomena and an overview of current experimental situation in neutrino oscillation physics (Chapter 1). In the final picture of the neutrino oscillation parameters, still a precise value of the θ_{13} mixing angle is missing. This subject is of most interest for current and future neutrino experiments. The first one, called T2K, is already running. The details of this project with its physical goals and justification for needed pion and kaon cross section measurements are introduced in Chapter 2. The last part of this chapter is focused on the T2K requirements of the

NA61/SHINE measurements. Chapter 3 briefly describes different experimental components of the NA61/SHINE experiment which were used during pilot 2007 run and which are of interest for results presented in this dissertation. In Chapter 4 methods of reconstruction and particle identification possible within NA61 are discussed with special emphasis put on the ionization measurements which are used further in order to perform particle identification. Results of the analysis are given in Chapter 5 and 6. At first, data collected on thin graphite target have to pass the selection criteria described in Chapter 5 in order to obtain clean sample of well defined tracks on which the particle identification will be performed. The next chapter deals with the procedures of particle identification developed by the author especially for the low momentum region. The main part of the Chapter 7 is devoted to discussion of Monte Carlo corrections which need to be applied to the spectra of identified charged pion mesons and protons. These corrections take into account several experimental effects like: detector geometrical acceptance, reconstruction efficiency, decays of particles, secondary interactions. In the last section of this chapter we illustrate corrected spectra of low momentum π^+, π^- mesons and protons. Chapter 8 deals with the procedure of cross section measurements and normalization of particle yields which was performed for the NA61 2007 data. As a result the charged pion and proton low momentum, inclusive differential cross sections and mean multiplicities in production processes are obtained. In Chapter 9 vital sources of systematic uncertainties which are taken into consideration are introduced with detailed studies of each contributor. In the Chapter 10 we present how the NA61 measurements compare with different hadron production models. Secondly, impact of the NA61 results on the T2K beam simulation is shown. Finally in the last chapter summary of presented analysis is introduced.

Chapter 1

Neutrinos

Discovery of neutrinos is strongly correlated with the studies of radioactivity: α (charged helium), β (electrons) and γ (high-energy light) radiation. It was found that both α and γ spectra emitted in nuclear decays were discrete which is natural consequence of the kinematics of two-body decays with conservation of energy and momentum laws. In 1930, however, James Chadwick observed that the energy spectrum of electrons emitted in nuclear β decay was continuous which under the assumption of two-body decay would break the conservation laws [3]. In order to explain these observations Wolfgang Pauli proceeded to propose a "desperate remedy" which would explain the puzzling situation and allow to save the conservation of energy and momentum laws. He suggested that the missing energy was being carried away by the third particle emitted in the decay. It was Enrico Fermi [4] who three years later called this new particle the neutrino and used it in his theory of weak interactions. It took another 23 years before Frederick Reines and Clyde Cowan made the first experimental observation of neutrinos. Their pioneering experiment for which Reines was awarded with the Nobel Prize in 1995 [5] took place at the Savannah River reactor [6]. In the experiment they used the inverse of the β decay reaction:

$$\bar{\nu_e} + p \rightarrow e^+ + n \tag{1.1}$$

The target was water with $CdCl_2$ dissolved in it. The positron was detected by its slowing down and annihilating with an electron producing two 0.5 MeV gamma rays in opposite directions. The neutron was also slowed down and captured by the Cd microseconds after the positron capture [6]. In this way antielectron neutrino was discovered. Scientists still wondered if they could find more types of these ghostlike particles that pass through everything. Subsequent accelerator experiments found that there are two more distinct types of neutrinos according to the type of charged particles found in the interaction. Thus, in 1962 Leon Lederman, Melvin Schwartz and Jack Steinberger discovered muon neutrinos with the usage of neutrino beam method. As a result of their discovery in 1988 they were awarded with Nobel Prize [5]. The last known neutrino - tau neutrino was found in 2000 by the Direct Observation of the Nu Tau (DONuT) experiment at Fermilab [7].

Up to know, experimental discoveries show that neutrinos come in three types electron, muon and tau neutrinos, called flavors. In the Standard Model of Particle Physics [8] they belong to the family of leptons. This three different neutrinos are complemented by antineutrinos, a set of mirror particles with the same mass as their matter equivalents. Neutrinos are neutral particles which interact with matter only weakly - this allows them to travel very long distances without any disturbances. As an example, the value of the mean free path for neutrinos in water is larger than a light year. For many years we believed that neutrinos are massless particles as introduced in Standard Model. However, recent results on neutrino oscillations coming from last 13 years provide clear evidence that there is a spectrum of masses for neutrinos.

In this chapter at first we will focus on explanation of the neutrino oscillation mechanism (Sec. 1.1). Secondly, an overview of the current situation in neutrino oscillation physics will be introduced in Sec. 1.2.

1.1 Neutrino oscillation mechanism

Available data on the oscillations of the solar (ν_e), atmospheric (ν_μ and $\bar{\nu_\mu}$), accelerator (ν_μ) and reactor ($\bar{\nu_e}$) neutrinos can be described with three flavor neutrino mixing. Note that the results obtained by LSND [9] and Miniboone [10] experiments suggesting transitions to a fourth neutrino state are still controversial and we do not discuss them here. Moreover, studies of Z^0 production in e^+e^- collisions at LEP give the most actual number of light neutrino types, which is equal to $N_\nu = 2.984 \pm 0.008$ [11]. Oscillations among all three neutrino species can be expressed by 3 x 3 unitary matrix, called Pontecorvo-Maki-Nakagawa-Sakata (PMNS) [12, 13]:

$$U = \begin{pmatrix} c_{13}c_{12} & c_{13}s_{12} & s_{13}e^{-i\delta} \\ -c_{23}s_{12} - s_{13}c_{12}s_{23}e^{i\delta} & c_{23}c_{12} - s_{13}s_{12}s_{23}e^{i\delta} & c_{13}s_{23} \\ s_{23}s_{12} - s_{13}c_{12}c_{23}e^{i\delta} & -s_{23}c_{12} - s_{13}s_{12}c_{23}e^{i\delta} & c_{13}c_{23} \end{pmatrix} \begin{pmatrix} 1 & & \\ & e^{i\alpha} & \\ & & e^{i\beta} \end{pmatrix}$$

where $c_{ij} = \cos\theta_{ij}$ and $s_{ij} = \sin\theta_{ij}$, δ is Dirac phase and α, β are Majorana phases. When CP violation occurs these phases are not equal to zero. However, if neutrinos are Dirac particles this implies that Majorana phases are zero and we can forget about the right hand side of given formula. Anyhow Majorana phases do not affect the oscillation mechanism so for the simplicity we will assume that they vanish. For this situation neutrino mixing matrix U is similar to the CKM quark mixing matrix in terms of three mixing angles and one CP violation phase. The oscillation probability is given by the formula:

$$P(\nu_\alpha \to \nu_\beta) = \delta_{\alpha\beta} - 4\sum_{i>j} Re(U^*_{\alpha i}U_{\beta i}U_{\alpha j}U^*_{\beta j})\sin^2\Phi_{ij} + k \cdot 2\sum_{i>j} Im(U^*_{\alpha i}U_{\beta i}U_{\alpha j}U^*_{\beta j})\sin 2\Phi_{ij} \tag{1.2}$$

Here α and β are observable neutrino flavors states *i.e.* e, μ, τ, and:

$$\Phi_{ij} = 1.27\frac{\Delta m^2_{ij}[eV^2]L[km]}{E_\nu[GeV]} \tag{1.3}$$

with i and j referring to the mass states. The third term is responsible for CP violation with k equal to 1 for neutrinos and -1 for antineutrinos. For three neutrino mass states, there are three different Δm^2 parameters, although only two are independent. The neutrino mass states ν_1, ν_2 and ν_3 are defined in sucha way that the difference between ν_1 and ν_2 represents the smallest splitting. However, the mass of ν_3 relative to ν_1 and ν_2 is arbitrary and the sign of Δm^2 which includes the third mass state may be positive or negative. That is when $m_{\nu_3} > m_{\nu_1}, m_{\nu_2}$ then Δm^2_{23} will be positive but if $m_{\nu_3} < m_{\nu_1}, m_{\nu_2}$ then Δm^2_{23} will be negative. The former is called a "normal mass hierarchy" and the latter is the "inverted mass hierarchy". This is one of the open questions to the neutrino physics as for oscillations in vacuum it is still not known which scenario is correct as Δm^2 appears in a term which is squared.

One has to remember that neutrino oscillations only occur if the two mass states involved have sufficiently small Δm^2 with respect to their energy that the neutrino flavor is produced in superposition of two mass states. If the mass splitting is too large, a given neutrino flavor would be produced in one or the other of two mass eigenstates and interference (*i.e.* oscillations) would not occur.

The PMNS can be split into three factors describing rotations around three mixing angles, θ_{12}, θ_{13} and θ_{23} [16]:

$$U = \begin{pmatrix} 1 & & \\ & c_{23} & s_{23} \\ & -s_{23} & c_{23} \end{pmatrix} \begin{pmatrix} c_{13} & & s_{13}e^{-i\delta} \\ & 1 & \\ -s_{13}e^{i\delta} & & c_{13} \end{pmatrix} \begin{pmatrix} c_{12} & s_{12} & \\ -s_{12} & c_{12} & \\ & & 1 \end{pmatrix}$$

where each group of oscillation parameters (Δm^2_{ij} and θ_{ij}) may be placed into three given sectors: sector 12, sector 13 and sector 23. Although, in general there will be mixing among all three flavors of neutrinos, two-generation mixing may be often assumed. If the mass scales are quite different (for example $m_3 >> m_2 \approx m_1$), then the oscillation phenomena tend to decouple and the two-generation mixing model is a good approximation in limited regions. This is the case when we investigate sector 12 often called solar neutrino sector as well as sector 23 (atmospheric neutrino) as will be shown in the following section. In case of neutrino oscillations for just two flavors, the formalism is simplified. As an example let us consider two flavors, name as $|\nu_\mu\rangle$ and $|\nu_e\rangle$. In the oscillation mechanism they are treated as linear combinations of two mass eigenstates, denoted as $|\nu_1\rangle$ and $|\nu_2\rangle$, respectively:

$$\begin{pmatrix} |\nu_\mu(t)\rangle \\ |\nu_e(t)\rangle \end{pmatrix} = \begin{pmatrix} \cos\theta & \sin\theta \\ -\sin\theta & \cos\theta \end{pmatrix} \begin{pmatrix} |\nu_1(t)\rangle \\ |\nu_2(t)\rangle \end{pmatrix}$$

The mass eigenstates propagate in space and for ($\hbar = c = 1$) are given by $|\nu_i(t)\rangle = |\nu_i(t=0)\rangle e^{-iE_i t}$ where index "i" may be equal 1 or 2, respectively. These two states evolve differently, thus:

$$\begin{aligned} |\nu_\mu(t)\rangle &= \cos\theta e^{-iE_1 t}|\nu_1(t=0)\rangle + \sin\theta e^{-iE_2 t}|\nu_2(t=0)\rangle, \\ |\nu_e(t)\rangle &= -\sin\theta e^{-iE_2 t}|\nu_1(t=0)\rangle + \cos\theta e^{-iE_2 t}|\nu_2(t=0)\rangle \end{aligned} \tag{1.4}$$

A state originally $|\nu_\mu\rangle$ may oscillate into $|\nu_e\rangle$ with the probability:

$$P(\nu_\mu \to \nu_e) = \sin^2 2\theta \sin^2\left(\frac{E_2 - E_1}{2}\right) \tag{1.5}$$

and the probability for it to remain as itself is:

$$P(\nu_\mu \to \nu_\mu) = 1 - P(\nu_\mu \to \nu_e) = 1 - \sin^2 2\theta \sin^2\left(\frac{E_2 - E_1}{2}\right) \tag{1.6}$$

In experiments for which $m_i/p_i \ll 1$ the energy and momentum of two mass eigenstates are very close ($E_i = p + \frac{m_i^2}{2p}$, $t = \frac{L}{c}$), and we can rewrite the term:

$$\frac{E_2 - E_1}{2} = \frac{\Delta m^2 c^4}{4\hbar c}\frac{L}{E} = 1.27\frac{\Delta m^2[eV^2]L[km]}{E[GeV]} \tag{1.7}$$

where E is the neutrino energy, and L is the distance that neutrino travels from its source to the detector and $\Delta m^2 = m_2^2 - m_1^2$.

Thus, the expression for the oscillation probability may be rewritten as follows:

$$\begin{aligned} P(\nu_\mu \to \nu_e) &= \sin^2 2\theta \sin^2\left(\frac{1.27\Delta m^2 L}{E}\right) \\ P(\nu_\mu \to \nu_\mu) &= 1 - P(\nu_\mu \to \nu_e) \end{aligned} \tag{1.8}$$

To conclude, the oscillation wavelength depends upon the experimental parameters L (distance neutrino source - detector) and E (neutrino energy) as well as the oscillation parameter

Δm^2. The amplitude of the oscillation is constrained by the mixing term, $\sin^2 2\theta$. Finally, neutrino oscillations are quantum mechanical consequence of existence of neutrino masses and the small relative difference between them. In other words, if neutrino were massless particles or the difference between masses would be too large we would not be able to observe oscillation phenomena.

All introduced considerations for neutrino oscillation were assuming that we study this mechanism in vacuum. In case of dense matter, like in Sun or Earth, we encounter interactions of ν_e with electrons which are present along neutrinos way. This scatter off electrons has an influence on the probability of changing from one flavor to another. This phenomenon is known as Mikhayev-Smirnov-Wolfensten (MSW) effect [14, 15] and is taken into account by solar neutrino experiments in order to explain of observed electron neutrino deficit (see Sec. 1.2). This effect is negligible for ν_μ and ν_τ.

1.2 The Current Situation in Neutrino Oscillation Physics

In general, there are two types of oscillation searches: *disappearance* and *appearance*. Let's consider a pure source of neutrino type x. In a *disappearance* experiment, one looks for a deficit in the expected flux of ν_x. This requires accurate knowledge of the flux, which is often difficult to predict precisely without corresponding hadron production measurements as well as near-far detector design (like T2K experiment - see Chapter 2). The near detector measures the flux without oscillations, which is later on used to predict the unoscillated event rate in the far detector. A deficit compared to prediction indicates *disappearance*.
Appearance experiments search for $\nu_x \rightarrow \nu_\beta$ oscillations by directly observing interactions of neutrinos type β.

In our overview of the neutrino oscillation experiments we separately describe given sectors of oscillation parameters Δm^2_{ij} and θ_{ij}, where ij stands for 12, 23, 13 respectively. We review neutrino experiments, starting from the earliest measurements. As a result, at first sector 12 known as solar sector is investigated. Next sector 23, named atmospheric, is introduced. Finally the last and the most unmeasured part *i.e.* sector 13 is studied.

Solar neutrino experiments - oscillation parameters Δm^2_{12} and θ_{12}

Sector 12 is mainly investigated by the neutrinos produced in Sun, which is the reason why in the literature we may also encounter a name - solar neutrino sector. This field was probed by several experiments using different detection techniques. All projects listed below were directly examining solar neutrinos:

- radiochemical detectors: Chlorine (Homestake [19]), Gallium (SAGE [20], GALLEX [21] and its successor GNO [22]).
- water Cherenkov detectors: with H_2O (Kamiokande-II [23] and Super-Kamiokande (SK) [24, 25]) and with D_20 (SNO [27]).
- liquid scintillator detector: Borexino [29].

In addition to direct solar neutrino projects there was also very vital contribution to θ_{12} and Δm^2_{12} measurements coming from the long baseline reactor experiment KamLAND [30].

The Sun's core emits neutrinos in series of thermonuclear interactions, amongst which the most significant ones are placed in Tab. 1.1. The first one listed in this table makes up over 92% of the entire solar flux [17] and is the one which initialises the *pp* chain.

Reaction	abbreviation
$p + p \rightarrow d + e^+ + \nu_e$	*pp*
$p + e^- + p \rightarrow d + \nu_e$	*pep*
$^3\mathrm{He} + p \rightarrow {}^4\mathrm{He} + e^+ + \nu_e$	*hep*
$^7\mathrm{Be} + e^- \rightarrow {}^7\mathrm{Li} + \nu_e + (\gamma)$	^{7}Be
$^8\mathrm{B} \rightarrow {}^8\mathrm{Be}^* + \nu_e + e^+$	^{8}B

Table 1.1: The most significant thermonuclear reactions from *pp* chain producing neutrinos in the Sun with their abbreviations.

Scientists were able to gather all relevant information for the Sun into so called Standard Solar Model (SSM) with the aim to predict solar neutrino fluxes on Earth. The most reliable model of this type was created in 1962 and developed from then on by John Bahcall and others [18]. The SSM predictions for the neutrino fluxes and spectra are presented in Fig. 1.1. The neutrinos labeled *pp*, *pep*, ^{7}Be, ^{8}B and *hep* belong to the *pp* chain which for a star like the Sun dominates over those from the CNO cycle. Of the neutrinos in the *pp* chain, those from the initial reaction $p + p \rightarrow d + e^+ + \nu_e$ make up over 92% of the entire solar flux [17].

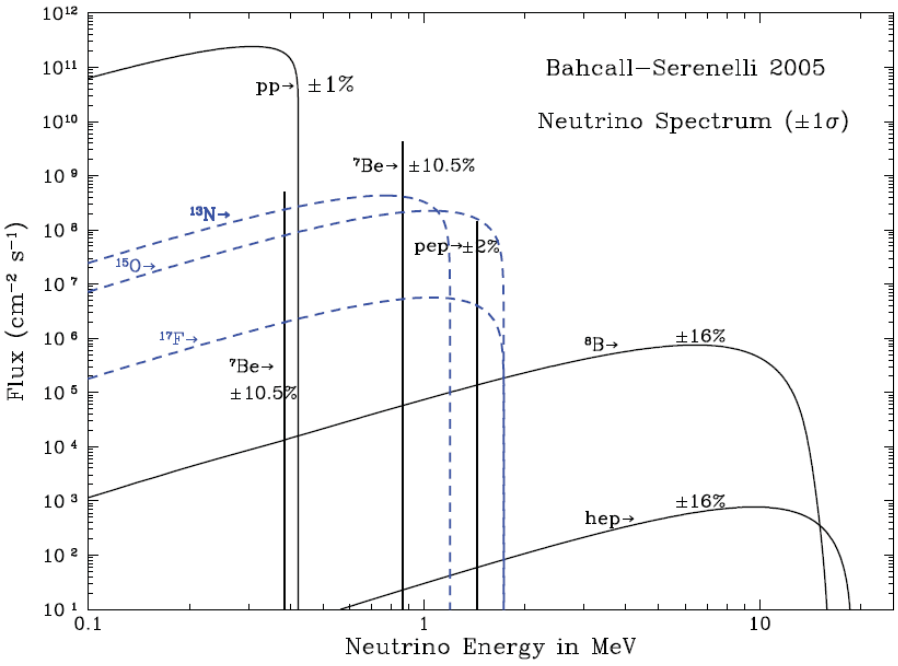

Figure 1.1: Differential Standard Solar Model neutrino fluxes. The neutrino fluxes are given in units of $\mathrm{cm}^{-2}\mathrm{s}^{-1}\mathrm{MeV}^{-1}$ (continuous spectra) and $\mathrm{cm}^{-2}\mathrm{s}^{-1}$ (line spectra). This figure may be found in John Bahcall's web site (see Ref. [17]).

Different parts of the solar neutrino spectrum have been studied by various experiments. The first indication of neutrino oscillations came from the Chlorine solar neutrino experiment conducted by Raymond Davis in the Homestake mine in South Dakota in 1968 [19]. It was a

radiochemical experiment which detected neutrinos via the reaction:

$$\nu_e + {}^{37}\mathrm{Cl} \rightarrow e^- + {}^{37}\mathrm{Ar} \tag{1.9}$$

The energy threshold for this reaction is 0.8 MeV, so experiment of this kind cannot see *pp* neutrinos (see Fig. 1.1). Produced radioactive atoms of ^{37}Ar have half life time ($\tau_{1/2}$) of 34.8 days, and after time of 2-3 $\tau_{1/2}$ values Davis and other collaborators could extract radioactive products from the tank through chemical methods and count them with the help of proportional counters. The problem which aroused afterwords, was the fact that this experiment observed only a third of the neutrinos coming from the Sun predicted by the SSM. The "solar neutrino problem" as it came to be known was sustained by the findings of the Gallium experiments GALLEX [21] and GNO [22] at Gran Sasso, Italy and SAGE [20] at Baksan, Russia. The threshold for the reaction was about 0.2 MeV, significantly lower than in the Chlorine case and as a result they were able to see also *pp* neutrinos. Obtained results, however, still were pointing out to decreased neutrino flux in comparison to that predicted by SSM.
Next information on the neutrino flux but this time in higher energy range ($E_\nu > 5\ MeV$) was delivered by the Kamiokande [23] and its successor Super-Kamiokande [24, 25] experiments using totally different observation technique. Both detectors were located in Kamioka mine in Japan. They use Cherenkov radiation to detect particles produced in neutrino interactions in water. This detection technique is based on the fact that a particle moving with the speed greater than the speed of light in given medium will emit light in a cone around particle direction, called Cherenkov radiation. Detection of this light by the photomultipliers (PMTs) installed on the walls of the detector enables determination of the particle energy as well as its incoming direction. Super-Kamiokande is the far station in the T2K experiment and detailed overview of the detector is given in Sec 2.3 on page 24. Now, for example, when a neutrino enters the water tank it may interact via elastic scattering (ES):

$$ES : \nu_x + e^- \rightarrow \nu_x + e^- \tag{1.10}$$

and what is recorded is the recoil electron while x represents all types of neutrinos, *i.e.* ν_e, ν_μ and ν_τ. However, the sensitivity to ν_μ and ν_τ is smaller than for the ν_e because of the relation between corresponding cross sections: $\sigma_{(\nu_{\mu,\tau}+e)} \approx 0.16\sigma_{(\nu_e+e)}$ [26]. The detection thresholds were 7 MeV and 5 MeV for Kamiokande and Super-Kamiokande experiments, respectively. They were able to detect only neutrinos coming from the ^{8}B decays (see Tab 1.1). The applied detection technique allowed Kamiokande to give for the first time a proof that measured neutrinos do really come from the direction of the Sun. Both these detectors observed again massive deficit in the number of neutrinos in comparison to SSM. For example, in case of the Super-Kamiokande the relative rate of observed to expected neutrinos was equal to 0.39 ± 0.06 [25].

Still the "solar neutrino problem" was unsolved and what scientist began to think was that maybe something is happening to the neutrinos as they come from Sun to Earth or simply predictions of SSM are not correct. In case of the first point one should remember that in the Sun only electron neutrinos are produced and detectors on Earth have been sensitive mainly to these electron neutrinos. So if the neutrinos were undergoing a "flavor" oscillation the probability to detect those electron neutrinos would reduce the observed rate. The solution was provided by the Sudbury Neutrino Observatory (SNO), which was underground heavy water (D_2O) Cherenkov experiment located in Creighton mine, Ontario in Canada [27, 28]. What makes SNO better from the Super-Kamiokande was the fact that SNO was filled with

heavy water which allowed to detect solar neutrinos with three reactions:

$$\begin{aligned} CC &: \nu_e + d \to p + p + e^- \\ NC &: \nu_x + d \to p + n + \nu_x \\ ES &: \nu_x + e^- \to \nu_x + e^- \end{aligned}$$

where $x = e, \mu, \tau$. The first reaction with charged current exchange (CC) is sensitive only to ν_e as solar neutrinos energies (few MeV) allow only to produce electrons in the final state and not μ or τ leptons. Other reactions NC (neutral current exchange) and ES may happen to all three types of neutrinos. The threshold of NC reaction is 2.2 MeV. In D_2O it was measured by neutron capture in deuterium, which resulted in 6.25 MeV γ-ray. For pure D_2O the capture efficiency was low thus SNO collaboration decided to add 2 tons of salt (NaCl) into the heavy water. Data taking period with enriched D_2O was named Phase-II of the experiment. In the third stage (Phase-III) NaCl was removed and neutron counters were installed in order to provide independent NC measurements with different systematics than in Phase-II. The final results from SNO Phase-II are the following [27]:

$$\begin{aligned} \Phi_{SNO}^{CC} &= (1.68 \pm 0.06^{+0.08}_{-0.09}) \times 10^6 \mathrm{cm}^{-2}\mathrm{s}^{-1} \\ \Phi_{SNO}^{ES} &= (2.35 \pm 0.22 \pm 0.15) \times 10^6 \mathrm{cm}^{-2}\mathrm{s}^{-1} \\ \Phi_{SNO}^{NC} &= (4.94 \pm 0.21^{+0.38}_{-0.34}) \times 10^6 \mathrm{cm}^{-2}\mathrm{s}^{-1} \end{aligned}$$

Comparison of presented results with SSM, show that Φ_{SNO}^{NC} finally agreed with expectations of the SSM. This measurement provided direct evidence for flavor conversion of solar neutrinos of type $\nu_e \to \nu_{\mu,\tau}$ which was the reason why previous measurements could observe deficit in solar electron neutrino flux. All the results from SNO Phase-II are presented in Fig. 1.2. The illustration shows combined flux of $\nu_{\mu+\tau}$ versus flux of ν_e. In addition, the Super-Kamiokande results for ES [25] are also included with the narrow band parallel to the SNO ES results. For all measured fluxes we observe a region of overlap (see black dot representing the best fit point). Moreover, previously missing ingredient, *i.e.* the $\nu_{\mu+\tau}$ flux was determined for the first time and its contribution to the total solar neutrino flux is very significant. In the best fit point it is almost two times larger than ν_e flux.

Another important contribution to solar neutrino oscillation physics came from the Kamioka Liquid Scintillator Anti-Neutrino Detector (KamLAND) experiment [30]. KamLAND is located at the site of the earlier Kamiokande experiment at a depth of 2700 m water equivalent. The heart of the detector is 1 kton of highly purified liquid scintillator enclosed in balloon suspended in purified mineral oil. The detector is inside 18 m diameter stainless steel sphere. An array of 50 cm diameter photomultiplier tubes (PMTs) is mounted on the inner surface of the sphere (around 1900 PMTs). The KamLAND is surrounded by the 55 Japanese nuclear power reactor units, each being an isotropic $\bar{\nu_e}$ source. This $\bar{\nu_e}$ have energies similar to those of solar neutrinos and should therefore by subject to the same kind of oscillation phenomena. In the reaction of interest, *i.e.* inverse β decay: $\bar{\nu_e} + p \to e^+ + n$, prompt scintillation light is seen from the outgoing positron and light from 2.2 MeV γ ray emitted when the neutron captured on a proton is seen some 200 μs later. Kamland was the first experiment to observe reactor neutrino oscillations, by seeing a significant deficit in measured flux.

It is important to mention also about another real time solar neutrino experiment, Borexino, placed at Gran Sasso in Italy, which started data taking in 2007 [29]. Detection of solar neutrinos is based on $\nu_e + e$ scattering in very pure liquid scintillator. Reaction threshold is very low, *i.e.* 250 keV which allows to measure monochromatic 0.861 MeV ^{7}Be (see Fig. 1.1) for the first time.

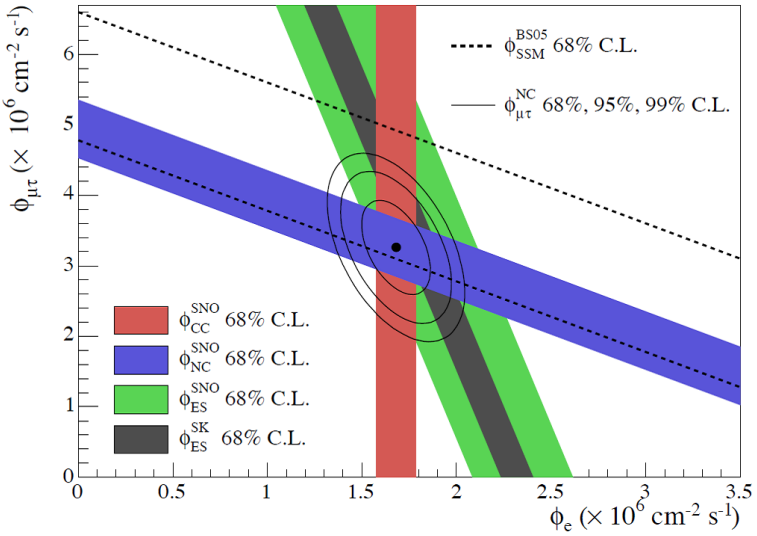

Figure 1.2: SNO results after Phase-II: flux of $\nu_{\mu+\tau}$ versus flux of ν_e ^{8}B solar neutrinos. Contributions coming from all three reactions: CC, NC and ES are indicated by the filled bands. The 68% limits on total ^{8}B solar neutrino flux predicted by the SSM are shown as dashed lines. In addition, the Super-Kamiokande results [25] are also shown with the narrow band parallel to the SNO ES results. Black dot indicates the best fit point together with contours for 68, 95, and 99% CL. Figure is taken from Ref. [27]

All solar neutrino results (from SNO, Super-Kamiokande, Chlorine, Gallium and Borexino experiments) have been included into so-called global neutrino oscillation analysis performed by the SNO collaboration. The results of global analysis with KamLAND data are shown in Fig. 1.3. We may observe that KamLAND measurements provided the most precise constrain on Δm^2_{12} in the solar sector up to now. The joint results from global neutrino oscillation analysis give [26]:

$$\begin{aligned} \Delta m^2_{21} &= 7.59^{+0.20}_{-0.21} \times 10^{-5} eV^2 \\ \theta_{12} &= 34.06^{+1.16}_{-0.84} \quad \text{degrees} \\ \tan^2\theta_{12} &= 0.457^{+0.040}_{-0.029} \end{aligned}$$

Atmospheric neutrino experiments - oscillation parameters Δm^2_{23} and θ_{23}

The next sector to be investigated is the one defined by the oscillation parameters θ_{23} and Δm^2_{23}. This time sector 23 is named atmospheric sector as evidence suggesting oscillation were coming from atmospheric neutrino observations which resulted in measurements of θ_{23} and Δm^2_{23}. Similarly to solar neutrino physics, here several different detection techniques were used. They are based on:

- water Cherenkov detectors: Kamiokande [23], IMB [33] and Super-Kamiokande [34].
- fine grained tracking detectors: NUSEX [35], Frejus [36], MACRO [37] and Sudan-2 [38].

All projects listed above were measuring directly atmospheric neutrinos. In addition there was also a significant impact from long baseline accelerator experiments like: K2K [40], MINOS [41] and OPERA [42]. In all of them neutrinos were produced artificially in the laboratories.

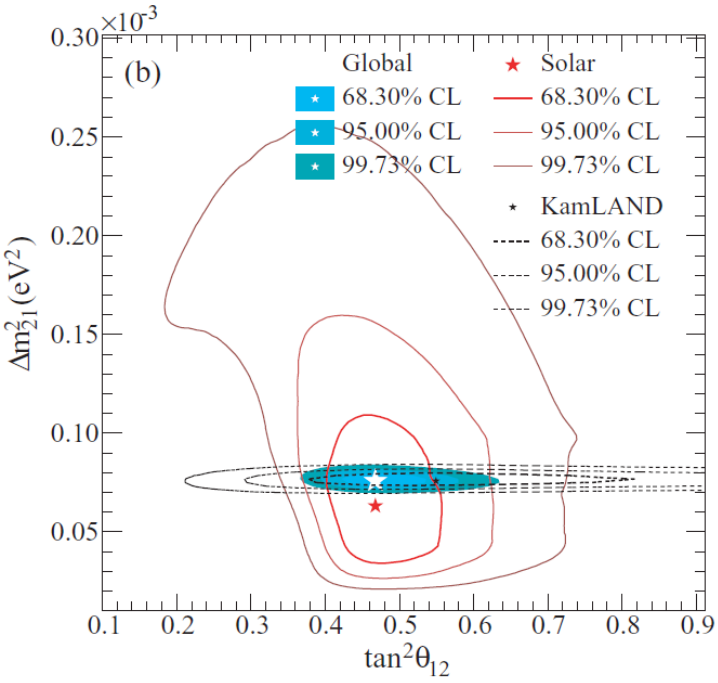

Figure 1.3: Solar and KamLAND oscillation parameter analysis. The solar data include resultsfrom SNO, SAGE, GALLEX, Borexino and Super-Kamiokande experiments. Figure is taken from Ref. [28]

Atmospheric neutrinos are produced in the interactions of primary cosmic rays (mainly protons) with the nuclei present in the atmosphere. These interactions generate secondary particles, which include all the hadrons and their decay products. In particular, many secondary pions are produced. They decay into:

$$\pi^+ \to \mu^+ + \nu_\mu$$
$$\pi^- \to \mu^- + \nu_\mu$$

The muons which decay before hitting the ground generate electrons, electron neutrinos and muon neutrinos through processes:

$$\mu^+ \to e^+ + \nu_e + \bar{\nu_\mu}$$
$$\mu^- \to e^- + \bar{\nu_e} + \nu_\mu$$

Energies of neutrinos produced in such a way range up to TeV.
At low energies ($E \leq$ 1-2 GeV) for which most of the muons decay before hitting the ground, we expect to have two $\nu_\mu + \bar{\nu_\mu}$ components for each produced $\nu_e + \bar{\nu_e}$. The ratio (R):

$$R \equiv \frac{\nu_\mu + \bar{\nu_\mu}}{\nu_e + \bar{\nu_e}} \tag{1.11}$$

increases with the energy as more energetic muons reach the Earth's crust before they decay.

The first experimental observations of atmospheric neutrinos started in 1960 by F. Reines and colleagues [32]. Next IMB [33] and Kamiokande [23] as well as NUSEX [35] and Frejus [36] were also studying this physics field and the conclusions from the observations were not changed. Similarly to solar sector, scientists began to call the measured deficit of atmospheric neutrinos as "atmospheric neutrino anomaly".

The first direct solution to problem of "atmospheric neutrino anomaly" was presented by the Super-Kamiokande in 1998 [34]. This report gave also the first essential proof for the neutrino oscillation phenomena. Super-Kamiokande collaboration examined μ-like events, which are mostly muon-neutrino and muon antineutrino CC reactions as well as e-like events. They were looking at those events which were fully contained (FC) as well as partially contained (PC). The first sample was required to have signal in the 22.5 kton fiducial volume of the SK detector (for details of the detector overview please refer to Sec 2.3 on page 24), whereas PC by definition should have also PMTs signals in outer part of SK. Moreover, FC as well as PC events are classified into single-ring and more complicated multi-ring. Those single-ring events have only one charged lepton which radiates Cherenkov light in the final state, making the particle identification very reliable and clean. In Fig. 1.4 the illustration of the zenith-angle distributions of e-like and μ-like events from the SK measurements [39] is presented. Note, that $\cos\theta$=1 (-1) corresponds to the downward (upward) direction, respectively. These plots are made of single-ring FC events as well as multi-GeV events (they are visible for energy $>$ 1.33 GeV). The dotted, red histograms show simulated expectations without assumption on the neutrino oscillation phenomena, whereas the solid, green histograms show the best-fit expectations for the $\nu_\mu \to \nu_\tau$ oscillations. This oscillation pattern was assumed basing on the observations of the e-like and μ-like events. For the first sample we see that both measurements as well as expectations are consistent. On the other hand the zenith-angle distributions of the μ-like events show a large discrepancy from the expectations for the upward neutrino flux. This fact is explained as follows: muon neutrinos coming from the opposite side of the Earth's atmosphere, travel 10,000 km and oscillate into other neutrino flavors. As we do not see indication of electron neutrino appearance this other flavor could be only tau neutrinos.

Studies of atmospheric neutrino sector show that the most precise measurements of the oscillation parameters Δm^2_{23} and θ_{23} were performed by the accelerator experiments. The first accelerator-based, long-baseline oscillation experiment was K2K (KEK-to-Kamioka) project. It was *disappearance* type of experiment and was designed to provide another confirmation of neutrino oscillation phenomena. K2K used wide-band focused by horns muon neutrino beam, produced by 12 GeV protons from KEK-PS. The beam was measured 300 m from the target station (near detector) and 250 km away in the Super-Kamiokande. Data were taken from 1999 till November 2004. They observed 112 FC events while $158.1^{+9.2}_{-8.6}$ were expected without oscillations. Next the second oscillation long-baseline project called MINOS entered the game with near and far detectors system [41]. This time neutrinos were produced by the NuMI (Neutrinos at the Main Injector) research complex. They were using 120 GeV protons from Fermilab Main Injector. What was different from the K2K experiment was the detection technique used. In MINOS both near and far stations were made of iron-scintillator tracking calorimeters placed in the magnetic field, which allowed to determine the sign of produced particles due to neutrino interactions. Far detector is located 735 km away from the Fermilab, *i.e.* in the Soudan mine. MINOS started data taking in 2005. In Fig. 1.5 MINOS results are presented in terms of the oscillation parameters Δm^2_{23} and $\sin^2 2\theta_{23}$ (see Ref. [43]). Different CL allowed regions are shown (68% and 90%). The black dot represents the best fit point for the MINOS measurements. Results of SK-I and K2K 90% CL allowed regions are also included. Consistency is observed between experimental results. Extracted values of the atmospheric oscillation parameters are given below [43]:

$$\begin{aligned} \Delta m^2_{23} &= (2.43 \pm 0.13) \times 10^{-3} eV^2 \qquad (68\%\text{CL}) \\ \sin^2 2\theta_{23} &> 0.90 \qquad (90\%\text{CL}) \end{aligned}$$

Finally we would like to mention another accelerator long-baseline project - OPERA [42]. Its main purpose is to observe *appearance* transition of a type $\nu_\mu \to \nu_\tau$ by identifying τ

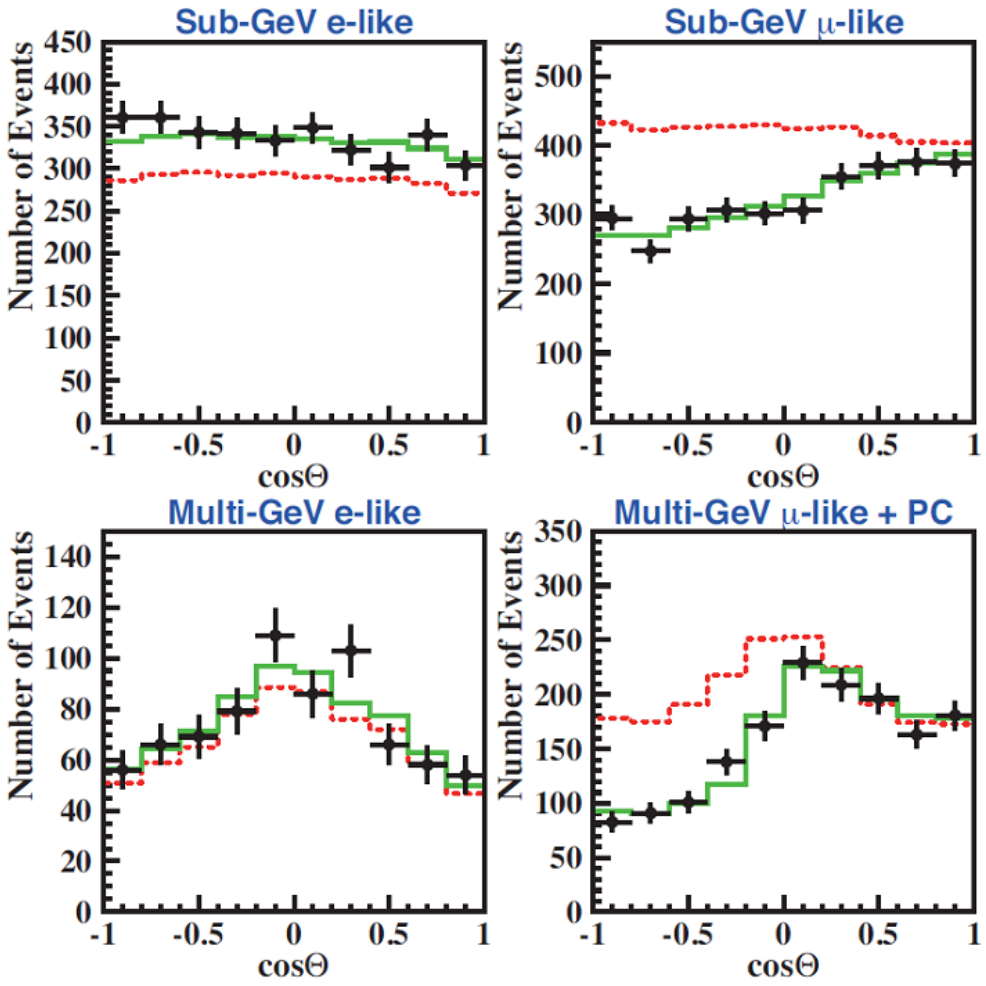

Figure 1.4: First Super-Kamiokande results on the neutrino oscillation phenomena. All plots show zenith-angle distributions for e-like and μ-like events which are grouped into one with visible energy $<$ 1.33 GeV (sub-GeV) and $>$ 1.33 GeV (multi-GeV). The dotted histograms represent non-oscillated expectations, while the solid ones stand for the best-fit expectations for the transition of the $\nu_\mu \to \nu_\tau$. This figure is prepared by the Super-Kamiokande Collaboration in 1998 but is taken from Ref. [26].

leptons with the help of emulsion technique. OPERA is using CNGS (CERN Neutrinos to Gran Sasso) muon neutrino beam with average energy of 17 GeV produced by CERN SPS. OPERA has only far detector placed 730 km away from the neutrino source in the Gran Sasso Underground Laboratory in Italy. After two years of data taking the collaboration managed to observe one τ candidate with a significance of 2.36σ. The expected number of events in the analysed sample is 0.54 ± 0.13(syst) [42].

Measurements of unknown mixing angle θ_{13}

Up to now much less is known about θ_{13} - an angle which is considered to be small compared to the other two. Among several conducted neutrino projects the ones which have any constraints on the θ_{13} measurement are listed below:

- short baseline reactor experiments: CHOOZ [44], Palo Verde [45].

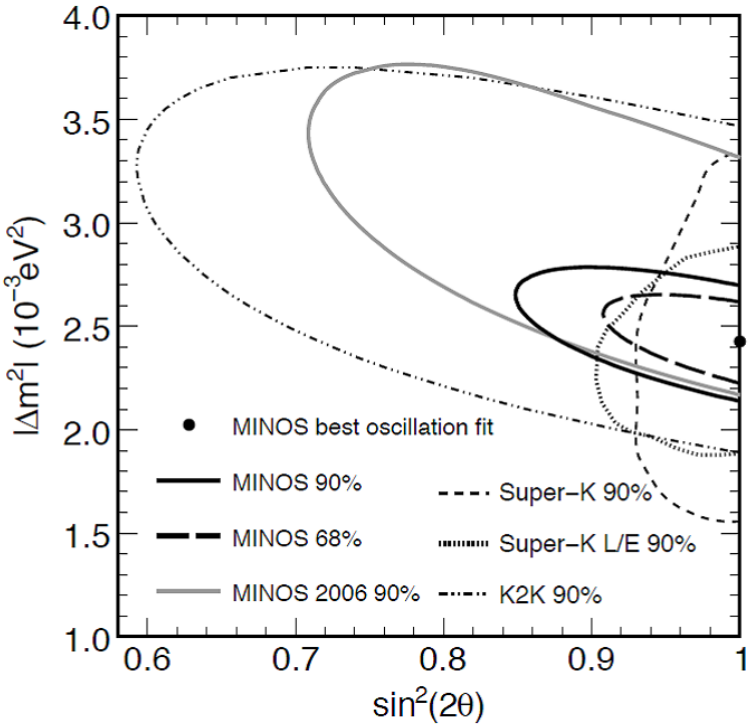

Figure 1.5: $\nu_\mu \to \nu_\tau$ oscillation results from MINOS. Different CL allowed regions are shown (68% and 90%). The black dot represents best-fit point. Results of SK-I and K2K 90% CL allowed regions are also included. This figure is taken from Ref. [43].

- long-baseline experiments: K2K [46], SNO [47].

Short baseline reactor experiments, *i.e.* with $L \sim 1$ km and $E \sim 3$ MeV are sensitive to Δm^2_{23} about $3 \times 10^{-3}\text{eV}^2$ which means that influence of the solar neutrino sector in the oscillation physics is negligible. This fact was used by the CHOOZ experiment [44] located in France to determine θ_{13}. CHOOZ detector was placed under 300 mwe (meter water equivalent) rock overburden. Its central part was made of Gadolinium loaded liquid scintillator. The reaction of interest was the inverse β decay (see Eq. (1.1)). The CHOOZ experiment didn't find any indication of $\bar{\nu_e}$ *disappearance* but it has put the best limit on the value of $\sin^2 2\theta_{13} < 0.19$ for $\Delta m^2_{23} = 2.0 \times 10^{-3}$ eV^2 at 90% CL. Consistent with CHOOZ but less restictive were the limits from similar experiment, *i.e.* Palo Verde at Arizona [45]. In case of accelerator long-baseline experiments like K2K the *appearance* signal of $\nu_\mu \to \nu_e$ was investigated and none was found [46]. At $\Delta m^2_{23} = 2.8{\times}10^{-3}\text{eV}^2$, the best fit value of the K2K ν_μ disappearance analysis, K2K sets an upper limit of $\sin^2 2\theta_{13} < 0.13$ at 90% CL. Finally, it may be stated that as a results of all the experimental data, including SNO, the best upper bound on $\sin^2\theta_{13} <$ 0.031 (0.047) at 90% CL (3σ) [48].

Summary and conclusions

All available neutrino oscillation data give constraints on the values of oscillation parameters. The mass-squared differences are determined relatively accurately from the spectral data in the KamLAND [31], K2K [40] and MINOS [41] experiments, respectively:

$$\begin{aligned} \Delta m^2_{23} &= (2.40^{+0.12}_{-0.11}) \times 10^{-3} eV^2 \\ \Delta m^2_{12} &= (7.59^{+0.20}_{-0.21}) \times 10^{-5} eV^2 \end{aligned}$$

We know that two out of the three mixing angles are large:

$$\begin{aligned} \sin^2\theta_{23} &= 0.50^{+0.07}_{-0.06} \\ \sin^2\theta_{12} &= 0.318^{+0.019}_{-0.016} \end{aligned}$$

and one θ_{13} is small, but it is still not precisely measured:

$$\sin^2\theta_{13} < 0.031(0.047) \text{ at } \quad 90\%\text{CL}(3\sigma) \tag{1.12}$$

In Fig. 1.6 the current knowledge on oscillation parameters coming from various neutrino experiments is demonstrated. One can observe regions of neutrino oscillation parameters which are allowed or excluded by different experiments.

Clearly what is still missing is the precise value of the θ_{13}. This subject is of most interest for current and future neutrino experiments. The first one, called T2K, is already running. The details of this project are introduced in next chapter. Here we will just point out that in June 2011 T2K published a paper [2] in which the first indication of electron neutrino *appearance* from artificially produced off-axis muon neutrino beam was presented. Six candidate events were left after all selection criteria while only 1.5 ± 0.3 were expected. The T2K plans to take data for five years and more significant results in the nearest future may be expected. Besides the T2K, there are several neutrino oscillation experiments currently under construction, which are designed to investigate θ_{13}. These are the reactor neutrino experiments Daya Bay [49], Double Chooz [50], RENO [51] and the accelerator experiment NOVA [52].

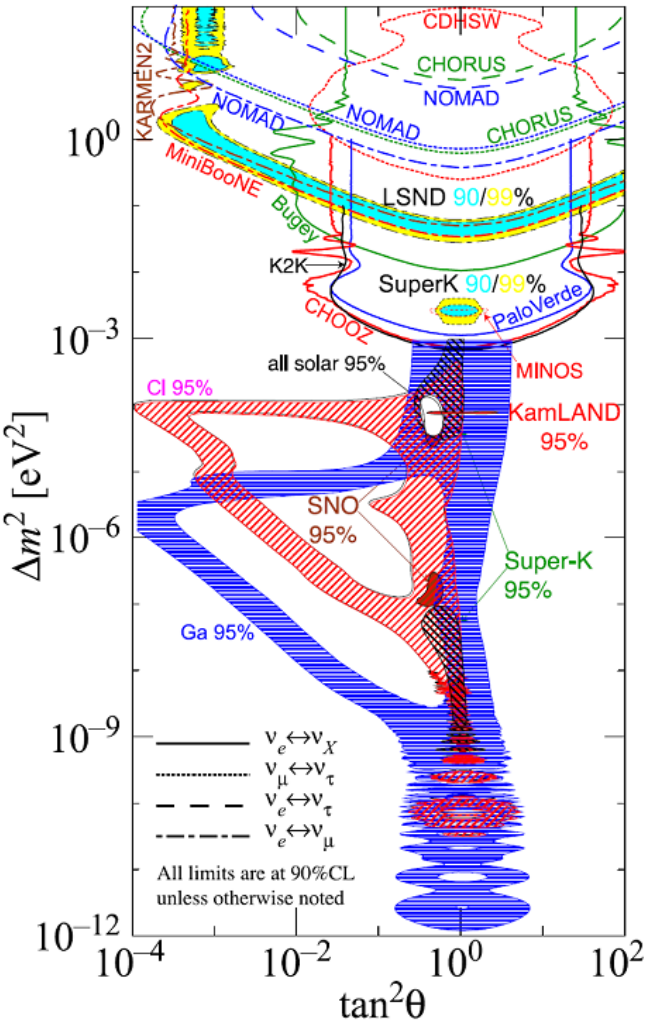

Figure 1.6: Results from various neutrino oscillation experiments. One can observe regions of neutrino oscillation parameters which are allowed or excluded by different experiments. This figure is taken from Ref. [26].

Chapter 2

T2K experiment and its prerequisites for NA61/SHINE measurements

The T2K (Tokai-to-Kamioka) is a second generation long baseline neutrino oscillation experiment which aims at precise measurements of the neutrino masses and mixing angles [53]. The most significant search concerns examination of still unknown θ_{13} which will be carried out by detection of $\nu_\mu \to \nu_e$ *appearance*. Moreover, T2K will be able to achieve an order of magnitude better precision in the measurements of θ_{23} as well as Δm_{23} in the ν_μ *disappearance* channel. In order to accomplish it, high intensity narrow band neutrino beam is produced at Japan Proton Accelerator Research Complex (J-PARC) in Japan [54] from secondary pions and kaons created by interactions of 30 GeV (kinetic energy) protons on 91 cm long carbon target. The neutrino beam is tuned to the oscillation maximum at ~ 0.6 GeV and is directed at 2.5^0 off-axis towards near station, placed at 280 m from the target, named ND280 [55, 56] and far station located 295 km away - the world largest water Cherenkov detector Super-Kamiokande (SK) [34]. It is designed to study neutrino oscillations by comparing measured with predicted neutrino flux at SK. The latter one is obtained using measured flux in ND280 which is later on extrapolated to the SK with the help of Monte Carlo (MC) simulations of neutrino beam. These neutrino beam predictions require knowledge of the hadron productions which is strongly model dependent. In order to diminish uncertainty on the knowledge of pion and kaon production mechanism off the carbon target, precise hadron production measurements are very crucial. They would be used in order to tune results with existing MC predictions to be as precise as possible with measurements. Unfortunately, in the history of the hadron production experiments no one carried out needed measurements. In this scenario the NA61/SHINE [79, 80, 81] comes into importance as in the first stage of data taking (2007-2010) it aims to deliver for the data needed for T2K.

In this chapter we introduce T2K experiment with its physical goals and justification of needed pion and kaon cross section measurements coming from the 30 GeV kinetic energy p+C interactions. Later on, *i.e.* in Sec. 2.6 we give a brief summary of existing hadron production measurements. The last part of the chapter is focused on the T2K requirements on the NA61/SHINE measurements.

2.1 The T2K long baseline neutrino oscillation experiment

The T2K experiment is a long baseline neutrino oscillation experiment which uses an intense proton beam produced by the J-PARC accelerator in Tokai, Japan. It is composed of neutrino beamline, near detector complex (ND280), both of which were newly constructed and far detector Super-Kamiokande located 295 km away from J-PARC (see Fig. 2.1). Comprehensive

review of the instrumentation aspect of the T2K experiment may be found in Ref. [57]. We will only introduce here its major subjects.

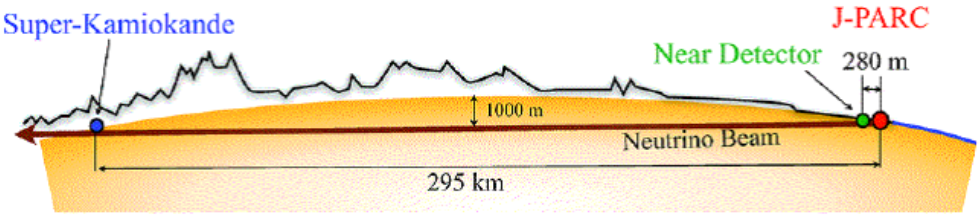

Figure 2.1: Schematic view of the T2K experiment. Neutrino beam is produced at J-PARC facility and measured by near detectors (green dot) used to determine the properties of the neutrino beam, and 295 km away far detector Super-Kamiokande. Figure is taken from Ref. [57]

T2K adopts an off-axis method [58] to generate the narrow band beam using the new proton synchrotron at J-PARC. In this approach the neutrino beam is deliberately directed at given angle with respect to the baseline connecting the proton target and the far detector, Super-Kamiokande. The off-axis angle is set at 2.5^0. This corresponds to the peak in energy at 0.6 GeV (see Sec. 2.5.2) which maximizes the effect of the neutrino oscillations at the 295 km as well as minimizes the background to the electron-neutrino *appearance* detection.

The near detector facility, placed at 280 m from the target, consists of on-axis and off-axis detectors. The neutrino beam direction and profile is measured by the on-axis setup (INGRID). Measurements of muon neutrino flux and its energy spectrum as well as intrinsic electron neutrino contamination are the major purpose of the off-axis detectors. All these measurements are vital for the precise characterization of the signal and backgrounds which are measured in the SK. More details of ND280 complex are covered in Sec. 2.2.3.

The far detector SK is located in the Mozumi mine of the Kamioka Mining, near the village of the Higashi-Mozumi, Gifu prefecture, Japan. The detector is placed under Mt. Ikenoyama with 1000 m overburden of rock. It is water Cherenkov detector in a shape of cylinder made of stainless-steel, with 39 m diameter and 42 m height. It is equipped with around 13.000 photomultiplier tubes (PMTs) which detect Cherenkov light from the neutrino interactions in pure water. It has been running since 1996 and was able to deliver many results that involve: measurement of oscillation mechanism in atmospheric, solar and artificially produced neutrinos in accelerator physics [59, 60, 61, 40] as well as set world leading limits on proton lifetime [62, 63, 64]. During this time we can assign to Super-Kamiokande four running periods: SK-I, SK-II, SK-III and the latest in which T2K takes place is SK-IV with upgraded PMT readout electronics. Super-Kamiokande has been running so far for the sixteen years which allowed to understand its detection features very well. A more detailed description of the Super-Kamiokande may be found in Sec. 2.3.

The synchronization between neutrino event trigger at Super-Kamiokande and beam spill produced at J-PARC is based on the Global Positioning System (GPS). As stated in Ref. [57] the accuracy of absolute time determination at two sites is demonstrated to be less than 50 ns. The coincidence of any entering background in Kamioka mine is negligibly low.

On 23^{rd} April, 2009 the first neutrino events from the T2K beam were detected in the Super-Kamiokande detector. The first physics run began in January 2010 and lasted till June. After the summer break continuous running began in November 2010. Unfortunately, Japan experienced very severe earthquake on March 11th 2011, which was the reason for stopping the data taking. J-PARC was somewhat damaged by the earthquake, but fortunately was not

affected by the tsunami.

The T2K experiment managed to collect 1.43×10^{20} protons on target (pot), which served as a basis for the *appearance* analysis. As a result of the analysis T2K reported an indication of ν_e *appearance* from off-axis muon neutrino beam [2]. This important finding used NA61/SHINE measurements presented in this dissertation. We will come to this subject in the last Chapter 10.

2.2 J-PARC facility

In the following sections we introduce the J-PARC complex, placed at Tokai, Ibaraki prefecture with its accelerator system, responsible for production of the T2K neutrino beam, as well as near detector station with on-axis and off-axis subcomponents.

2.2.1 J-PARC accelerator

J-PARC is equipped with three accelerators [66]: a linear accelerator (LINAC), a Rapid Cycle Synchrotron (RCS) and a Proton Synchrotron called Main Ring (MR). The design energies of the three acceleration stages are 400 MeV (181 MeV at present), 3 GeV and 30 GeV, respectively. The number of bunches in MR is eight (six before June 2010). There are two extraction points in the MR: slow extraction for the hadron beamline and fast extraction for the neutrino beamline. The design parameters of the J-PARC MR for the fast extraction are listed in Tab. 2.1.

Circumference	1567 m
Beam power	750 kW
Beam kinetic energy	30 GeV
Beam intensity	3×10^{14} p/spill
Spill cycle	∼0.5 Hz
Spill width	~ 5 μsec

Table 2.1: The characteristics of MR for the fast extraction in J-PARC. Numbers taken from Ref. [57].

2.2.2 Primary and secondary T2K beamline

The neutrino beamline consists of two complementary subsystems as shown in Fig. 2.2. These are: the primary and secondary beamlines. In the primary beamline we can distinguish preparation section (54 m long), arc section (147 m) and final focusing section (37 m). Preparation section is responsible for tuning the proton beam with the help of 11 normal conducting magnets. Proton beam may later on encounter arc section where it is bent towards the direction of Kamioka by 80.7^0, with 104 m radius of curvature. In the final focusing section ten super conducting magnets guide and focus the beam onto the target.

A well tuned proton beam is of great importance for the stable neutrino beam production, thus in J-PARC facility there are several beam monitors placed in order to control the proton beam intensity, profile, position or loss. Details of each monitor may be found in Ref. [57].

Three sections constitute the secondary beamline: the target station, decay volume and beam dump (see Fig. 2.3). The target station is equipped with a collimator which protects

the three magnetic horns, an optical transition radiation monitor (OTR) to control the proton beam profile upstream of the target, the carbon target placed inside the first horn and two additional magnetic horns which together with the first one work currently at 250 kA (designed to handle 320 kA) current pulse to focus secondary charged particles (amongst which of interest are mainly pions and kaons) produced during p+C interactions.

The T2K target is a 1.9 interaction length (91.4 cm long), 2.6 cm diameter and 1.8 g/cm^2 density graphite rod. It is placed inside the first horn as shown in Fig. 2.4. If the target material would be much denser than graphite it would be melted by the pulsed beam head load. When the 0.75 MW proton beam interacts with the target, the temperature at the center is expected to reach 700^0C, which is the reason why the target is cooled by helium gas flowing through the gaps between the tube and 0.3 mm thick titanium case.

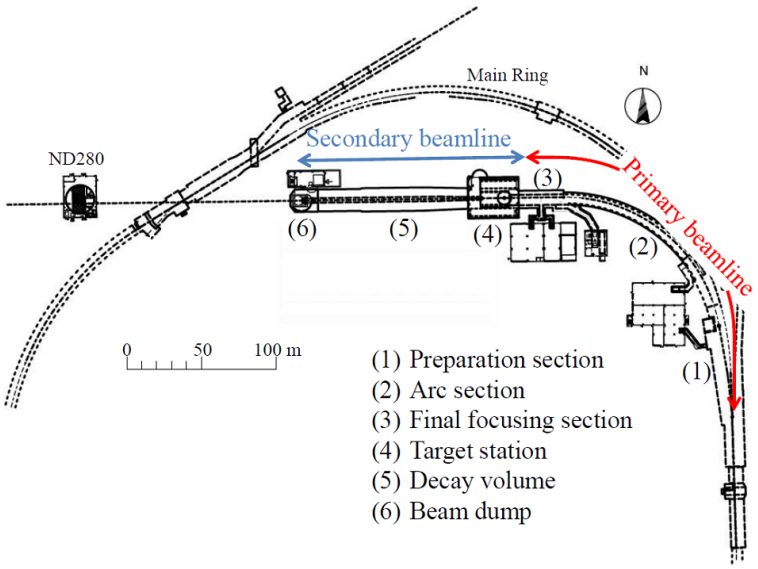

Figure 2.2: T2K beamline at J-PARC. Figure is taken from Ref. [57]

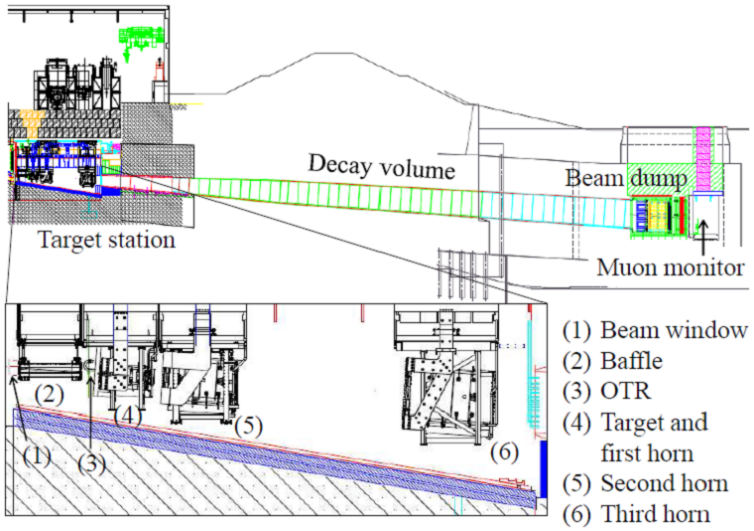

Figure 2.3: Secondary T2K beamline at J-PARC. Figure is taken from Ref. [57]

The T2K beamline uses three horns to select positive particles (mainly pions with admixture of kaons) and bend negative ones. Each magnetic horn is built of inner and outer conductors [67, 68]. The toroidal magnetic filed is generated inside the inner conductor and at radius r it is given with the help of Ampere's law, by the formula:

$$B(r) = \frac{\mu_0 I}{2\pi r} \frac{r^2 - a^2}{b^2 - a^2} \tag{2.1}$$

where μ_0 is the magnetic permeability, I is the current, r is the distance from the horn axis and a and b are, the inner and outer radii of the inner conductor, respectively. The first horn collects secondary positive charged particles mainly pions, which are produced during p+C interactions. The second and the third horn focuses secondaries. As stated in Ref. [57], when the horns are running with 320 kA currents the neutrino flux at Super-Kamiokande at the spectrum peak energy of about 0.6 GeV is increased by a factor of 16 (compared to horns at 0 kA). Thus application of magnetic horns in the T2K experiment is very essential.

Next on the way is the decay volume which is 96 m long steel tunnel. Pions decay there into muons and muon neutrinos:

$$\pi^+ \rightarrow \mu^+ + \nu_\mu \tag{2.2}$$

Some of the resulting muons can also decay producing muon antineutrinos and electron neutrinos:

$$\mu^+ \rightarrow e^+ + \bar{\nu_\mu} + \nu_e \tag{2.3}$$

Less numerous kaons also decay with production of electron neutrinos:

$$K^+ \rightarrow \pi^0 + e^+ + \nu_e \tag{2.4}$$

This way an intense neutrino beam is produced and directed towards ND280 and SK. Two last channels are source of the beam contamination. We would like to have pure muon neutrino beam but clearly we may expect contamination of other neutrinos. This subject will be investigated further in Sec. 2.5.2.

At the end of the decay volume we encounter beam dump which absorbs any hadrons as well as muons below 5 GeV/c that reach the end of the tunnel. It is built of graphite blocks cooled with water in aluminum pipes. Particles that pass the dump are, beside the neutrinos

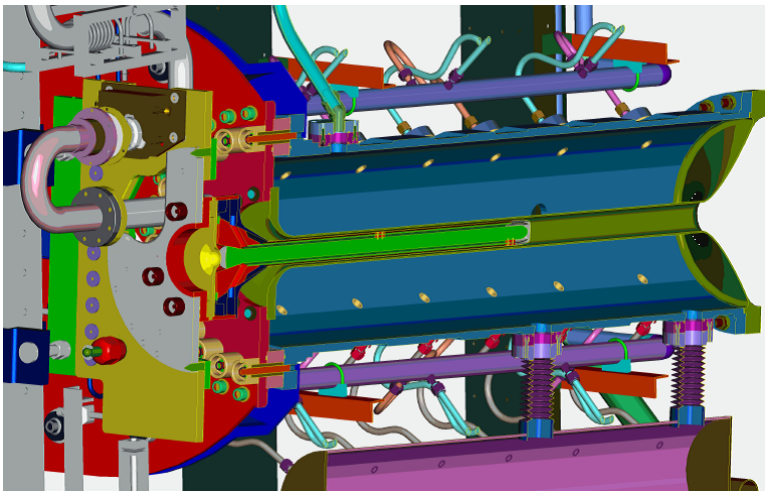

Figure 2.4: Cross section of the first horn with target (green cylinder). Figure is taken from Ref. [57]

of course, high energy muons (*i.e.* with $p > 5$ GeV/c). They are used by muon monitor situated downstream to the dump to keep an eye on the beam direction.

2.2.3 Near detector complex

As stated earlier the near detector complex consists of on-axis as well as off-axis subcomponents which aim is to deliver information on the neutrino energy spectrum, flavor content and interaction rates of the unoscillated beam. At first let's focus on the on-axis device which is INGRID. It was designed to monitor directly the neutrino beam direction and intensity. INGRID consists of 14 identical modules arranged as a cross of two identical groups along the horizontal and vertical axes. There are also two extra modules located at off-axis directions outside the main cross (see *left* plot in Fig. 2.5). These modules are made of 9 iron plates sandwiched between ten scintillator tracking planes. The center of INGRID cross, with two overlapping modules, corresponding to neutrino beam center, defined as 0^0 with respect to the direction of the primary proton beam. INGRID is able to determine the beam direction to better than 1 mrad on a day-by-day basis, which corresponds to a 1 mm shift at the target.

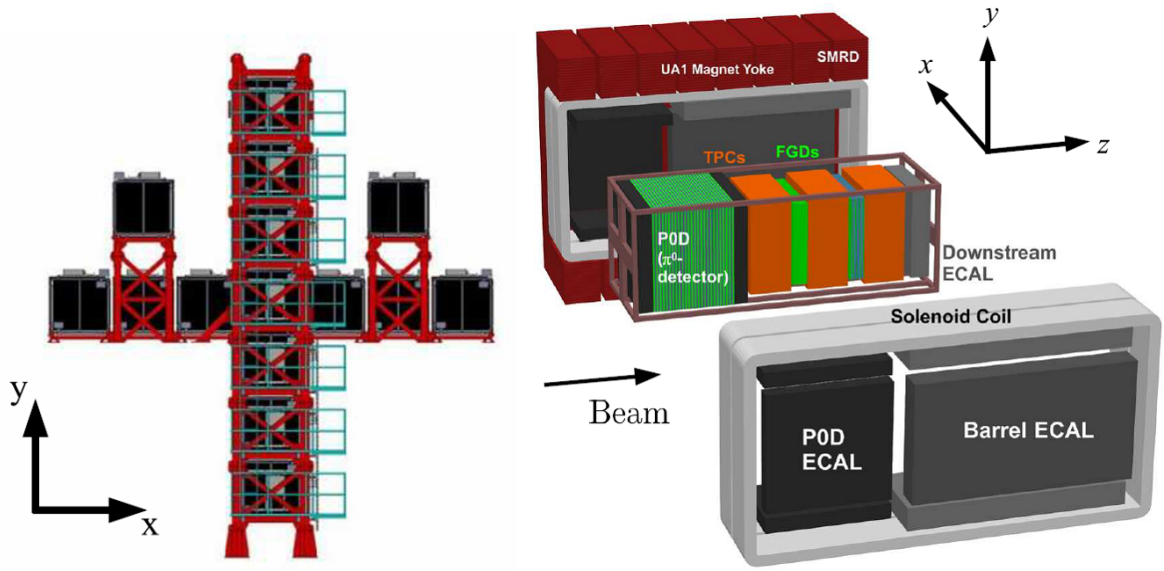

Figure 2.5: The near detector complex with INGRID *(left)* and ND280 *(right)*. Figures are taken from Ref. [57]

Next to INGRID, the near detector complex is equipped with the off-axis magnetized multipurpose detector ND280. The ND280 off-axis detector must satisfy several requirements. The most important one is to measure ν_μ flux which will be used next in order to determine the ν_μ flux at the Super-Kamiokande. Secondly, the ν_e content of the beam must be measured as a function of neutrino energy as it constitutes significant non-removable background in $\nu_\mu \to \nu_e$ *appearance* search (see Sec. 2.5.2). Thirdly, it must measure also such ν_μ interactions which may result in additional background to the ν_e *appearance* search at Super-Kamiokande. They are dominated by neutral current single π^0 production [69]. All of these requirements were considered while designing off-axis detector.

The ND280 off-axis detector is composed of several subcomponents, as illustrated in *right* panel in Fig. 2.5. These are: water/scintillator detector optimized to identify π^0 from NC interactions of ν_μ (the POD), the tracker consisting of time projection chambers (TPCs)

and fine grained detectors (FGDs) optimized to study CC ν_μ and ν_e interactions, and an electromagnetic calorimeter (ECal) that surrounds the POD and the tracker. ECal detects showering particles (like e^-, γ) which are escaping from the inner detectors. All these subcomponents are placed in a 0.2 T magnetic field produced by magnet coming from former experiment UA1/NOMAD at CERN, inside of which we may find also Side Muon Range Detector (SMRD). Plastic scintillation detectors of SMRD measure long range muon trajectories originating from the interactions in the detector. It is also used as a trigger on cosmic ray particles. More detailed description of the ND280 may be found in Ref. [55, 57].

2.3 Overview of the Super-Kamiokande detector

The geometry of the Super-Kamiokande detector consists of two major volumes, an inner and an outer detector with a cylindrical stainless steel structure placed between them. A schematic view of the Super-Kamiokande is presented in Fig. 2.6. Inner detector (ID) is a cylindrical space 33.8 m in diameter and 36.2 m in height. It is equipped with 11,129 inward-facing 50 cm PMTs. Enclosing the ID is the outer detector (OD) defined as a cylindrical space of 2 m thick radially on the axis at both ends. The OD contains on its walls 1,885 20 cm diameter PMTs. The PMTs detect the Cherenkov light produced by relativistic charged products of neutrino interactions. The shape of the Cherenkov rings depends on the particle type which is producing them. For example, muons which are used to measure ν_μ *disappearance* channel, undergo insignificant changes in their momentum direction due to their relatively large mass. As a consequence, they produce well-defined cones of Cherenkov radiation which are reflected by sharp rings seen by the PMTs. This scenario is not the case for the electrons, used to search for the *appearance* channel. Electrons are much lighter than muons and they are very sensitive to change of their momentum directions resulting from the multiple Coulomb scattering. The rings produced by electrons in the electromagnetic cascade have "fuzzy" pattern, as it consists of sum of many overlapping Cherenkov cones. These differences between sharp and "fuzzy" rings are used by the Super-Kamiokande event reconstruction software to distinguish whether rings are coming from muon-like or electron-like particles. A more detailed description of the Super-Kamiokande may be found elsewhere [34, 65].

2.4 T2K physical goals

The T2K experiment is designed to search for ν_e *appearance* with the sensitivity to $\sin^2 2\theta_{13} \approx 0.008$ (90% C.L.) [53, 57] from the ν_μ neutrino beam. As we have learned from the Chapter 1 *appearance* probability is strongly correlated with the knowledge of the athmospheric oscillation parameters: θ_{23} as well as Δm^2_{23} which means that it is very crucial to measure them as precisely as possible. In this case ν_μ *disappearance* measurement is also of interest for the T2K. Under the assumption of five years of running with 0.75 MW on target, the T2K would be able to improve current measurements from MINOS [41], SK [34] and K2K [40] (see Sec 1.2 on page 11) of $\delta(\sin^2 2\theta_{23})$=0.01 and $\delta(\Delta m^2_{23}) = 10^{-4}$ eV^2. In order to achieve this goals T2K has to fulfill several conditions. One of the crucial part is to understand as precisely as possible the T2K neutrino beam about which we will write more in the next sections.

2.5 T2K off-axis neutrino beam

In this section at first we will introduce advantages of the off-axis neutrino beam over the on-axis configuration. Secondly, predictions of the T2K fluxes at near and far detectors will

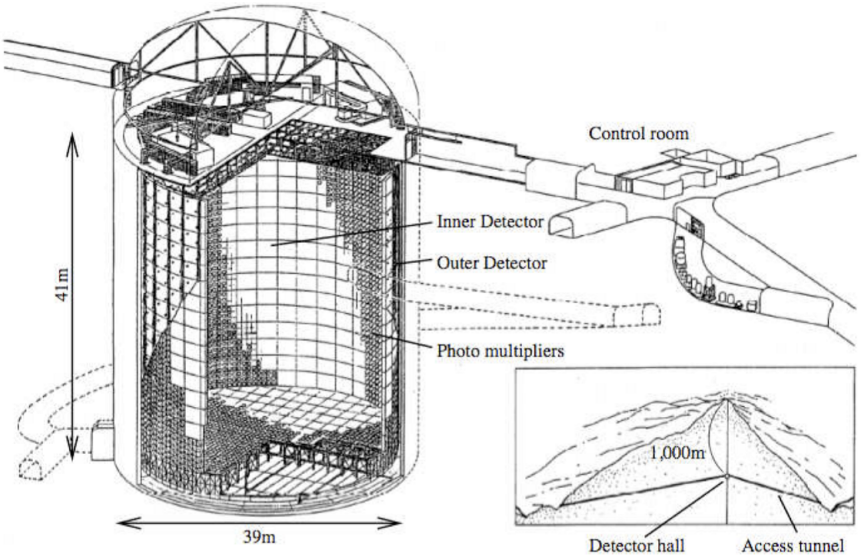

Figure 2.6: Schematic view of the Super-Kamiokande detector. The inner and outer detectors are also shown. Figure is taken from Ref. [53]

be studied using the Monte Carlo simulation tool, JNUBEAM, which belongs to the T2K software package. At the end, the importance of the far-to-near flux ratio will be discussed.

2.5.1 General properties of the off-axis neutrino beams

In order to study the properties of the off-axis neutrino beam we will take into account pion decays which are of major interest for the neutrino beam production. Branching ratio for pions decaying into muons and muon neutrinos (see Eq. 2.2) is 100%. The pion has spin zero and as a result the decay in its rest frame is isotropic. Neutrino energy in pion rest frame, denoted as E^*_ν, is constant and equal to:

$$E^*_\nu = \frac{m^2_\pi - m^2_\mu}{2m_\pi} \simeq 30MeV \tag{2.5}$$

where m_π and m_μ are the charged pion and muon mass, respectively. The laboratory angle between neutrino and pion direction will be denoted as θ. Note, that for pions focused by horns in the forward direction this angle will be also a good approximation of the off-axis angle, *i.e.* angle between primary proton and neutrino beam direction. The θ angle can be expressed by the transverse p_t and longitudinal, p_l, components of the laboratory ν_μ momentum p:

$$\tan\theta = \frac{p_t}{p_l} \tag{2.6}$$

Assuming massless neutrinos the Lorentz transformation gives:

$$\begin{aligned} p_t &= p^*_t = E^*_\nu \sin\theta^* \\ p_l &= \gamma_\pi(p^*_l + \beta_\pi E^*_\nu) = \gamma_\pi(E^*_\nu \cos\theta^* + \beta_\pi E^*_\nu) = \gamma_\pi E^*_\nu(\cos\theta^* + \beta_\pi) \\ E_\nu &= \gamma_\pi(E^*_\nu + \beta_\pi p^*_l) = \gamma_\pi E^*_\nu(1 + \beta_\pi \cos\theta^*) \end{aligned} \tag{2.7}$$

where all quantities with star denote pion rest frame and others represent laboratory frame. Let's consider relativistic pions $E_\pi \gg m_\pi$ with $\beta_\pi = 1$. Then:

$$p_l = E_\nu = \gamma_\pi E^*_\nu(1 + \cos\theta^*) \tag{2.8}$$

and:

$$\tan\theta \cong \frac{E_\nu^* \sin\theta^*}{E_\nu} \tag{2.9}$$

As $E^* \simeq$30 MeV is much smaller than the laboratory neutrino energies of interest, we see that the θ angle are very small and limited:

$$\tan\theta < \frac{30\text{MeV}}{E_\nu} \tag{2.10}$$

It is also seen that:

$$E_\nu \cong \frac{E_\nu^* \sin\theta^*}{\tan\theta} < \frac{30\text{MeV}}{\tan\theta} \tag{2.11}$$

i.e. for a fixed θ angle the neutrino energy does not depend on the pion momentum and maximum E_ν gets smaller with increasing θ angle. On the other hand one can see that for $\theta = 0$ which implies that $\theta^* = 0$ the neutrino energy is equal to:

$$E_\nu = 2\gamma_\pi E_\nu^* = 2E_\pi \frac{E_\nu^*}{m_\pi} \tag{2.12}$$

i.e. neutrino energy E_ν is proportional to the pion energy E_π. In Fig. 2.7 we display effects of these considerations. Note that small dependence of E_ν on E_π provides narrow almost monoenergetic distribution of E_ν. In this way one gets narrow band beam, which is very desired for precise neutrino experiments, like the T2K.

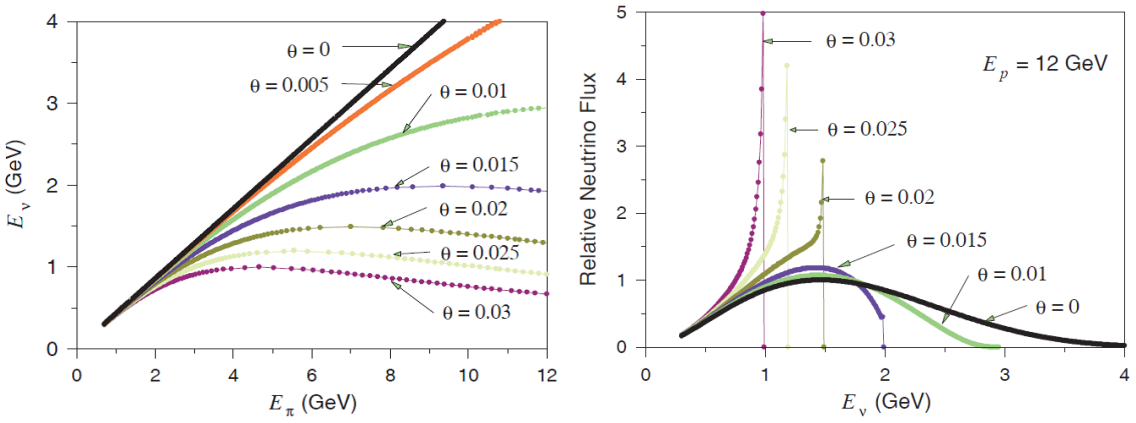

Figure 2.7: Characteristics of the off -axis beam. *Left:* neutrino energy as a function of pion energy. *Right:* neutrino fluxes versus neutrino energy. Both plots are performed for proton with energy 12 GeV interacting with carbon target. The angle θ is the angle between pion direction and produced neutrino direction (in radians). This angle is also a good approximation of the off-axis angle. Figures are taken from Ref. [70]

2.5.2 Prediction of the T2K neutrino flux

In order to predict the neutrino fluxes at ND280 and SK, a neutrino beam Monte Carlo (MC) simulation, called JNUBEAM, is developed [71, 119]. JNUBEAM is a part of to the T2K software package and is based on GEANT 3.21 simulation tool [72]. In simulations protons with kinetic energy of 30 GeV are injected into the 90 cm long graphite target. Secondaries, mainly pions and kaons are produced and focused in the horn magnets. They are tracked

until decay into neutrinos. The tracks of neutrinos are extrapolated to ND280 and SK. Then, the corresponding fluxes and the energy spectrum are provided.

In order to predict production of secondaries particles, *i.e.* pions and kaons JNUBEAM was relying on different hadron production models: GHEISHA [72] (default GEANT 3.21 hadronization model), GFLUKA [72] and GCALOR [73].

The neutrino flux as well as energy spectrum at ND280 and SK depends mainly on the kinematics of produced pions and kaons. Fig. 2.8 displays (p, θ) phase space for positive pions *(left)* and kaons *(right)* where p is the momentum and θ is the polar angle with respect to the beam direction. In the figure only π^+ and K^+ whose daughter neutrinos pass through the Super-Kamiokande detector are included. We may observe that π^+ mainly collected by horns are produced at $\theta = (100 - 200)$ mrad and with momentum around 2 GeV/c (red area on the *(left)* plot in Fig. 2.8). These pions are responsible for the peak around 0.6 GeV in ν_μ neutrino spectrum as will be shown later. In case of the kaons wider distribution in (p, θ) phase space is observed.

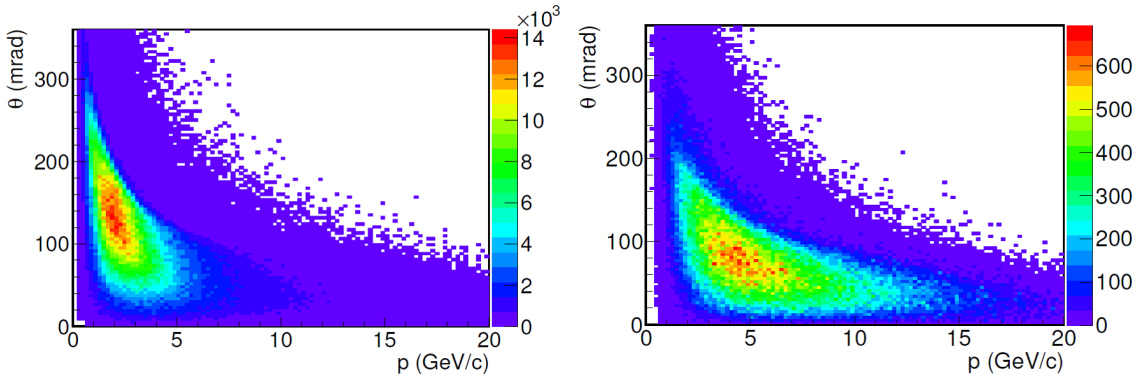

Figure 2.8: Results of JNUBEAM simulation of the T2K neutrino beam. The meson production angles versus momenta are shown for positively charged pions *(left)* and kaons *(right)* whose daughter neutrinos pass through the Super-Kamiokande detector. Figure is taken from Ref. [119].

As stated in Sec. 2.2.2, the T2K beam consists mainly of muon neutrinos, however other neutrino or antineutrino species may also be produced during decays of pions and kaons. Detailed studies of parent decays and its impact on the T2K neutrino beam were carried out, as written in Ref. [71], and we will point here their main conclusions. The most important are ν_μ neutrinos, which are mainly produced via π^+ (95.5%) and K^+ (4.5%) two-body decays. As far as three-body decays are concerned we have also very small input from K^+ (0.2%) and K^0_L (0.1%). Note that contribution from μ^- is negligible (<0.01%) as this particles are defocused by the horns. Next to consider are $\bar{\nu_\mu}$. They originate mainly from π^- (85.8%) and K^- (4.6%) two-body decays. Flux from μ^+ this time is not affected by the defocusing of the magnetic horns and as a result their decays are also important source of $\bar{\nu_\mu}$ (8.0%). For three-body decays we have K^+ (0.2%) and and K^0_L (1.3%). The $\bar{\nu_\mu}$ flux is 7.0% of the ν_μ flux.

The important source of background to ν_e *appearance* search comes from ν_e component of the T2K neutrino beam as it is impossible to distinguish interactions caused by ν_μ oscillated into ν_e from the beam ν_e events at SK. The ν_e beam composition is expected to be at level of about 1.1% of ν_μ flux integrated over all energies. The main contribution to the ν_e flux is from μ^+ (57.2%) decays. There are also three-body decays of K^+ (33%) and K^0_L (12.5%) that need to be taken into account. The last to discuss is $\bar{\nu_e}$ flux compontent which is around 0.17% of the nominal ν_μ flux. Its main sources are three-body decays of: K^0_L (77.6%) and

K^- (14.7%). We have also smaller input from μ^- (7.2%) decays. All the rates are given for the Super-Kamiokande detector.
In Fig. 2.9 we demonstrate the T2K flux for ν_μ (*black*), $\bar{\nu_\mu}$ (*red*), ν_e (*blue*) and $\bar{\nu_e}$ (*pink*) at the ND280 near detector *(left)* and Super-Kamiokande *(right)*. Note that for ND280 detector transverse fiducial volume of 150×150 cm^2 was taken. The predictions are based on the JNUBEAM simulation tool with GCALOR model used for calculation of primary and secondary interactions. In the peak energy of around 0.6 GeV we observe the earlier discussed contribution of around 0.5% of the whole beam of ν_e flux.

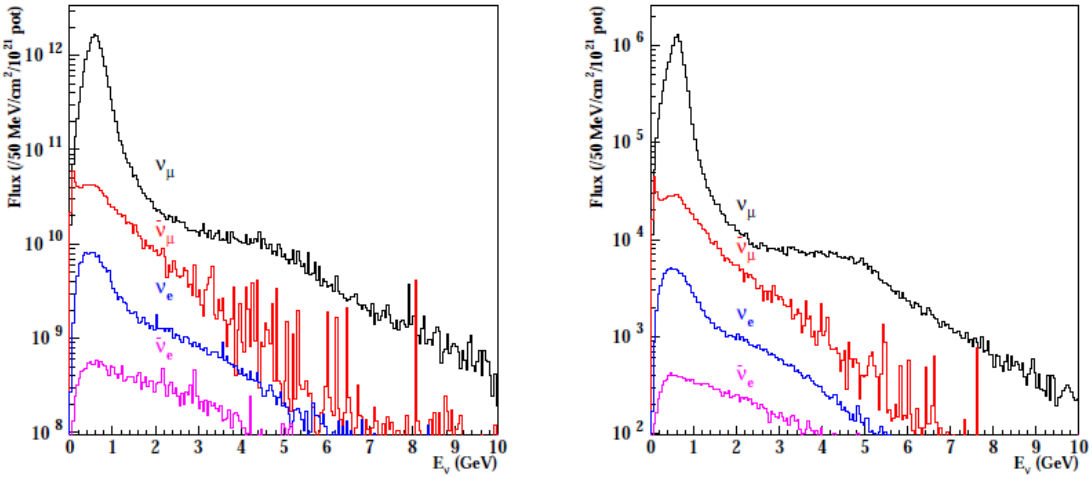

Figure 2.9: Energy spectra for ν_μ (*black*), $\bar{\nu_\mu}$ (*red*), ν_e (*blue*) and $\bar{\nu_e}$ (*pink*) at the ND280 near detector *(left)* and Super-Kamiokande *(right)*. Note that for ND280 detector transverse fiducial volume of 150×150 cm^2 was taken. The predictions are based on the JNUBEAM simulation tool with GCALOR model used for calculation of primary and secondary interactions. Figure is taken from Ref. [71].

In Fig. 2.10 we illustrate how flux prediction for different hadron production models looks like in case of ND280 (*left*) and SK (*right*). We can see that the absolute neutrino fluxes may be different by a factor of 2 depending upon the choice of hadronization models. This fact will play very significant role for the systematic uncertainties coming from the T2K beam predictions. If oscillation parameters are to be measured with precision stated in Sec. 2.4, we have to reduce uncertainty on the flux prediction, which requires precise hadron production measurements adequate for the conditions (energy of protons, choice of target) as the T2K is using.

2.5.3 The importance of the far-to-near flux ratio

Neutrino oscillations are probed by comparing interaction rates at Super-Kamiokande with predictions with and without oscillations. The expected neutrino fluxes at SK, $\Phi^{SK}_{\nu_e}$ and $\Phi^{SK}_{\nu_\mu}$, will be obtained from $\Phi^{ND}_{\nu_e}$ and $\Phi^{ND}_{\nu_\mu}$ fluxes measured in the near detector multiplied by the so-called far-to-near ratios, denoted R_{ν_μ} and R_{ν_e}, respectively:

$$\Phi^{SK}_{\nu_\mu,\nu_e}(E_\nu) = R_{\nu_\mu,\nu_e}(E_\nu) \cdot \Phi^{ND}_{\nu_\mu,\nu_e}(E_\nu) \tag{2.13}$$

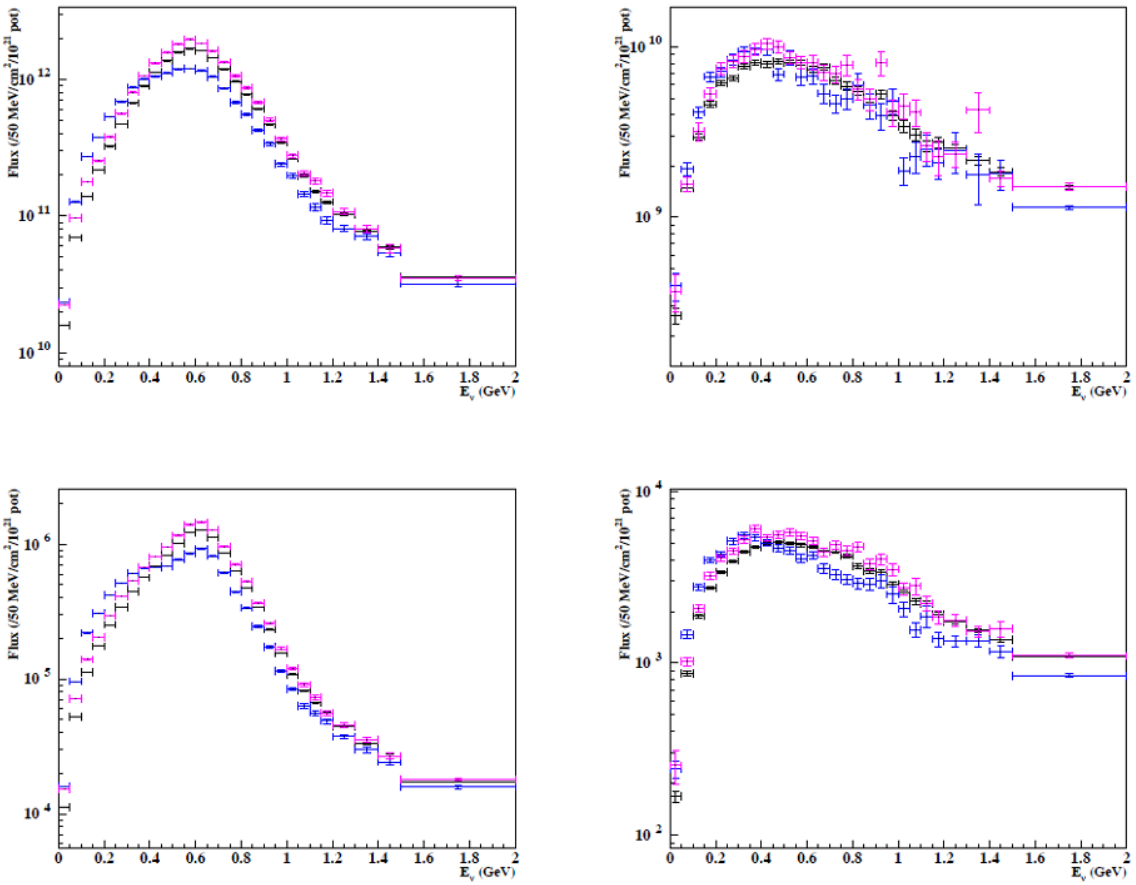

Figure 2.10: The spectra predictions for ν_μ *(left)* and ν_e *(right)* at the ND280 near detector with fiducial transverse area 150×150 cm^2 (*top*) and Super-Kamiokande detector (*bottom*). Predictions are calculated for different hadron production models used for simulation of primary and secondary interactions: GCALOR (*black*), GFLUKA (*pink*) and GHEISHA (*blue*). Figure is taken from Ref. [71].

Fig. 2.11 shows both R_{ν_μ} and R_{ν_e} ratios derived from the JNUBEAM simulations using different hadron production models: GCALOR (*black*), GFLUKA (*pink*) and GHEISHA (*blue*). Clearly we may come to the conclusion that the far-to-near ratio has a complicated dependence on neutrino energy, especially for E_ν <1 GeV, which is the most crucial range for the T2K measurements as the oscillations are expected around 0.6 GeV. The explanation of this not trivial far-to-near ratio is as follows. If the neutrino source was point-like and isotropic, the R_{ν_μ,ν_e} ratios would be given by the ratio of the squared distances from the neutrino source and energy independent. However, the neutrinos are born along the 96 m decay pipe which means that they constitute a point-like source only for the far detector. In addition near and far detectors see quite different solid angles. These effects lead to slightly different energy spectra at the near and far detectors. Moreover, we observe differences between predictions obtained using different models responsible for simulation of primary and secondary interactions: GCALOR (*black*), GFLUKA (*pink*) and GHEISHA (*blue*). If we plot ratio of the far-to-near ratios, with the reference of predictions obtained using GCALOR, as shown in Fig. 2.12, we observe discrepancies larger than 10%. In the same time if we want to gain precision measurements, as stated already in Sec. 2.4, we should know far-to-near ratio at the level of $\delta(R_{\nu_\mu,\nu_e}) \approx 2-3\%$ (see Refs. [80, 74]). Clearly this fact requires precise

information on the pion and kaon production on the T2K target measured independently in other experiments. As we may learn in the next section, experimental data are very poor in this subject and none exact measurements were carried out with the 30 GeV (kinetic energy) protons impinging on the carbon target. This is where NA61/SHINE is coming into play.

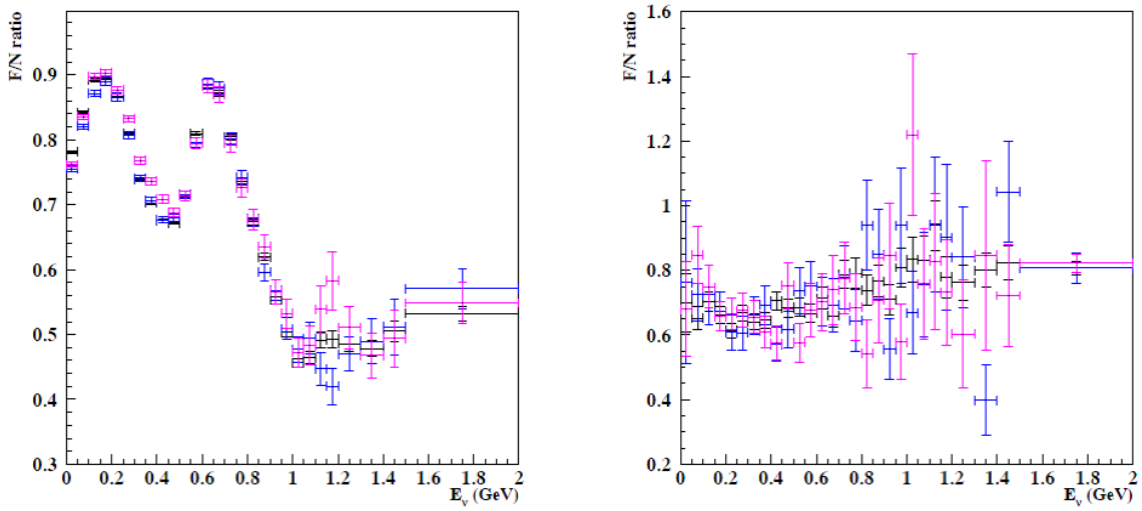

Figure 2.11: Far-to-near flux ratio for ν_μ *(left)* and ν_e *(right)* neutrinos calculated using JNUBEAM simulation of the T2K beam. Results are shown for different used hadron production models: GCALOR (*black*), GFLUKA (*pink*) and GHEISHA (*blue*). The flux ratios are multiplied by the squared distances $L^2_{SK}/L^2_{ND280} \sim 8 \times 10^6$ from the far and near detector to the target. Figure is taken from Ref. [71].

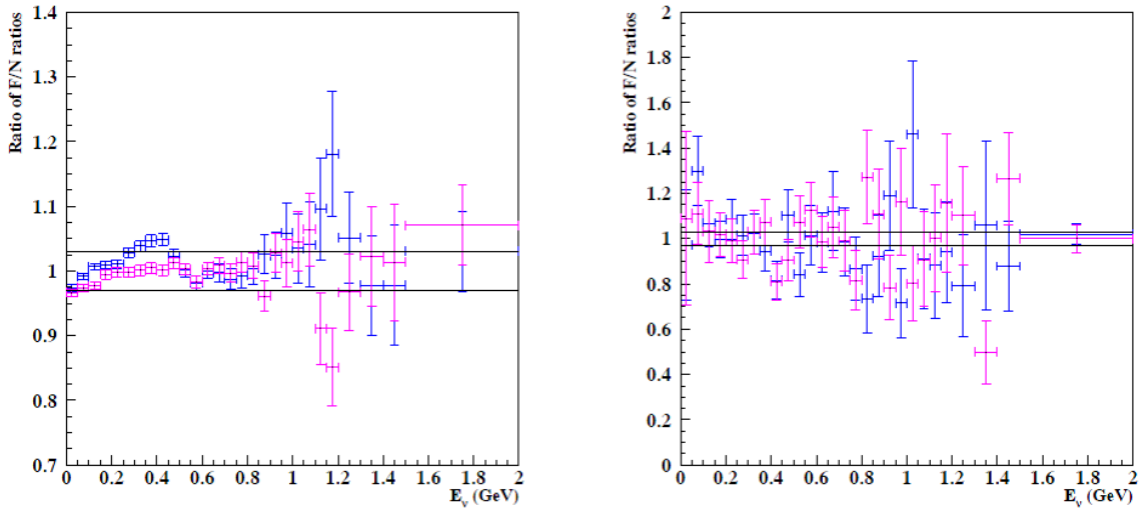

Figure 2.12: Ratios of the far-to-near ratios computed with GFLUKA (*pink*) and GHEISHA (*blue*) models with respect to the reference ratio computed with GCALOR. Black lines illustrate ±3% band. Figure is taken from Ref. [71].

2.6 Overview of the hadron production measurements

Before NA61/SHINE there were no direct measurements of the pions and kaons produced from 30 GeV (kinetic energy) proton interactions on carbon target. The closest available data points are only for pions at 12 GeV from HARP [75], and again only for pions at 158 GeV from NA49 [76].
HARP at the CERN SPS performed extensive measurements of hadron production cross sections and secondary particle yields, on different nuclear targets using beams of protons and pions in the energy range from 3-15 GeV. These results were used by other experiments like K2K [40] and MiniBooNe [10]. In case of K2K, its final *disappearance* analysis uses Sanford-Wang parametrization of the HARP data on positive charged pion production in proton-aluminum collisions at 12.9 GeV/c [40]. MiniBooNe [10] results use also Sanford-Wang parametrization of the HARP data but this time for pions from proton-beryllium collisions at different beam momenta. HARP measured also pion production in proton-carbon interactions at energies of 12 GeV and their application to T2K beam MC predictions would need again use of Sanford-Wang parametrization in order to tune this data to 30 GeV (kinetic energy) interacting protons. This would not satisfy the precision needed for the T2K and therefore exact measurements of the pions and kaons produced at 30 GeV (kinetic energy) were carried out by the NA61/SHINE project.

2.7 Prerequisites for the NA61/SHINE measurements to be used by T2K

As we have already learned, the precision of T2K measurements is strongly correlated with the knowledge of the far-to-near ratio. The aim is to know it at the level of around 3% [80, 74], which requires exact measurements of the pions and kaons in the (p, θ) phase space of interest for T2K (see Fig. 2.8). In this scenario several conditions on the NA61/SHINE measurements were formulated. They are as follows. The first and the most natural one is to take data with 30 GeV (kinetic energy) proton beam, the same as for the T2K. Secondly, data collected for T2K should be taken on different carbon targets *i.e.* thin carbon target with no more than 2 cm length as well as T2K replica target, of 90 cm length and 2.6 cm diameter. The first configuration would allow to measure the primary pion and kaon cross sections without distortions due to reinteractions in the target as the interaction length is only 4% of nuclear interaction length. These measurements can be used for tuning the JNUBEAM simulations for the direct contribution to the neutrino flux coming from primary interactions. In case of T2K replica target, measurements also of secondary and sometimes even tertiary interactions would be possible, which allows to study the full particle yield in the T2K target. Note that both these targets were provided by the T2K Collaboration and they were built of the same graphite grade as original T2K target. Moreover NA61/SHINE data should cover (p, θ) phase space of interest for T2K. All these conditions will be fulfilled within NA61 as will be shown in the next chapters.

Chapter 3

The NA61/SHINE experiment

The NA61/SHINE (SHINE = SPS Heavy Ion and Neutrino Experiment) experiment uses a large acceptance hadron spectrometer located in the North Area H2 beam line of the European Organization for Nuclear Research (CERN) in Geneva. The experiment uses beams from the Super Proton Synchrotron (SPS). The main components of the detector have been inherited from its ancestor NA49 [77] which has been designed to handle the most complex hadronic final states like high multiplicity (around 1800) charged particles produced in lead-lead collisions. At the same time it is able to deal with charged multiplicity as low as $\geq 3-10$, in elementary hadronic (p+p) as well as proton-nucleus collisions.
In this chapter we briefly describe different experimental components used during pilot 2007 run which were of interest for results presented in this dissertation.

3.1 The NA61/SHINE physics program

The NA61/SHINE experiment combines a rich physics program in three different fields: auxiliary measurements for neutrino experiments, cosmic-ray simulations, and the behavior of strongly interacting matter at high density (see references: [79, 80, 81] for details). In its first stage of data taking (years 2007, 2009 and 2010) NA61/SHINE performed measurements of p+C interactions at 31 GeV/c and π^-+C interactions (at 158 GeV/c and 350 GeV/c). Such data are needed for neutrino (T2K) and cosmic-ray (Pierre Auger and KASCADE) experiments.

NA61/SHINE will also continue the program of the NA49 experiment with the main aim of searching for the critical point and studying in detail the onset of the deconfinement. This will be achieved by varying collision energy (13A-158A GeV, where A is the atomic mass of the particle) and size of the colliding systems (p+p, p+Pb, B+C, Ar+Ca, Xe+La).

3.2 The CERN accelerator complex

The CERN accelerator complex is a succession of particle accelerators that can reach increasingly high energies. Each accelerator boosts the speed of a beam of particles, before injecting it into the next one in sequence [78]. The first and the smallest circular accelerator is the Proton Synchrotron Booster which takes protons with an energy of 50 MeV from the LINear ACcelerator (LINAC2), and accelerates them up to 1.4 GeV. The next in the accelerator chain is the Proton Synchrotron (PS), where proton energy reaches 25 GeV. The final acceleration is performed in the Super-Proton Synchrotron (SPS). Measuring nearly 7 km circumference, it provides proton beam with maximum possible energy of 450 GeV. The beam is transported along the H2 beam line towards the experiment. In the H2 beam line 450 GeV protons hit

beryllium target and produce a secondary particle beam that provides hadrons, electrons or muons of energies between 10 and 450 GeV. The H2 beam line setup for the secondary beam is installed in the SPS North Area and is used by NA61/SHINE experiment. Several collimators and magnets in the H2 beam line are used to select particle of interest and control beam momentum and intensity.

3.3 Trigger and beam setup

The setup of beam detectors used in the NA61 experiment is illustrated in Fig. 3.1.

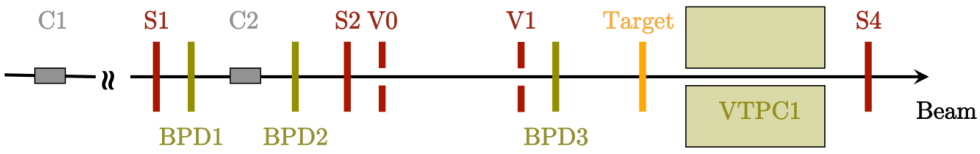

Figure 3.1: Layout of the beam line (from Ref. [110]).

Protons from the secondary hadron beam are identified by two Cherenkov counters, a CEDAR [83] and a threshold counter, labelled C1 and C2, respectively. The CEDAR counter provides positive identification of protons, while the threshold Cherenkov counter, operated at pressure lower than the proton threshold, is used in anti-coincidence in the trigger logic. The fraction of protons in the beam was about 14%.

Two scintillation counters, S1 and S2, provide the beam definition, together with two veto counters V0 and V1 with a 1 cm diameter hole, which are collimating the beam on the target. The S1 counter provides also the timing (start time for all counters). Beam protons are then selected by the coincidence $\mathrm{S1} \cdot \mathrm{S2} \cdot \overline{\mathrm{V0}} \cdot \overline{\mathrm{V1}} \cdot \mathrm{C1} \cdot \overline{\mathrm{C2}}$. A selection based on signals from Cherenkov counters allowed the identification of beam protons with a purity of about 99%. A consistent value for the purity was found by bending the beam into the TPCs with the full magnetic field and using the dE/dx identification method: $(0.6 \pm 0.6)\%$ kaons and $(0.3 \pm 0.2)\%$ pions. Trajectories of individual beam particles are measured in a telescope of beam position detectors along the beam line (BPD-1/2/3 in Fig. 3.1). These counters are small (3×3 cm) proportional chambers with cathode strip readout, providing a resolution of about 200 μm in two orthogonal directions, see Ref. [77] for more details. The beam profile and divergence obtained from the BPD measurements are presented in Fig. 3.2.

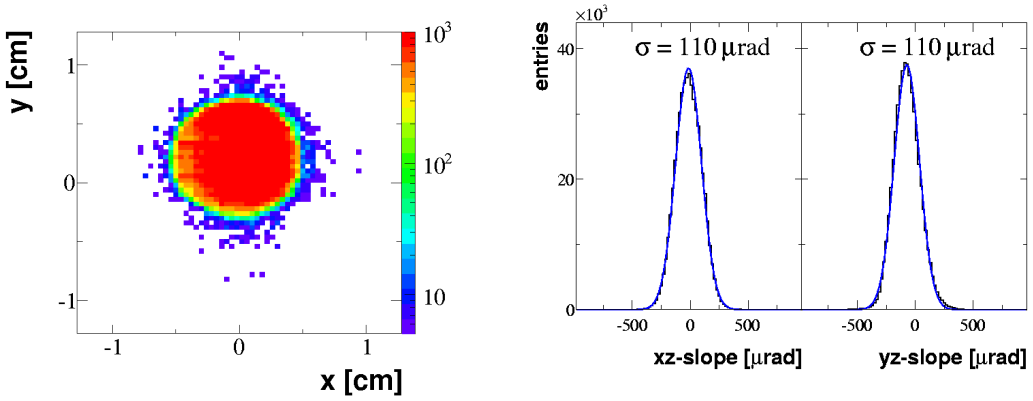

Figure 3.2: *Left:* The beam spot as measured by BPD-3 after the veto counters described in the text ($\overline{\text{V1}}$ and $\overline{\text{V0}}$). *Right:* The beam divergence in x and y (from Ref. [1]).

The beam momentum was measured directly in a dedicated run by bending the incoming beam particles into the TPCs with the full magnetic field. The measured beam momentum distribution is shown in Fig. 3.3. The mean value of 30.75 GeV/c agrees with the set value of 30.92 GeV/c within the available precision of setting the beam magnet currents (≈0.5%) in the H2 beam line.

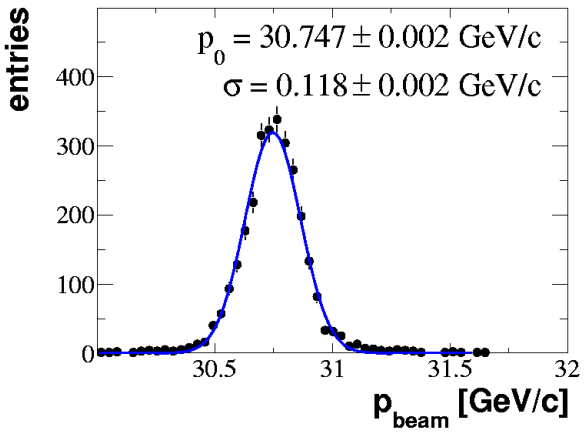

Figure 3.3: The beam momentum distribution measured by the reconstruction of beam particles in the TPCs. Only statistical errors are shown (from Ref. [1]).

Interactions in the target are selected by an anti-coincidence of the incoming beam protons with a small, 2 cm diameter, scintillation counter (S4) placed on the beam trajectory between the two vertex magnets (see Fig. 3.5). This minimum bias trigger is thus based on the disappearance of the incident proton.

3.4 Graphite targets used during pilot 2007 run

Two isotropic graphite targets (see Fig. 3.4) were used during 2007 run (the justification of using both targets was discussed in Sec. 2.7 on page 31):

- a 2 cm long target with dimensions 2.5(W)×2.5(H) cm (about 4% of nuclear interaction length, λ_I) with density $\rho = 1.84$ g/cm^3, so-called thin target,
- a 90 cm long cylinder of 2.6 cm diameter and about 90 cm length (about 1.9 λ_I), so-called T2K replica target.

The center of the targets was positioned about 80 cm upstream from the VTPC1 entrance window. In total about 678 k events with thin target, 230 k events with the T2K replica target

Figure 3.4: *Left:* Thin graphite target. *Right:* T2K replica.

and 46 k events with target removed [82] (those events will be used for the normalization procedure which is explained in the Sec. 8.2 on page 109) were registered during 2007 data taking.

3.5 Experimental setup

The NA61 schematic layout is shown in Fig. 3.5. The main tracking devices are four large volume Time Projection Chambers (TPCs). Two of them, the vertex TPCs (VTPC1 and VTPC2), are located in the magnetic field of two superconducting dipole magnets. Two others MTPC-L and MTPC-R (blue boxes in Fig. 3.5) are positioned downstream. Note that there is also present additional chamber between both vertex TPCs, called Gap TPC (GTPC) but it was not used for the results presented in this thesis.

Two time-of-flight detectors (ToF-L/R) were inherited from NA49 and are able to provide time measurement resolution of $\sigma \approx 60$ ps. In 2007 the experiment has been updated with a new forward time-of-flight detector (ToF-F) in order to extend the acceptance for pion and kaon identification as required for T2K measurements [82]. The ToF-F wall is installed downstream of the main TPCs (black line in Fig. 3.5), closing the gap between the ToF-L and ToF-R walls. The ToF-F time resolution is $\sigma \approx 115$ ps. In NA61 coordinate system horizontal z axis corresponds to the nominal beam line with downstream direction. Point with z=0 is in the center of the VTPC2. The target is placed approximately at z=-580 cm. The y axis is defined by the drift direction (vertically upwards). The y (drift) direction is divided into 512 time bins. The horizontal x axis completes the system to be right-handed (see Fig. 3.5 which is x-z plane).

3.6 Time Projection Chambers

3.6.1 Introduction

The basic principle of operation of TPCs is widely available in the literature [84, 85, 86]. We will just describe a basic concept on which the NA61 chambers are based. The high energy charged particle flying through the sensitive volume of the TPCs interacts with the gas atoms, and loses kinetic energy by excitation of bound electrons and by ionization. The average energy loss by ionization and excitation can be transformed into a number of electron-ion pairs.

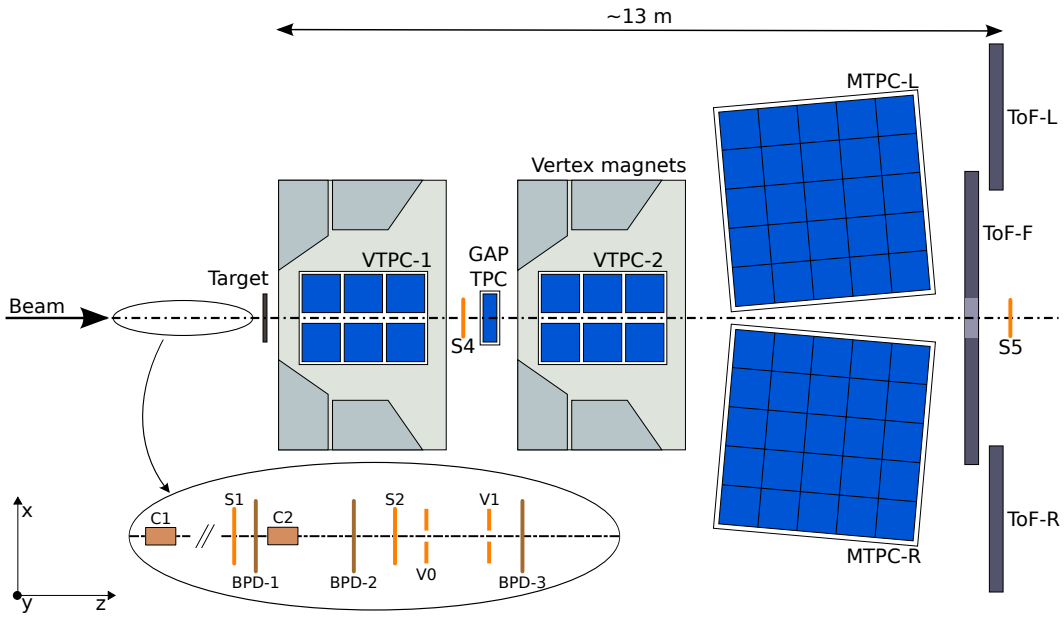

Figure 3.5: The layout of the NA61 experiment at the CERN SPS (top view, not to scale, from [1]).

At the beginning the free electrons are located along the trajectory of the charged particle (called track) and due to influence of the homogeneous electric field they drift to the top of the chamber (see Fig. 3.6). When they reach sense wire plane they induce the electron avalanche (multiplication by a factor of 10^4) which creates voltage pulse on the segmented horizontal plane (called pad). This approach allows us to obtain information on the three space coordinates (location on the horizontal plane and duration of the drift) and the specific ionization of the particle (pulse heights).

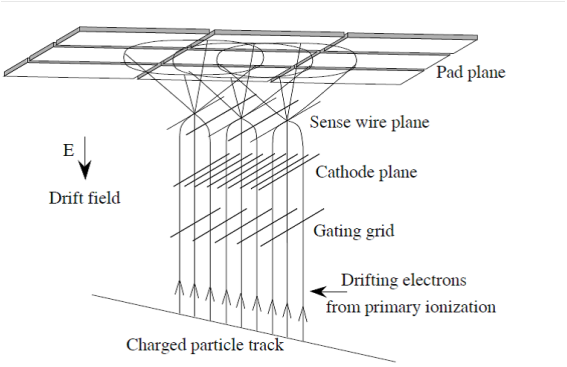

Figure 3.6: TPC readout chamber layout (from Ref. [77]).

3.6.2 Geometrical dimensions of the TPCs

The two VTPCs provide precise momentum measurement using track curvature in the presence of the magnetic field. The MTPCs are much larger (see Table 3.1) and for tracks at forward angles provide most of the sensitivity for the ionization energy loss measurement.

The detectors consist of a top plate supporting the read-out planes, the electronics and the frames for the field cage and the surrounding gas box (for details please refer to [77]). The gas box consists of a double layer of 125 μm Mylar foil glued to a double frame system made of 6 mm thick fiberglass-epoxy. The field cage which provides uniform drift field inside the gas envelope is made of strips of aluminized Mylar foil which are supported by ceramic rods at the corners. Each VTPC contains two separate field cages, left and right of the beam.

dimensions [m]	VTPC1	VTPC2	MTPC
width	2	2	3.9
length	2.5	2.5	3.9
height	0.98	0.98	1.8

Table 3.1: Geometrical dimensions of the TPCs.

There is around 20 cm gap located between the cages symmetrically around the (neutral) beam line. The hole was introduced in order to exclude the highly ionizing Pb-ions (and very high density region of secondary particles in Pb-Pb collisions) from the active volume.

Each pad in the TPC readout corresponds to x-z coordinate pair, and has assigned a sector number, pad-row number and pad number. The VTPC readout pads are assembled in 6 sectors, while the MTPCs pads in 25 sectors each. Thus there are 62 sectors in total as shown in Fig. 3.7.

The sector rows closest to the beam (21..25 in MTPC-L and 1...5 in MTPC-R) are the High Resolution (HR) sectors the pads being narrower there. The other MTPC sectors contain Standard Resolution (SR) pads. In Tab. 3.2 we present the number of pads, pad-rows and sectors in the NA61 TPCs. Note that each pad is tilted with respect to the nominal beam to agree with the average track angles at the given x-z position. This approach allows to optimize the tracking procedure. Pad angles and dimensions are presented in Table 3.2. Schematic view of the pad-rows and tilted pads in each pad-row for the first two left sectors of the VTPC1 are shown in Fig. 3.8. All pad-rows for VTPCs are straight and parallel to the chamber edges. MTPCs are rotated by 0.98 degrees away from the beam as seen in Fig. 3.7 and the pads are parallel to the chamber edges, except from three outer sector rows (1..15 in MTPC-L and 11..25 in MTPC-R) where pads are tilted by ±15 degrees in order to follow the actual track angles better.

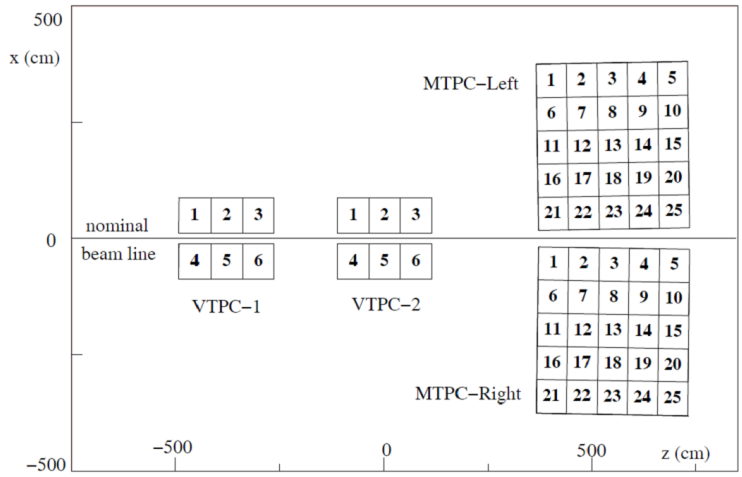

Figure 3.7: Numbering conventions of the TPCs sectors. Top view (from Ref. [97]).

3.6.3 Gases in the TPCs

The detector gases have been selected for their low diffusion constants, because during the drift time of the ionization electrons, diffusion widens the electron clouds arriving to the top of the chambers and giving recognizable hit, called cluster, at the plane of the readout pads. If the diffusion is high the wide and close to each other clusters cannot be separated any more. For the VTPCs (MTPCs) the choice of gas is the $Ar : CO_2$ mixture with the ratio of 90:10 (95:5). The inclusion of CO_2 in the gas mixture greatly reduces the diffusion coefficients.

left/right side of:	VTPC1	VTPC2	MTPC
number of sectors	3	3	25
number of pad-rows	72	72	90
pad-rows per sector	24	24	18
pads per pad-row	192	192	192 (HR) 128(SR)
pad dimensions [mm]			
pad length	16.28	28	40
pad width	3.5	3.5	3.6,5.5
pad angles	12-55^o	3-20^o	0-15^o

Table 3.2: Number of pads and pad-rows, pad dimensions and angles in the TPC readout chambers.

However, the amount of drifting electrons is decreased by the electron attachment, a feature of gases containing CO_2 in the presence of O_2 and H_2O vapor. This introduces a drift length dependence into the ionization measurements. In order to minimize this effect oxygen and water is filtered out and fresh gas mixture is circulated in the chambers.

3.6.4 Magnetic field

The magnetic field is generated by two super- conducting dipole magnets with a maximum combined bending power of 9 Tm over 7 m length. During 2007 run the field was directed downwards, bending positive particles to the $x > 0$ direction (left) and negatives to $x < 0$ (right) in the x-z plane. The magnetic field is homogeneous in the central parts of the vertex TPCs, while the inhomogeneities are encountered at the edges of TPCs. At 158 AGeV/c beam energy the magnetic field is set to 1.5 T in the magnet surrounding VTPC1 and to 1.1 T in the VTPC2 magnet. In the 2007 run the NA61 nominal magnet currents were scaled down by a factor of 20/158 which resulted in 1.14 Tm of bending power. NA61 uses the field maps calculated by the NA49 Collaboration. This is possible due to the fact that magnets positions remain unchanged since the beginning of the NA49 operation.

3.7 Time-of-Flight System

There are several sets of ToF detectors in the experiment (see Fig. 3.5) but only ToF-F was used in the analysis of 2007 data. The ToF-F consists of 64 scintillator bars with photomultiplier (PMT) readout at both ends resulting in a time resolution of about 115 ps. Particles hitting a scintillator rod leave a signal in the two corresponding photo-multipliers (PMTs) providing the stop signal for ToF measurement. The start signal is given by the S1 counter positioned upstream of the target (see Fig. 3.5). The measurement of the t_{ToF} is carried out by taking the difference in time between the S1 signal and the mean value of the two PMTs signals (t_{up} and t_{down}) of the scintillator,

$$t_{ToF} = t_{S1} - \frac{t_{up} + t_{down}}{2} + t_0 \tag{3.1}$$

where t_0 is a reference time which is specific to each channel because it depends on the cable length, PMTs gains etc. Studies concerning ToF-F calibration may be found in Ref. [101].

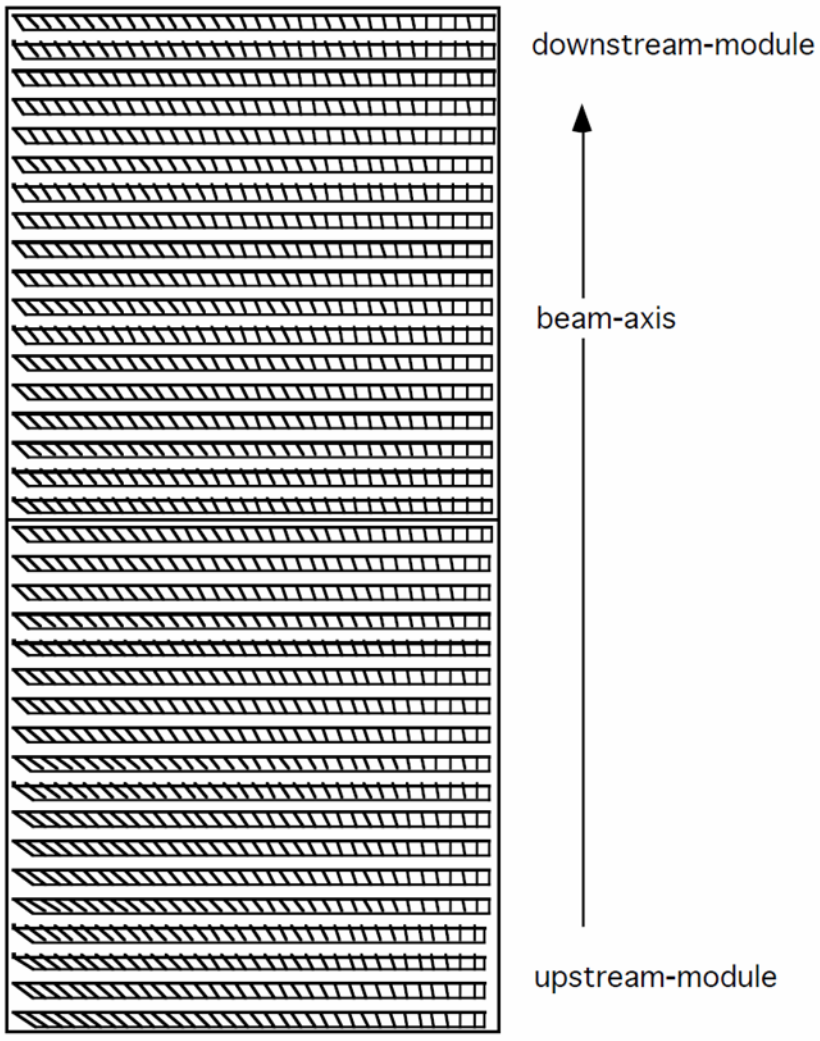

Figure 3.8: Schematic view of the VTPC1 straight pad-rows and turned pads inside each row for sector 1 and 2 (from Ref. [89]).

Chapter 4

Methods of reconstruction and particle identification

The reconstruction procedure of the 2007 NA61 data was largely based on the approach developed for the NA49 experiment [77]. It performs the task of track recognition, momentum determination by track fitting, the calculation of the energy loss dE/dx and the calculation of the particle masses from the time-of-flight measurements.
In the next sections we will briefly introduce the main aspects of the reconstruction procedure together with the ionization measurements as these are the most crucial points for the analysis results presented in the next chapters. In the final section all possible methods of particle identification will be discussed.

4.1 Track reconstruction and momentum measurement

The track reconstruction can be divided into several consecutive parts:

1. cluster finding,
2. construction of local track elements in each TPC separately,
3. matching of track elements from different TPCs into a global track
4. track fitting through the magnetic field and momentum determination.

4.1.1 Cluster finding

At first, two dimensional charge clusters are formed using information from neighbouring pads and time bins (measurement of the drift time and velocity) in a given pad-row. For each cluster the center of gravity method is applied in order to determine the x and y coordinates. The position of the z coordinate is delivered by the position of the given pad-row in the NA61 coordinate system. In other words for each cluster its average time and pad position is available. These coordinates define the points which are used by the tracking algorithm. The position of the points in space is calculated using the known geometry, and the gas pressure and temperature dependent drift velocity. Moreover, the total deposited charge is also calculated for each point and used for further dE/dx measurement. For proper measurement of the cluster position we need to have electric and magnetic field lines parallel to each other, otherwise we have to correct for so-called $\vec{E} \times \vec{B}$ effect. In the center of the TPC chambers both mentioned fields are uniform thus drift of the electrons upwards is not affected. However, at the edges of the detector drifting of the electrons is not completely vertical, due to not parallel electric

and magnetic field lines. This fact leads to deflections in measured position of the clusters, which needs to be taken into account and corrected for.

4.1.2 Track finding and fitting

In general, at first all tracks with the same interaction vertex at the target plane, called main vertex, are treated. Target plane, defined in x-y coordinates, is accurately determined by the beam position detectors. During 2007 run the thin target was installed at z= -580 cm. In MTPCs, which is out of the magnetic field, a straight line is used as a track model. In the VTPCs we are able to determine the momentum because in the presence of the magnetic field the curvature of the track is accessible. As a result we can use helix as a track model in order to determine the initial parameters of the fit as well as momentum components.
Track finding algorithm is the following: first straight line tracks are reconstructed in the MTPCs and they are extrapolated to the target plane. During extrapolation in VTPCs all clusters are collected along track trajectories. If no straight tracks are found in the MTPCs the reconstruction algorithm looks for the clusters in the next upstream detector which is VTPC2, later on in VTPC1. In this way candidates for the clusters in the VTPC1 are always searched at the end of the reconstruction procedure. If points are expected in VTPCs, so-called potential points, and none are found, the clusters on the MTPCs are released. Potential points are calculated assuming that particles start from the main vertex and effects as multiple scattering, secondary interactions, decays, detector resolution are neglected. As a result global tracks matched between detectors are obtained and the fits give the momentum and the charge of the particles (± 1 is assumed in all cases) at the first measured TPC cluster. Furthermore refitting the particle trajectory using the interaction vertex as an additional point and determining the particle momentum at the interaction vertex is performed. In addition matching of ToF-F hits with the TPC tracks is performed. The last step of the tracking procedure is to find all the remaining tracks in the MTPCs, including so-called *kink* tracks and *V0* (daughters of weakly decaying particle).

As a cross check each track is also fitted without assuming that it comes from the main vertex. The distances in x and y directions between the extrapolation of the track to the target plane and the position of the main vertex are so-called impact parameters B_x and B_y. Impact parameters were studied in detail in Sec. 5.2.1 on page 59.

In Fig. 4.1 we show an example of the reconstructed event coming from 31 GeV/c protons impinging on thin carbon target.

4.2 Total energy loss of charged particles

In general, in momentum range of several GeV/c, the total energy loss of charged particles in good approximation can be expressed by [86]:

$$\left\langle \frac{dE}{dx} \right\rangle = \left\langle \frac{dE}{dx}_{coll} \right\rangle + \left\langle \frac{dE}{dx}_{rad} \right\rangle \tag{4.1}$$

where $\frac{dE}{dx}_{coll}$ describes the energy loss due to collision processes, while the second term represents energy loss due to the emission of electromagnetic radiation coming from scattering in the electric field of a nucleus (*bremsstrahlung*).

The high energy charged particle flying through the sensitive volume of the TPCs interacts with the gas atoms, and loses kinetic energy by atomic collisions in which two processes are involved: excitation of bound electrons and ionization. When the particle excites an atomic state by depositing energy, no free electrons arise but deexcitation by photon emission takes

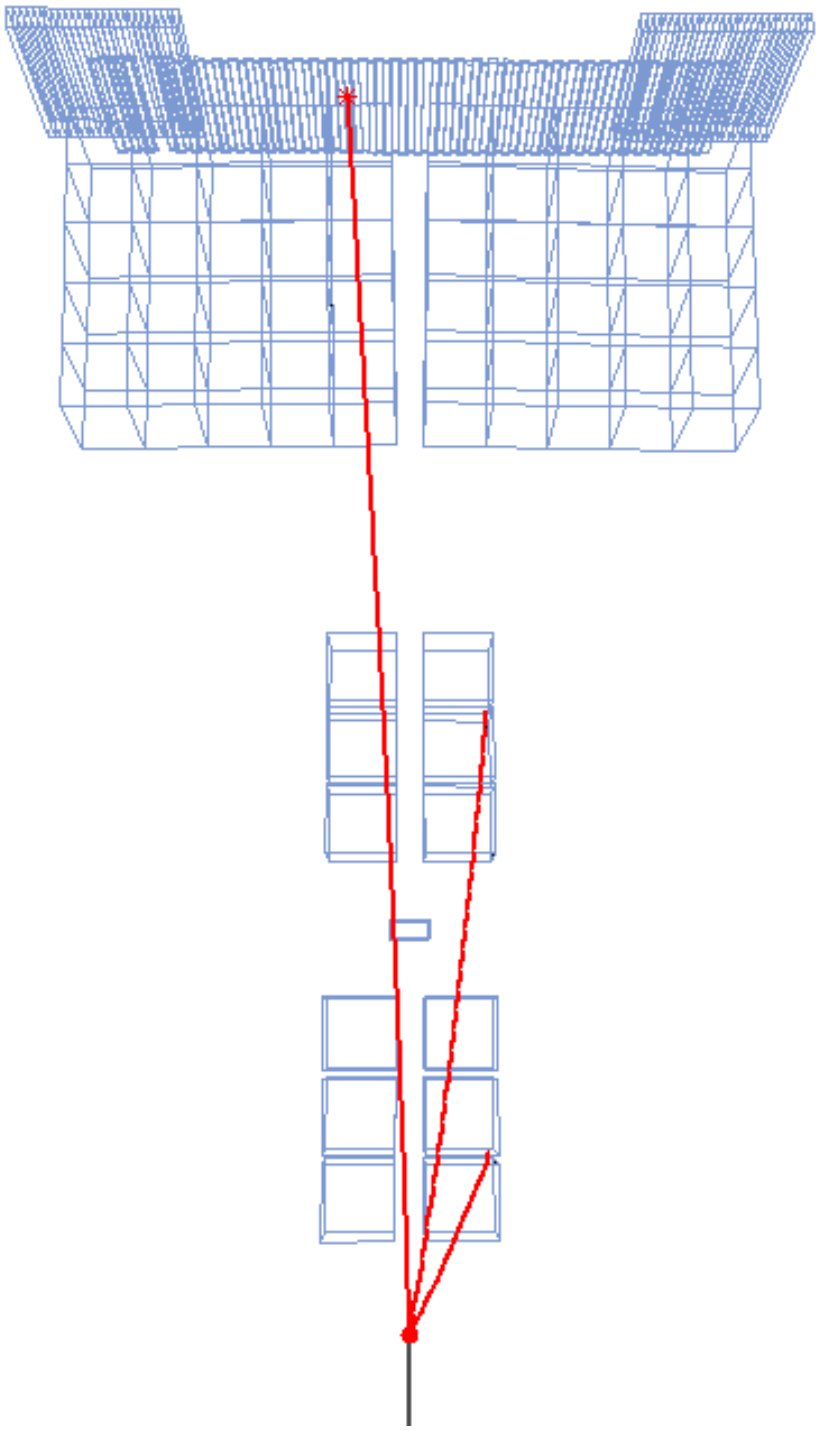

Figure 4.1: Example of an interaction of a 31 GeV/c proton on thin carbon target. Reconstructed tracks are shown as red lines.

place. Of much greater importance are ionization mechanisms with pure scattering processes in which incident particles transfer a certain amount of their energy to atomic electrons so that they are liberated from the atom. The average energy loss is transformed into a number of electron-ion pairs which detected in the TPCs define the specific ionization measurements.

The energy at which collision and *bremsstrahlung* processes are equal is called *critical energy* E_c.

$$\left\langle \frac{dE}{dx}_{coll}(E_c) \right\rangle = \left\langle \frac{dE}{dx}_{rad}(E_c) \right\rangle \tag{4.2}$$

The critical energy scales as the square of the mass of the incident particles (m_i). In good approximation the critical energy of particles can by expressed by [86]:

$$E_c^i \approx E_c^e * (\frac{m_i}{m_e})^2 \tag{4.3}$$

where E_c^e stands for the value of critical energy for electrons. In gaseous Argon E_c^e =0.038 GeV for the electrons and E_c^e =0.037 GeV for positrons [96]. If we take the next heavy particle muon ($m_\mu = 106\ MeV/c^2$) with the help of the relation (4.3) we get E_c^μ ∼1.7 TeV. The NA61 measurements are performed for 31 GeV/c protons impinging on carbon target, which implies that *bremsstrahlung* measurements can only be further considered for e^+ and e^-.

In Fig. 4.2 we illustrate the total energy loss for the electrons inside the gaseous argon with the impact of the ionization (pink points) and *bremsstrahlung* processes (blue points). At energies above *critical energy*, *bremsstrahlung* dominates completely. At large energies ionization loss rates rise logarithmically with the energy, while *bremsstrahlung* losses rise nearly linearly. We see from Fig. 4.2 that for 1 GeV electron the energy loss due to *bremsstrahlung* is an order of magnitude larger than due to atomic collisions. Using the argon density of $1.2{\times}10^{-3}$ g/cm^3 we get that for 1 GeV electron the $\frac{dE}{dx}_{coll}$ ≈$2.4{\times}10^{-3}$ MeV/cm. Thus 1 GeV electron uses a tiny fraction of $2{\times}10^{-6}$ of its energy per 1 cm due to collisions. On the other hand the radiation length X_0 for the gaseous argon is equal to X_0 ∼118 m which means that electrons (positrons) need to fly the mean distance of 118 m in order to be left with $1/e$ energy in *bremsstrahlung* processes. In other words in one act of radiation its energy decreases by a large factor of $1/e$ on average, but it happens so infrequently that we cannot measure it because in the NA61 experiment most of the electrons (positrons) leave the detector, before they lose energy by the emission of electromagnetic radiation. However, we are not intrested in the total electron (positron) energy loss measurement but we want to identify particles and $\frac{dE}{dx}_{coll}$ is sufficient for this task even though it is very small.

As a conclusion, we should state that within NA61 detector we are able to measure energy losses only by atomic collisions. Such mechanism proceeds differently for heavy charged particles (those with $M \gg m_e$, where m_e stands for electron mass) as compared to electrons (positrons). We will come back to this subject in following sections. Now let us investigate the measurement of ionization losses within NA61 apparatus.

4.3 Measurement of the ionization

In Sec. 4.1 we presented how charge clusters are obtained and here we describe determination of the final deposited charge.

The optimization of the parameters required for the determination of the specific energy loss in the TPCs follows the method developed by NA49 and is described in detail in Ref. [97]. We will just briefly summarize main points of this procedure.

At first krypton calibration is performed in order to obtain electronic channel gain values. Radioactive ^{83}Kr which is injected in the detector gas during dedicated calibration runs (without beam) emits well-known spectrum of electrons [77]. By comparing reference values

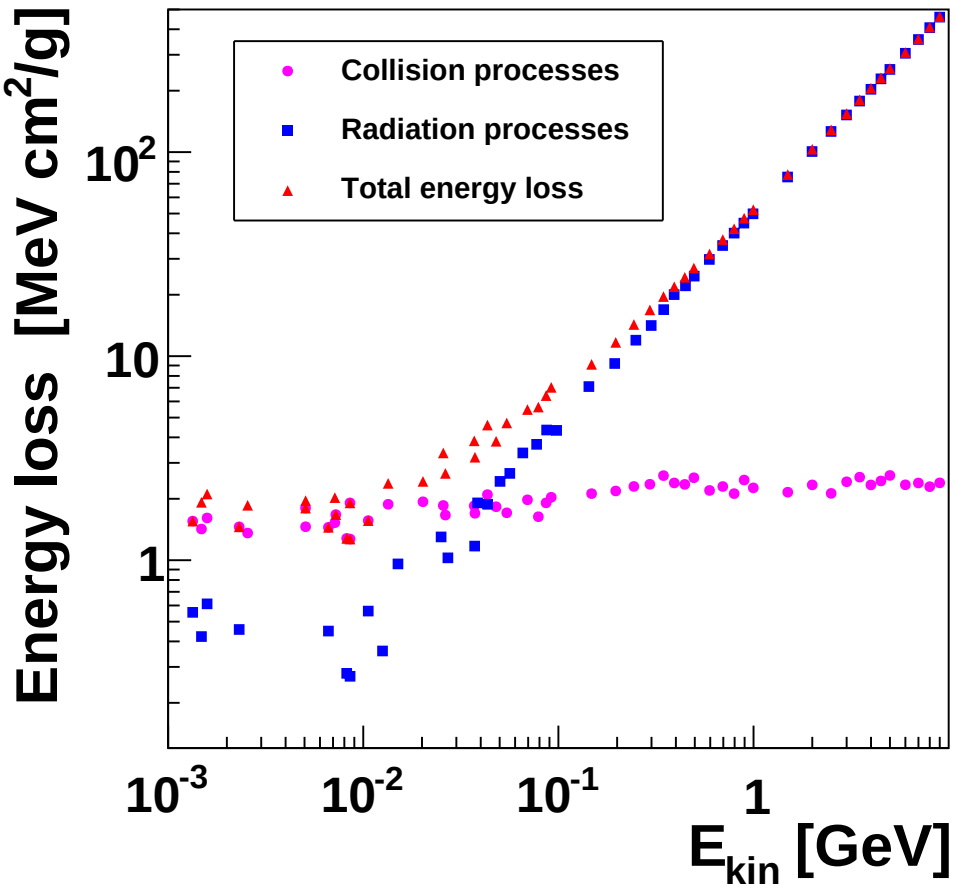

Figure 4.2: Total energy loss versus electron energy in the gaseous argon (*red*). Contribution from the ionization (*pink*) and *bremsstrahlung* processes (*blue*) is also shown. Figure plotted by author using data from ESTAR program, for details please refer to Ref. [95].

with the measured ones the relative gains for each pad separately are obtained. This calibration was not performed for 2007 run and gain factors obtained from krypton calibration from NA49 measurements have been used.

Several modifications to measured charge had to be calculated for the NA61 2007 data. They took into account the following experimental effects:

- signal loss due to threshold cuts and charge absorption during the drift,
- time dependence of the TPC gas pressure and temperature,
- differences in the TPC sector gain factors,
- edge effects at sector boundaries.

Each of given experimental distortion is described below in detail.

4.3.1 Drift length and angle dependent losses

The measured total cluster charge, after $\vec{E} \times \vec{B}$ corrections mentioned in Sec. 4.1.1 on page 40, still depends on the distance between the track and the readout plane. This is partly due to the capture of the electrons by the detector gas. The ionization electrons produced along particle trajectory are drifting up even 110 cm before they reach read-out plane. During this drift they can be captured by O_2 (and H_2O) molecules which after constant filtering and circulating gas mixture can still be present in it due to continuous diffusion from outside. As stated in [97] this effect leads to approximately 2% charge loss per metre in MTPCs and around 10% in VTPCs, thus cannot be neglected.

Additional reason for the charge losses comes from the read-out electronics, the so-called *threshold* losses, which are much more difficult to correct for.

We take for further consideration only those signals which were recorded in the electronic channels with at least 5 ADC units (see Fig. 4.3). When the total cluster charge is calculated by summing these ADC values the smallest hits are left out and the tail of the cluster (in x and y direction) is cut off. In order to correct for *threshold* losses special Monte Carlo simulation of the cluster shape was developed. All relevant information like: tilt angles, the width of the pads and time slice, diffusion constants and pad lengths were used as an input to the cluster simulation. One has to keep in mind that for MTPC sectors the angles between the tracks and the pads are relatively small and the simulated cluster shape is better described in comparison to the VTPCs where mentioned angles can be large leading to much broader clusters which are not easy to model. This fact will demonstrate its influence on the analysis procedure described in detail in Sec. 6.2 on page 75. Moreover, this argument implies that the precision for the energy loss measurement in the MTPCs is better in comparison to VTPCs.

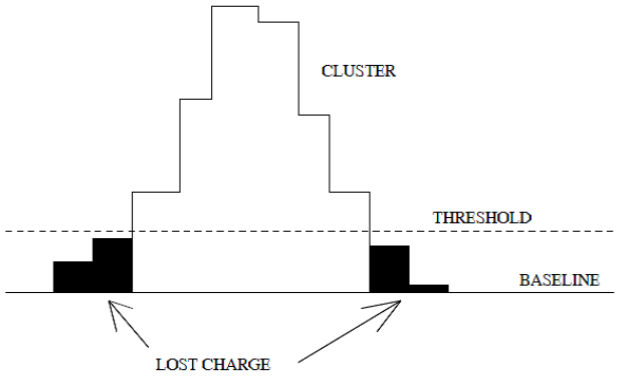

Figure 4.3: Schematic view of the one dimensional cluster charge signal measured in ADC units. Only hits $\geq$5 ADC enter in the sum of the total cluster charge. This plot is one dimensional and in reality cluster has two (x and y) dimensions. Figure taken from Ref. [97].

The output of the simulation is a look-up table where in order to get corrected cluster charge one has to specify the sector number and two angles describing the track trajectory.

Drift length and angle dependent losses of the charge are the largest and the most difficult corrections which need to be applied in specific energy loss calibration. It is not possible to extract these corrections from data itself but only from the cluster shape simulation compared with the measured data.

4.3.2 Pressure and temperature

The TPCs operate in the regime where drift velocity and gas gain are strongly dependent on the temperature and pressure. In other words the density of the gas mixture will have large influence on the gas gain. In order to minimize temperature variations, the TPCs are placed inside the thermally insulated room (using air-conditioners), where temperature is stabilized to better than 0.1^oC. However, the atmospheric pressure variations are difficult to

keep constant. During each data taking atmospheric pressure is monitored, and we correct measured pad gain and drift velocity for this effect during off-line analysis. During data taking period one needs also to take into account all residual time-dependent variations like sudden jumps in the gain of a few % which occur due to unexpected experimental conditions like jumps in power cycling of chambers. Separately for each 62 sectors all measured ionization values were collected from a given sector as a function of time, and after averaging over small time intervals, the gain history for each sector was tabulated.

Finally all remaining gain variations have been derived from data measurements (using only good particle tracks, without delta rays and spirals) and used to correct the data. Applied procedure provides also off-line monitoring and quality of the TPC performance.

4.3.3 Sector calibration

All 62 TPC sectors (where 50 of them belong to the MTPCs) operate as individual units, which can change their gain factors independently. After krypton calibration which is performed in conditions different from the actual data taking period, an additional constant is determined for each sector individually. These constants are adjusted in such a way that measured dE/dx for pions follows the Bethe-Bloch parametrization for fixed set of parameters. This is iterative procedure and became a part of all particle ionization measurements in the former experiment NA49.

4.3.4 Determination of track dE/dx for separate TPCs

As already discussed in Sec. 4.1.1 in TPC chambers we measure charges of a number of clusters (N) along the track trajectory. N can extend from 10, which is the minimal value used for further ionization measurement, up to 234 which is the sum of all possible clusters for a track passing all three TPCs. In a first approach one could simply sum up these N charges (corrected for all experimental effects described in above sections) and as a result we would have a number proportional to the total amount of ionized electrons along the entire path in the chambers. Division by the total length of the track in the gas would give the ionization over a unit length, i.e. the variable which we want to measure. However, this approach is not the best when precision and separation between different particle species becomes crucial. The energy lost through collision processes follows Landau distribution [98]. The Landau distribution in analytical form is not available. Often in the literature one can see approximate formula written by Moyal [99]:

$$M(z) = \frac{1}{2\pi} e^{-\frac{1}{2}(z+e^{-z})} \tag{4.4}$$

where z characterizes the deviation from the most probable energy loss:

$$z = \frac{(dE/dx - dE/dx_{prob})}{K} \tag{4.5}$$

while dE/dx_{prob} is the most probable amount of the energy loss and K is a constant dependent on the medium.

In Fig. 4.4 we illustrate an approximation to the Landau distribution which is clearly asymmetric and has long tail of large energy deposits coming from the clusters of high ionization. These clusters introduce a large fluctuation in the sum of all charges. Moreover the mean value of energy loss measurements strongly depends on those fluctuations and is not equal to the most probable value. This fact will result in poor dE/dx resolution. In order to reduce the impact of large energy deposits on mean value of energy loss a **truncated mean technique** is used. In this method we sort the track cluster charges values into increasing order and remove the first (a) and the last (b) fraction of these cluster charges and average over the remaining ones. During NA49 times several studies were performed in order to optimize the minimal a and maximal b truncation limits. As stated in Ref. [97] the a=0 and b=50% parameters maximize the energy loss resolution. For 2007 data analysis the same (0:50) truncation was applied and only 50% of the smallest clusters were kept for the determination of the dE/dx. By truncating the larger values in the distribution of charge clusters, the sensitivity to large fluctuations is reduced and the truncated mean is able to characterize the most probable value of the distribution in a stable way. Truncation is performed independently for VTPCs and MTPCs clusters. Note that from now on when we write dE/dx we mean truncated mean.

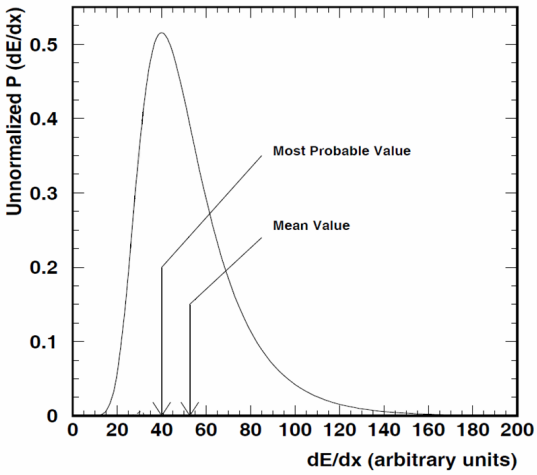

Figure 4.4: The Moyal's function- an approximation to the Landau distribution, describing the probability density of the energy loss per unit length. Plot taken from Ref. [100].

4.3.5 Global *dE/dx*

As shown in previous section for tracks reaching all NA61 detector components we have independent dE/dx measurements and its uncertainties for VTPCs and MTPCs. One has to remember that the energy loss measurement for the MTPCs is superior first of all because of larger size. As a result the MTPCs performance is better studied which resulted in more optimized corrections. Moreover ionization measurements are more complicated in the VTPCs, due to several conditions like for an example, the presence of the magnetic field, which is causing many experimental distortions in the cluster positions. From experimental point of view it would be better to use dE/dx values obtained for the MTPCs track segments only. This strategy was widely followed during NA49 times. Unfortunately the important part of the phase space covered by the NA61 system is in the low momentum region (p$\leq$ [3] GeV/c) where most of the tracks are measured only in VTPC1. As a result, dE/dx value measured in VTPCs still has to be taken into account for the analysis. Thus, in case of tracks with segments belonging to different TPCs we define global dE/dx as weighted mean of dE/dx values from VTPCs and MTPCs, otherwise global dE/dx is equal to energy loss measurement in the VTPCs.

Finally, for each track we use one experimental value of the global dE/dx and its uncertainty $\sigma_{dE/dx}$. In the next section we discuss the Bethe-Bloch parametrization which was fitted to measured dE/dx values.

4.4 The Bethe-Bloch parametrization

The analysis presented in this dissertation relies heavily on predictions of the ionization produced by a particle with a measured momentum and mass hypothesis. In our considerations on the Bethe-Bloch parametrization we make separation into heavy particles (those with $M \geqslant m_e$, where m_e stands for electron mass) and positrons and electrons. At first, we introduce theoretical description of the Bethe-Bloch formula and next the procedure of derivation of Bethe-Bloch parametrization from the measured data is shown separately for both groups of particles.

4.4.1 Energy loss of heavy charged particles by atomic collisions

The mean differential energy loss dE per unit length dx which a particle suffers by ionization and excitation was first calculated by Bethe and Bloch for particles heavier than electrons [90, 91, 92]. Integration over all energies lost to the individual atoms of the medium yields to so-called **Bethe-Bloch Formula** (BB) [85]:

$$\left\langle \frac{dE}{dx} \right\rangle = 4\pi m_e c^2 r_e^2 z^2 \frac{Z\rho N_A}{A} \frac{1}{\beta^2} \left(\frac{1}{2} \ln \left(\frac{2m_e c^2 \beta^2 \gamma^2 E_{max}}{I^2} \right) - \beta^2 \right) \tag{4.6}$$

With:

m_e:	electron mass
z:	charge of incident particle
Z:	atomic number of absorber
A:	atomic mass of absorber $[g/mol]$
ρ:	density of the absorber
N_A:	Avogadro constant
r_e:	classical electron radius $[r_e = \frac{e^2}{4\pi\epsilon_0 m_e c^2}]$
ϵ_0:	vacuum permittivity
β:	$\frac{v}{c}$ of the incident particle
c:	velocity of light
I:	mean excitation potential
γ:	Lorentz factor $[\gamma = \frac{1}{\sqrt{1-\beta^2}}]$

E_{max} is the maximum kinetic energy which can be imparted to a free electron in a single head-on collision:

$$E_{max} = \frac{2m_e c^2 \beta^2 \gamma^2}{1 + 2\gamma \frac{m_e}{M} + (\frac{m_e}{M})^2} \tag{4.7}$$

where M is the mass of the incident particle.

Using definition of classical electron radius in Eq. 4.6 we obtain :

$$\begin{aligned} \left\langle \frac{dE}{dx} \right\rangle &= \frac{2\pi e^4 z^2}{m_e c^2} (\frac{1}{4\pi\epsilon_0})^2 \frac{Z\rho N_A}{A} \frac{1}{\beta^2} \left(\ln \left(\frac{2m_e c^2 E_{max}}{I^2} \right) + \ln(\beta^2\gamma^2) - 2\beta^2 \right) \\ &= \frac{e^4 z^2}{8\pi m_e c^2 \epsilon_0^2} N \frac{1}{\beta^2} \left(\ln \left(\frac{2m_e c^2 E_{max}}{I^2} \right) + 2\ln(\beta\gamma) - 2\beta^2 \right) \end{aligned} \tag{4.8}$$

where $N = \frac{Z\rho N_A}{A}$ represents the density of the electrons in the absorbing material.

At non-relativistic energies, dE/dx is dominated by the overall $1/\beta^2$ factor and decreases with increasing velocity until about $v \approx 0.96\ c$, where a minimum is reached. Particles at this

point are referred to as *minimum ionizing particles (mip)*. As the energy increases beyond this point, the term $1/\beta^2$ becomes almost constant and dE/dx rises due to logarithmic dependence of (4.8).

Later it has been found that the relativistic rise would not continue to indefinitely large velocities ($\beta \to 1$). This fact was attributed to a coherent polarization of the surrounding atoms which shield the field of the travelling particle. Fermi [93] calculated a corresponding correction term $\delta(\beta\gamma)$ which is added to (4.8).

$$\left\langle \frac{dE}{dx} \right\rangle = \frac{e^4 z^2}{8\pi m_e c^2 \epsilon_0^2} N \frac{1}{\beta^2} \left(\ln\left(\frac{2m_e c^2 E_{max}}{I^2} \right) + 2\ln(\beta\gamma) - 2\beta^2 - \delta(\beta\gamma) \right) \quad (4.9)$$

As a result, in the limit of $\beta \to 1$ the BB function approaches the *Fermi plateau* value (see Appendix A).

Further it has to be taken into account that for the case of gas drift chambers Eq. (4.9) cannot describe the energy loss, because high energy transfers will result in an electron that is knocked out (δ electron) of the atom and will form a separate track which ionization cannot be associated with the parent contributor (so-called *secondary ionization*). To reflect this a maximum energy transfer to an electron, referred as a *cut-off* energy E_{cut}, has to be introduced into the calculation [94]. Energy transfer larger than the E_{cut} will not be regarded in the calculation. Integration gives the following expression for the energy loss (from [26]):

$$\left\langle \frac{dE}{dx} \right\rangle = \frac{e^4 z^2}{8\pi m_e c^2 \epsilon_0^2} N \frac{1}{\beta^2} \left(\ln\left(\frac{2m_e c^2 E_{cut}}{I^2} \right) + 2\ln(\beta\gamma) - \beta^2\left(1 + \frac{E_{cut}}{E_{max}}\right) - \delta(\beta\gamma) \right) \quad (4.10)$$

This *restricted* energy loss is more adequate to be used in atomic collisions measurements. This form approaches the Bethe-Bloch function (Eq. (4.9)) when $E_{cut} \to E_{max}$. In NA61 TPCs we have $E_{cut} \ll E_{max}$ which is reducing Eq. 4.10 to:

$$\left\langle \frac{dE}{dx} \right\rangle = \frac{e^4 z^2}{8\pi m_e c^2 \epsilon_0^2} N \frac{1}{\beta^2} \left(\ln\left(\frac{2m_e c^2 E_{cut}}{I^2} \right) + 2\ln(\beta\gamma) - \beta^2 - \delta(\beta\gamma) \right) \quad (4.11)$$

4.4.2 Parametrization for heavy charged particles

Introduced in Eq. 4.11 Bethe-Bloch formula for heavy particles is adequate to be used in ionization measurements. Unfortunately, the parameters describing absorbing material cannot be calculated precisely from the first principles. For example the electron density, N, is not a constant value and depends on properties of gas mixture which is changing with experimental conditions (like varying atmospheric pressure in the TPCs huts, described in detail in above Sec. 4.3.2 on page 45). Although the absolute value of dE/dx is not measured in NA61, we still require the consistency between different particle types (referred as $\beta\gamma$ scaling). It is necessary to parametrize the shape of Bethe-Bloch function as precisely as possible. For this purpose we use functional shape of the BB formula considering the parameters depending on composition, pressure and temperature of the detector gas mixture as free fit parameters that can be adjusted to experimental measurements:

$$\left\langle \frac{dE}{dx} \right\rangle = \frac{e^4 z^2}{8\pi m_e c^2 \epsilon_0^2} N \frac{1}{\beta^2} \left(K + 2\ln(\beta\gamma) - \beta^2 - \delta(\beta\gamma) \right) \quad (4.12)$$

with K equal to:

$$K = \ln\left(\frac{2m_e c^2 E_{cut}}{I^2}\right) \tag{4.13}$$

As parametrization of the $\delta(\beta\gamma)$ term we use a description that was introduced by Sternheimer and Peierls [103] :

$$\delta(\beta\gamma) = \begin{cases} 0 & \text{if } X < X_0 \\ 2\ln(10)(X - X_A) + a(X_1 - X)^3 & \text{if } X_0 \leq X < X_1 \\ 2\ln(10)(X - X_A) & \text{if } X \geq X_1 \end{cases} \tag{4.14}$$

where $X = \log_{10}(\beta\gamma)$. The constants X_0, X_A, X_1, F, K, and a are six parameters to be adjusted. However X_0 and X_1 result from the boundary condition that equation (4.14) should be smooth function at $X = X_0$ and $X = X_1$ (for details see Appendix A):

$$\begin{aligned} X_0 &= X_A - \frac{1}{3}\sqrt{\frac{2\ln(10)}{3a}} \\ X_1 &= X_A + \frac{2}{3}\sqrt{\frac{2\ln(10)}{3a}} \end{aligned} \tag{4.15}$$

Experimentally it is convenient to use the energy loss value s at Fermi plateau in order to determine N (the relation between s and other parameters is also derived in the Appendix A):

$$\frac{e^4 z^2}{8\pi m_e c^2 \epsilon_0^2} N = \frac{s}{K + 2\ln(10)X_A - 1} \tag{4.16}$$

Finally Bethe-Bloch parametrization (4.12) and (4.14) may be rewritten in terms of four unknown parameters: X_A, a, K, and s, all dependent on properties of the absorbing material:

$$\left\langle \frac{dE}{dx} \right\rangle = \left(\frac{s}{K + 2\ln(10)X_A - 1}\right) \frac{1}{\beta^2}\left(K + 2\ln(\beta\gamma) - \beta^2 - \delta(\beta\gamma)\right) \tag{4.17}$$

4.4.3 Calibration of Bethe-Bloch parametrization

In order to determine the parameters of the Bethe-Bloch parametrization (see Eq. (4.17)), we need data samples of clearly separated particle types with their measured values of $\beta\gamma = \frac{p}{m_j}$. The $\beta\gamma$ scaling does not depend on particle charge. In other words we expect to have the same value of energy loss for both charges of given particle type with the same momentum. In Fig. 4.5 we present the measured values of *dE/dx* versus momenta for positively and negatively charged particles. Clearly there are regions of *dE/dx* and momentum range, where a given particle identification is explicit and unique. These are:

- region where *dE/dx* is dominated by the overall $1/\beta^2$ factor and decreases with increasing velocity. This area may be covered by points of low momentum ($p < 1$ GeV/c and $\beta\gamma < 1$) protons and deuterons which are completely separated within *dE/dx* >2 mip (see Fig. 4.5 *(left)*).

- *dE/dx* reaching its minimum can be populated by π^+ points. For $p \simeq [0.4 - 0.8]$ GeV/c we can see very little overlapping with other particle species and separation is sufficient ($1 < \beta\gamma < 10$).

- relativistic rise (covering momentum range $p \simeq [3-10]$ GeV/c and $10 < \beta\gamma < 100$) is very well represented with π^- candidates where contribution from antiprotons is negligible. This fact makes identification in selected area more adequate, in comparison to π^+ candidates (see Fig. 4.5 *(right)*).

- the Fermi plateau (s_e) represented by e^- candidates with dE/dx =[1.4, 1.7] mip will be treated separately in the following section (see Fig. 4.5 *(right)*).

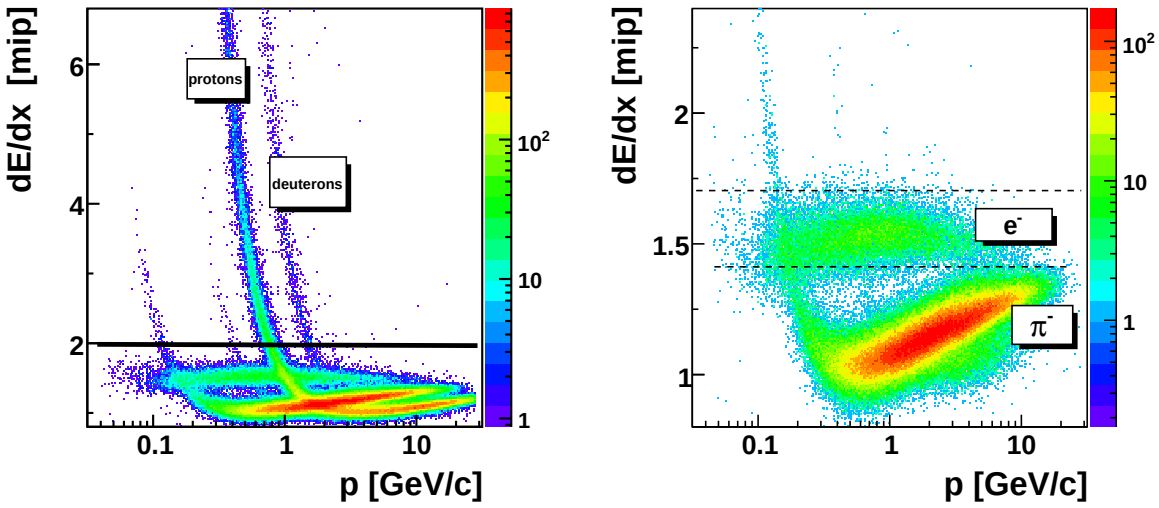

Figure 4.5: Measured dE/dx as a function of momentum for positively *(left)* and negatively *(right)* charged particles. Each point represents one track. Protons and deuterons with $dE/dx \geq 2$ mip are marked above black line in the regions of explicit particle identification. π^- candidates represent relativistic rise region. The Fermi plateau (s_e) is shown for e^- candidates with dE/dx =[1.4, 1.7] mip.

The shape of the fitted Bethe-Bloch parametrization to the data samples of protons, pions and deuterons as a function of $\beta\gamma$ from 0.2 up to 100 is shown in Fig. 4.6. The region of relativistic rise for $dE/dx < 2.3$ [mip] is exposed in Fig. 4.6 *(right)*. Values of fitted parameters are shown in Table 4.1. Parameters a and X_A are sensitive to the relativistic rise region ($\beta\gamma \geq 10$), whereas s defines the value of the theoretical Fermi plateau for heavy particles ($\beta\gamma > 100$).

Parameter:	Fitted value
K	16.8±0.6
s [mip]	1.68± 0.05
a	0.05±0.01
X_A	3.3±0.2

Table 4.1: Values of parameters obtained from the Bethe-Bloch parametrization, described with (4.17) and (4.14), fitted to the experimental measurements.

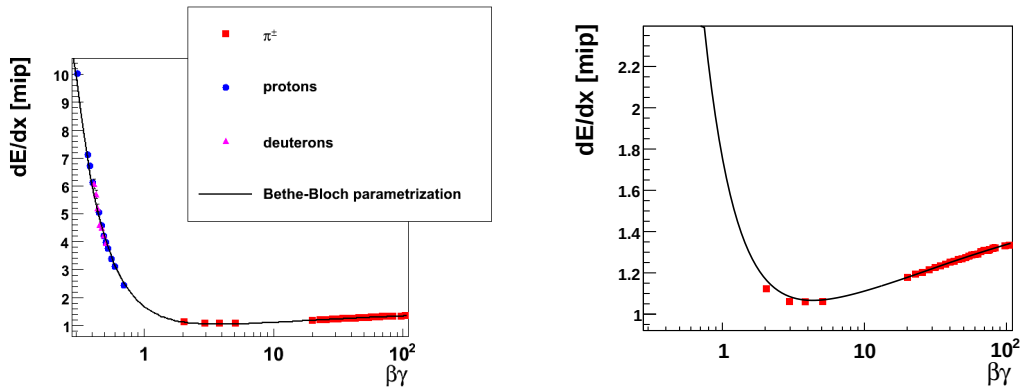

Figure 4.6: Measured dE/dx versus value of $\beta\gamma$. The colorful points show different particle species. Black line represents fitted Bethe-Bloch parametrization described with (4.17) and (4.14). *Left*: the whole dE/dx range. *Right*: area with $dE/dx < 2.4$ [mip]. The region of dE/dx relativistic rise is clearly observed.

4.4.4 Energy loss of electrons and positrons

Ionization energy loss by electrons and positrons differs from the loss by heavy particles because of the kinematics, spin and the identity of the incident electron with the electrons which on which it settles [26]. The Bethe-Bloch formula (4.11) must be modified for two main reasons. One, as already mentioned is their small mass. The assumption that the incident particle remains not deflected during the collisions process in no longer valid. The second is that for the electrons the collisions occur between identical particles and calculation must take into account their indistinguishability.

The Bethe-Bloch formula for electrons and positrons becomes [85, 86]:

$$\left\langle \frac{dE}{dx} \right\rangle |_{e^+,e^-} = \frac{e^4 z^2}{4\pi m_e c^2 \epsilon_0^2} N \frac{1}{\beta^2} \left(\ln \left(\frac{m_e c^2 \gamma \beta \sqrt{\gamma - 1}}{\sqrt{2} I} \right) + F(\beta\gamma) - \delta(\beta\gamma) \right) \quad (4.18)$$

where $F(\beta\gamma)$ accounts for differences between electrons and positrons. They are observed for low energy range (in good approximation $E \ll 100$ MeV, depending on detector material) where very fast change of energy loss with incident particle energy is observed. Above 100 MeV, thus in the region of interest here, the energy loss by ionization mechanism for electrons and positrons becomes equal, as reported in Ref. [26].
As seen in Fig. 4.2, the total energy loss of electrons (positrons) due to collisions is approximate by a constant [86]:

$$\left\langle \frac{dE}{dx} \right\rangle |_{e^+,e^-} = s_e \quad (4.19)$$

Both electrons and positrons in our energy range reach their Fermi plateau, referred as s_e.

4.4.5 Parametrization for electrons and positrons

In order to determine s_e we decided to take into account all electron and positron candidate tracks with dE/dx =[1.4, 1.7] mip starting from p=0.6 GeV/c. We divided the selected range into 0.2 GeV/c momentum bins. For each bin a Gaussian function was fitted to energy distribution loss and mean dE/dx and its sigma was obtained ($< dE/dx >$ and $\sigma_{dE/dx}$). The obtained mean dE/dx values of $\beta\gamma$ *(left)* and mean momentum $< p >$ *(right)* for electrons and positrons are illustrated in Fig. 4.7.

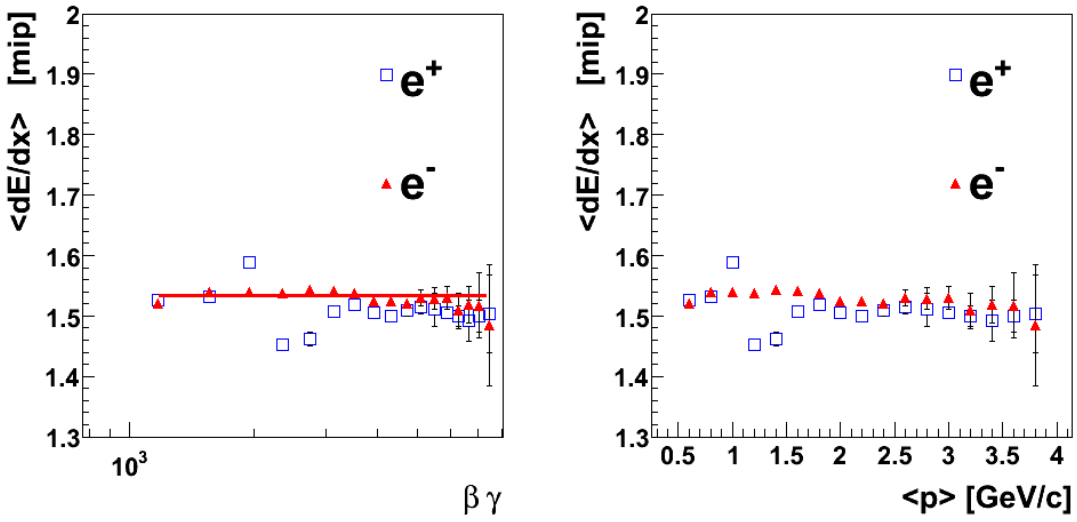

Figure 4.7: Measured mean dE/dx versus value of $\beta\gamma$ *(left)* and mean momentum $< p >$ *(right)* for electrons (*blue*) and positrons (*red*). The red, solid line represents the value of parametrization s_e obtained from the fit to e^- points.

In the momentum range between 0.8 and 1.5 GeV/c dE/dx for positrons overlap with those of protons and deuterons. This fact explains the differences in value of mean dE/dx of electrons, as contribution from antiprotons or antideuterons is almost negligible. Clearly one can observe that for momentum range $p < 0.8$ GeV/c and $p > 1.5$ GeV/c the average energy loss for electrons and positrons is close enough and almost constant (s_e=const). We decided to fit s_e for the electrons (red line in Fig. 4.7 *(left)*) as their specific energy loss is less disturbed by other particle types. Value of:

$$s_e = [1.53 \pm 0.01] \text{ mip} \tag{4.20}$$

was used as a BB parametrization for electrons and positrons.

4.5 Methods of Particle Identification

As we have already learned from the previous sections particle identification in NA61 was possible using energy loss measurements (dE/dx) in active volume of the TPCs and time-of-flight information from the ToF-F detector. In order to obtain particle yields in broad momentum range, two different analyses were developed.

4.5.1 Method based on energy loss measurement only

If measured dE/dx values are plotted versus momenta for data collected during 2007, a clear mass dependence can be seen, as shown in Fig. 4.8. When the resolution of the ionization measurement is sufficient, the separation of different species is possible, excluding of course regions where Bethe-Bloch curves cross each other like in momentum range of $1 < p$ [GeV/c] $\leqslant 3$ for positively charged particles. For negative particles situation in this region of phase space is better as we do not see antiprotons and antideuterons in the data. This momentum range

of $1 < p$ [GeV/c] $\leqslant 3$ is very important for the T2K neutrino predictions (see Sec. 2.5.2 on page 26). A combined analysis with dE/dx and ToF-F measurements (tof - dE/dx) was conducted in this range.

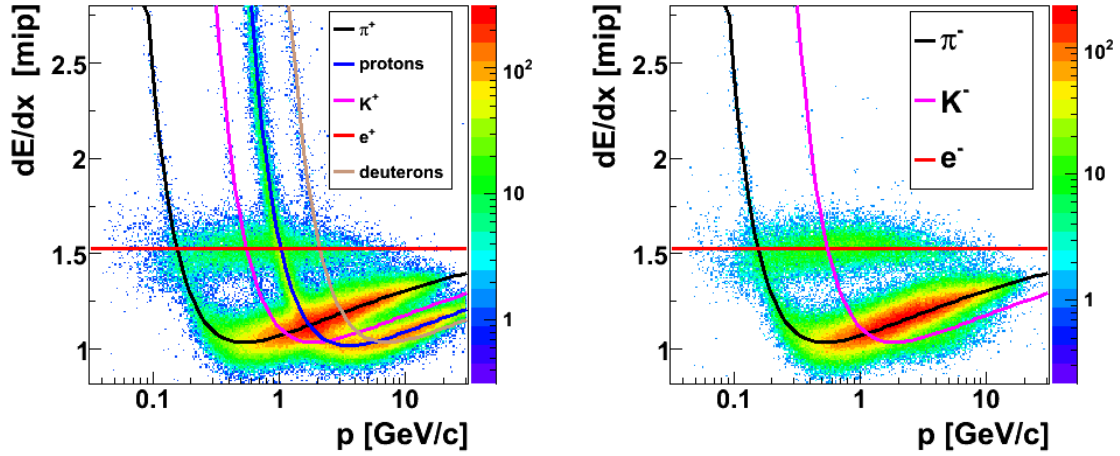

Figure 4.8: The measured dE/dx values are plotted versus momentum for positively *(left)* and negatively *(right)* charged particles together with the parametrized BB curves for positrons (electrons), pions, kaons, protons and deuterons. Each point represents one track.

Moreover, one has to also keep in mind that methods developed for the identification should be different for low momentum particles, where fast change of energy loss is observed with momentum, in comparison to the relativistic rise. To conclude, particle identification based only on energy loss measurement is reliable in two different momentum regions:

- low momentum region, *i.e.* for tracks with $0.2 < p$ [GeV/c] $\leqslant 1$ for positive particles and $0.2 < p$ [GeV/c] $\leqslant 3$ for negative particles,
- relativistic rise region, *i.e.* for tracks with $p \geq$3 GeV/c.

4.5.2 Combined energy loss and time-of-flight measurement.

This analysis was a subject of Ph.D thesis and is extensively described in Ref. [101]. Determination of the the total particle path length l and time-of-flight measurement t_{ToF} (see Eq. 3.1 on page 38) allows to calculate the particle mass squared:

$$m^2 = p^2 \left(\frac{c^2 \cdot t_{ToF}^2}{l^2} - 1 \right) \tag{4.21}$$

In Fig. 4.9 *(left)* we illustrate the mass squared derived from the above formula versus momentum p for positive particles. The lines show the expected mass squared values for different particles. A good separation between particle species is observed for track momentum p$\sim$[1-6] GeV/c. For larger momenta we have to rely only on dE/dx. An example of two-dimensional m^2 vs dE/dx plot in momentum range 2 <p [GeV/c]< 3 is shown in Fig. 4.9 *(right)*. The 2σ contour around fitted pion peak is also seen.

In *left* plots in Figs.[4.10, 4.11] we illustrate the phase space in (p, θ), where θ is production angle, covered by NA61 measurements in 2007 for all positive and negative particles. In the *right* plots we demonstrate only those particles which left signal in the scintillators of the

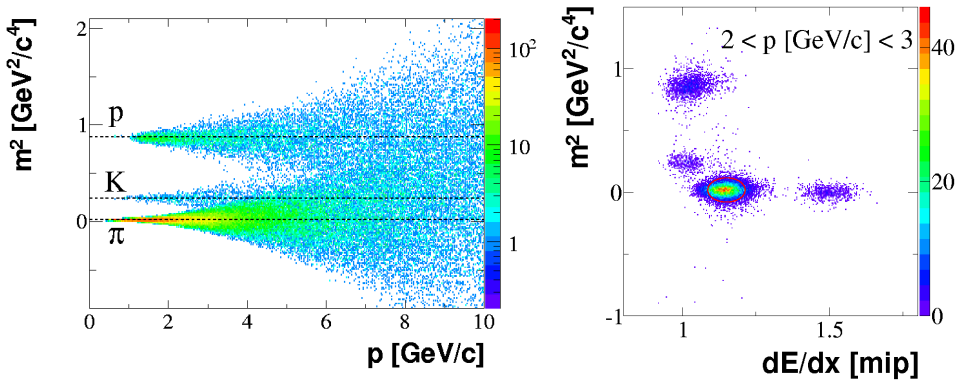

Figure 4.9: Identification of positive particles using both dE/dx and ToF-F measurements. *Left*: Measured mass squared, derived from the ToF-F measurement versus momentum p. The lines show the expected mass squared values for different particles. *Right*: An example of two-dimensional m^2 vs dE/dx plot in momentum range 2 <p [GeV/c]< 3. The 2σ red contour around fitted pion peak is shown. Each point represents one track. Figures are taken from Ref. [1].

ToF-F. One can observe that most of the particles detected in the ToF-F have production angles θ below 200 mrad. To see closer the ToF-F acceptance Fig. 4.12 zooms the momentum region below 5 GeV/c for both positive and negative particles. Below 1 GeV/c only dE/dx information alone has to be used to distinguish pions from electrons/positrons, kaons and protons. Low momentum region is also very important for the T2K physics as a lot of positive pions with $0.2 < p$ [GeV/c] $\leqslant 1$ contribute to the neutrino flux (see Sec. 2.5.2 on page 26).

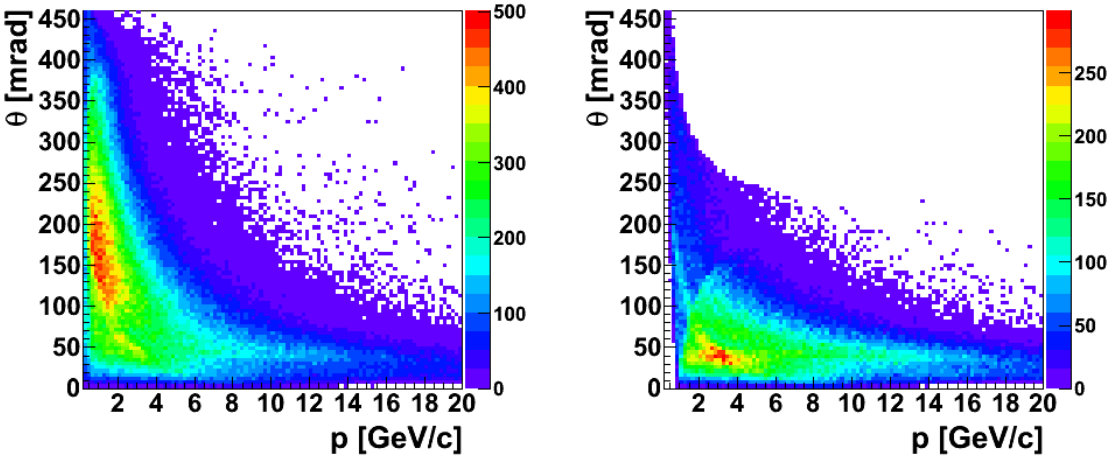

Figure 4.10: Production angle versus momentum for all positive particles *(left)* and only those of positive particles which read the ToF-F detector *(right)*. Each point represents one track.

Finally, while comparing plots in Fig. 4.10 with Fig. 2.8 on page 27 one concludes that the NA61/SHINE measurements fully cover the phase space region in (p, θ) of interest for the T2K.

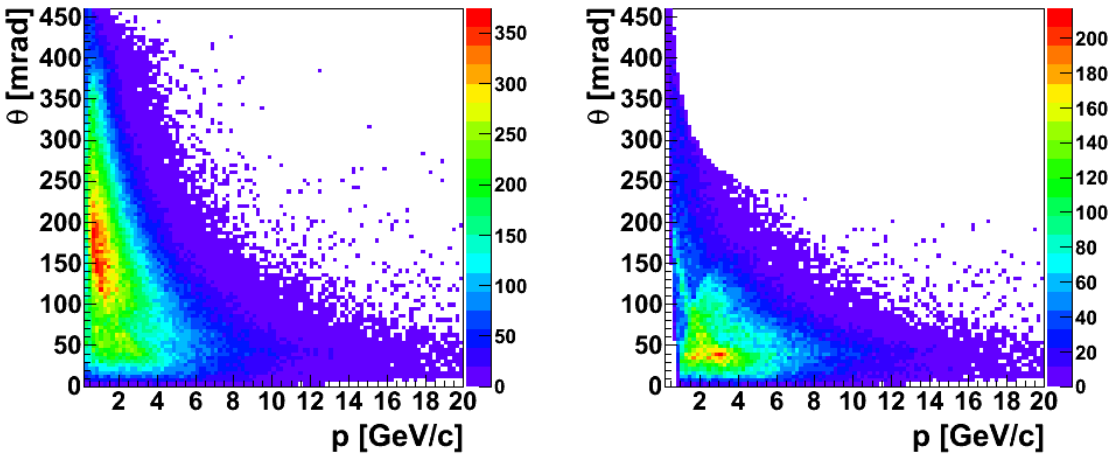

Figure 4.11: Production angle versus momentum for all negative particles *(left)* and only those of negative particles which read the ToF-F detector *(right)*. Each point represents one track.

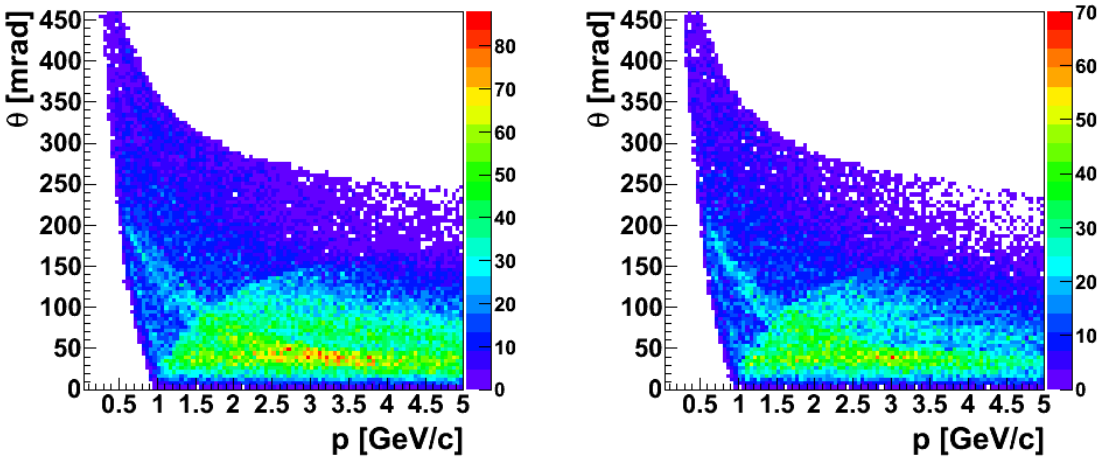

Figure 4.12: Zoom of the right plots of Fig. 4.10 and Fig. 4.11 for momenta below 5 GeV/c .

4.6 Analysis of negatively charged particles

Analysis of negatively charged particles further referred to as h^- analysis, is based on the theoretical and experimental premises that negative particles produced by 31 GeV/c protons consist mainly of negative pion mesons with an admixture of electrons, negative kaons and a negligible fraction of antiprotons. This procedure allows to obtain spectra of π^- mesons in the broad momentum range. The Monte Carlo simulation described in Sec. 7.3 on page 99 was used to calculate corrections for the contribution of electrons, primary K^- and $\overline{p}$. This analysis is a subject of Ph.D thesis [102].

4.7 Analyses map

To conclude, yields of positive pions, which are of interest for the T2K neutrino flux constrain as well as negative pions, could be obtained in the following regions of phase space:

- Low momentum region, defined with $0.2 < p$ [GeV/c] $\leqslant 1$ for positive particles and $0.2 < p$ [GeV/c] $\leqslant 3$ for negative particles, where information of the particle type can be obtained with the *dE/dx* measurements. We developed tools and performed the analysis, details of which are extensively reported in the next chapters.

- Region of $p \geq$1 GeV/c where *tof* - *dE/dx* information was used. Yields for both pion charges were obtained. For details see Refs. [1, 101].

- Broad momentum range treated with h^- analysis allowed to extract only negative pion yields. The h^- analysis played important role while performing many cross checks of results obtained with particle identification methods. Extensive description of the analysis method can be found in Refs. [1, 102]

In this dissertation we concentrate on the low momentum region. The details of this analysis are introduced in Chapters 5 and 6.

Chapter 5

Event and track selection

This chapter deals with event and track selection criteria which were applied in order to obtain clean sample of well defined tracks on which the particle identification will be performed. The phase space used in the analysis is defined by momentum and production angle (p, θ) bins. For the final results momentum intervals of 0.1 GeV/c for $0.2 < p$ [GeV/c] $\leqslant 1$ and 0.2 GeV/c for $0.2 < p$ [GeV/c] $\leqslant 3$ and ten polar angle bins covering the range from 0 up to 420 mrad were chosen. The last section is devoted to studies which were performed in order to understand different track topologies used for the analysis after all selections.

5.1 Event selection

Total sample of registered and reconstructed thin target events during 2007 run consists of around 669 thousands. The sample is reduced to ∼521 thousands by selecting only those events which had signals in each plane of all three BPD detectors (later referred to BPD cut) together with correctly reconstructed beam tracks which have measured points on both planes of BPD-3 (see Fig. 3.1). The aim of this criterion is to remove significantly contamination of interactions upstream of the target. In order to estimate a rate of off-target interactions a special run was devoted to take data with target removed. For this case the BPD selection reduces events from 46000 to 17000. Detailed reduction rates are presented in Table 5.1. In the following discussion of track selection we take into account only the selected event sample.

5.2 Track selection

For the selected event sample we also apply several track selection criteria. They are chosen in order to reduce the contamination of tracks coming from secondary interactions and weak decays as well as incorrectly reconstructed tracks. We focus here on the low momentum particles, by which, as explained in Sec. 4.7 on page 57, we understand those with $0.2 < p$ [GeV/c] $\leqslant 1$ for positive tracks and $0.2 < p$ [GeV/c] $\leqslant 3$ for negative ones. Below we introduce the applied quality track selection criteria. These are:

- the distance between a track extrapolated to the target plane and the interaction point, referred as impact parameter, in both transverse directions should be less than 4 cm,
- total number of reconstructed points (N) should be ≥30 ($N \geq 30$),
- sum of number of reconstructed points in VTPC1 and VTPC2 should be ≥12 ($N_{VTPC1} + N_{VTPC2} \geq 12$),

- number of reconstructed points should exceed half of the maximum potential points ($r \equiv N/N_{pot,point} > 0.5$).

List of the event and track cuts together with their impact on the event and track sample is presented in Table 5.1.

Impact of the cut		
	target inserted	target removed
Event cuts		
BPD	N^I_{trig} 521238 (78% out of all events)	N^R_{trig} 17104 (38%)
Track cuts - all sample		
Impact parameter	1116086, (93% out of all tracks)	4856 (69%)
$N \geq 30$	818007, (68%)	3669 (52%)
$N_{VTPC1} + N_{VTPC2} \geq 12$	759494, (63%)	1575 (23%)
$N/N_{pot,point} > 0.5$	757115, (63%)	1567 (22%)
Positive low momentum tracks with 0.2<p [GeV/c]≤1		
Impact parameter	171225, (91%)	467 (55%)
$N \geq 30$	91734, (49%)	298 (36%)
$N_{VTPC1} + N_{VTPC2} \geq 12$	89161, (48%)	112 (13%)
$N/N_{pot,point} > 0.5$	88322, (47%)	107 (13%)
Negative low momentum tracks with 0.2<p [GeV/c]≤1		
Impact parameter	123623, (91%)	359(51%)
$N \geq 30$	70212, (52%)	217 (31%)
$N_{VTPC1} + N_{VTPC2} \geq 12$	68085, (50%)	77 (11%)
$N/N_{pot,point} > 0.5$	67400, (49%)	76 (11%)
Negative low momentum tracks with 1<p [GeV/c]≤3		
Impact parameter	164063, (94%)	721 (75%)
$N \geq 30$	125417, (72%)	520 (54%)
$N_{VTPC1} + N_{VTPC2} \geq 12$	119104, (68%)	239 (25%)
$N/N_{pot,point} > 0.5$	118913, (68%)	239 (25%)

Table 5.1: Event and track cuts. (All values quoted in brackets refer to the percentage of events/tracks which survive the selection corresponding to chosen momentum range and charge sign). N^I_{trig} (N^R_{trig}) is the number of thin target (removed target) events which survive the BPD cut described in the text.

Each track selection was studied in detail and the results of this task are presented below.

In addition to track cuts defined in Table 5.1 we apply one more selection on the track azimuthal angle which should be within an azimuthal angle wedge around the horizontal plane. The wedge size depends on polar angle and its value was adjusted while comparing Monte Carlo and real data which is described in the details in Sec. 7.2 on page 90.

5.2.1 The track selection based on impact parameter cut

The impact parameter is defined as the distance between a track extrapolated to the target plane and the interaction point in both transverse directions (B_x and B_y, separately) and is

used in order to check the quality of the reconstruction algorithms, described in Sec 4.1 on page 40.
Figs. 5.1 and 5.2 illustrate distributions of impact parameter B_x for positive and negative low momentum particles in different production angle intervals without (*blue*) and with (*red*) track selections listed in Table 5.1. The corresponding distributions of B_y are shown in Figs. 5.3 and 5.4. It is seen that:

- For most polar angle intervals impact parameters are centered around zero (note the logarithmic vertical scale), as expected, showing tails coming from badly reconstructed tracks. A few mm shift in the central value of the impact parameter is seen for the largest θ interval. However it is not a concern if we apply the cut on impact parameters to be a few cm as majority of tracks still survive the discussed selection.

- One observes an asymmetry of B_x distributions (for $\theta \geq$40 mrad) which is opposite for tracks with opposite charge sign. This asymmetry disappears in case of B_y distributions which indicates that it is related to the magnetic field, oriented along the y axis.

- The cuts applied for the track selection significantly reduce tails of badly reconstructed tracks, especially for larger polar angels.

To conclude this part of the selection we decided to take all the tracks for further consideration with both impact parameters being less than 4 cm.

5.2.2 The track selection based on total number of reconstructed points

By reconstructed points we understand those which correspond to measured clusters of a track. Each cluster is measured on one pad-row, thus the maximum number of clusters as well as reconstructed points, is equal to sum of all pad-rows in each of the TPCs, *i.e.*. N_{max}=234 ($N_{max} = N_{VTPC1} + N_{VTPC2} + N_{MTPC}$=72+72+90, see Tab. 3.2 on page 38). Fig. 5.5 *(left)* illustrates distributions of reconstructed number of points for low momentum ($0.2 < p \leq 1$ GeV/c) tracks (positive (*black*) and negative (*red*)) before applying any track selection criteria. The most significant sample of low momentum tracks has $N < 72$ which is the maximum number of points that can be reconstructed for particles reaching VTPC1 only. This observation leads us to the very important fact: most (around 85%) of the low momentum tracks ($p \leq 1$ GeV/c) pass only through VTPC1.

We studied the dependence of the dE/dx resolution on number of reconstructed points on a track. The results are presented in *(right)* plot in Fig. 5.5, where as an example, positive low momentum particles were chosen. One can see a Poisson dependence of a type:

$$\frac{\sigma_{\mathrm{dE/dx}}}{\mathrm{dE/dx}} \sim \frac{1}{\sqrt{N}} \tag{5.1}$$

The track which has large number of reconstructed points is passing through different sectors of TPCs, having its energy loss more accurately measured, as explained in Sec. 4.3.5 on page 47. On the other hand one has to take into account the fact that for low momentum tracks the statistics with large N is getting small. Combining these two arguments the cut on tracks with $N \geq 30$ was set. It allows us to achieve dE/dx resolution better than 10%. One needs to keep in mind that this resolution corresponds to tracks measured by VTPC. For particles with small angles reaching MTPC typical energy loss resolution varies between 4-5%. In addition impact of this cut is large while we look at the target removed data (see Table 5.1). It reduces contamination of the tracks originated in background events for around 20%.

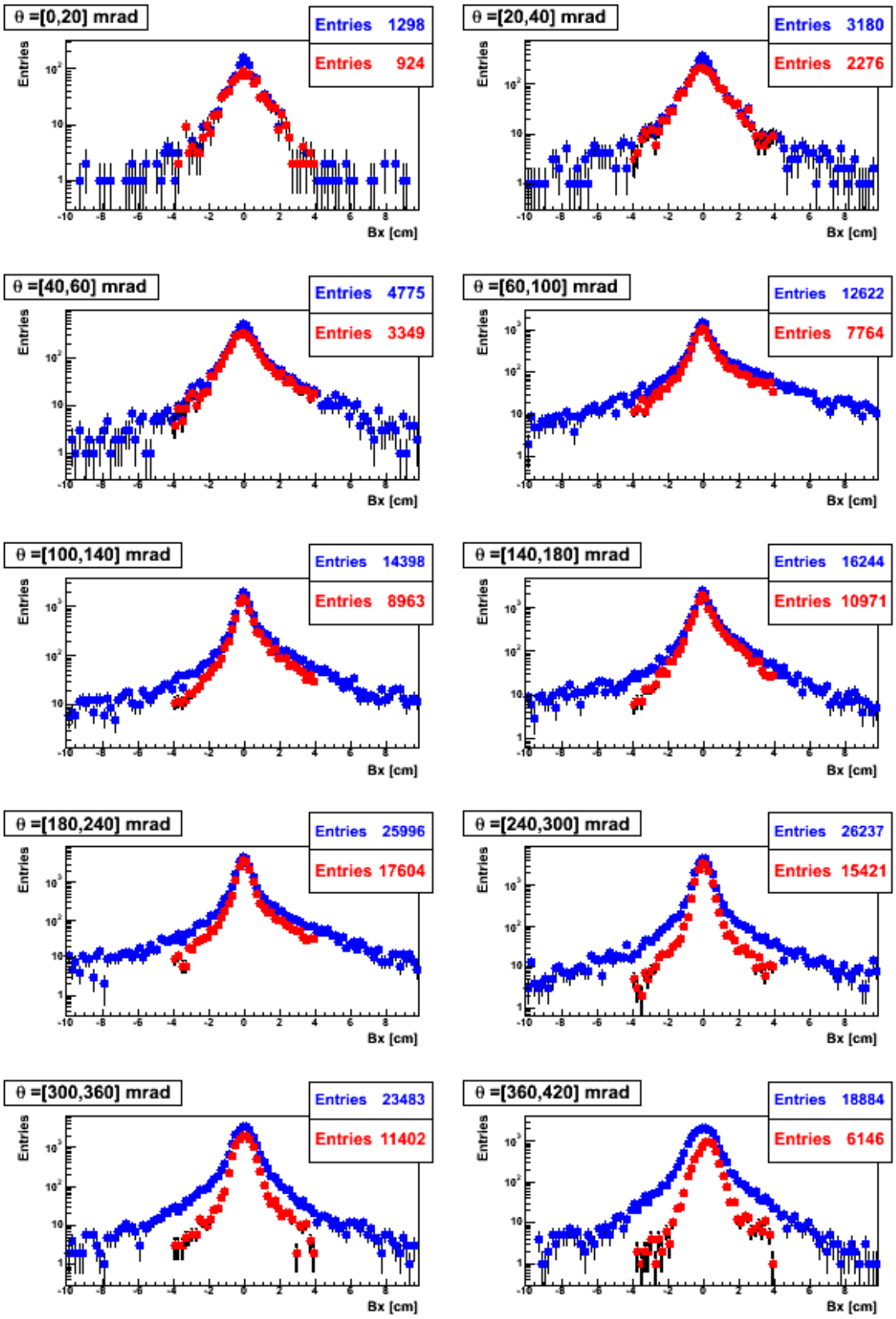

Figure 5.1: Impact parameter defined along x axis (B_x) for positive low momentum tracks and for different production angle intervals without (*blue*) and with (*red*) track selections described in Table 5.1 is presented.

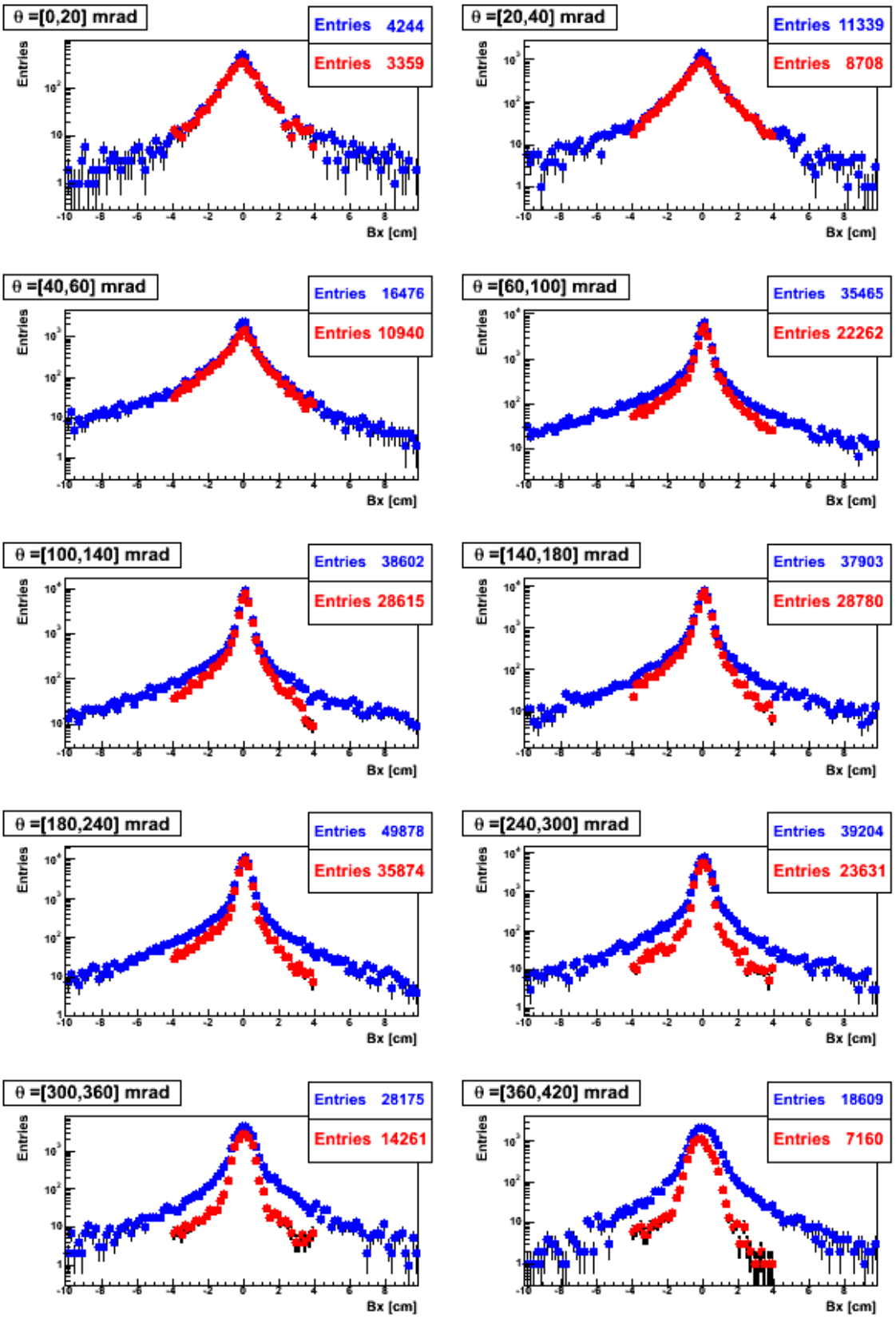

Figure 5.2: Impact parameter defined along x axis (B_x) for negative low momentum tracks and for different production angle intervals without (*blue*) and with (*red*) track selections described in Table 5.1 is presented.

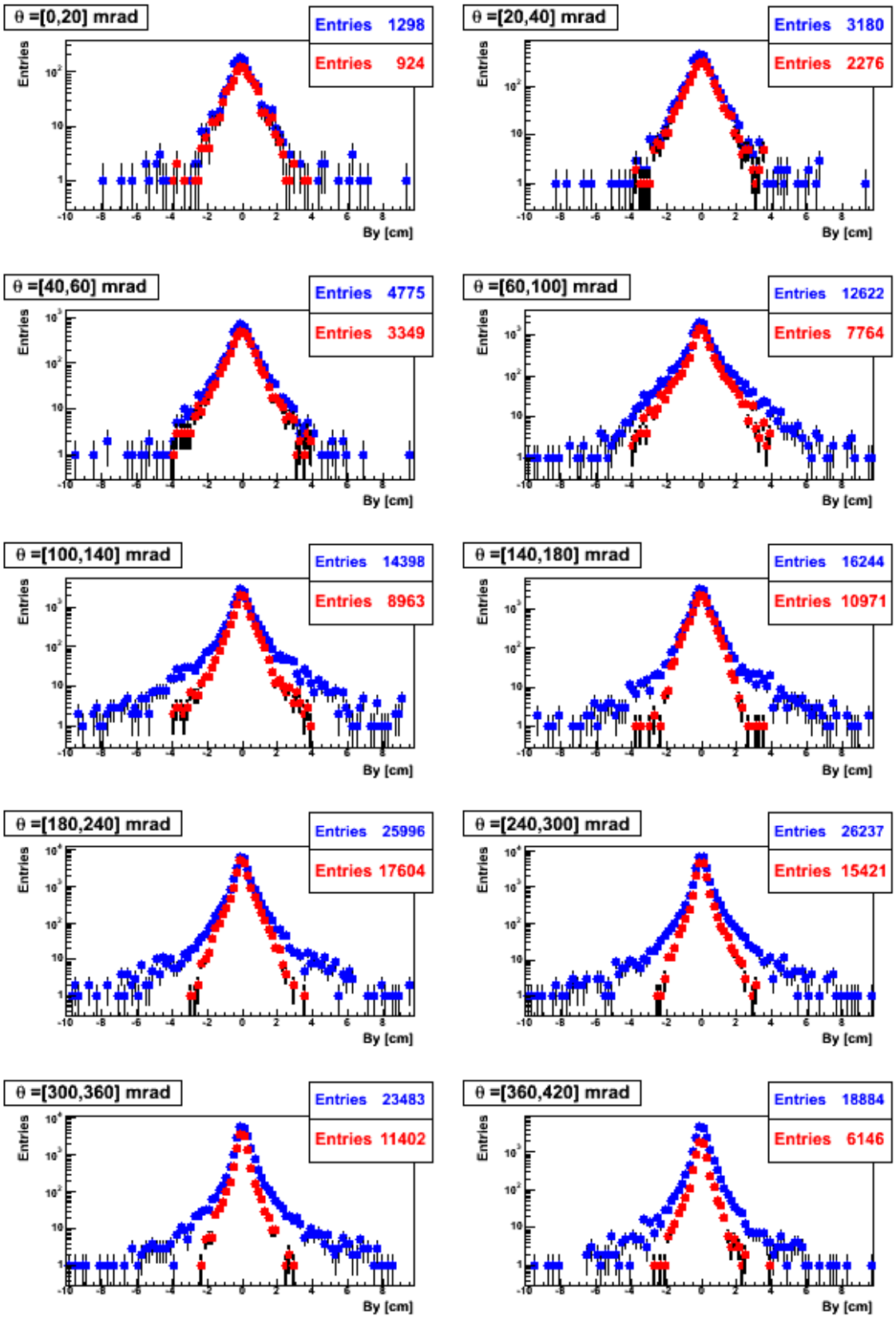

Figure 5.3: Impact parameter defined along y axis (B_y) for positive low momentum tracks and for different production angle intervals without (*blue*) and with (*red*) track selections described in Table 5.1 is presented.

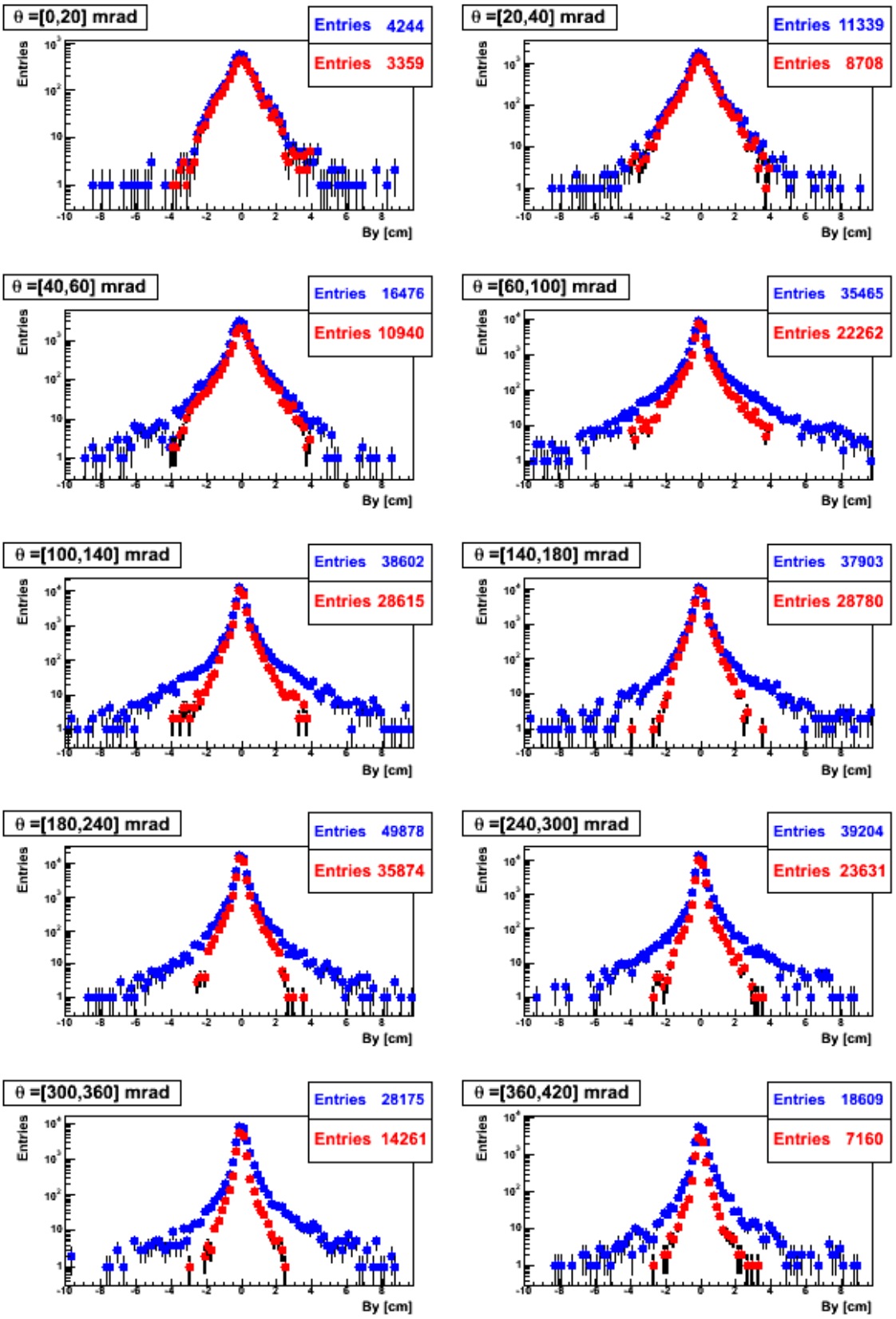

Figure 5.4: Impact parameter defined along y axis (B_y) for negative low momentum tracks and for different production angle intervals without (*blue*) and with (*red*) track selections described in Table 5.1 is presented.

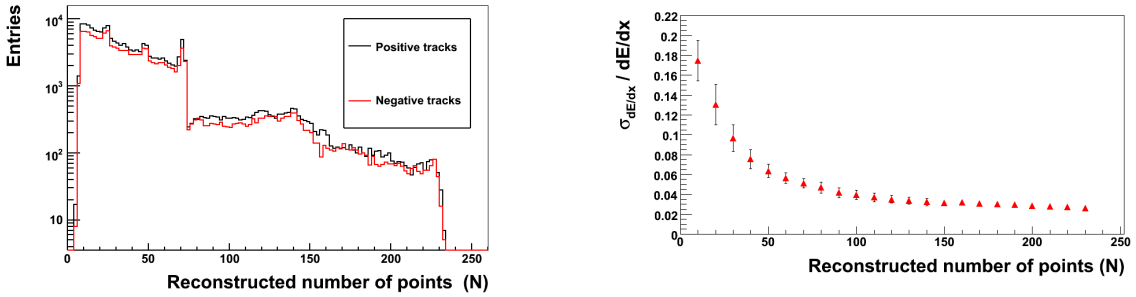

Figure 5.5: *Left*: Reconstructed number of points (N) for low momentum $0.2 < p$ [GeV/c] $\leqslant 1$ positively (*black*) and negatively (*red*) charged particles, respectively. Most of the tracks have less than 72 measured points which is the maximum number of points that can be measured in VTPC1 only. Note the logarithmic vertical scale. *Right*: Resolution of dE/dx versus reconstructed number of points (N) for low momentum positively charged particles. For both plots no track selections were applied.

5.2.3 The track selection based on sum of numbers of reconstructed points in VTPC1 and VTPC2

Another quality selection applied to the data is based on sum of the number of reconstructed points in VTPC1 and VTPC2. Aim of this cut is to choose tracks which are passing at least through one of the VTPCs, where track momentum is being determined. In Fig. 5.6 we illustrate the correlation beetwen sum of number of reconstructed points in VTPC1 and VTPC2 and the total number of reconstructed points for positive *(left)* and negative *(right)* particles. Selections on impact parameter ($B_x \leq 4$ cm and $B_y \leq 4$ cm) and reconstructed number of points $N \geq 30$ have been applied. There are still visible tracks which have no measured points in the VTPCs and were detected only in MTPC. At the end we decided to take all the tracks with $N_{VTPC1} + N_{VTPC2} \geq 12$.

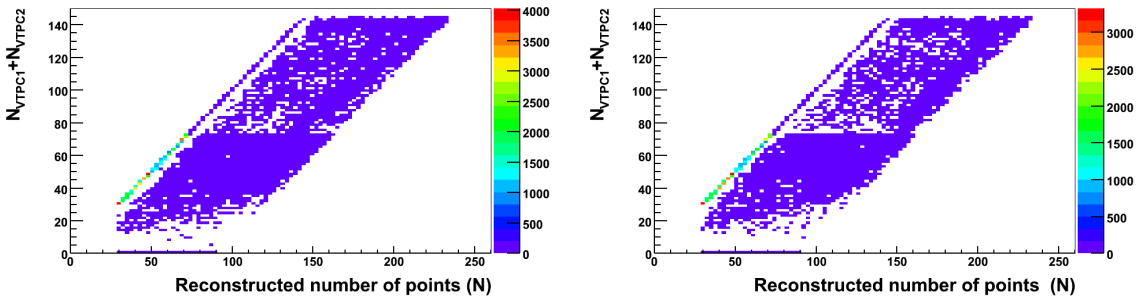

Figure 5.6: Sum of number of reconstructed points in VTPC1 and VTPC2 versus reconstructed number of points for positively *(left)* and negatively *(right)* charged particles. Selections on impact parameter ($B_x \leq 4$ cm and $B_y \leq 4$ cm) and reconstructed number of points $N \geq 30$ have been applied.

5.2.4 The track selection based on a fraction of total number of potential points

An important information about quality of a track reconstruction is given by fraction of a total of potential points, $N_{pot,point}$, which were reconstructed ($r \equiv N/N_{pot,point}$). Potential points are calculated assuming that particles start from the main vertex and effects as multiple scattering, secondary interactions, decays, detector resolution are neglected. The tracks are accepted when the number of the reconstructed points N exceeded half of the $N_{pot,point}$. Figs. 5.7 and 5.8 illustrate distributions of r ratio for different polar angle intervals for positive and negative low momentum tracks. For each θ interval we see a sharp peak at one (note the logarithmic vertical scale) and tails to the left and right. The right tail is due to tracks not coming from the main vertex and biases causing deviation from the track ideal trajectory. The left tail is also partly due to the above effects but in addition it contains also admixture of so-called split tracks. Split tracks can be created in situation when one track is passing through different TPCs and due to a bad reconstruction algorithms its parts from different detectors are not fitted as one track but are treated as two (or more) independent ones. The cut on r>0.5 rejects this kind of tracks. The impact of this cut for low momentum tracks is at the level of 1% (after applying previous selection criteria) again due to the fact that most of low momentum tracks are mainly in VTPC1 only.

5.3 Different track topologies: Right Side and Wrong Side Tracks

The knowledge of the possible track topologies which we encounter during the analysis is very significant. Our sample of selected tracks is not uniform. It is important to introduce tracks with:

$$q \cdot p_x > 0 \tag{5.2}$$

where p_x stands for x coordinate of the momentum and q is the charge of the track, which will be called right side tracks (RST). There is also a sample of wrong side tracks (WST) chosen by the rule:

$$q \cdot p_x < 0 \tag{5.3}$$

Looking at the detectors from above the RST particles start out in the direction to which the magnetic field will bend them anyway, thus avoiding the difficult regions close to the beam line and edges of the TPCs with presence of different experimental distortions (i.e. inhomogeneities in magnetic field). Note that RST tracks match with the pad tilts better in comparison to WST [87, 88, 89]. Pads design was optimized for high energy particles produced in high multiplicity collisions (like Pb-Pb), during NA49 experiment, with most of the tracks of RST type only. In case of NA61 we are interested in low energy particles which occur more often in WST configuration. In Table 5.2 we present population of RST and WST subsamples after all selections described in Table 5.1. Clearly WST group is at the level of 45% of all tracks at minimum and has to be taken into account.

The RST and WST samples characterize very different track topology. In order to illustrate the difference we use x and z coordinates of the first point on a track (x_{first}, z_{first}) as shown in Fig. 5.9 (top view). Projections include low momentum positively and negatively charged particles. Each point represents a measured track. Positive RST (WST) are expected to have their first point for $x_{first}>0$ ($x_{first}<0$) while negative RST (WST) in the opposite, *i.e.* $x_{first}<0$ ($x_{first}>0$). For the definition of coordinate system see Fig. 3.5 on page 36. In addition, for WST sample, we observe admixture of tracks with more complicated trajectory. As an example let's look at positive WST with $x_{first}>0$. These tracks by definition and charge sign have $p_x < 0$. Moreover the value of p_x is very small (what was checked) and due

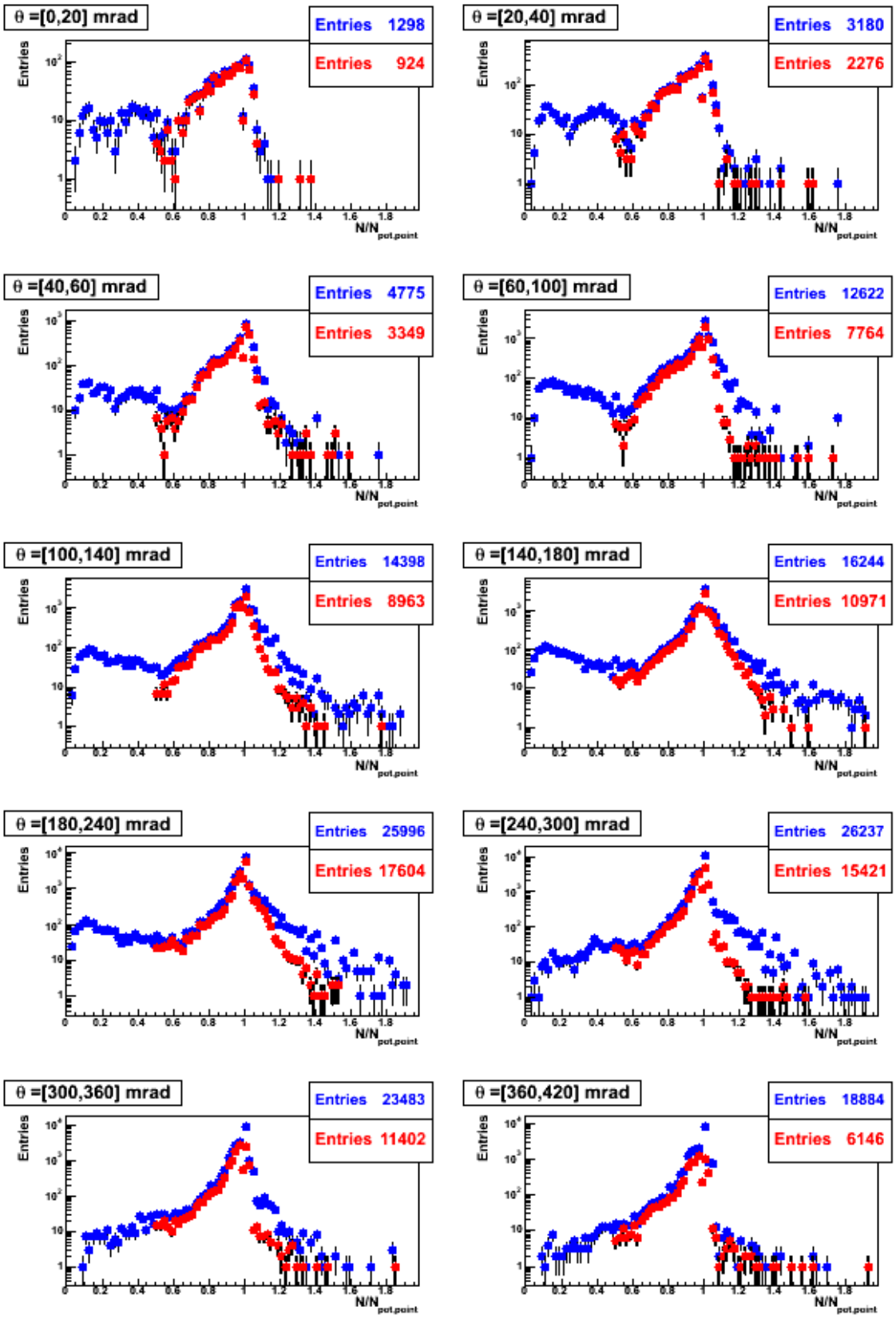

Figure 5.7: Distributions of the total number of reconstructed points to the maximum possible number of points derived from the track trajectory for positive low momentum tracks and for different production angle intervals without (*blue*) and with (*red*) track selections described in Table 5.1 is presented.

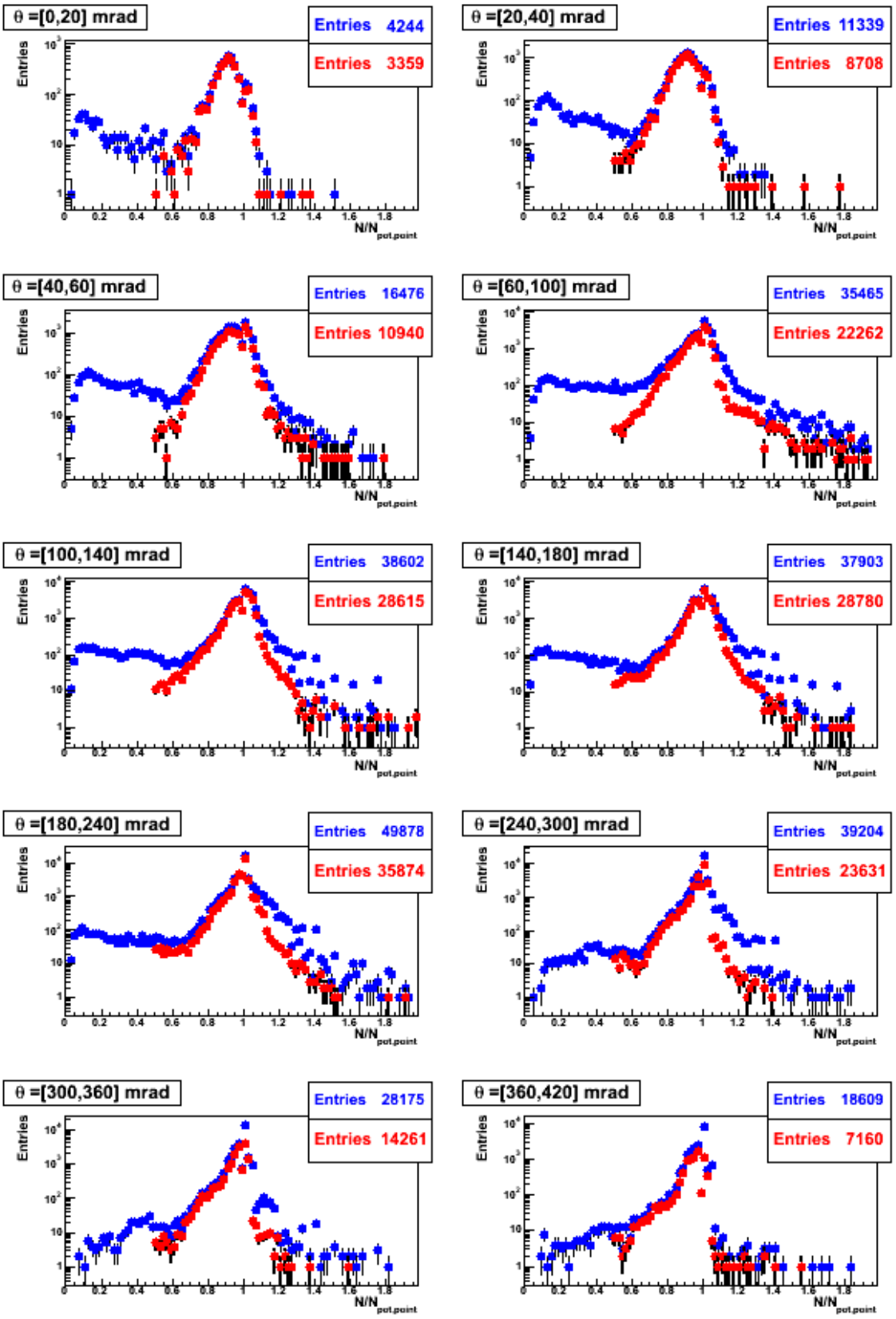

Figure 5.8: Distributions of the total number of reconstructed points to the maximum possible number of points derived from the track trajectory for negative low momentum tracks and for different production angle intervals without (*blue*) and with (*red*) track selections described in Table 5.1 is presented.

Positive low momentum tracks with 0.2<p [GeV/c]≤1	
all sample	88322
RST	46249 (52% among all tracks of 88322)
WST	42073 (48%)
Negative low momentum tracks with 0.2<p [GeV/c]≤1	
all sample	67400
RST	35816 (53%)
WST	31584 (47%)
Negative low momentum tracks with 1<p [GeV/c]≤3	
all sample	118913
RST	65219 (55%)
WST	53694 (45%)

Table 5.2: Low momentum track population. All thin target data, which passed the selections described in Table. 5.1 were used as a starting value.

to presence of magnetic field, their trajectory is curved. As a result, tracks are crossing the 20 cm hole placed between VTPC sectors and reaching the left part of TPC chambers from only side wall, in case of VTPC1, or front and side wall for the VTPC2, as seen on the botton left plot in Fig. 5.9.

Fig. 5.10 shows how the RST and WST track topologies influence the phase space in momentum p and production angle θ. At first we can state that the population of tracks belonging to these subsamples covers the range of θ from 0 to 420 mrad (except the first bin of momentum for RST where $\theta > 360$ mrad). However as seen in Fig. 5.10 WST tracks significantly improve the available statistics at large angles, especially at low momenta. Unfortunately, the sample of WST is not as uniform as RST. It consists of already mentioned two types of tracks which can be separated by the sign of x_{first}. For positive particles WST with $x_{first} > 0$ are represented by those with θ<120mrad whereas for $x_{first} < 0$ one can see only tracks which were produced with range of θ=[120,500] mrad. Clearly at the edges of transition for $\theta \sim 120$ mrad we can expect larger differences between results obtained with only WST or RST sample, than for the rest of production angle intervals. Moreover, it is important to emphasize that on the experimental side we have also an argument which plays in favor of the RST sample. As stated in Sec. 3 on page 32 pads are tilted with respect to the nominal beam to agree with the average angles of RST at the given x-z position, reaching the TPCs in horizontal direction. In addition, tracking performace for WST will be more difficult in comparison to RST, as some of these tracks are sliding at the edges of TPCs, where all experimental distortions are the largest.

For details concerning comparison of results obtained with only one RST or WST sample, which is a major source of systematic error coming from different track topologies, the reader is referred to review Sec. 5.3 on page 66.

In order to better understand the characteristics of the low momentum tracks several real events were scanned. The next Figs.[5.11, 5.12, 5.13] illustrate example tracks from the real data for different track topologies.

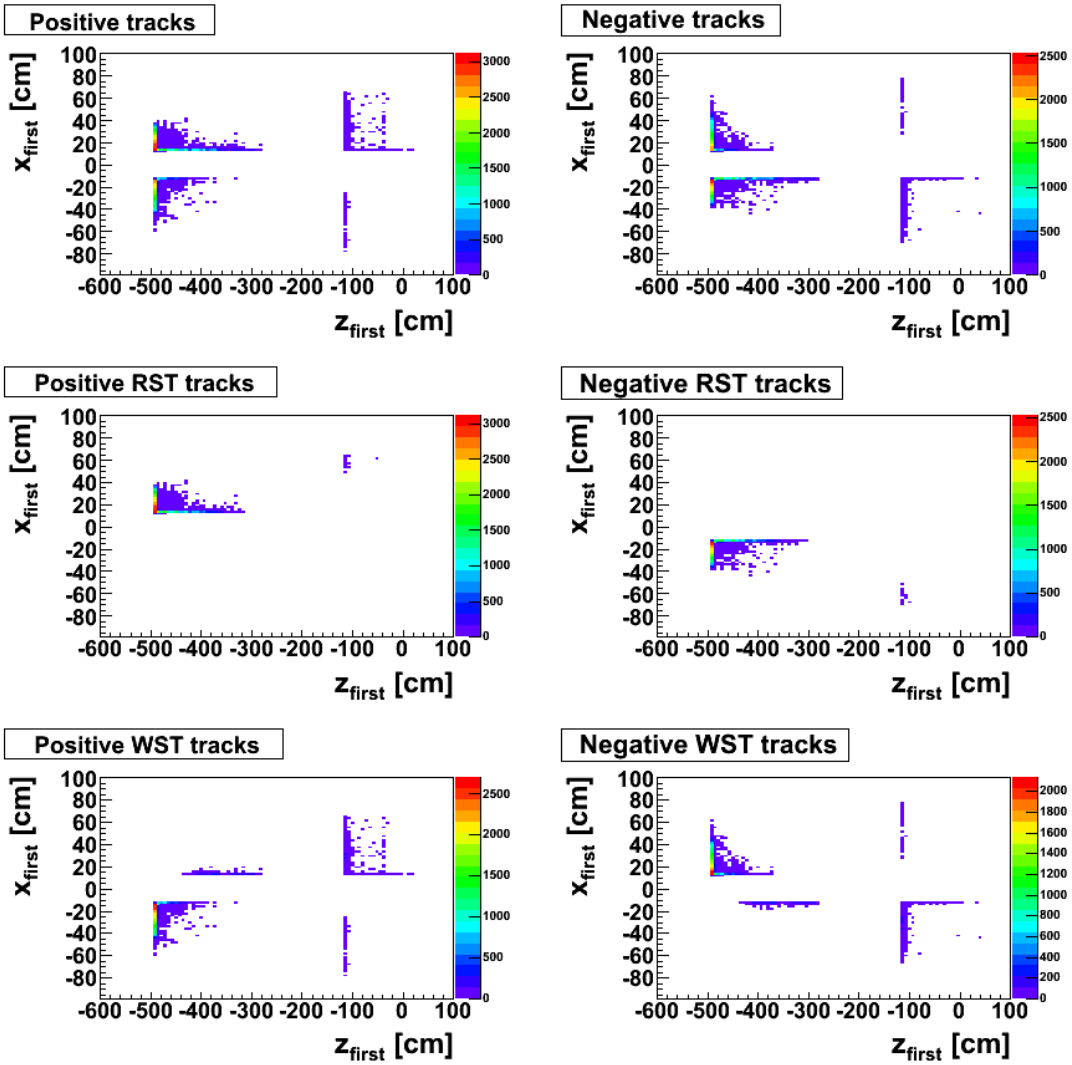

Figure 5.9: x and z coordinates of the first points of tracks for positive *(left)* and negative *(right)* low momentum particles. Results for RST and WST are also shown, both VTPC1 and VTPC2 are seen. Point with z=0 is in the center of the VTPC2. The target is placed approximately at z=-580 cm. Each point represents a track measured in 2007. See Fig. 3.5 on page 36 for the definition of coordinate system.

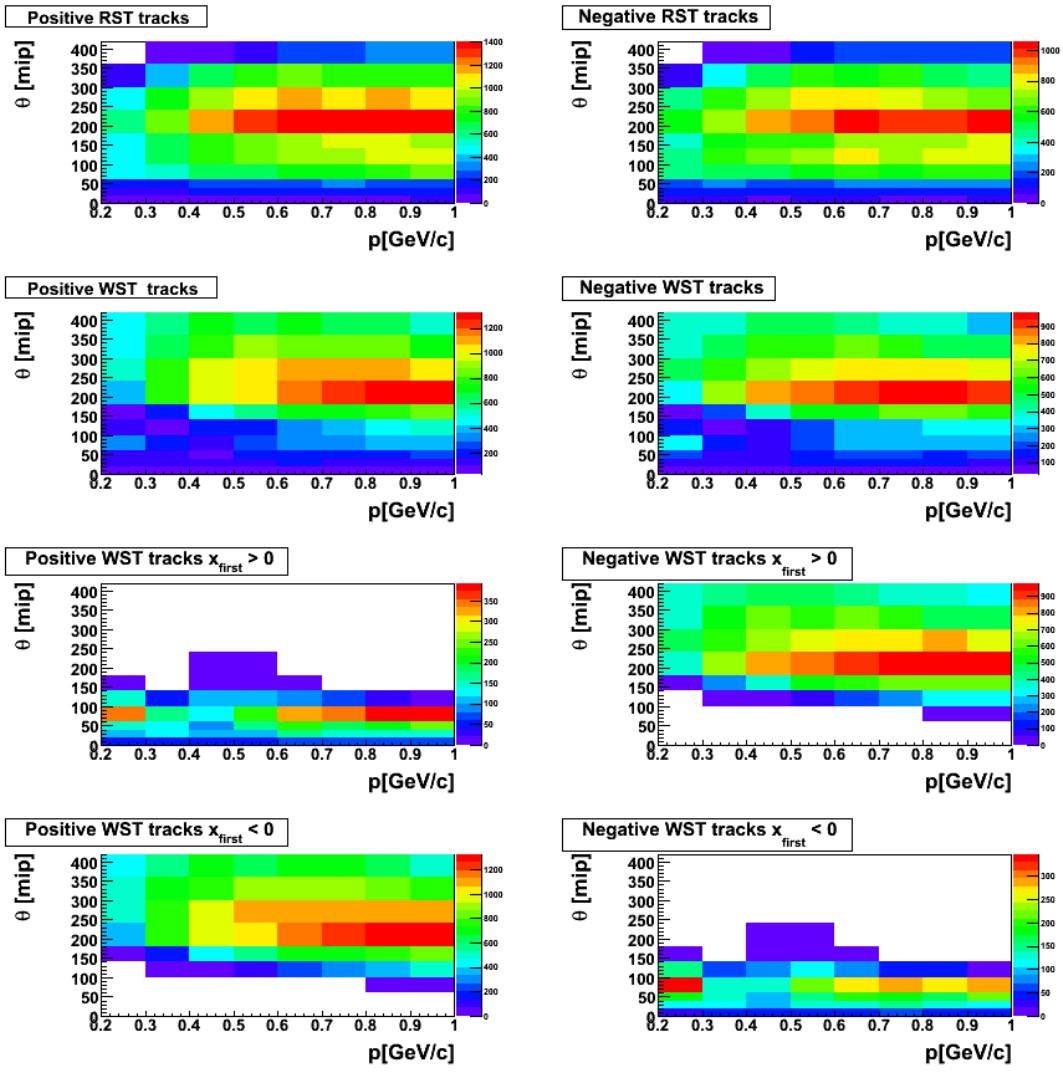

Figure 5.10: Population of measured tracks in bins of production angle θ and momentum p. *Left (right)* diagrams show positive (negative) tracks. Results for RST and two WST samples (sample with $x_{first} > 0$ and sample with $x_{first} < 0$) are also shown.

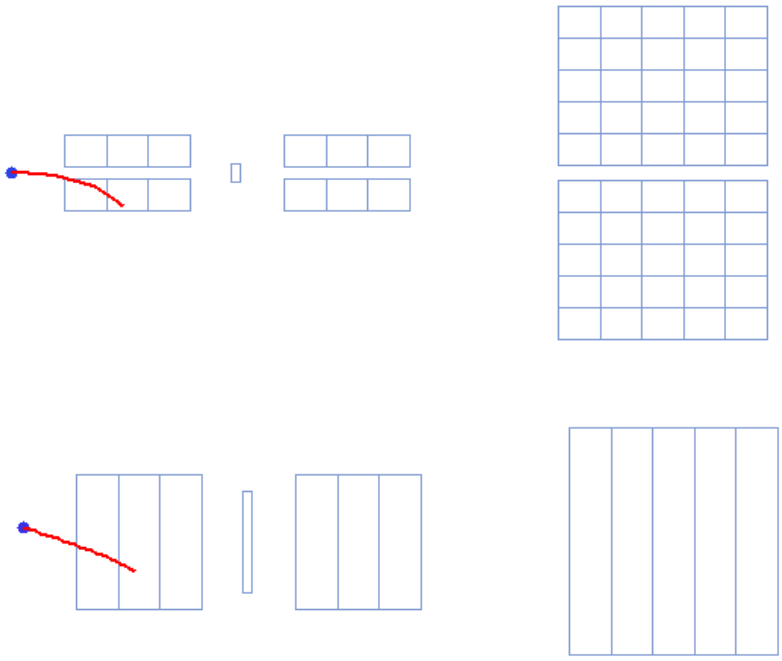

Figure 5.11: An example of negatively charged RST ($p_x < 0$). Blue dot represents the main vertex. *Upper* picture: x-z top view. *Lower*: y-z side view. All NA61 TPCs are also visible.

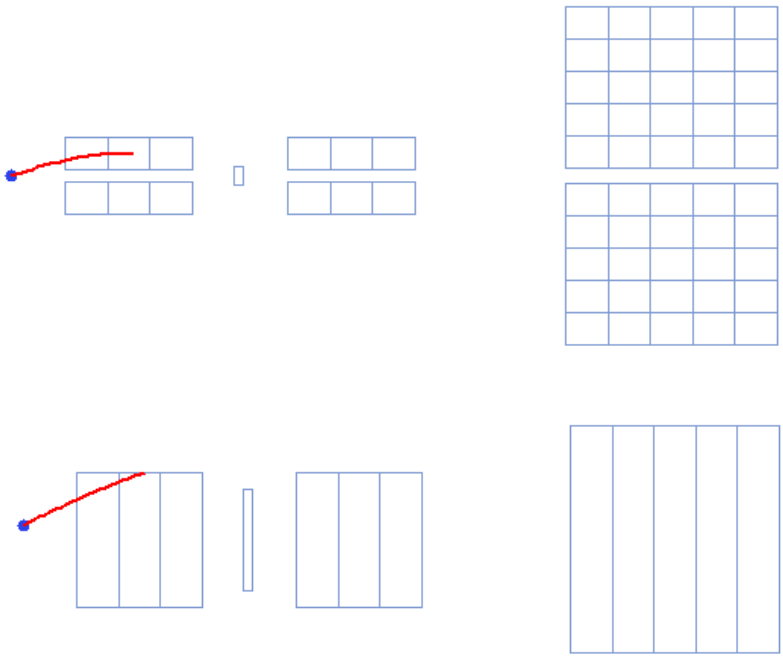

Figure 5.12: An example of negatively charged WST ($p_x > 0$) with $x_{first} > 0$. Blue dot represents the main vertex. *Upper* picture: x-z top view. *Lower*: y-z side view. All NA61 TPCs are also visible.

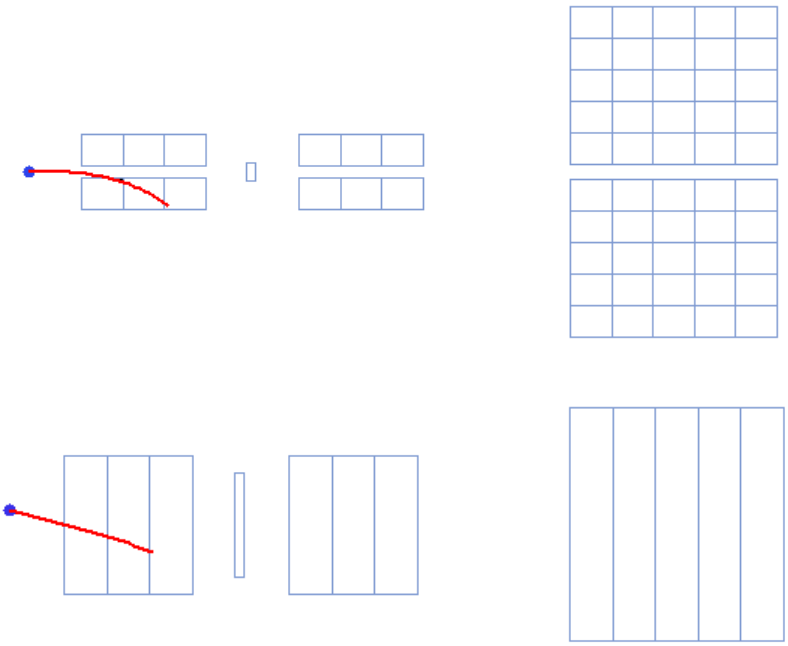

Figure 5.13: An example of negatively charged WST ($p_x > 0$) with $x_{first} < 0$. Blue dot represents the main vertex. *Upper* picture: x-z top view. *Lower*: y-z side view. All NA61 TPCs are also visible.

Chapter 6

Particle Identification by Energy Loss Measurement

The analysis presented in this dissertation is based on a set of data collected during the first NA61/SHINE run in 2007 with thin graphite target which passed the selections described previously. In this chapter we deal with the procedures of particle identification developed especially for the low momentum region where fast change of energy loss with momentum is observed. The identification procedure was performed in bins of particle momentum p and polar angle θ. Narrow momentum intervals of 0.1 GeV/c for $0.2 < p$ [GeV/c] $\leqslant 1$ and 0.2 GeV/c for $1 < p$ [GeV/c] $\leqslant 3$ were chosen to account for the strong dependence of *dE/dx* on momentum. For the final results ten polar angle intervals covering the range from 0 up to 420 mrad were chosen.

6.1 Expected distributions of particle energy loss

In order to perform particle identification for every bin of phase space, knowledge of the expected distributions of energy loss is very essential, especially in the region of particle hypothesis overlap, where identification is made difficult. To get realistic *dE/dx* distribution shapes we simulated samples of particle tracks for each (p, θ) bin using the measured momentum and angle distributions. For every particle type (π^+, e^+, K^+ and protons for positive and π^-, e^-, K^- for negative) the same number of N tracks was generated in every bin with statistics ten times larger than data sample, to obtain simulated *dE/dx* distributions as similar to the real one as possible. We decided to distribute N tracks in the following steps:

1. the tracks have momentum and angle distributions the same as data in given bin (p, θ),
2. every track gets $\mathrm{dE/dx}_{BB}$ value according to the Bethe-Bloch curve for given momentum and particle identity "i", where i=$e^{\pm}, \pi^{\pm}, K^{\pm}$ or protons,
3. the $\mathrm{dE/dx}_{BB}$ values are smeared with Gaussian functions according to the parameters given above:
   (a) mean=$\mathrm{dE/dx}_{BB}$,
   (b) sigma=$\sigma_{\mathrm{dE/dx}} \cdot \frac{\mathrm{dE/dx}}{\mathrm{dE/dx}_{BB}}$.

   where *dE/dx* and $\sigma_{\mathrm{dE/dx}}$ are the actual measured values for a given track.

This procedure allows us to obtain simulated histograms of expected energy loss distributions (refereed to $\mathrm{dE/dx}_{theor}$) for all given particle types in all bins of (p, θ).

Let's denote by N_i^j a number of given type "i" of particles in a $\mathrm{dE/dx}_{theor}$ bin "j". The normalization can be written as:

$$\sum_j^{all} N_i^j \quad = \quad N \tag{6.1}$$

In Fig. 6.1 we present an example of simulated sample for negative tracks in bin of p=[0.6-0.7] GeV/c and θ=[100,140] mrad. The *left* plot displays a projection of theoretical values of $\mathrm{dE/dx}_{BB}$ on *dE/dx* axis for N tracks. It is seen that energy loss for kaons (*pink*) change significantly in the considered momentum bin while pions (*black*) and electrons (*red*) are practically constant. The histograms in the *right* plot represent normalized distributions after smearing with Gaussian functions.

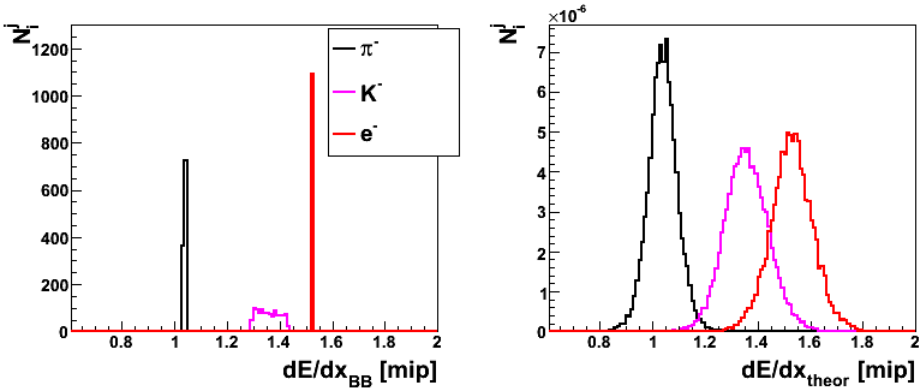

Figure 6.1: *Left*: Projection of theoretical values of $\mathrm{dE/dx}_{BB}$ on *dE/dx* axis. *Right*: Smeared, normalized distributions for pions (*black*), kaons (*pink*) and electrons (*red*). An example plot prepared in bin of p=[0.6-0.7] GeV/c and θ=[100,140] mrad for negatively charged particles.

6.2 Dependence of energy loss measurement on production angle

The expected distributions of energy loss $\mathrm{dE/dx}_{theor}$ were comapared with the measured ones *dE/dx*. For this purpose we decided to choose bins for which pion candidates were very well separated, as pions are particles which are of major interest for the T2K neutrino beam physics. In order to compare expected and measured dE/dx distributions Gaussian fits were performed. An example is shown in Fig. 6.2 where in the *upper* plot one sees dE/dx for π^+ from data together with the Gaussian fit (green line) and in the *lower* $\mathrm{dE/dx}_{theor}$ for π^+ with Gaussian fit (red line). A difference between the mean value of *dE/dx* and $\mathrm{dE/dx}_{theor}$ for this selected bin (p, θ) is observed.

For all bins (p, θ) differences between the mean values of energy loss distributions for pions (called δ) were calculated:

$$\delta = < \mathrm{dE/dx} > - < \mathrm{dE/dx}_{theor} > \tag{6.2}$$

They are displayed as function of θ in Figs.[6.3, 6.4] for π^+ and π^- for various momentum intervals. It is seen that the highest discrepancies are for the largest (θ>360 mrad) production angles (up to 8-9 %). While we increase the momentum of the track the correction value

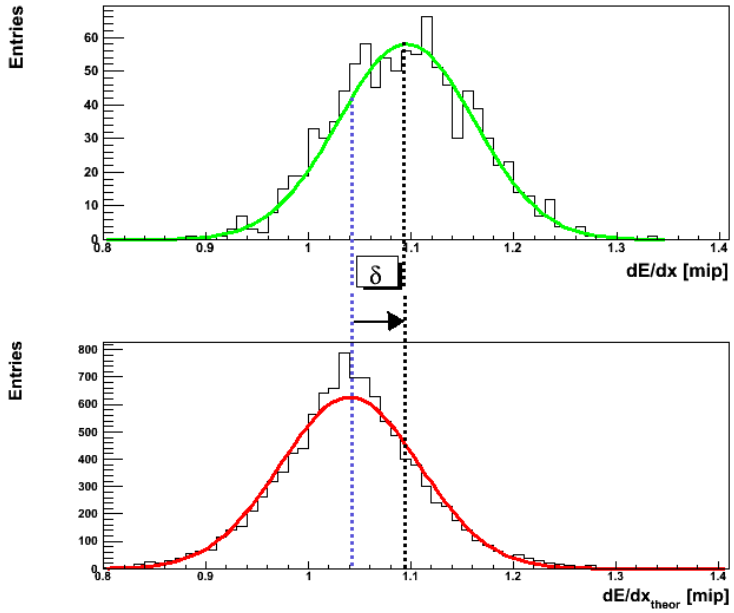

Figure 6.2: Gaussian fits to *dE/dx (upper)* and $\mathrm{dE/dx}_{theor}$ *(lower)* distributions for p=[0.4,0.5] GeV/c and θ=[300,360] mrad. A difference (δ) between the mean value of *dE/dx* and $\mathrm{dE/dx}_{theor}$ for this selected bin (p, θ) is illustrated between two dotted lines: blue and black.

decreases. As we have learned, from Sec. 3.6.2 on page 36, the VTPC pads are not optimized for vertical but more for the horizontal tracks. The low momentum tracks pass mainly VTPC1 only, which during NA49 times, as already explained in earlier chapters, was used for momentum determination and not high resolution ionization measurements. Therefore for this analysis of low momentum particles we need to introduce additional corrections.

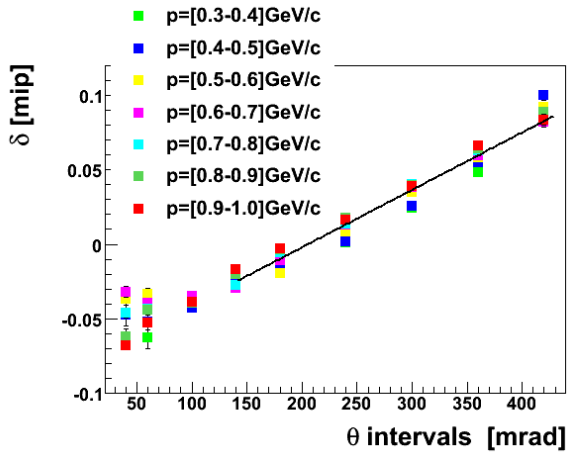

Figure 6.3: Differences (δ) between mean of *dE/dx* from data and theory $\mathrm{dE/dx}_{theor}$ versus polar angle θ for π^+ together with the fitted parametrization marked with black line. Different momentum bins are illustrated by different marker colors.

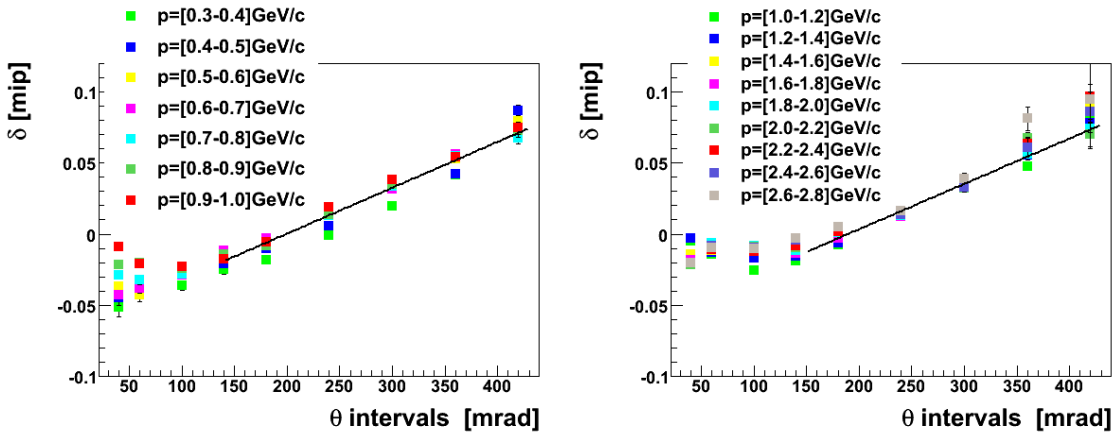

Figure 6.4: Differences (δ) between mean of dE/dx from data and theory $\mathrm{dE/dx}_{theor}$ versus polar angle θ for π^- with $0.2 < p\ [GeV/c] \leq 1$ *(left)* and with $1 < p\ [GeV/c] \leq 3$ *(right)* together with the fitted parametrization marked with black line. Different momentum bins are illustrated by different marker colors.

Dependence of energy loss measurement on production angle seen in Fig. 6.3 for $\theta \geq 140$ or 160 mrad, was parametrized as follows:

$$\delta = a \cdot \theta + b \tag{6.3}$$

where a,b are free parameters in the fit. The remaining θ intervals were treated with a constant value $\delta = c$.
Using the fitted parameters the energy loss measurements for all data tracks with low momentum below $p \leq$3 GeV/c were corrected for this effect:

$$\mathrm{dE/dx} = \mathrm{dE/dx}_{old} - \delta \tag{6.4}$$

The results obtained from applied procedure are gathered in Tab. 6.1.

Particle	θ range	Parametrization	Results of the fit
π^+ with $0.2 < p \leqslant 1$ GeV/c	θ <140 mrad $\theta \geqslant$140 mrad	$\delta = c$ $\delta = a \cdot \theta + b$	c=(-0.037± 0.005) [mip] a=(0.00039± 0.00004) [mip/mrad] b=(-0.079± 0.001) [mip]
π^- with $0.2 < p \leqslant 1$ GeV/c	θ <140 mrad $\theta \geqslant$140 mrad	$\delta = c$ $\delta = a \cdot \theta + b$	c=(-0.023± 0.004) [mip] a=(0.00032± 0.00003) [mip/mrad] b=(-0.064± 0.001) [mip]
π^- with $1 < p \leqslant 3$ GeV/c	θ <160 mrad $\theta \geqslant$160 mrad	$\delta = c$ $\delta = a \cdot \theta + b$	c=(-0.013± 0.002) [mip] a=(0.00032± 0.00004) [mip/mrad] b=(-0.060± 0.001) [mip]

Table 6.1: The values of the fitted parameters needed to correct for dependence of energy loss measurement on production angle θ.

Figs.[6.5, 6.6, 6.7] show how resolution of corrected energy loss measurement has significantly improved. One can see a better separation between pions and electrons.

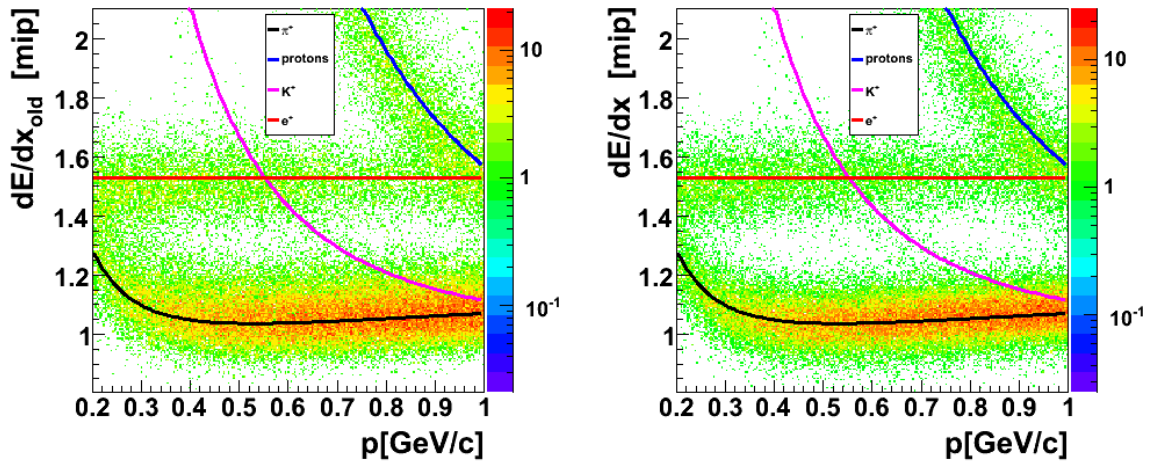

Figure 6.5: Energy loss measurements versus particle momentum for positively charged particles (with $0.2 < p\ [GeV/c] \leq 1$) before *(left)* and after *(right)* applying angular corrections.

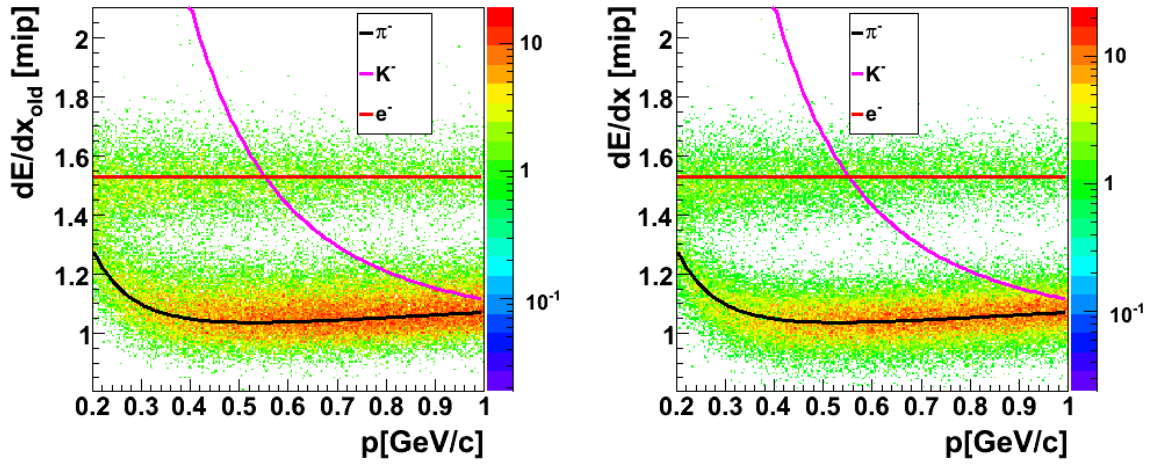

Figure 6.6: Energy loss measurements versus particle momentum for negatively charged particles (with $0.2 < p\ [GeV/c] \leq 1$) before *(left)* and after *(right)* applying angular corrections.

For further considerations all data with dE/dx corrected values were used.
In selected bins (p, θ) of phase space the particle identification was performed using methods described below.

6.3 Particle separation in selected range of energy loss and momentum

In some selected bins one can make separation of particles simply by choosing range of dE/dx and momentum in which one can see only selected type of particles. This method was already

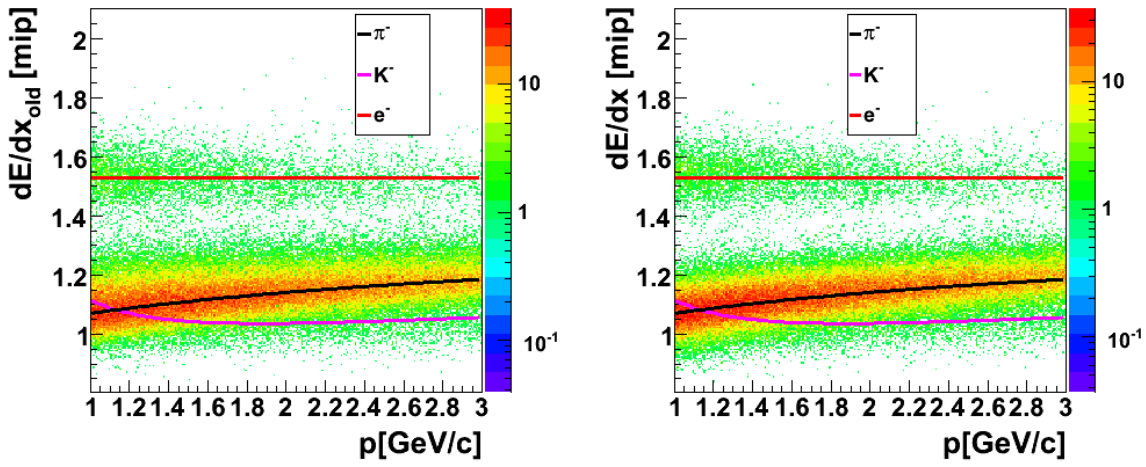

Figure 6.7: Energy loss measurements versus particle momentum for negatively charged particles (with $1 < p\ [GeV/c] \leq 3$) before *(left)* and after *(right)* applying angular corrections.

used in the procedure of Bethe-Bloch curve parametrization using the data samples, described in Sec. 4.4 on page 48. We use this elementary procedure mainly for identification of low momentum protons (see Sec. 6.8), which up to $p \leq$0.8 GeV/c are completely separated, as shown in Fig. 4.5.

6.4 Preliminary particle identification based on relative probability functions

The preliminary identification of particles was performed using a procedure based on calculation of probability functions for every (p, θ) bin. For every particle identification hypothesis, we define relative probability for particle "i" in bin "j" of $\mathrm{dE/dx}_{theor}$:

$$P_i^j = \frac{N_i^j}{N_\pi^j + N_K^j + N_e^j + N_p^j} \tag{6.5}$$

An example of the relative probabilities is illustrated in Fig. 6.8. In order to find out how many particles "i" are in the (p, θ) bin we decided to sum up corresponding tracks from $\mathrm{dE/dx}_{theor}$ bins where $P_i^j > 95\%$ and correct for the remaining bins on the basis of expected energy loss distributions. The corrections are given by:

$$L_i = \frac{\sum_{j95} N_i^j}{N} \tag{6.6}$$

where $\sum_{j95}$ denotes summing up over bins with $P_i^j > 0.95$. When in a given bin (p, θ) particles of a type "i" happen to be completely separated from other particle species then $L_i = 1$.
Fig. 6.9 illustrates corrections made for *(left)* π^+ and *(right)* π^- track. Clearly one can see that in most of the bins pions are almost completely separated, except the first and the last one for which the corrections are mostly below 0.8 .

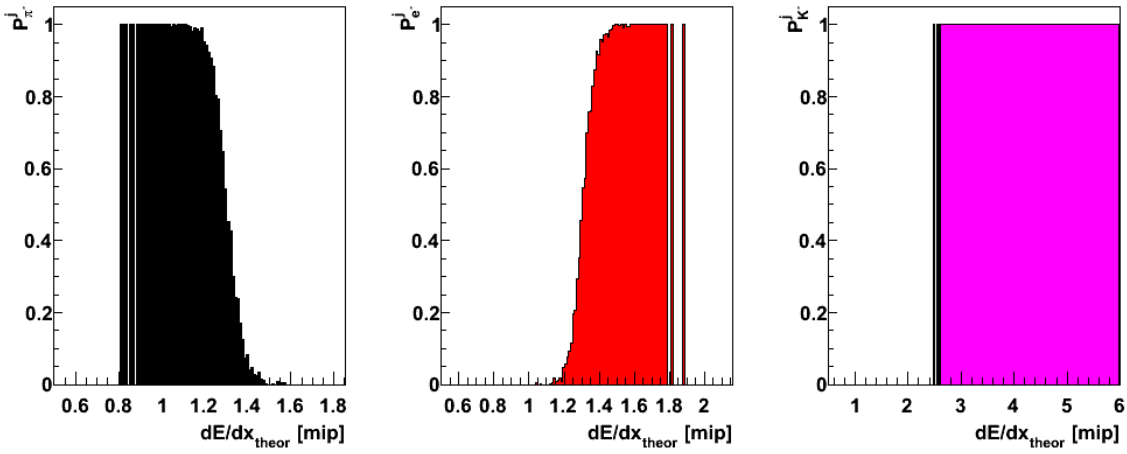

Figure 6.8: An example of relative probabilities for negatively charged particles for selected bin in p=[0.2,0.3] GeV/c and θ=[180,240] mrad.

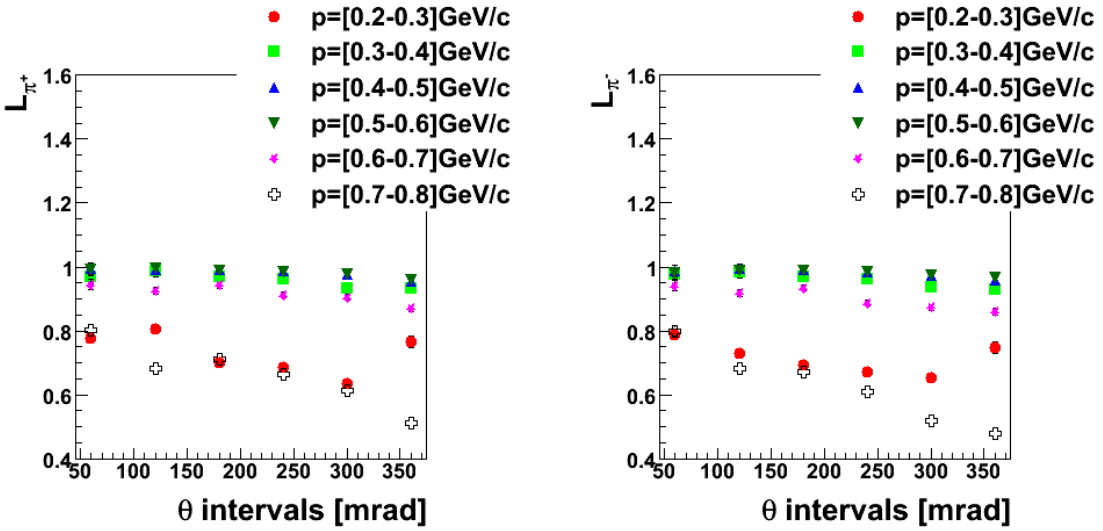

Figure 6.9: Corrections $L_{\pi+}$ *(left)* for π^+ and $L_{\pi-}$ *(right)* for π^- for selected θ intervals.

This procedure was mainly used in order to obtain preliminary spectra of pions from p+C interactions on thin target data, published in [104, 105]. The method could be used only for the tracks with momentum p≤0.8 GeV/c, as tracks populating other bins were not satisfying the rule with $P_i^j > 95\%$. Moreover, bins with momentum p≥0.8 GeV/c and p≤1 GeV/c were not covered by the $tof - dE/dx$ analysis, which resulted in a "hole" in the spectra of identified pions. We decided to extend the analysis for higher momenta, which required usage of more advanced procedure of particle identification, *i.e.* the *maximum likelihood* (ML) method. For (p, θ) bins with crossing BB curves the ML is more effective. The results obtained with the probability functions are compared with that obtained in ML method in the next section.

6.5 Maximum likelihood method for particle identification

In each (p, θ) bin the *maximum likelihood* (ML) fit (suggested in Ref. [106]) was performed to extract particle yields. The details of the method are described in Appendix B. In the π^+ analysis three independent relative abundances were fitted (π^+, K^+ and proton) while in the π^- analysis we were left with only two independent abundances (π^- and K^-). Protons are included in the fit procedure starting from $p \geq 0.7$ GeV/c as for lower momenta their identification is trivial (see Sec. 6.3). The e^+ and e^- abundances were determined as a result of normalization condition.

In Fig. 6.10 an example of the *dE/dx* distribution is shown for positively *(left)* (negatively *(right)*) charged particles in the momentum bin [0.7,0.8] GeV/c and angular bin [180,240] mrad, (in the momentum bin [0.8,0.9] GeV/c and angular bin [140,180] mrad), and compared with normalized N_i^j distributions scaled by fitted relative abundances. For both charges contribution for K yields is almost negligible. Clearly 2007 data statistics does not allow to extract K yields in low momentum region.

A small systematic shift between the fit curves and data is observed. This effect results in a contribution to the total systematic error in the particle identification procedure (see Sec. 9.1.3 on page 123).

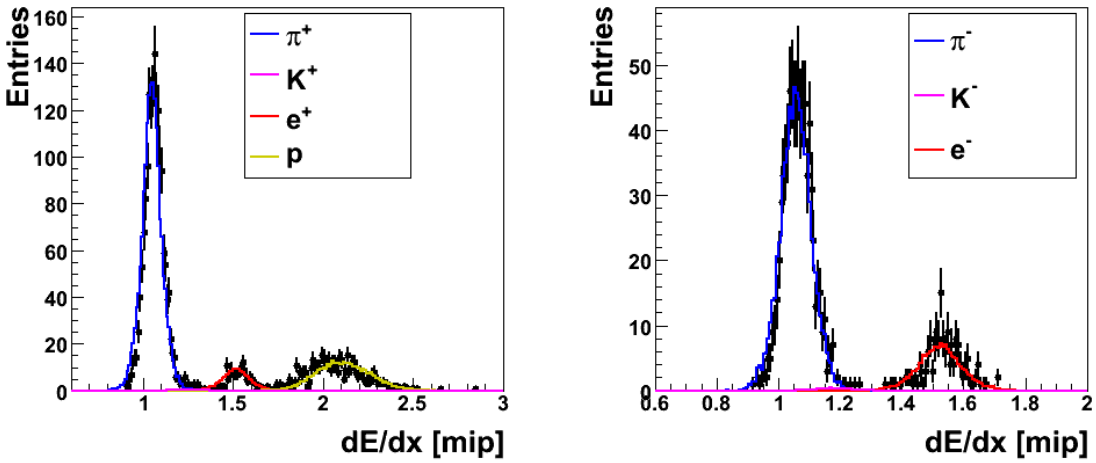

Figure 6.10: The *dE/dx* distribution for positively *(left)* (and negatively *(right)*) charged particles in the momentum bin [0.7,0.8] GeV/c and angular bin [180,240] mrad (in the momentum bin [0.8,0.9] GeV/c and angular bin [140,180] mrad) and compared with normalized N_i^j distributions scaled by fitted relative abundances.

We checked the adopted ML method of particle identification with the one based on the calculation of relative probability functions. As an example, results for positively *(left)* and negatively *(right)* charged pions which were identified using both approaches for $\theta = [180, 240]$ mrad *(left)* and $\theta = [240, 300]$ mrad *(right)* are shown in Fig. 6.11. Comparison was possible only for bins where relative probability functions method was applicable, *i.e.* $p < 0.8$ GeV/c as stated in previous section. A good agreement between both methods is observed.

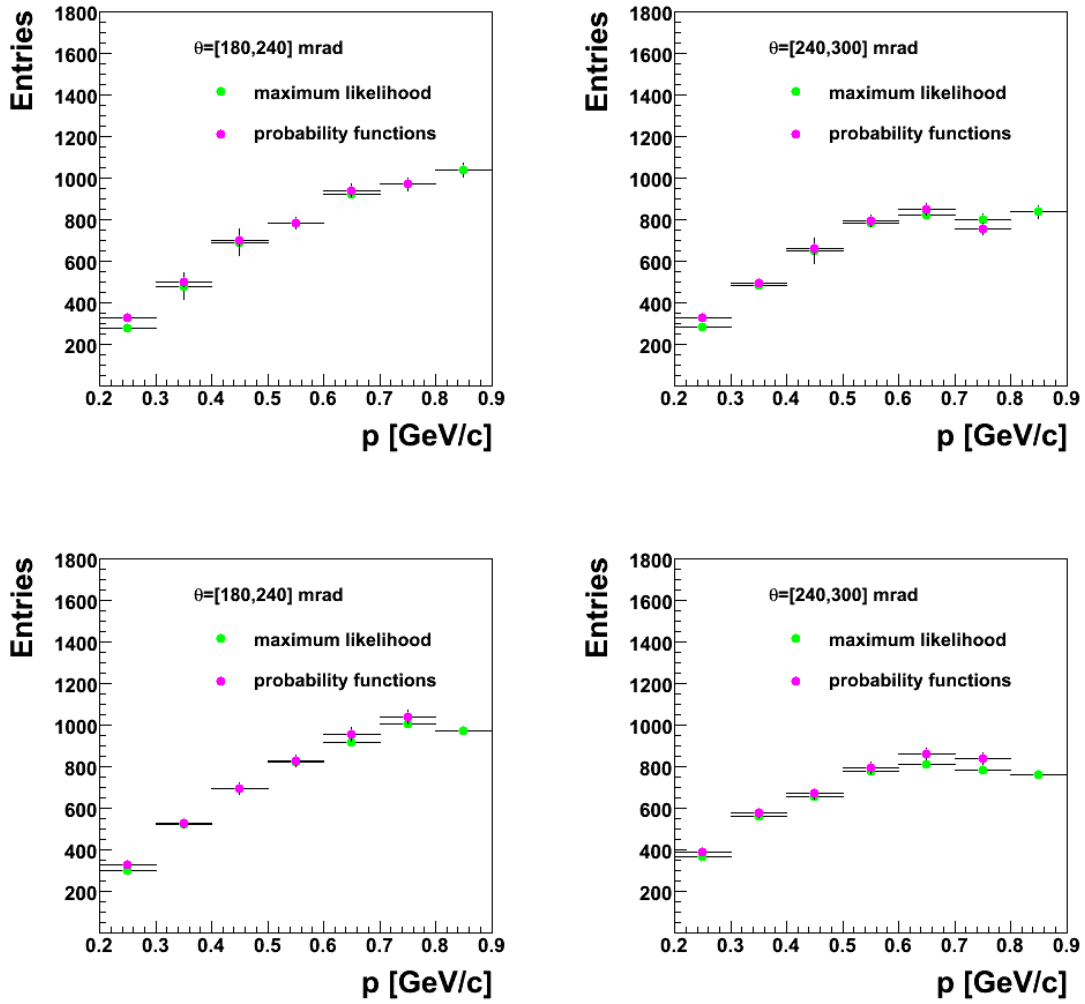

Figure 6.11: Comparison of identified π^+ *(upper)* and π^- *(lower)* spectra using *maximum likelihood* method (*green*) and calculating relative probability functions (*pink*). Example plots are for $\theta = [180, 240]$ mrad *(left)* and $\theta = [240, 300]$ mrad *(right)*.

6.6 Results on charged pion identification

The results of charged pion identification using *maximum likelihood* are displayed in Figs.[6.12, 6.13]. For different production angle intervals the pion spectra are compared with momentum distributions of all tracks with $dE/dx < 4$ mip taken for the identification procedure. As we increase production angle we observe maximum of the distribution to move towards lower momentum value. This is demonstrated especially for negatively charged pions where identification was extended in momentum range (till $p \leqslant 3$ GeV/c). Moreover, for largest θ angles most of the identified tracks are pions. This is clearly seen in Fig. 6.13 where antiprotons contribution is negligible and partially in Fig. 6.12 till $p < 0.7$ GeV/c. In smaller θ intervals mostly $e^{\pm}$ contribute (see Sec. 6.7). The *raw* spectra presented here have to be corrected for detector acceptance, contribution from secondary particles and other (see Chapter 7).

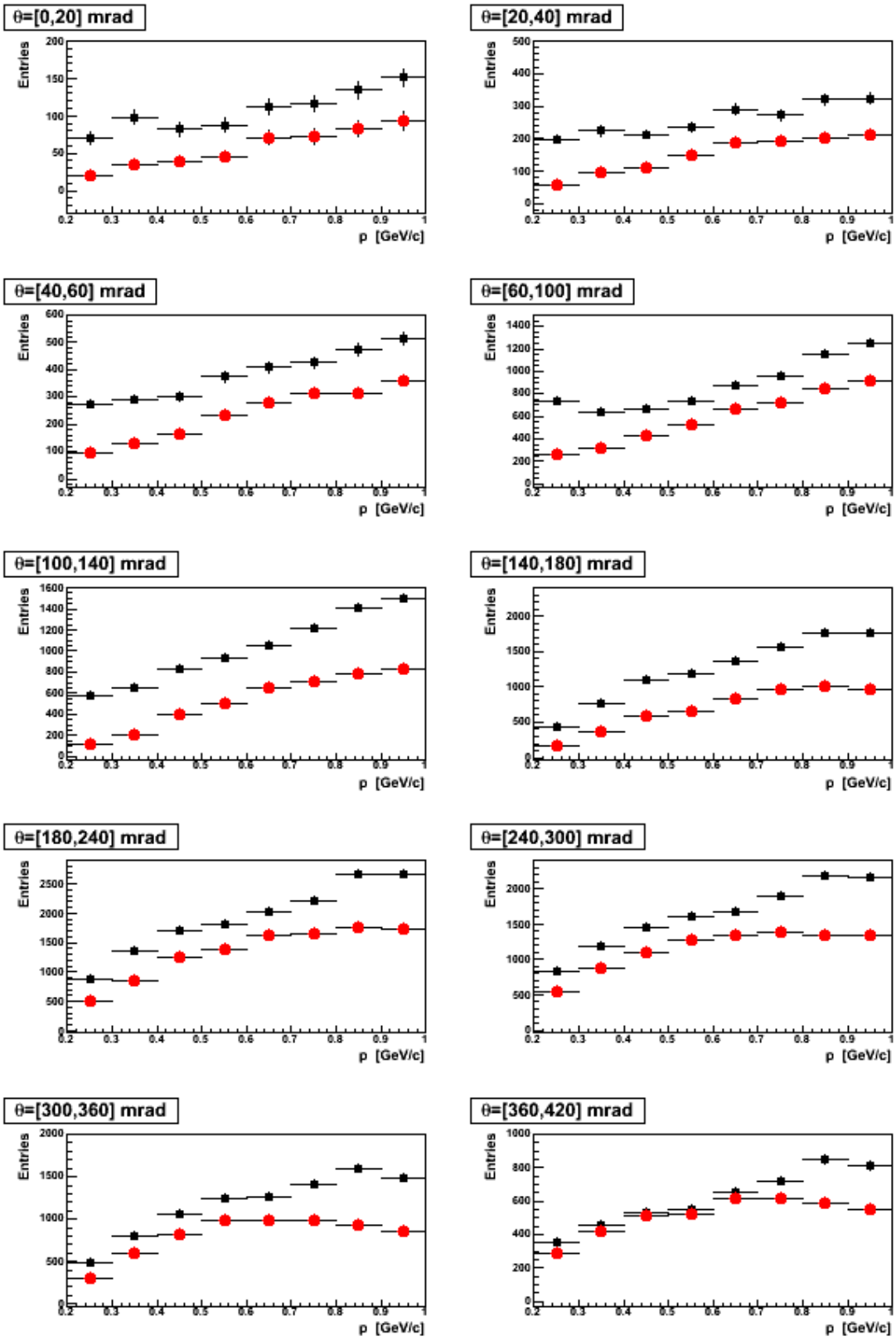

Figure 6.12: Fitted yields of π^+ tracks (*red*) versus momentum compared to all positive tracks (*black*) with $dE/dx < 4$ mip used in identification procedure at different production angle intervals.

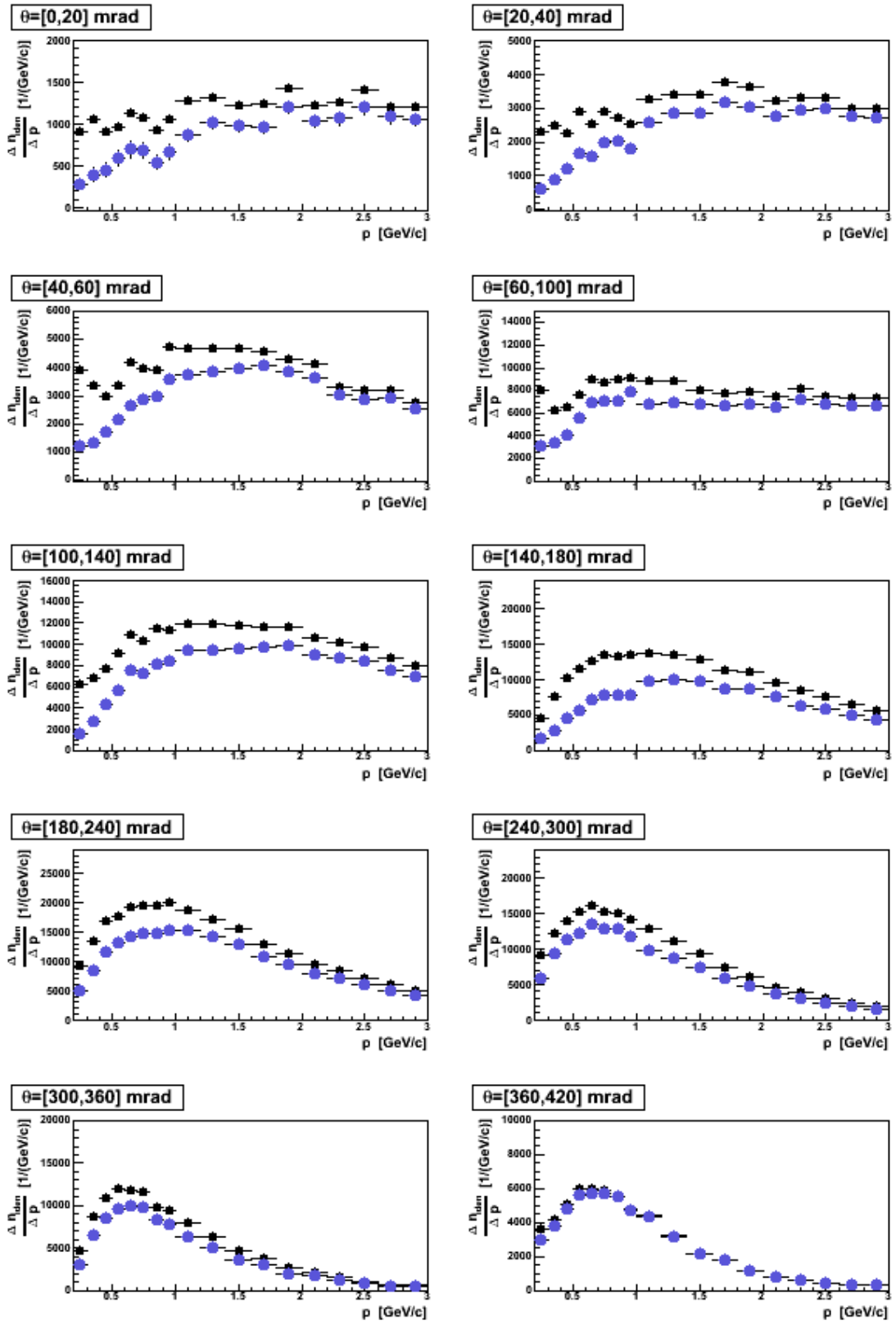

Figure 6.13: Fitted yields of π^- tracks (*blue*) versus momentum compared to all negative tracks (*black*) with $dE/dx < 4$ mip used in identification procedure at different production angle intervals.

6.7 Results on electron and positron identification

In the same manner as for pions we were able to extract electrons and positrons *raw* yields using *maximum likelihood* method, which both are illustrated in Fig. 6.14 till $p \leqslant 1$ GeV/c. While we look at the comparison of both lepton yields we can observe that for almost all θ bins the number of identified electrons and positrons is almost the same. This is due to common origin of e^+e^- pairs from π^0 decays and γ conversion in the target. The exceptions are listed below.

- For $\theta < 60$ mrad there is slightly more electrons than positrons at low momenta, where we can expect some δ electrons exiting the target.

- In bins $p > 0.8$ GeV/c and for several θ intervals the number of identified positrons is larger than electrons. However we still have to remember that starting from this momentum bins the proton BB curve is very close to that of positrons (see Fig. 6.5).

The second effect may be due to the fact that mixture between positrons and protons makes identification procedure not reliable when proton and positron BB are almost crossing each other. Because of that the yields of positrons for larger momenta ($p > 1$ GeV/c) could not be determined with *maximum likelihood* method. However, identification of e^- is straightforward for p>0.8 GeV/c as there are very few antiprotons and antideuterons in the negative sample (see Fig. 4.8 on page 54). In order to compare e^+ and e^- yields we measure positive particle yields with the same method as electrons candidates remembering that in the overlap bins we have a sum of e^+ and protons and deuterons. We take points between dE/dx =[1.4,1.7] mip and count how many tracks we observe for each 0.2 GeV/c momentum bin. The results of described procedure are shown in Fig. 6.15. We observe the same number of electrons and positrons within 5% uncertainty before and after overlapping region with protons and later deuterons, i.e. p=[0.8,1.5] GeV/c.

To conclude we observe that positrons and electrons with $p > 0.4$ GeV/c originate both from π^0 decays and the yield differences come from inefficiency of identification procedure at momenta for which curves almost cross for e^+ and for protons.

6.8 Results on proton identification

Proton identification is performed using two methods described above. The procedure depends on the momentum interval:

(A) for $p < 0.8$ GeV/c we have trivial situation, i.e protons are completely separated (see Sec. 6.3),

(B) for $p \geq 0.7$ GeV/c we have to rely on the fit with ML method (see Sec. 6.5).

There is one overlapping bin for p=[0.7-0.8] GeV/c where we can check results of both methods. In Fig. 6.16 we present *raw* yields of identified protons obtained with both methods. For bin p=[0.7-0.8] GeV/c we observe the same number of identified protons within uncertainties, which proves that ML method works well outside of BB function cross-over region. However, for the last two bins in the region where protons mix strongly with positrons we may suspect that ML method is insufficient what was shown for e^+ in the previous section. Inefficiency of ML method in reflected by the fact that it underestimates protons by assigning almost 50% yields for both particle proton and e^+ hypothesis.

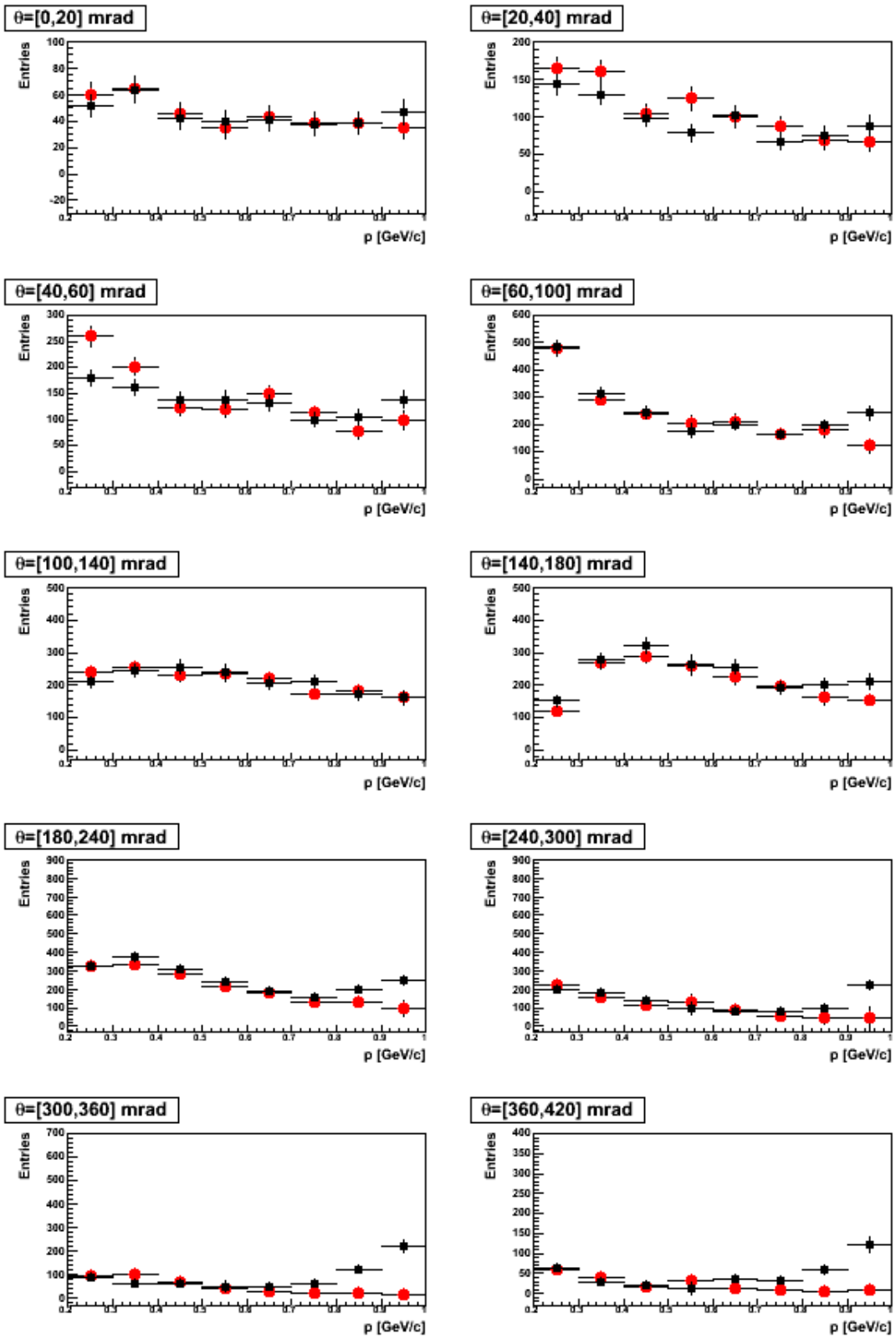

Figure 6.14: Fitted yields of e^- (*red*) and e^+ (*black*) tracks versus momentum at different production angle intervals.

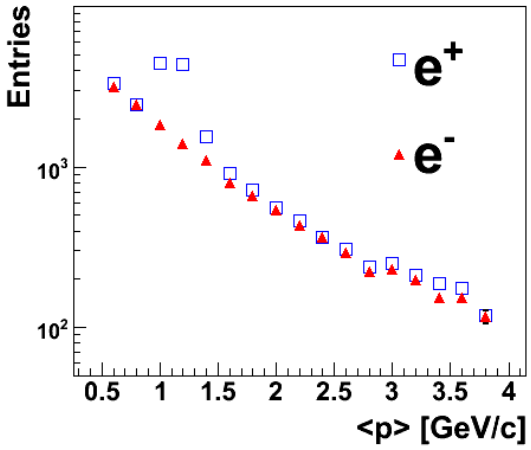

Figure 6.15: Yields of e^- (*red*) and e^+ (*blue*). The same number of electrons and positrons within uncertainties before and after overlapping region with protons and later deuterons, *i.e.* p=[0.8,1.5] GeV/c is observed.

We may observe from Fig. 6.11 and Fig. 4.8 that:

- In p=[0.8,1] GeV/c protons are mixing only with the positrons. ML fit gives correct sum of positrons and protons but not separate yields.
- It has been shown in the previous section that we can use the number of electrons N_{e^-} instead of the number of positrons where BB curves are almost crossing with protons.

Using this knowledge we can improve the fitted yield of identified protons (method C). We take the fitted sum of protons and positrons $N_p + N_{e^+}$ obtained from the ML method applied to positive tracks and subtract the number of electrons N_{e^-} obtained from the analysis of negative tracks:

$$N_{p,corr} = N_p + N_{e^+} - N_{e^-} \tag{6.7}$$

In term of fitted abundances (see Appendix B) we get:

$$m_{p,corr} = m_p + m_{e^+} - m_{e^-}\frac{N^-_{all}}{N^+_{all}} \tag{6.8}$$

where N^-_{all} (N^+_{all}) represent the total number of negatively (positively) charged tracks in given bin of momentum and polar angle θ. In Fig. 6.17 corrected proton yields are shown in *black* for the last momentum bins in addition to results presented in Fig. 6.16. As a result of applied correction we see improvement especially observed for the larger theta intervals.

As a final proton spectra we take results from method A for $p \leqslant 0.8$ GeV/c and corrected values of protons yields from method C for the last two momentum bins.

It is important to emphasize that the presented spectra of pions and protons still have to be corrected for several experimental effects like: detector acceptance, reconstruction efficiency, secondary interactions and decays of strange particles. This subject is further investigated in the next chapter.

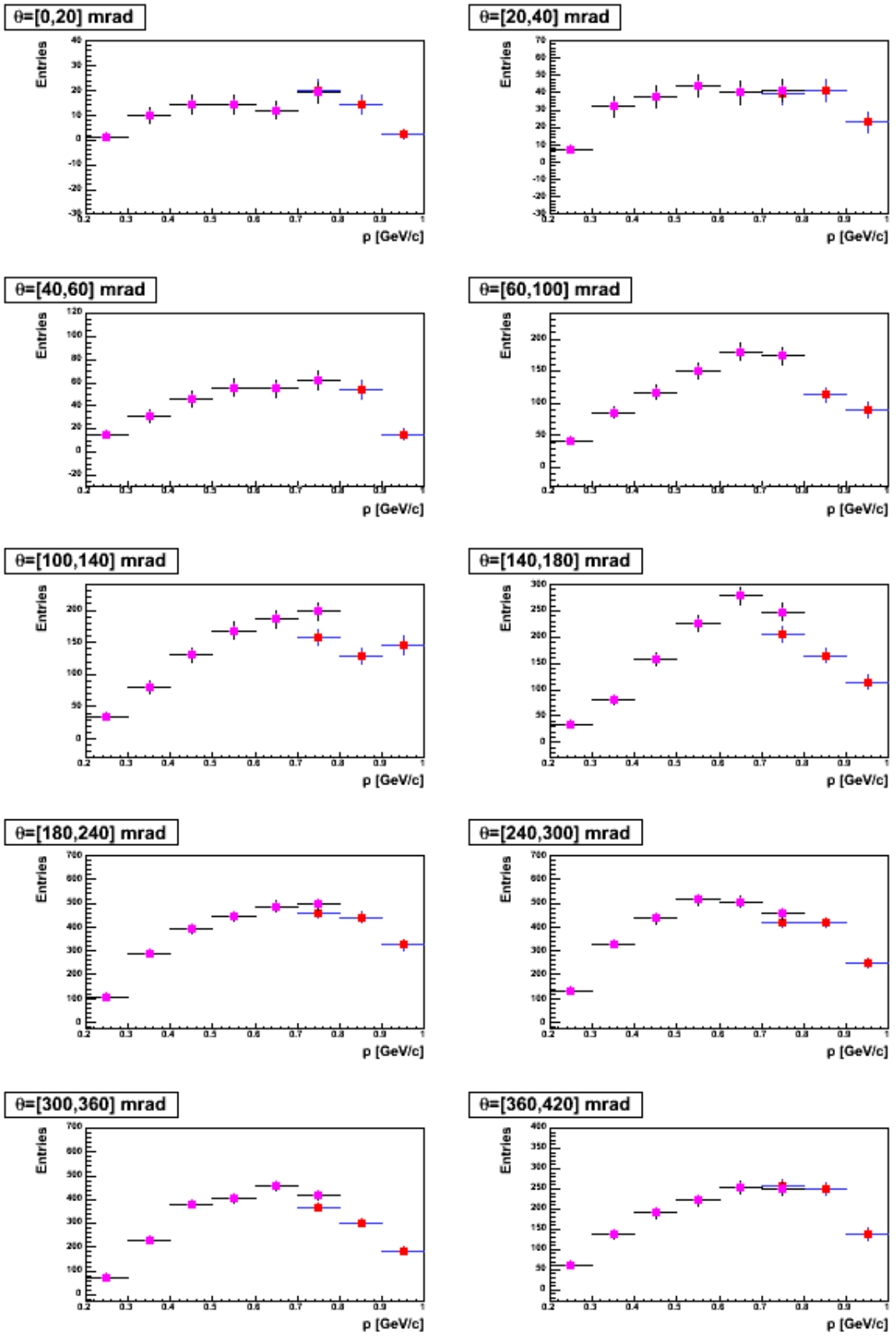

Figure 6.16: Yields of identified protons with method A for $p < 0.8$ GeV/c (*pink*) and method B for $p > 0.7$ GeV/c (*red*) for different production angle intervals. Note that in bin [40,60] mrad and [60,100] mrad the yields from two methods overlap for $0.7 < p$ [GeV/c] < 0.8 (differences smaller than the point sizes).

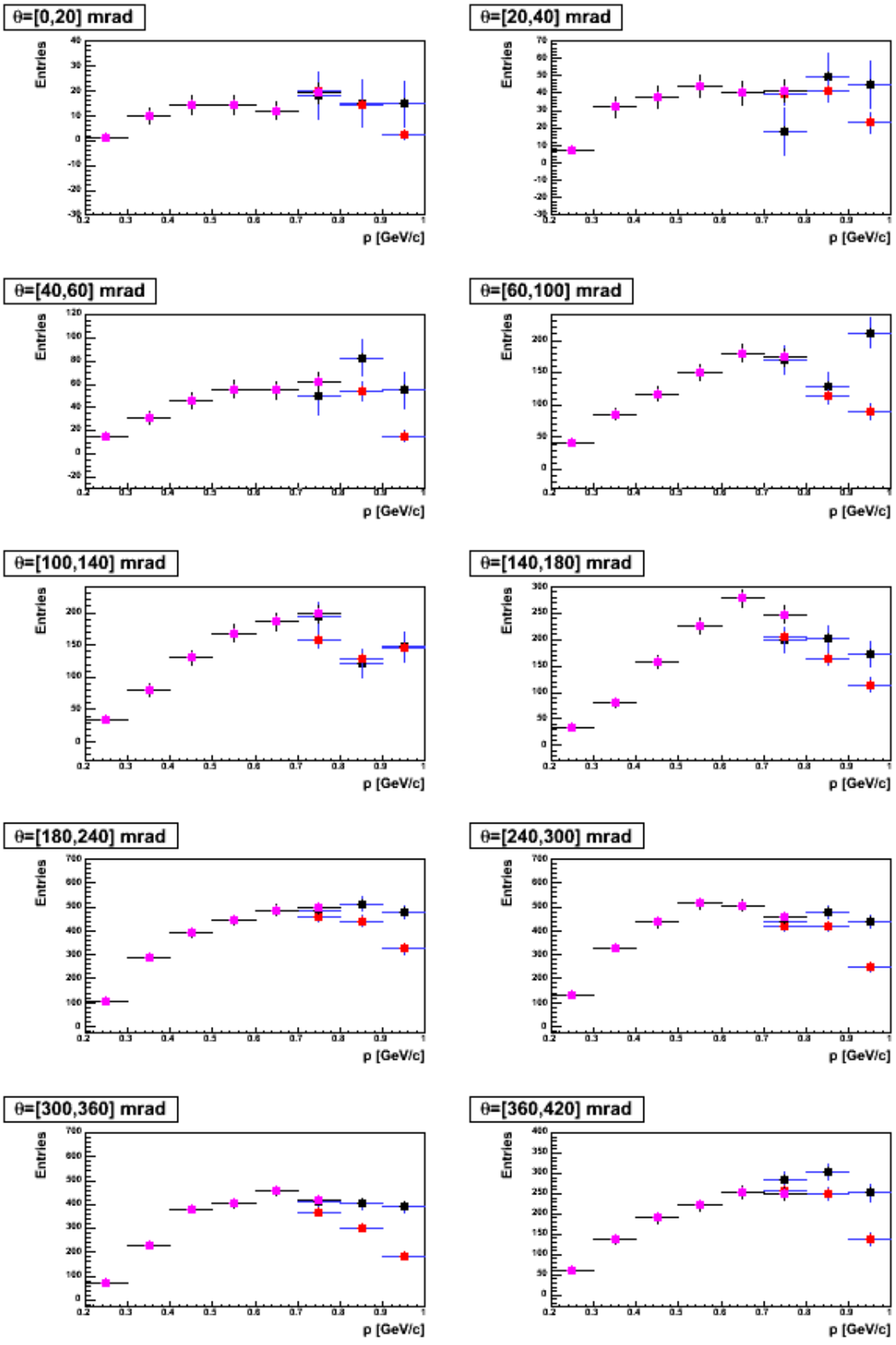

Figure 6.17: Yields of identified protons with method A for $p < 0.8$ GeV/c (*pink*) and for $p > 0.7$ GeV/c with methods: B (*red*) and C (*black*) for different production angle intervals.

Chapter 7

Monte Carlo Corrections

This chapter is organised as follows. At first we introduce simulation chain used to generate 31 GeV/c proton interactions on thin carbon target which are subject of the presented analysis. Further on studies on a comparison of the Monte Carlo (MC) and measured data sample are shown. The main part of the chapter is devoted to discussion of MC corrections which need to be applied to the identified spectra of charged pion mesons and protons. These corrections take into account several experimental effects like: detector geometrical acceptance, reconstruction inefficiency, decays of particles, secondary interactions. In the last section we illustrate corrected spectra of π^+, π^- and protons.

7.1 Simulation

The NA61 simulation chain is largely inherited from the software developed for the NA49 experiment. Particle propagation through the detector is performed by GEANT 3.21 [72]. For the primary kinematics we used model based input (VENUS4.12 [107]). MC events are produced in the same format as raw data so both are reconstructed with the same chain.
The NA61 simulation chain comprises several packages (see [108] for more details):

1. **Event generation** of p+C interactions at 31 GeV/c using the VENUS4.12 model.
2. **Propagation:** GEANT 3.21 propagates the particle through the whole NA61 geometry and accounts for relevant secondary physics processes, such as particle interactions and decays.
3. **Simulation of detector response** using dedicated NA61 packages which introduce all corrections applied to the real data, (see Chapter 4).
4. **Reconstruction** of the simulated events with the same reconstruction chain as used for the real data.

Additionally for MC sample one had to perform also the matching procedure in order to have for each reconstructed track also information available from simulation.

7.2 Validation of the Monte Carlo sample

Validation of the simulation was performed by comparison of distribution of several variables with the measured ones. In order to compare data and MC we had to produce equivalent sample for both cases.
For further studies we took into account tracks which:

- were reconstructed to the main vertex,
- successfully matched with simulated ones.
- passed the same cuts as those applied to the data defined in Chapter 5.

For simplicity all tracks which fulfill three mentioned conditions will be called further as *reconstructed* tracks.

Comparison of the event and track reduction for the thin target data and MC sample is presented in Table 7.1. Simulation of beam line is not included in the MC chain thus there is no event reduction on BPD cut. Simulated MC statistics is about 10 times larger than the data statistics, as seen in Table 7.1. It is seen that the MC reduction rates are sufficiently close to that for the data.

Impact of the cut		
	Data	MC
Event cuts		
BPD	N^I_{trig}	N^{MC}
	521238 (78% out of all events)	5000000 (100%)
Positive low momentum tracks with 0.2<p [GeV/c]≤1		
Impact parameter	171225, (91%)	2262692 (93%)
$N \geq 30$	91734, (49%)	1238850 (51%)
$N_{VTPC1} + N_{VTPC2} \geq 12$	89161, (48%)	1218402 (50%)
$N/N_{pot,point} > 0.5$	88322, (47%)	1203996 (50%)
Negative low momentum tracks with 0.2<p [GeV/c]≤1		
Impact parameter	123623, (91%)	1632228 (93%)
$N \geq 30$	70212, (52%)	929507 (53%)
$N_{VTPC1} + N_{VTPC2} \geq 12$	68085, (50%)	912466 (52%)
$N/N_{pot,point} > 0.5$	67400, (49%)	901537 (51%)
Negative low momentum tracks with 1<p [GeV/c]≤3		
Impact parameter	164063, (94%)	2103532 (95%)
$N \geq 30$	125417, (72%)	1656348 (74%)
$N_{VTPC1} + N_{VTPC2} \geq 12$	119104, (68%)	1581517 (71%)
$N/N_{pot,point} > 0.5$	118913, (68%)	1577678 (71%)

Table 7.1: Event and track cuts - comparison of data and MC samples. (All values quoted in brackets refer to the percentage of events/tracks which survive the selection corresponding to chosen momentum range and charge sign). N^I_{trig} is the number of thin target data events which survive the BPD cut described in the Sec. 5.1 on page 58.

The first examined distributions include impact parameter B_x and B_y. They are displayed in Fig. 7.1 for data (*black*) and MC (*blue*) sample. We examined these distributions in Fig. 5.1 on page 61 and Fig. 5.3 on page 63 for the data sample before and after all track selection cuts. They illustrated that the cuts reduced an admixture of wrongly reconstructed tracks especially for larger polar angles. Here we can see that the MC sample well reproduces the reconstruction effects. We observe a few mm shift between mean values of measured and simulated B_x. This discrepancy is still acceptable within applied cut on $B_x < 4$ cm. Simulated B_x distributions are slightly narrower in comparison to the measured ones as they are less sensitive to different experimental distortions.

When we take into account the reconstructed number of points (N) as well as their ratio with respect to total of potential points ($r = N/N_{pot,point}$) we observe very similar behavior for the MC and data, as shown in Fig. 7.2. The example is chosen for positively charged low momentum tracks with θ=[140,180] mrad *(left)* and θ=[180,240] mrad *(right)*, however the same results are observed also for negative tracks.

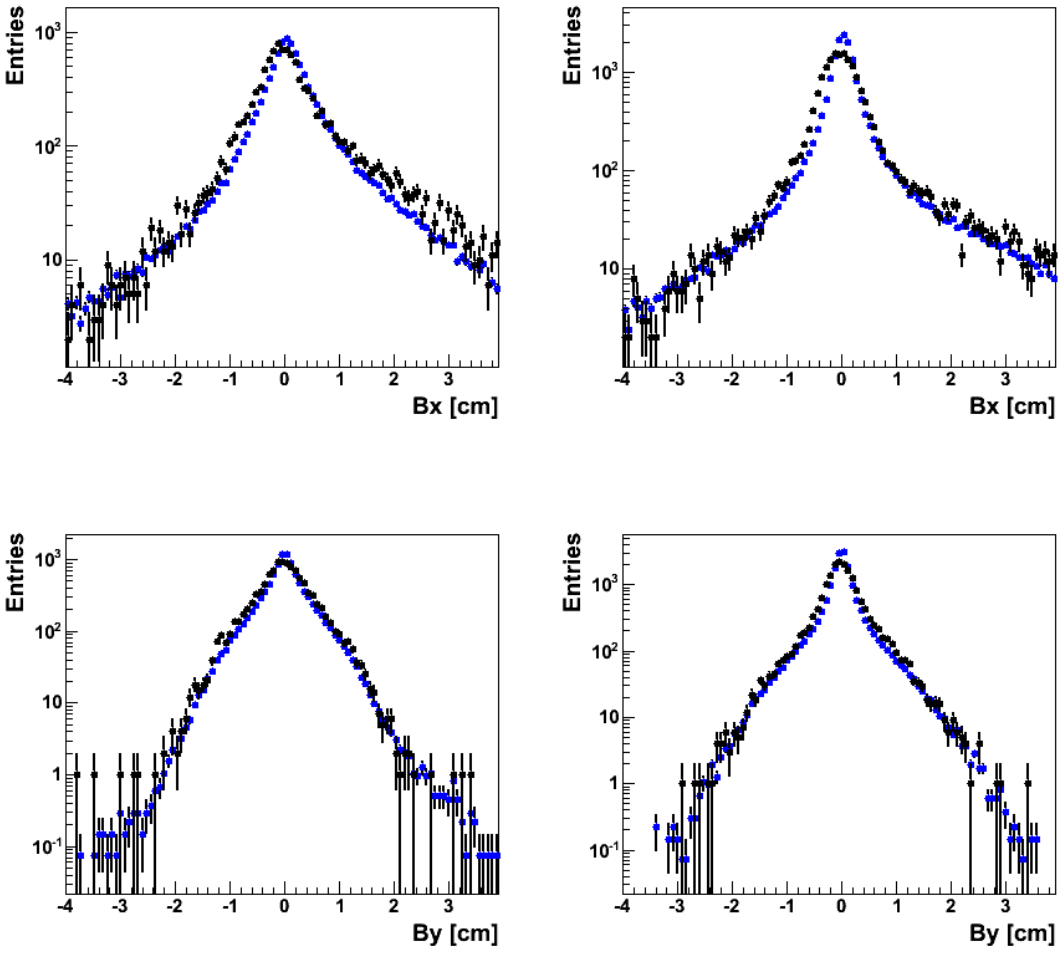

Figure 7.1: Impact parameter distributions B_x *(upper)* and B_y *(lower)* for data (*black*) and MC (*blue*) samples for positively charged low momentum *reconstructed* tracks. Examples are shown for: θ=[140,180] mrad *(left)* and θ=[180,240] mrad *(right)*. Note the logarithmic vertical scale.

Next studies involved azimuthal angle distributions (ϕ) to which following section is devoted.

7.2.1 Limited geometrical acceptance in azimuthal angle

As is explained in Sec. 5.2.2 on page 60 most of the low momentum tracks (especially those with p$\leqslant$ 1 GeV/c) may be detected only in the VTPC1. One should keep in mind that height of the front walls of VTPC1 is only 1 m (see Table. 3.1 on page 37) which means that the vertex chambers are relatively flat and as a result we are not able to measure all ϕ angles for

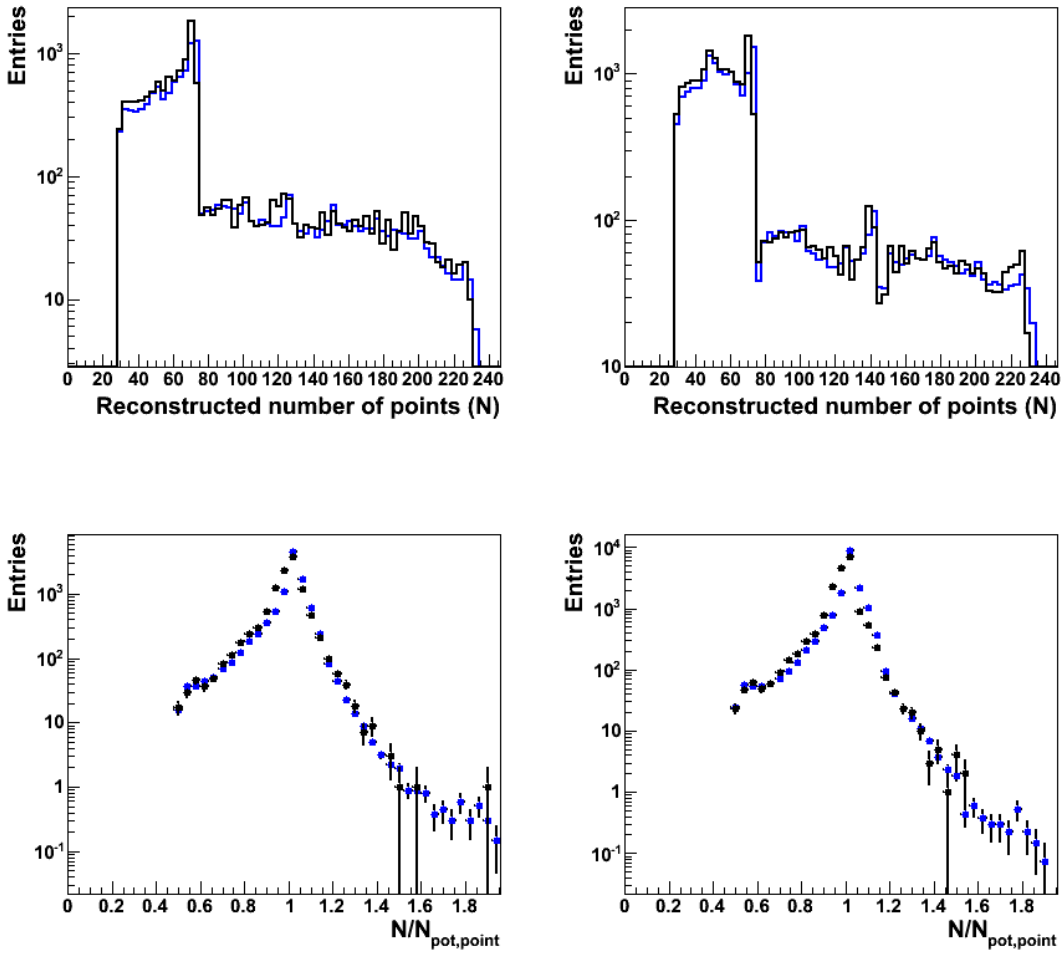

Figure 7.2: Distribution of the number of reconstructed points (N) *(upper)* and fraction of a total of potential points ($r = N/N_{pot,point}$) *(lower)* for data (*black*) and MC (*blue*) samples for positively charged low momentum *reconstructed* tracks. Examples are shown for: θ=[140,180] mrad *(left)* and θ=[180,240] mrad *(right)*. Note the logarithmic vertical scale.

all θ intervals. We may even make very rough estimates for the maximal θ_{max} angle at $\phi = 0$ for VTPC1 using the known geometry:

$$\theta_{max} = \arctan\frac{y}{z} = \arctan\frac{50}{80} \backsimeq 30\text{deg} \backsimeq 500\text{mrad} \tag{7.1}$$

where z is the distance target-front wall of the VTPC1 and y denotes the distance between the middle of the VTPC1 and its top/bottom walls. As a consequence we are left with limited acceptance in azimuthal angle, depending on chosen θ bin. This fact is illustrated in Fig. 7.3, where the azimuthal angle distributions are shown for all *reconstructed* tracks in MC sample of positively and negatively charged particles. Instead of isotropic azimuthal angle distribution which may be expected for unpolarized beam and target, we observe deficit of vertical tracks. In particular we see that for both track charges we are able to fully cover ϕ with production angles only up to 40 mrad. For larger θ angles the regions of azimuthal angle acceptance are decreasing, as expected.

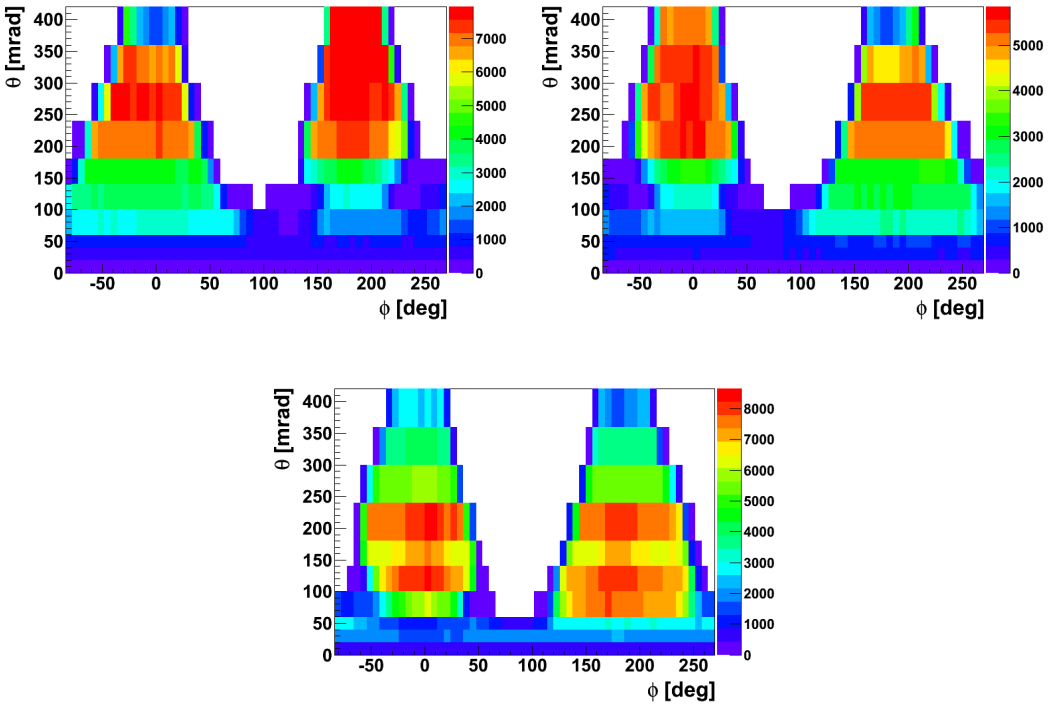

Figure 7.3: Polar angle (θ) versus azimuthal angle (ϕ) distributions for *reconstructed* tracks of: positively charged particles with 0.2<p [GeV/c]≤1 *(left)*, negatively charged particles with 0.2<p [GeV/c]≤1 *(right)* and with 1<p [GeV/c]≤3 *(lower)*. Plots are prepared for the MC sample.

In order to check how well we reconstruct the edges of the azimuthal acceptance in MC sample we decided to compare simulated with measured ϕ distributions as shown in Figs.[7.4 – 7.6] prepared for the positively and negatively charged particles with 0.2<p [GeV/c]≤1 and negatively charged particles with 1<p [GeV/c]≤3, respectively. In the first and third panel rows of each figure we illustrate ϕ distributions for both samples: data (*blue*) and MC (*black*) for various θ intervals with significantly reduced ϕ acceptance. In the second and fourth panel rows we also present the ratio between data and MC for consecutive production angle intervals. In each plot the dashed, red lines are placed to demonstrate regions of reduced azimuthal angle acceptance. Areas of ϕ angle populated by RST and WST samples, introduced in Sec. 5.3 on page 66, are seen in the figures. Let us remind that in case of positive particles the RST sample may occupy those ϕ regions for which $p_x > 0$. This fact implies that cosine of azimuthal angle has to be larger than zero ($\cos\phi > 0$) which is fulfilled only for $\phi = [-90, 90]$ deg. Consequently the sample WST populates the region of $\phi = [90, 270]$ deg. The situation is opposite for negatively charged particles, *i.e.* RST are those with $\phi = [90, 270]$ deg, whereas WST cover $\phi = [-90, 90]$ deg.

We thus see that we have to introduce large corrections for limited ϕ acceptance using MC simulations. As it is explained in next sections we introduce MC corrections in (p, θ) bins multiplying the observed particle yields by corresponding ratios of generated to reconstructed particle tracks. Before we apply this procedure we want to be sure that MC simulations describe sufficiently well the data which are corrected. We see in Figs.[7.4 – 7.6] that at the edges of ϕ regions with good acceptance we see points where the "data-to-MC" ratios deviate significantly from mostly flat shape. In order to reject these uncertain ϕ regions as

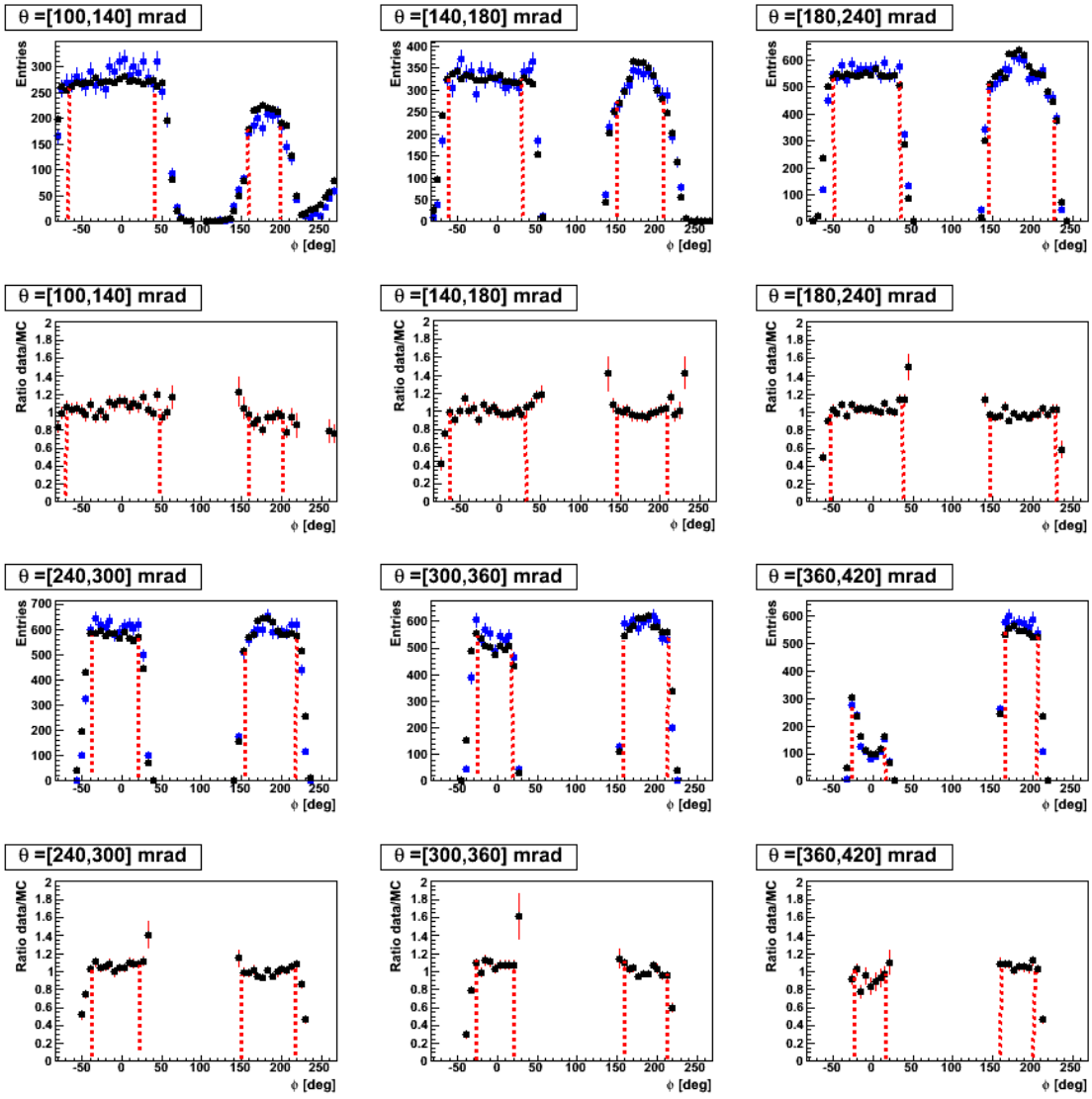

Figure 7.4: Azimuthal angle distribution - comparison between data (*blue*) and MC (*black*) for *reconstructed* positive tracks with ($0.2 < p \leqslant 1$ GeV/c). In the first and third panel rows we illustrate comparison between data (*blue*) and MC (*black*) for various polar angles ϕ. In second and fourth panel rows we also present the ratio between data and MC for consecutive production angle intervals. The dashed, red lines represent the applied ϕ - *wedge* cuts.

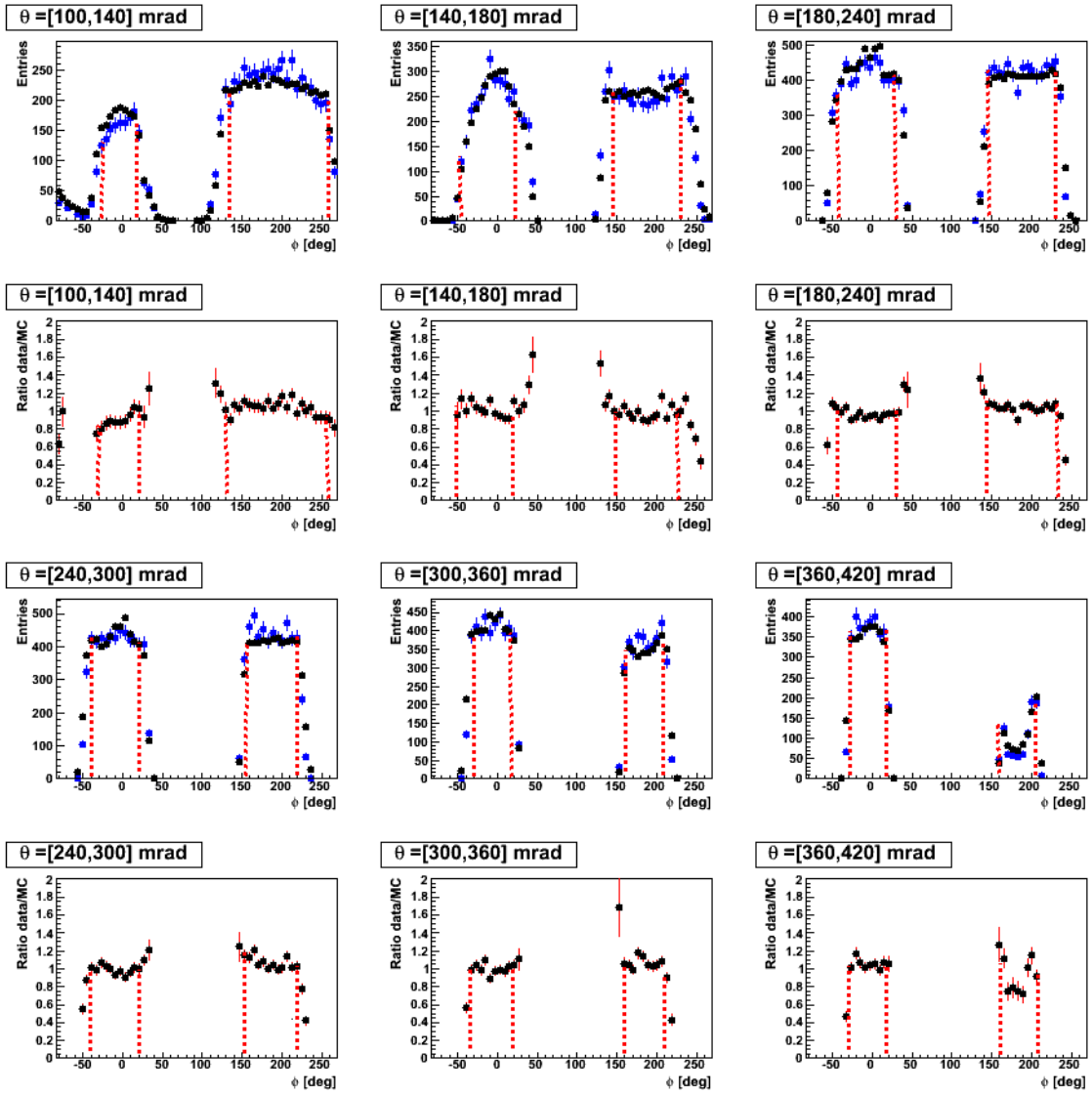

Figure 7.5: Azimuthal angle distribution - comparison between data (*blue*) and MC (*black*) for reconstructed negative tracks with ($0.2 < p \leqslant 1$ GeV/c). In the first and third panel rows we illustrate comparison between data (*blue*) and MC (*black*) for various polar angles ϕ. In second and fourth panel rows we also present the ratio between data and MC for consecutive production angle intervals. The dashed, red lines represent the applied ϕ - *wedge* cuts.

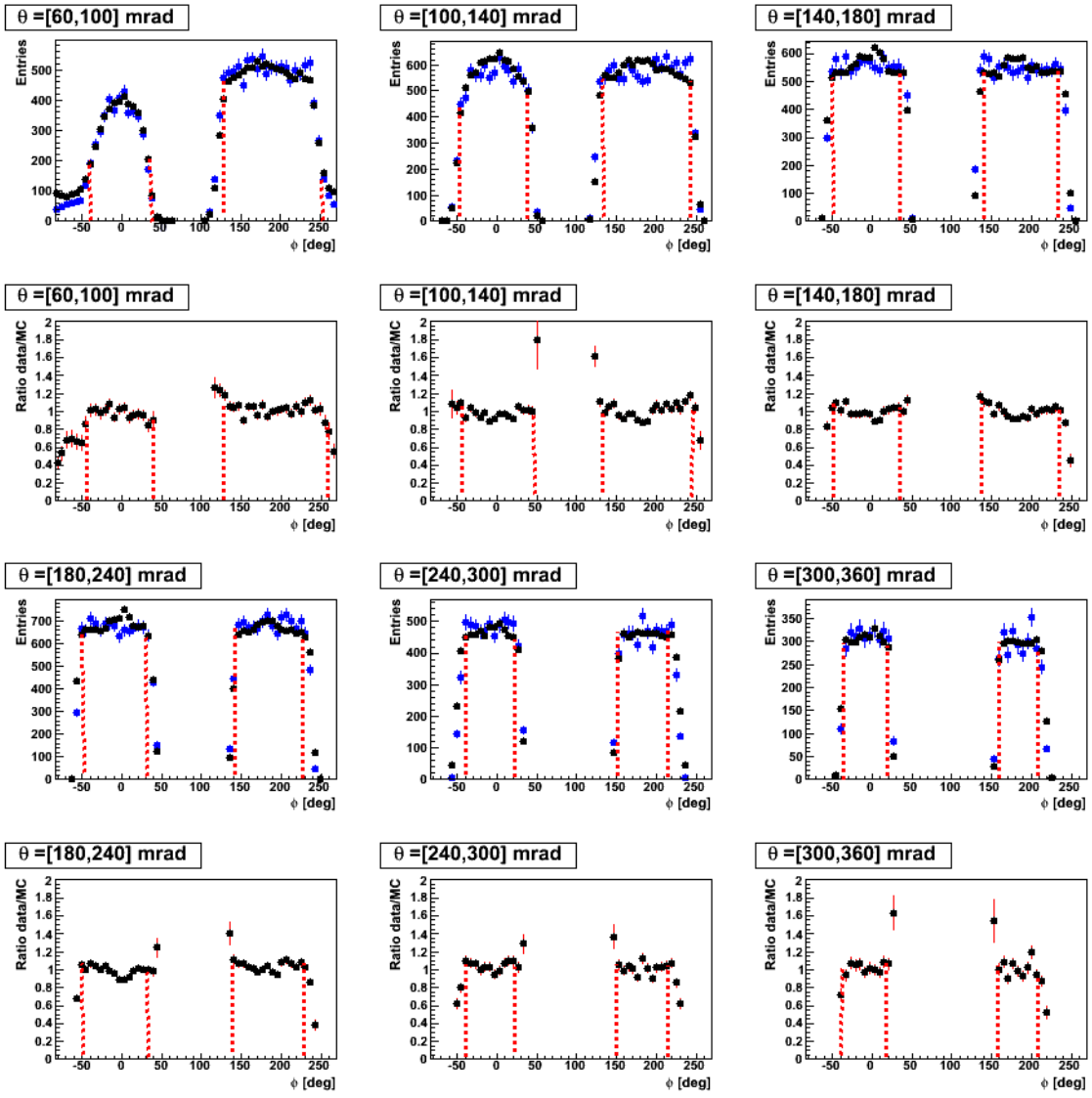

Figure 7.6: Azimuthal angle distribution - comparison between data (*blue*) and MC (*black*) for reconstructed negative tracks with ($1 < p \leqslant 3$ GeV/c). In the first and third panel rows we illustrate comparison between data (*blue*) and MC (*black*) for various polar angles ϕ. In second and fourth panel rows we also present the ratio between data and MC for consecutive production angle intervals. The dashed, red lines represent the applied ϕ - *wedge* cuts.

well as those with very small ϕ acceptance, we apply ϕ cuts, called ϕ - *wedge* cuts, which are indicated with dashed red lines in the figures. We also see in Figs.[7.4 – 7.6] that for some polar angles θ the ϕ distributions are quite complicated, especially at WST regions. In Appendix C we show that this happens when tracks pass through more than one detector.

Detailed values of ϕ - *wedge* cut for different polar angle bins together with their impact on the reduction rate in data and MC sample are presented in Table 7.2. The largest reduction is observed for the $\theta = [100, 180]$ mrad. We reject in maximum almost 30% (20%) of negative (positive) tracks with 0.2<p[GeV/c]⩽1 mainly in WST group.

θ bin [mrad]	ϕ - *wedge*	Reduction rate	
		Data	MC
Positive low momentum tracks with 0.2<p [GeV/c]≤1			
θ<100 mrad	no cut	-	-
[100,140]	RST: ϕ=[-70,50] deg, WST: ϕ=[160,200] deg	7538 (84 %)	98650 (83 %)
[140,180]	RST: ϕ=[-65,35] deg, WST: ϕ=[145,210] deg	9115 (82%)	116586 (84%)
[180,240]	RST: ϕ=[-55,40] deg, WST: ϕ=[145,230] deg	16682 (94%)	214964 (94%)
[240,300]	RST: ϕ=[-40,25] deg, WST: ϕ=[150,220] deg	14120 (91%)	183419 (90%)
[300,360]	RST: ϕ=[-25,20] deg, WST: ϕ=[160,215] deg	10568 (92%)	141811 (91%)
[360,420]	RST: ϕ=[-25,20] deg, WST: ϕ=[160,210] deg	6201 (97%)	90614 (97%)
Negative low momentum tracks with 0.2<p [GeV/c]≤1			
θ<100 mrad	no cut	-	-
[100,140]	WST: ϕ=[-30,20] deg, RST: ϕ=[130,260] deg	6624 (89 %)	85813 (90 %)
[140,180]	WST: ϕ=[-50,25] deg, RST: ϕ=[150,230] deg	6378 (72%)	78547 (73%)
[180,240]	WST: ϕ=[-45,30] deg, RST: ϕ=[145,235] deg	12209 (89%)	150031 (89%)
[240,300]	WST: ϕ=[-40,25] deg, RST: ϕ=[150,225] deg	10559 (94%)	134961 (93%)
[300,360]	WST: ϕ=[-35,20] deg, RST: ϕ=[160,210] deg	7067 (88%)	93913 (88%)
[360,420]	WST: ϕ=[-35,20] deg, RST: ϕ=[160,210] deg	4152 (98%)	60077 (97%)
Negative low momentum tracks with 1<p [GeV/c]≤3			
θ<60 mrad	no cut	-	-
[60,100]	WST: ϕ=[-45,40] deg, RST: ϕ=[120,250] deg	15200 (96%)	225291 (96%)
[100,140]	WST: ϕ=[-50,45] deg, RST: ϕ=[135,245] deg	19553 (92%)	255371 (93%)
[140,180]	WST: ϕ=[-50,35] deg, RST: ϕ=[140,235] deg	17216 (86%)	209527 (86%)
[180,240]	WST: ϕ=[-50,35] deg, RST: ϕ=[140,230] deg	20472 (92%)	235913 (91%)
[240,300]	WST: ϕ=[-40,25] deg, RST: ϕ=[150,215] deg	10818 (87%)	128463 (86%)
[300,360]	WST: ϕ=[-30,20] deg, RST: ϕ=[160,210] deg	5534 (87 %)	70440 (87%)
[360,420]	WST: ϕ=[-30,20] deg, RST: ϕ=[160,210] deg	3062 (98%)	40363 (98%)

Table 7.2: Track selection based on ϕ - *wedge* cut - rate reduction for data and MC samples is also shown. Separation of azimuthal angle region for RST and WST range is applied. (All values quoted in brackets refer to the percentage of tracks which survive the selection corresponding to chosen (p, θ) range and charge sign. Note that value of 100% corresponds to the number of tracks which were detected by the NA61 and survived the selections decribed in Chapter. 5).

Now as we have investigated MC sample we can come to the section devoted to corrections, which are derived from the simulated data.

7.3 Corrections

7.3.1 Introduction

Particle spectra presented in Chapter 6 need to be corrected for effects like: acceptance of the NA61 detector, vertex association and particle decays, reconstruction inefficiency or smearing between neighboring bins. All these corrections will be introduced by one correction factor matrix derived from the MC sample of *reconstructed* tracks. Note that by *reconstructed* tracks we mean those which were specified in Sec. 7.2 on page 90.

In our approach we define *global* correction factor matrix $C^{-1}(p,\theta)$ as:

$$C^{-1}(p,\theta) = \frac{\Delta n_{rec,\alpha}}{\Delta p, \Delta\theta} \quad / \quad \frac{\Delta n_{gen,\alpha}}{\Delta p, \Delta\theta} \tag{7.2}$$

where by $\Delta n_{rec,\alpha}$ we understand *reconstructed* number of tracks of particle type α, whereas $\Delta n_{gen,\alpha}$ represents number of generated tracks, originated in primary vertex. Next with the knowledge of number of identified particle type α ($\Delta n_{iden,\alpha}$) we are able to obtain corrected particle yields ($\frac{\Delta n_\alpha}{\Delta p, \Delta\theta}$):

$$\frac{\Delta n_\alpha}{\Delta p, \Delta\theta} = \frac{\Delta n_{iden,\alpha}}{\Delta p, \Delta\theta} \cdot C \tag{7.3}$$

7.3.2 Correction matrices for low momentum π^+, π^- mesons and protons

Following concept of *global* MC corrections introduced in previous section in Figs.[7.8 – 7.9] we demonstrate (p,θ) distributions for π^-, π^+ and protons, respectively. *Left* plots show generated particles, coming from the main vertex, *middle* plots display *reconstructed* tracks of given particle type and *right* present the calculated corrections C^{-1}. For comparison reasons we decided to prepare two sets of plots for the negatively charged pions with 0.2<p[GeV/c]$\leqslant$1 (see *upper* panel in Fig. 7.8) and with 1<p[GeV/c]$\leqslant$3 (see *lower* panel in Fig. 7.8). Illustrations of given particle corrections show that for polar angle intervals θ >100 mrad the average value of $C^{-1}(p,\theta)$ varies between 0.4-0.6. Note that the main contributor here to *global* correction comes from the limited acceptance in the ϕ angle discussed previously. Moreover, at very low momentum and angles we observe an excess of *reconstructed* tracks ($C^{-1} > 1$). We will study this effect in the next section.

7.3.3 Selection of primary and secondary particles

Tests were performed in order to check how many particles (π^+, π^- and protons) are reconstructed to the main vertex and they really do originate in it (referred to as primary particle tracks) and how many of them are produced in secondary interactions but still reconstructed to main one (referred to as secondary particle tracks). In MC sample we could separate among all *reconstructed* tracks those which are primary and which secondary:

$$n_{rec} = n_{rec,prim} + n_{rec,sec} \tag{7.4}$$

The result of this separation is illustrated in Figs.[7.10, 7.11] for π^+, π^- and protons, respectively. First let us note that the secondary tracks constitute per average 15%, 24%

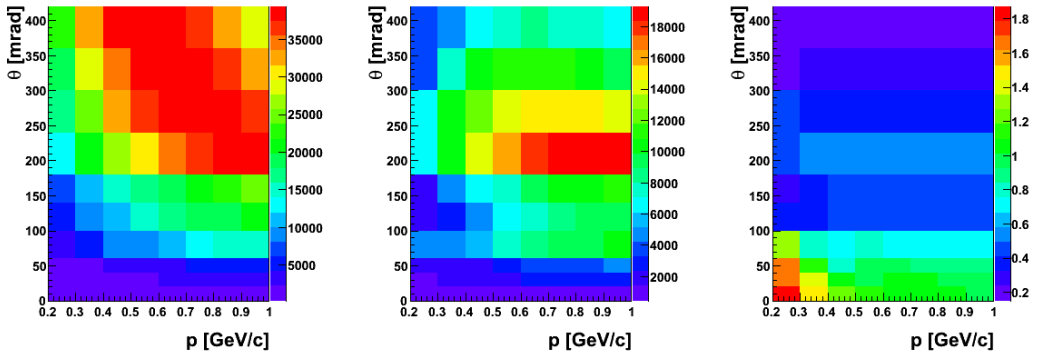

Figure 7.7: (p,θ) distributions for π^+: generated, coming from the main vertex *(left)*, *reconstructed* tracks *(middle)* and *global* correction matrix *(right)* giving a fraction of reconstructed tracks out of the total of generated particles.

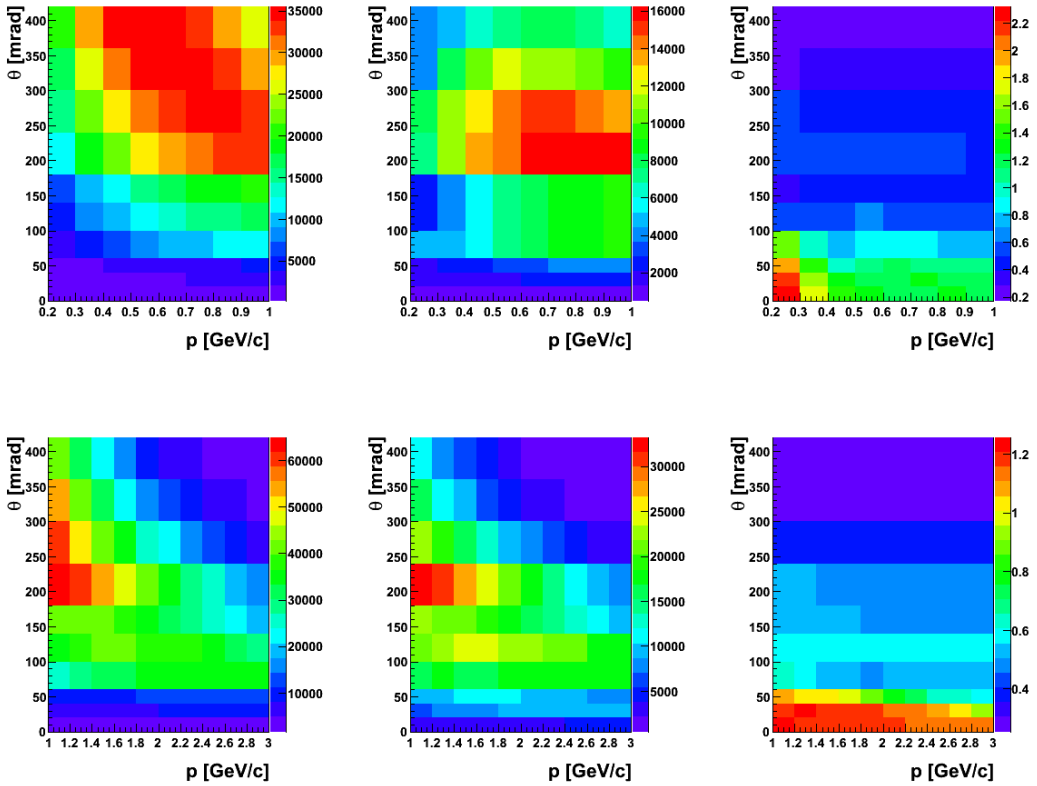

Figure 7.8: (p,θ) distributions for π^- with 0.2<p[GeV/c]$\leqslant$1 *(upper)* and with 1<p[GeV/c]$\leqslant$3 *(lower)*. For each panel we illustrate (p,θ) of generated pions, coming from the main vertex *(left)*, *reconstructed* tracks *(middle)* and *global* correction matrix *(right)* giving a fraction of reconstructed tracks out of the total of generated particles.

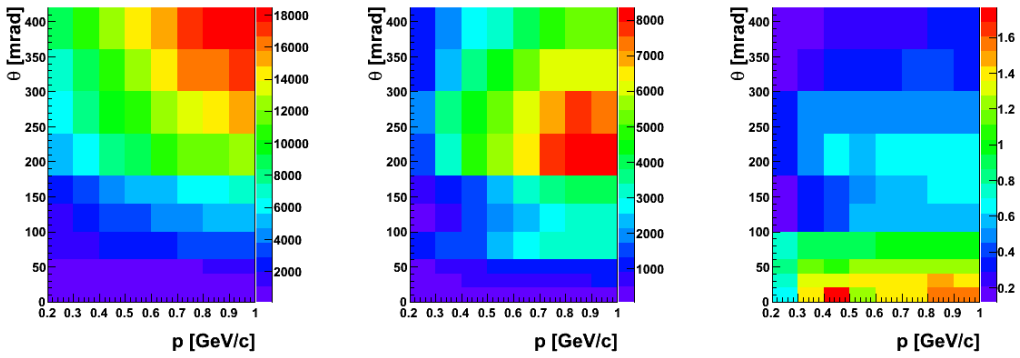

Figure 7.9: (p,θ) distributions for protons: generated, coming from the main vertex *(left)*, *reconstructed* tracks *(middle)* and *global* correction matrix *(right)* giving a fraction of reconstructed tracks out of the total of generated particles.

and 32% for π^+, π^- and protons with 0.2<p[GeV/c]$\leqslant$1 and 13% for π^- with 1<p[GeV/c]$\leqslant$3, respectively. It is seen that there are a lot of particles of each type especially for small production angles which are born in secondary vertexes but still are reconstructed to primary one. What is important to see is the relative fraction of primary *reconstructed* tracks of given particle type amongst all *reconstructed* tracks for different production angle bins. This would show if regions of large $C^{-1} > 1$ placed at low θ and momentum bins may be explained by a large fraction of secondary tracks out of all *reconstructed*. These studies are followed further in the next section.

7.3.4 Feed-down correction

Division on primary and secondary *reconstructed* particles introduced in previous section allows us to define correction for secondary interactions and for weak decays of strange particles, named as *feed-down* (C_{fd}). From Eq. (7.2) we know that *global* correction C for given particle type and selected (p, θ) bin is equal to:

$$C \equiv \frac{n_{gen}}{n_{rec}} \tag{7.5}$$

with the help of Eq. (7.4) we get:

$$C \equiv \frac{n_{gen}}{n_{rec,prim} + n_{rec,sec}} = \frac{n_{gen}}{n_{rec,prim}} \cdot \frac{1}{1+x} \tag{7.6}$$

where x is the ratio between *reconstructed* secondary and primary particles ($x = \frac{n_{rec,sec}}{n_{rec,prim}}$). We may factorize *global* correction C into:

$$C = C_{prim} \cdot C_{fd} \tag{7.7}$$

where C_{prim} represents the ratio of generated to primary *reconstructed* tracks, while C_{fd} defines the *feed-down* corrections. Thanks to the factorization in Eq. (7.7) we may sum up relative errors in quadrature in Sec. 9.2 on page 128 giving total errors. Now let us look in detail at C_{fd}:

$$C_{fd} \equiv \frac{1}{1+x} = \frac{n_{rec,prim}}{n_{rec,prim} + n_{rec,sec}} = \frac{n_{rec,prim}}{n_{rec}} \tag{7.8}$$

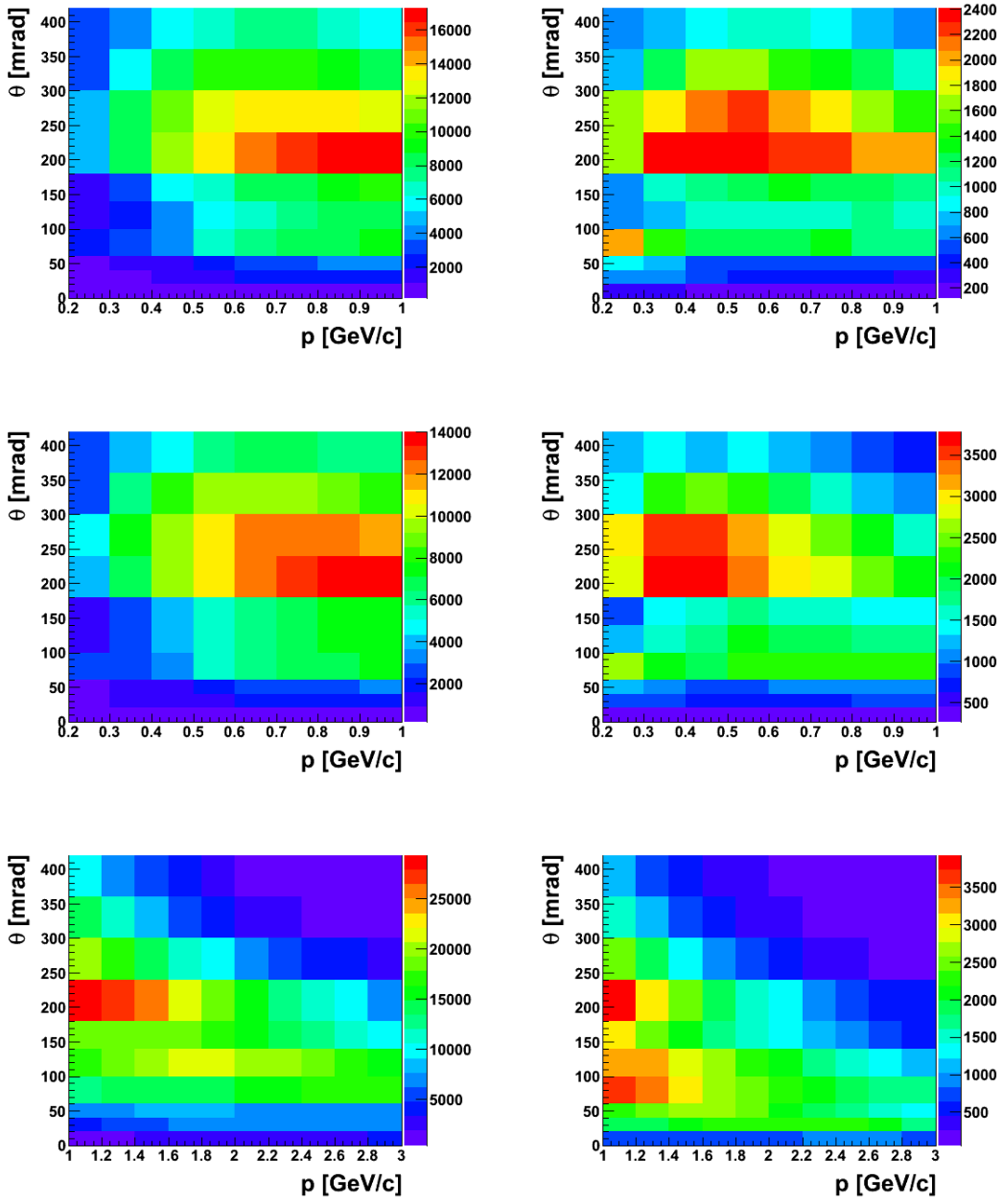

Figure 7.10: (p,θ) distributions for *reconstructed* π^+ *(upper)* and π^- with 0.2<p[GeV/c]$\leqslant$1 *(middle)* and with 1<p[GeV/c]$\leqslant$3 *(lower)*. *Left* plots contain only primary tracks, while the *right* plots-secondary.

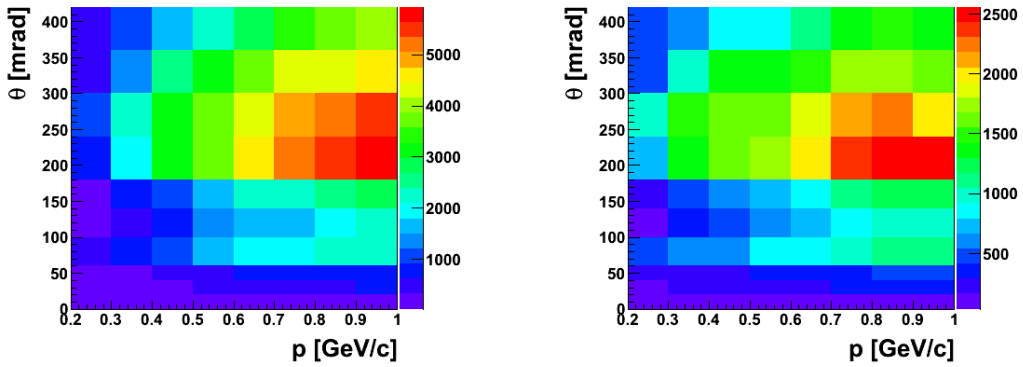

Figure 7.11: (p,θ) distributions for reconstructed primary *(left)* and secondary *(right)* protons.

Looking at Eq. (7.8) we see that C_{fd} values may vary only between 0 and 1. Moreover, when x is large due to large contamination of secondary interactions and decays of strange particles we get small C_{fd} and vice versa. The C_{fd} corrections are displayed in Fig. 7.12 for π^+, π^- and protons, respectively. The largest contamination is present for the smallest *feed-down* corrections, *i.e.* for low polar angles and momenta. We see that in case of protons situation is slightly better as C_{fd} is less sensitive to momentum. As we increase the polar angle and momentum bin contamination from $n_{rec,sec}$ tracks is decreasing. Moreover, the one of the sources to *feed-down* contributions are decay channels of strange particles listed in Tab. 7.3. In particular, the decays of Λ particle result in *feed-down* contamination only for π^- and for protons. This fact may explain why *feed-down* corrections have larger impact on π^- meson in comparison to its charge opponent π^+. It can also be noticed that the decrease of contamination at larger momenta p shows a characteristics $1/p$ dependence. This results from the expression for the decay length $\lambda = \frac{pc\tau}{m}$ for a particle of mass m and lifetime τ.

Decay channel	Branching ratio
$\Lambda \to p + \pi^-$	$\sim 64\%$
$K^0_s \to \pi^- + \pi^+$	$\sim 69\%$
$\Sigma^+ \to p + \pi^0$	$\sim 52\%$

Table 7.3: The sources of decays of strange particles which result in contribution to *feed-down* corrections.

At the end of this section we would like to mention that knowledge on secondary interactions and strange particle production which is used in the MC simulation is one of the main source of systematic errors and is studied in detail in the Chapter 9.

7.4 Corrected spectra of π^+, π^- and protons

Now we have gathered all components which are necessary to calculate corrected spectra of π^+, π^- and protons. With the help of Eq. 7.3 and identified particle yields in Chapter 6 as well as introduced in Sec. 7.3.2 *global* corrections we may obtain final results. In Figs.[7.13 – 7.15] we demonstrate (p,θ) distributions for identified *(left)* and corrected *(right)* yields of π^+, π^- and protons, respectively.

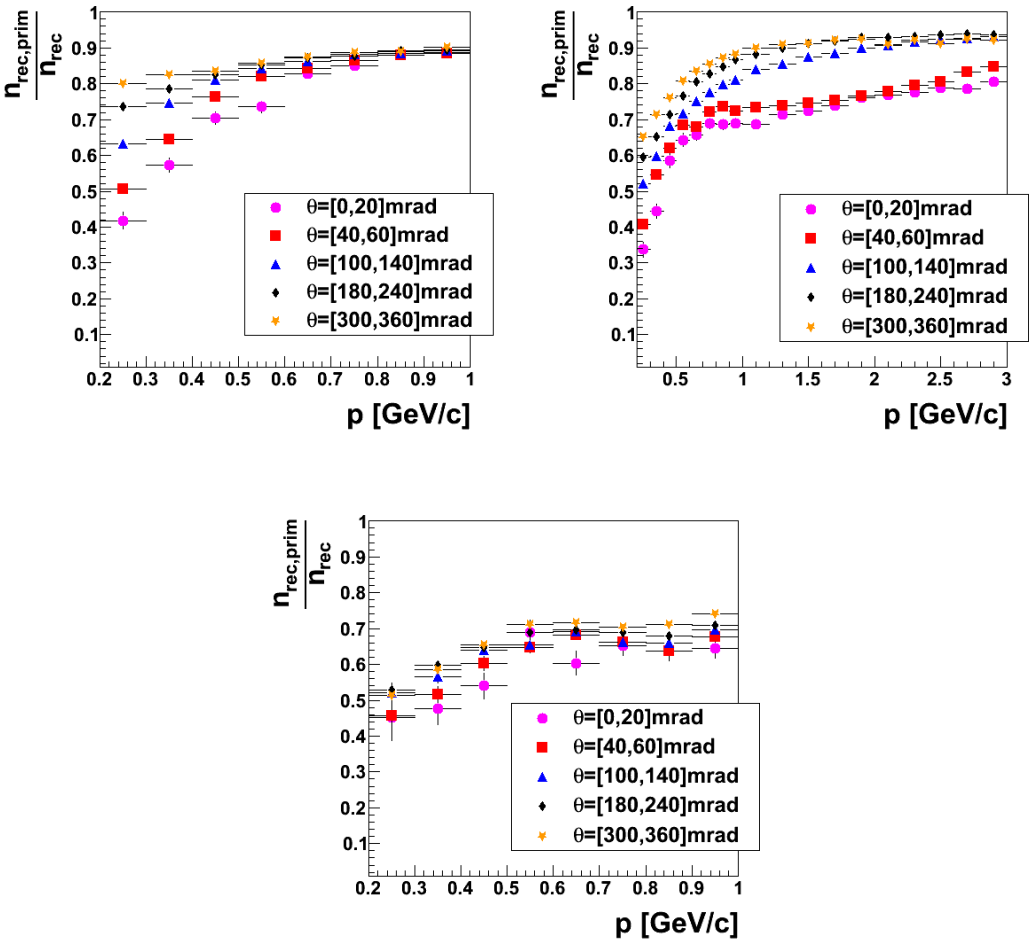

Figure 7.12: Fraction of primary particles amongst all *reconstructed* to the main vertex ($n_{rec,prim}/n_{rec}$) for different momentum bins for: π^+ *(left)*, π^- *(right)* and protons *(lower)*. Several polar angle bins are shown.

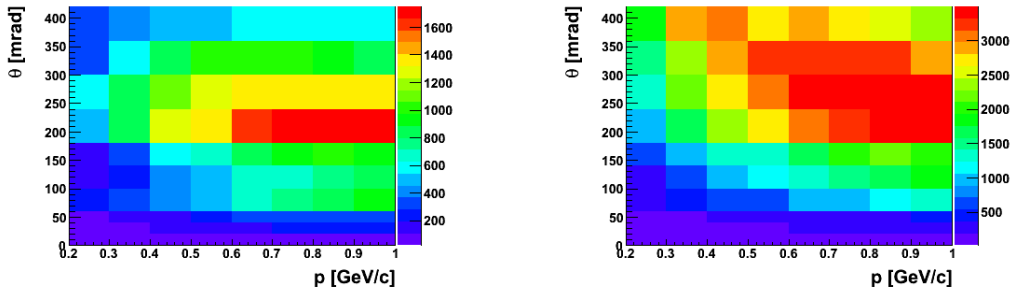

Figure 7.13: Yields of identified π^+ mesons in (p, θ) bins: before *(left)* and after *(right)* MC corrections.

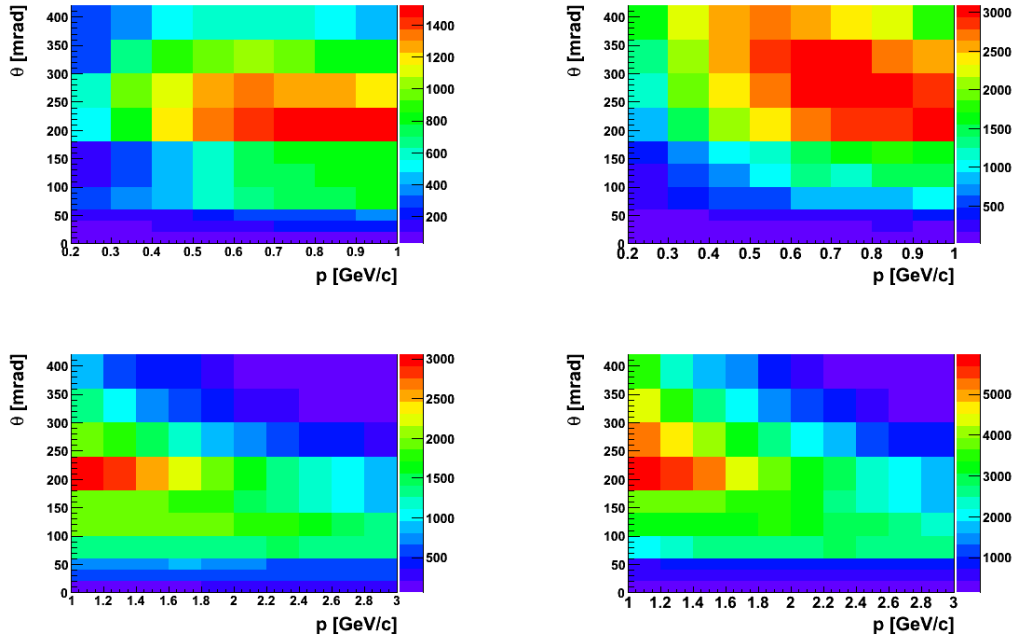

Figure 7.14: Yields of identified π^- mesons in (p, θ) bins: before *(left)* and after *(right)* MC corrections. Separation on momentum range was used: *(upper)* corresponds to π^- tracks with $0.2<$p[GeV/c]$\leqslant 1$ and *(lower)* with $1<$p[GeV/c]$\leqslant 3$.

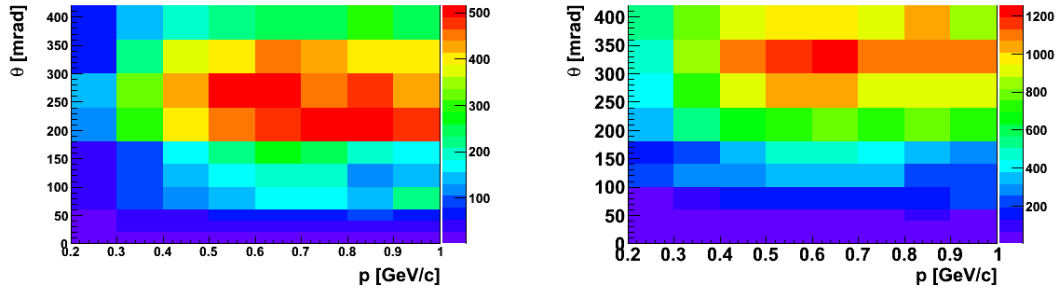

Figure 7.15: Yields of identified protons mesons in (p, θ) bins: before *(left)* and after *(right)* MC corrections.

Up to now we considered total yields of π^+, π^- and protons in all the events of proton interactions, in the next chapter we will consider mean multiplicities of pions and protons. We will discuss there the necessary normalization procedures.

Chapter 8

Cross section measurements and normalization of particle spectra

This chapter deals with the procedure of cross section measurements and normalization of particle yields which was performed for the NA61 2007 data. For this purpose the same concept as the one developed by the NA49 Collaboration [109] was adopted. In this approach the particle yields are derived from the data and then corrected for different experimental effects. The scheme of cross section evaluation of 2007 data was a subject of Claudia Strabel dissertation (see Ref. [110]). We will introduce here only major points of the procedure important for the normalized particle spectra presented in this chapter.

8.1 Inelastic and Production p+C Cross Sections

We take into consideration two kinds of processes: inelastic (σ_{inel}) and production (σ_{prod}) interactions. By production processes we understand those interactions where new hadrons are produced, whereas inelastic ones take also into account interactions which lead only to disintegration of target nucleus (quasi-elastic interactions (σ_{qe})). In other words one can say that:

$$\sigma_{inel} = \sigma_{prod} + \sigma_{qe} \tag{8.1}$$

where σ_{qe} for p+C interactions at 31 GeV/c amounts to 27.9 ± 1.5 (sys) mb according to Glauber model calculations [111]. Once we measure σ_{inel} then with the help of Eq. (8.1) we may derive σ_{prod}. Now let us focus on inelastic cross section measurements. As stated previously we rely on events registered with trigger configuration introduced in Sec. 3.3 on page 33. In ideal situation we would like to have trigger only on inelastic events, however in our experimental conditions this is not exactly the case as we are sensitive also to contribution of other interactions. The largest impact comes from coherent elastic scattering, *i.e.* events in which the incoming beam particle undergoes a large angle coherent elastic scattering on the carbon nuclei and misses the S4 counter. As a result we have triggered event but this is not what we would like to measure. Next also important fact is that some of the inelastic interactions of interest are lost. These are events in which emitted charged particles (protons, kaons and pions) hit the S4 counter. Now let us denote by *trigger* cross section (σ_{trig}) the real cross section which is actually measured within NA61 trigger. Then:

$$\sigma_{inel} = \sigma_{trig} - \sigma_{el,\ \text{out of S4}} + \sigma^{\pi,K}_{inel,loss} + \sigma^{p}_{inel,loss} \tag{8.2}$$

where $\sigma_{el,\ \text{out of S4}}$ represents contribution from unwanted events originated in coherent elastic scattering which are missing S4 counter, while $\sigma^{\pi,K}_{inel,loss}$ and $\sigma^{p}_{inel,loss}$ corresponds to loss of

inelastic events of given particle type. In order to estimate the values of corrections which need to be applied to our cross section measurements the GEANT4 [112] simulations were performed. Those calculations took into account measured profile and divergence of the proton beam. In Tab. 8.1 we present the results of this task. The numers are taken from Ref. [110].

Cross section	Value [mb]
$\sigma_{el,\text{ out of S4}}$	47.2 ± 0.2(stat) ± 5.0(syst)
$\sigma^{p}_{inel,loss}$	5.7 ± 0.2(stat) ± 0.5(syst)
$\sigma^{\pi,K}_{inel,loss}$	0.57 ± 0.02(stat) ± 0.35(syst)

Table 8.1: Values of corrections originated from NA61 trigger which need to be taken into account for inelastic cross section measurement. Numbers are taken from Ref. [110].

Now we discuss derivation of actually measured cross section within NA61 trigger, *i.e. trigger* cross section. In order to determine σ_{trig} we need to rely on target characteristics and actually measured quantities within 2007 data taking. In general, σ_{trig} is defined by:

$$\sigma_{trig} \equiv \frac{1}{\rho L N_A/A} \cdot \frac{N_{trig}}{N_{beam}} = \frac{1}{n} \cdot \frac{N_{trig}}{N_{beam}} \tag{8.3}$$

With:

N_A:	Avogadro constant	$N_A = 6.022 \times 10^{23}$ mol^{-1}
A:	atomic mass of the target	$A = 12.011$ g/mol
ρ:	density of the target	$\rho = (1.8395 \pm 0.0010)$g/cm^3
L:	target length	$L = 2$ cm
n:	in units of cm^{-2}	$n = \rho L N_A/A$

Moreover, N_{trig} is the number of triggered events originated only from thin target and N_{beam} stands for the number of incoming beam particles counted during data acquisition lifetime with used trigger.

In the same manner inelastic and production cross sections by their definitions are equal to:

$$\sigma_{inel} \equiv \frac{1}{n} \cdot \frac{N_{inel}}{N_{beam}}, \quad \sigma_{prod} \equiv \frac{1}{n} \cdot \frac{N_{prod}}{N_{beam}}, \tag{8.4}$$

Thus, in general we may derive following relations:

$$N_{inel} = N_{trig} \cdot \frac{\sigma_{inel}}{\sigma_{trig}} \quad \text{and} \tag{8.5}$$

$$N_{prod} = N_{trig} \cdot \frac{\sigma_{prod}}{\sigma_{trig}} \tag{8.6}$$

where N_{inel} (N_{prod}) denote the total number of inelastic (production) events. We will use Eq. (8.6) in the next section devoted to mean multiplicites in production interactions.

Note that in Eq. (8.3) we do not take into account all events which could give trigger but they were not born inside the target but rather outside in surrounding material. Thus, is its better to use real interaction probability (P_{int}) instead of ratio N_{trig}/N_{beam}. Next we have

to consider also the effective target length L_{eff} which accounts for beam attenuation in the target itself. Thus σ_{trig} should be evaluated with slightly modified Eq. 8.3:

$$\sigma_{trig} = \frac{1}{\rho L_{eff} N_A / A} \cdot P_{int} \tag{8.7}$$

with $L_{eff} = 1.946$ cm, while real interaction probability (P_{int}) has to be evaluated using measurements with configuration: target inserted (P_{in}) and target removed (P_{out}). In this approach one has to take into account all possible scenarios for both target operations by considering interactions in the material upstream as well as downstream of the target. This is schematically demonstrated in Fig. 8.1 and may be written as follows:

$$P_{out} = P_{up} + P_{down}(1 - P_{up}) \tag{8.8}$$

$$P_{in} = P_{up} + P_{int}(1 - P_{up}) + P_{down}(1 - P_{up})(1 - P_{int}) \tag{8.9}$$

where P_{up} (P_{down}) represent interaction probability in the material upstream (downstream) of the target.

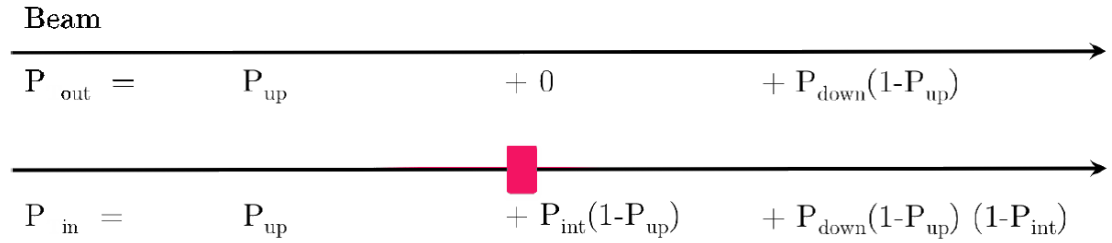

Figure 8.1: Scheme of contributions to the interaction probability with configurations: target removed *(upper)* and target inserted *(lower)*. The red box indicates target position. Figure is taken from Ref. [110] and is graphically modified.

We are interested in the value of interaction probability in the target and with the help of Eq. (8.8) and Eq. (8.9) we get:

$$P_{in} - P_{out} = P_{int}(1 - P_{out}) \tag{8.10}$$

Thus P_{int} is equal to:

$$P_{int} \simeq (P_{in} - P_{out}) \cdot (1 + P_{out}) \tag{8.11}$$

Moreover, both interaction probabilities with target inserted and removed are determined with the help of the number of corresponding triggered events (N^{in}_{trig} and N^{out}_{trig}). In addition those events should also survive reconstruction of the proton beam particles and requirements on BPD signals (see Sec. 5.1 on page 58). Here the number of beam particles counted during data acquisition lifetime with trigger is also needed (N^{in}_{beam} and N^{out}_{beam}):

$$P_{in} = \frac{N^{in}_{trig}}{N^{in}_{beam}}, \qquad P_{out} = \frac{N^{out}_{trig}}{N^{out}_{beam}} \tag{8.12}$$

In Tab. 8.2 we summarize values needed to derive the real interaction probability P_{int}. Using Eq. (8.11) and Eq. (8.12) we get $P_{int} = 5.351 \pm 0.035$ [%].

As the interaction probability is known we can derive actually measured quantity *trigger* cross section with the help of Eq. (8.7). Next we use σ_{trig} for the determination of the inelastic (see Eq. (8.2)) and production cross sections (see Eq. (8.1)). Tab. 8.3 summarizes values of these cross sections.

Target inserted	Value	Target removed	Value
N^{in}_{trig}	520143	N^{out}_{trig}	17302
N^{in}_{beam}	9367980	N^{out}_{beam}	2646283
P_{in}	6.022±0.034 [%]	P_{out}	0.709±0.007 [%]

Table 8.2: Interaction probabilities measured during 2007 data taking for different operations: target inserted (P_{in}) and removed (P_{out}). Note that quoted numbers for N^{in}_{trig} and N^{out}_{trig} are not exactly the same as shown in Tab. 5.1 on page 59 as those are obtained from the same data sample but processed with slightly modified reconstruction chain. Observed differences are still negligible within quoted uncertainties. Numbers are taken from Ref. [110].

Cross section	Value [mb]
σ_{trig}	298.1 ± 1.9(stat) ± 7.3(syst)
σ_{inel}	257.2 ± 1.9(stat) ± 8.9(syst)
σ_{prod}	229.3 ± 1.9(syst) ± 9.0(stat)

Table 8.3: Values of *trigger*, inelastic and production cross sections derived for the p+C interactions at 31 GeV/c . Numbers are taken from Ref. [110].

8.2 Normalization procedure

Experimentally, the double differential inclusive cross section for a fixed target experiment may be formulated as:

$$\frac{d^2\sigma_\alpha}{dpd\theta} = \frac{1}{nN_{beam}} \frac{\Delta n_\alpha}{\Delta p \Delta\theta} \tag{8.13}$$

where n, N_{beam} are defined in previous section, while Δn_α represents the number of identified (see Chapter 6) and corrected (see Chapter 7) tracks of type α in the experimental bins of Δp and $\Delta\theta$. The previous formula may be rewritten in term of *trigger* cross section (see Eq.(8.3)):

$$\frac{d^2\sigma_\alpha}{dpd\theta} = \frac{1}{nN_{beam}} \frac{\Delta n_\alpha}{\Delta p \Delta\theta} = \frac{N_{trig}}{nN_{beam}N_{trig}} \frac{\Delta n_\alpha}{\Delta p \Delta\theta} = \frac{\sigma_{trig}}{N_{trig}} \frac{\Delta n_\alpha}{\Delta p \Delta\theta} \tag{8.14}$$

Next to discuss is the derivation of the mean multiplicities of given particle type in production processes, denoted as $\frac{d^2n_\alpha}{dpd\theta}$. It is obtained from:

$$\frac{d^2n_\alpha}{dpd\theta} \equiv \frac{1}{N_{prod}} \cdot \frac{\Delta n_\alpha}{\Delta p \Delta\theta} \tag{8.15}$$

where N_{prod} can be calulated with Eq. (8.6) using σ_{trig}:

$$\frac{d^2n_\alpha}{dpd\theta} = \frac{1}{N_{trig}} \cdot \frac{\sigma_{trig}}{\sigma_{prod}} \cdot \frac{\Delta n_\alpha}{\Delta p \Delta\theta} = \frac{1}{\sigma_{prod}} \cdot \frac{d^2\sigma_\alpha}{dpd\theta} \tag{8.16}$$

The formulas used for the normalization of particle yields are still not final (see Eq. (8.14) as well as Eq. (8.16)) as they require one additional correction which accounts for the distortion of particle yields ($\frac{\Delta n_\alpha}{\Delta p \Delta\theta}$) due to events which are produced outside the carbon target. Introduced

in previous section interaction probabilities with target removed and inserted result in ratio $\epsilon \equiv \frac{P_{out}}{P_{in}} = 0.118$. In order to account also for the contribution of target removed interactions we had to treat those events with the same manner as with target inserted, *i.e.* analyze them with the procedures presented in Chapters 6 and 7. This approach allowed to obtain the corresponding corrected numbers of particles in p and θ bins, denoted as Δn_α^R for target removed. From now on we use Δn_α^I to represent results for the operation with target inserted. Finally the differential inclusive cross sections of particles type α for selected production angle θ interval is calculated as:

$$\frac{d\sigma_\alpha}{dp} = \frac{\sigma_{trig}}{1-\epsilon} \cdot \left(\frac{1}{N_{trig}^I} \frac{\Delta n_\alpha^I}{\Delta p} - \frac{\epsilon}{N_{trig}^R} \cdot \frac{\Delta n_\alpha^R}{\Delta p} \right) , \tag{8.17}$$

where:

1. $\sigma_{trig} = (298.1 \pm 1.9 \pm 7.3)$ mb is the *trigger* cross section as given in Sec. 8.1,
2. $\epsilon = 0.118 \pm 0.001$ is the ratio of the interaction probabilities for removed and inserted target operation,
3. N_{trig}^I and N_{trig}^R are the numbers of events selected (see Tab. 5.1 on page 59) for the analysis of events with the target inserted and removed, respectively,
4. Δp is the bin size in momentum.

The correction for the contribution of particles coming from events from outside the target (the term $\epsilon/N_{trig}^R \cdot \Delta n_\alpha^R/\Delta p$ in Eq. 8.17) amounts on average to about 7% and 3% in the first two polar angle intervals. It is smaller than about 2% for polar angle bins above 40 mrad. Note that for no contribution from interactions outside the target, *i.e.* $P_{out} = 0$ and $\epsilon = 0$ Eq. (8.17) reduces to Eq. (8.14) as expected.

The mean selected particle multiplicities in production interactions were calculated using Eq. (8.16) and Eq. (8.17):

$$\frac{dn_\alpha}{dp} = \frac{1}{\sigma_{prod}} \cdot \frac{d\sigma_\alpha}{dp} \tag{8.18}$$

The total error on the inclusive cross sections as well as mean multiplicities in production interactions, resulting from the normalization procedure, amounts to 2.5% and 2.3%, respectively (see Chapter 8 in Ref. [110]).

In the next section we present obtained differential cross sections and mean particle multiplicity distributions for low momentum pions and protons.

8.3 Inclusive cross sections and mean multiplicities in production interactions for low momentum π^+, π^- and protons

The charged pion and proton inclusive differential cross sections and mean multiplicities in production processes are shown in Figs.[8.2- 8.7] as functions of particle momentum in ten intervals of the polar angle. Error bars represent only statistical uncertainties. It is seen that in general when we increase the polar angle the maximum of the π^+ and π^- spectra is moving towards lower momentum range. The obtained results for both charged pion mesons could be compared with other analyses, while for protons only the results presented here were available in time of writting this dissertation.

8.4 Charged pion spectra-comparison of results obtained with other analyses

Presented spectra for negatively charged pion mesons are superimposed in Fig. 8.8 with results obtained using different analyses (introduced in Sec. 4.5 on page 53), namely *tof - dE/dx* and h^-. Three analysis methods are presented by different symbols: blue open circles for h^- analysis; red open squares for *dE/dx* only analysis; and black full triangles for *tof - dE/dx* analysis. The observed agreement between the methods is better than 10%. In case of π^+ mesons which are of major importance for the T2K neutrino beam simulations, we could only observe continuity of the spectra obtained using *tof - dE/dx* and those presented in this dissertation shown in Fig. 8.9. Note that all the analyses are statistically correlated as they use the same data set. For the final NA61 results measurements with the smallest total error (statistical and systematic added in quadrature) were selected in each (p, θ) bin. As a result of this procedure mostly *dE/dx* points from this dissertation were used in the region of overlap as final ones. Numerical values of all the results may be found in Ref. [1]. The reader may also find there the statistical as well as systematic uncertainty for each measurement which is subject of detailed discussion introduced in the next chapter.

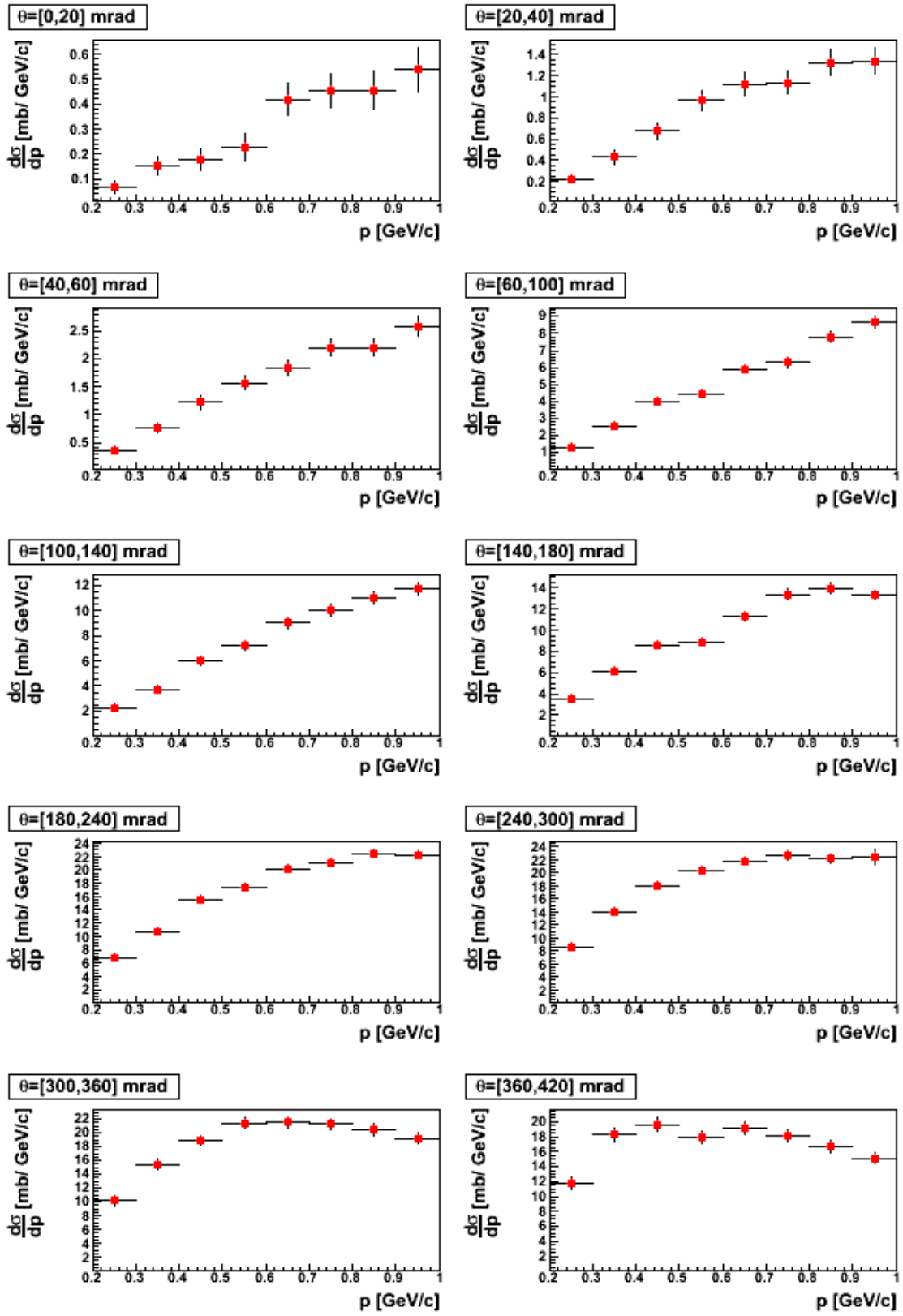

Figure 8.2: Differential cross sections for low momentum π^+ meson production in p+C interactions at 31 GeV/c , presented as a function of laboratory momentum (p) in different intervals of polar angle (θ). Error bars indicate only statistical uncertainties.

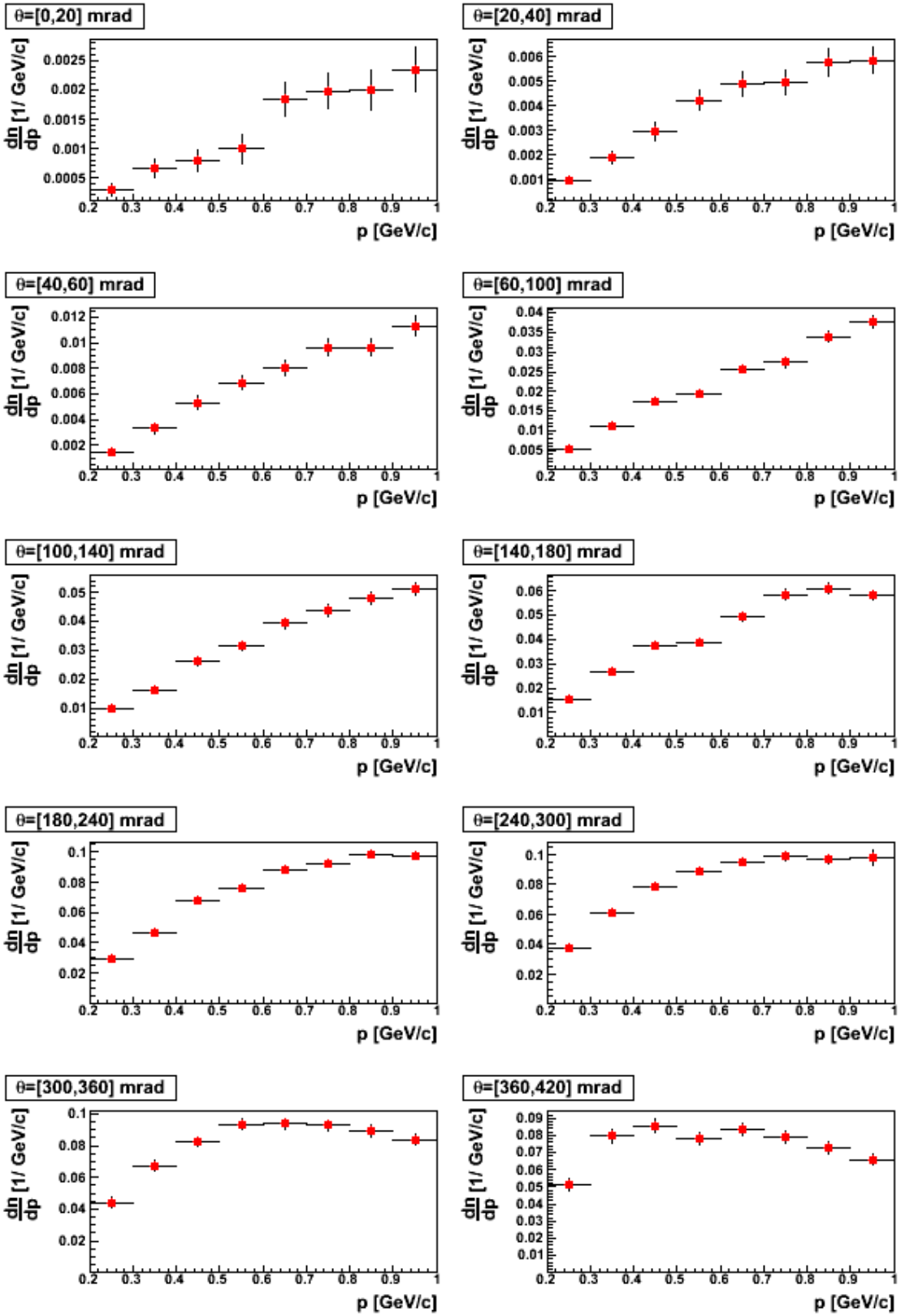

Figure 8.3: Mean π^+ multiplicities in p+C interactions at 31 GeV/c , presented as a function of laboratory momentum (p) in different intervals of polar angle (θ). Error bars indicate only statistical uncertainties.

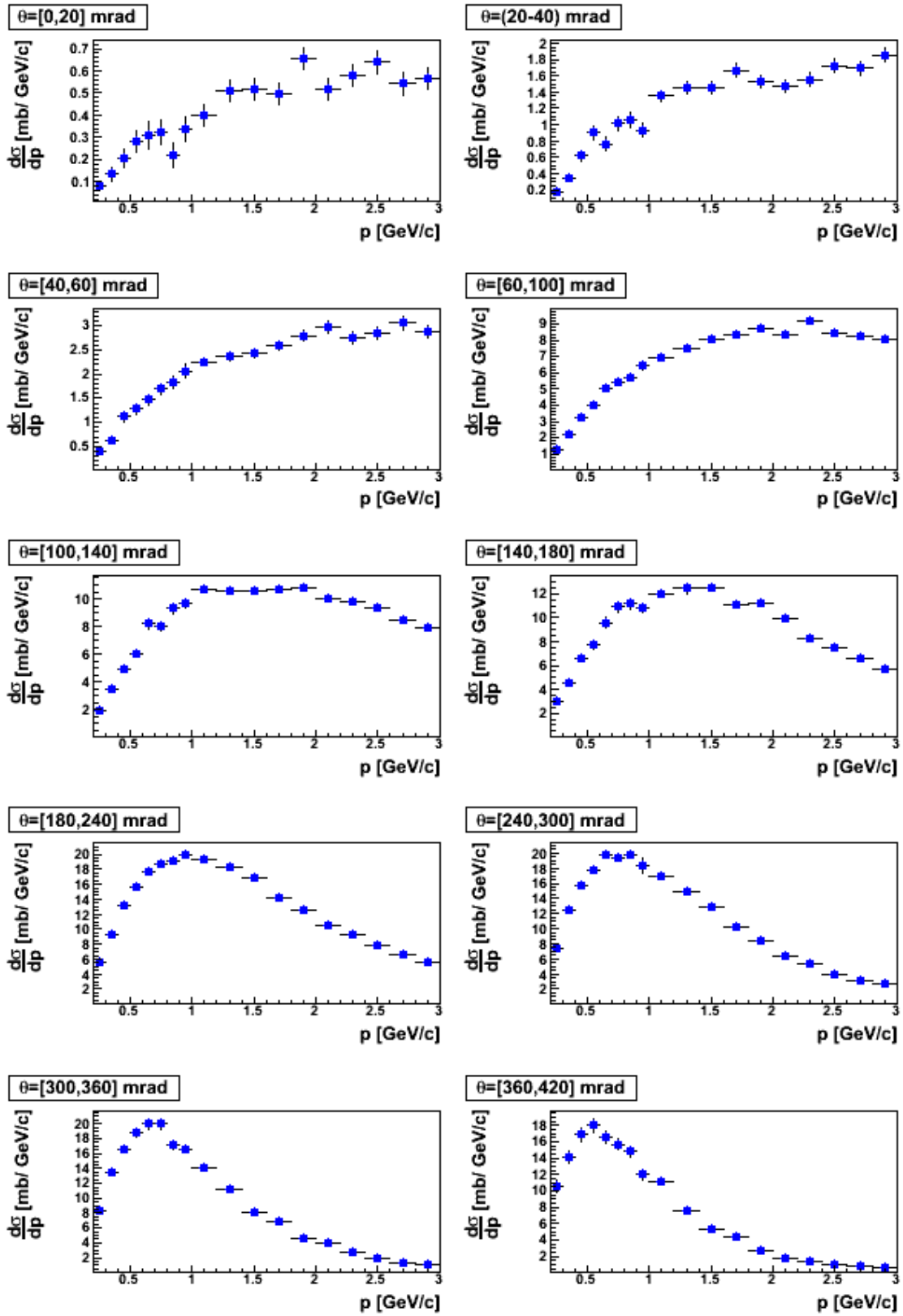

Figure 8.4: Differential cross sections for low momentum π^- meson production in p+C interactions at 31 GeV/c , presented as a function of laboratory momentum (p) in different intervals of polar angle (θ). Error bars indicate only statistical uncertainties.

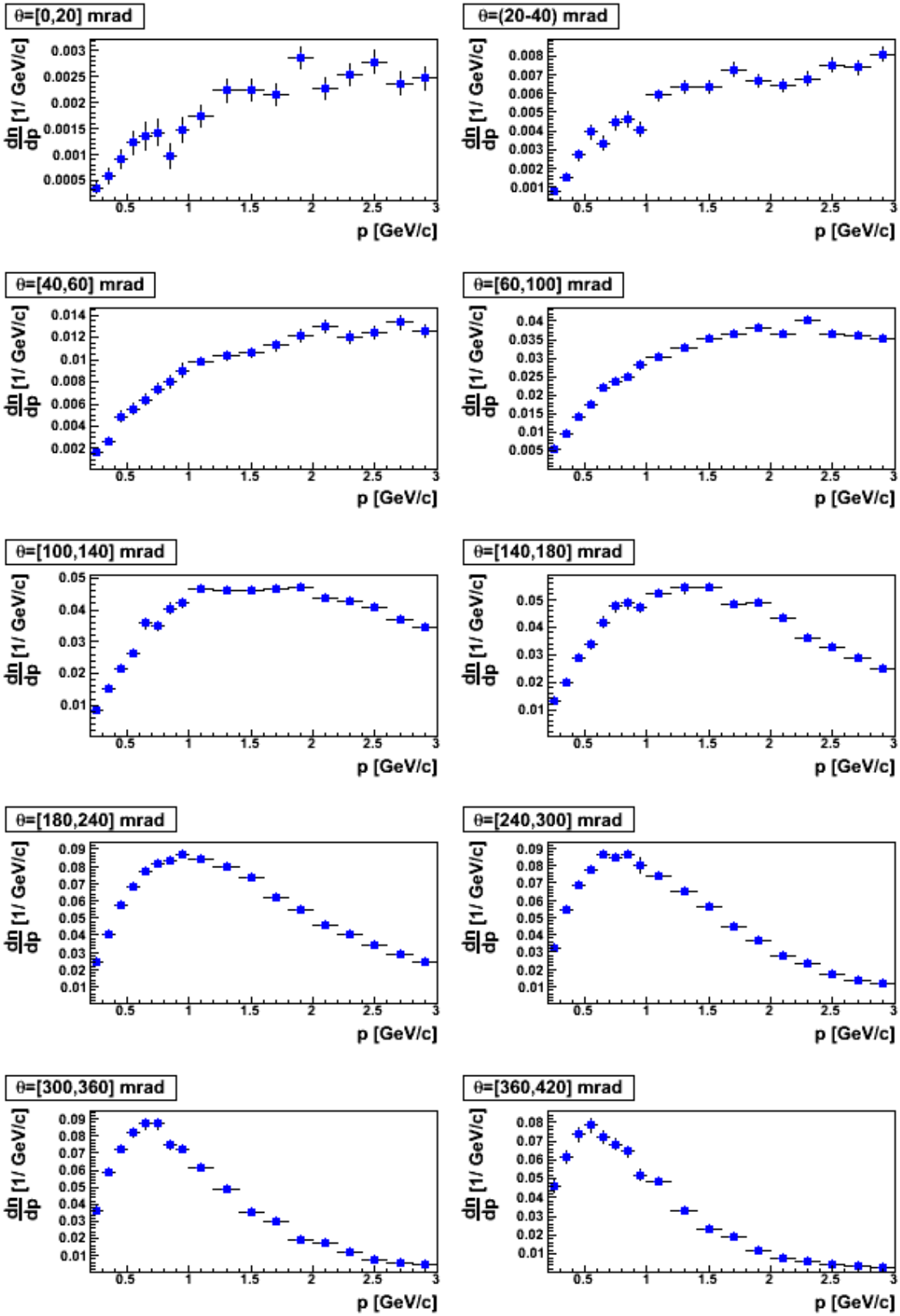

Figure 8.5: Mean π^- multiplicities in p+C interactions at 31 GeV/c , presented as a function of laboratory momentum (p) in different intervals of polar angle (θ). Error bars indicate only statistical uncertainties.

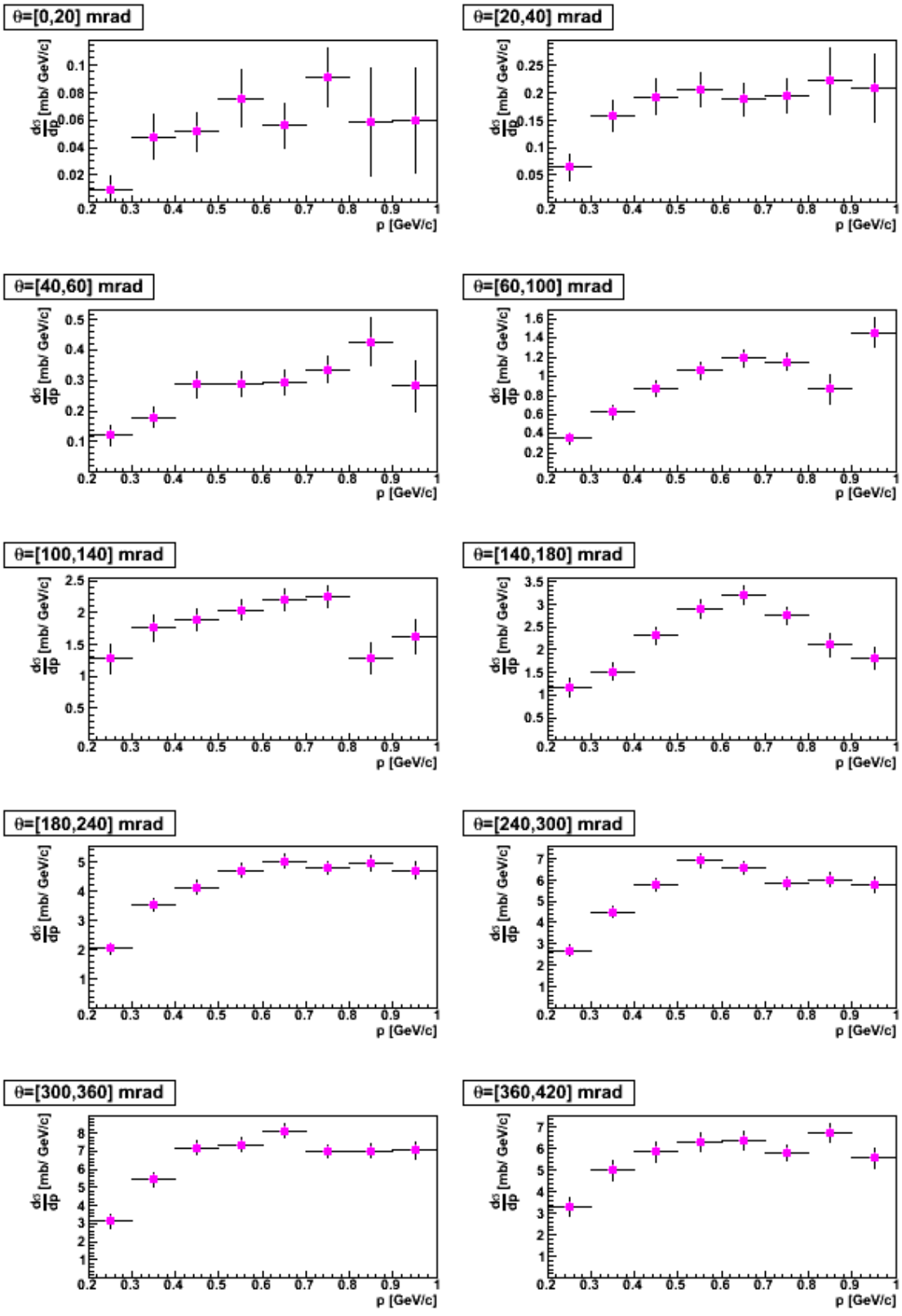

Figure 8.6: Differential cross sections for low momentum proton production in p+C interactions at 31 GeV/c , presented as a function of laboratory momentum (p) in different intervals of polar angle (θ). Error bars indicate only statistical uncertainties.

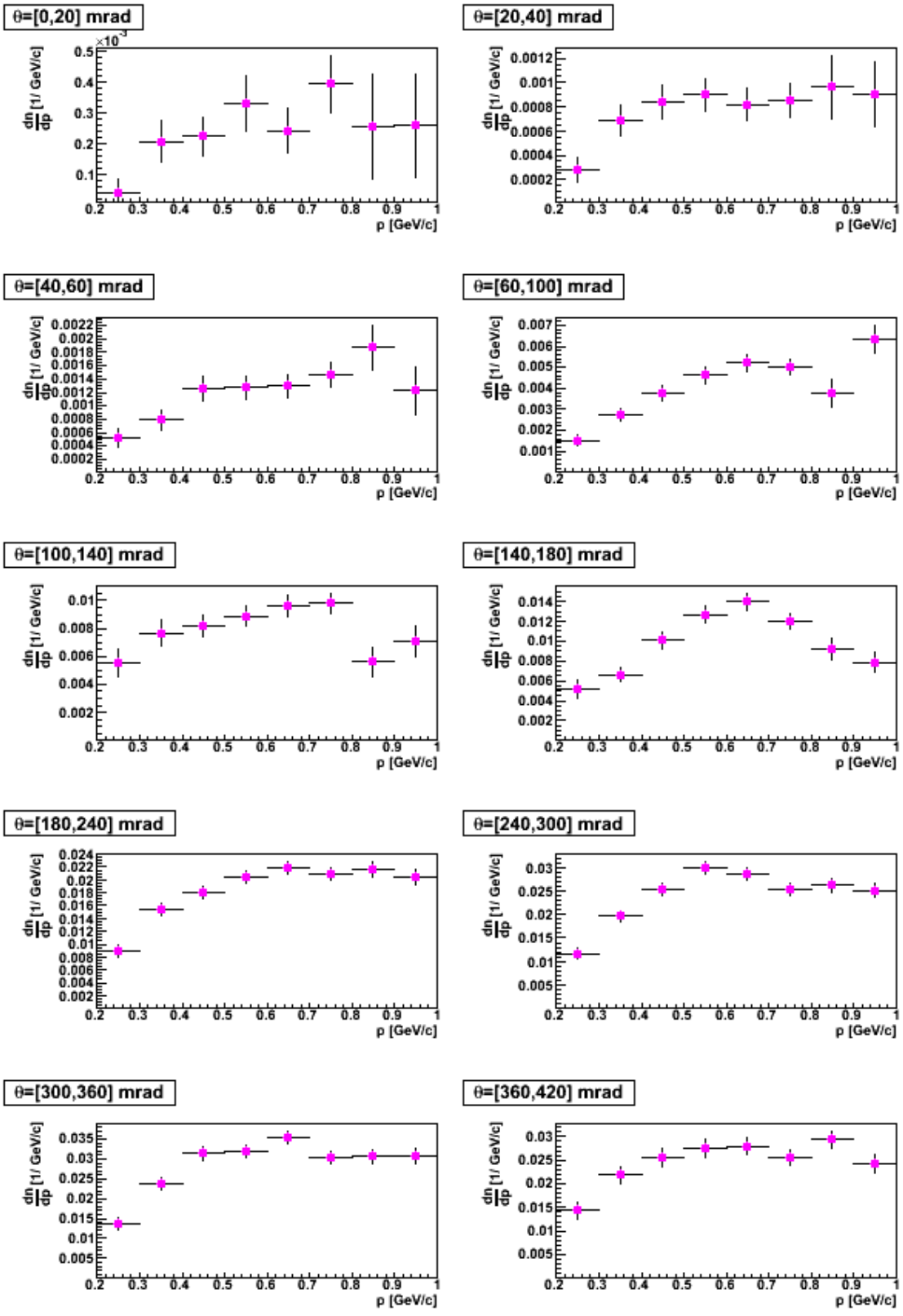

Figure 8.7: Mean proton multiplicities in p+C interactions at 31 GeV/c , presented as a function of laboratory momentum (p) in different intervals of polar angle (θ). Error bars indicate only statistical uncertainties.

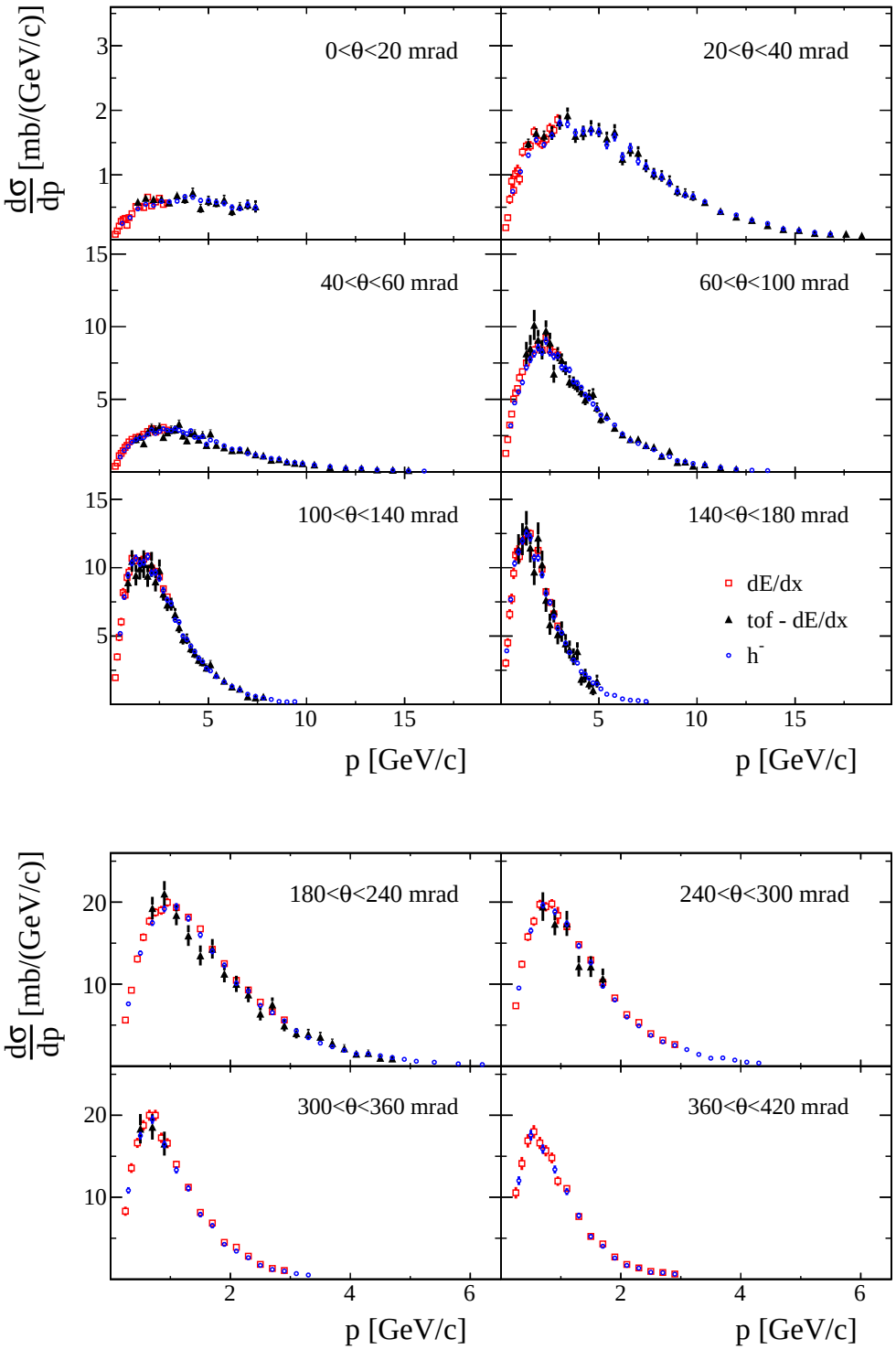

Figure 8.8: Differential cross sections for π^- meson production in p+C interactions at 31 GeV/c . The spectra are presented as a function of laboratory momentum (p) in different intervals of polar angle (θ). Results obtained using three analysis methods are presented by different symbols: blue open circles, h^- analysis; red open squares, *dE/dx* analysis; and black full triangles, *tof - dE/dx* analysis. Error bars indicate only statistical uncertainties. Figure taken from Ref. [1].

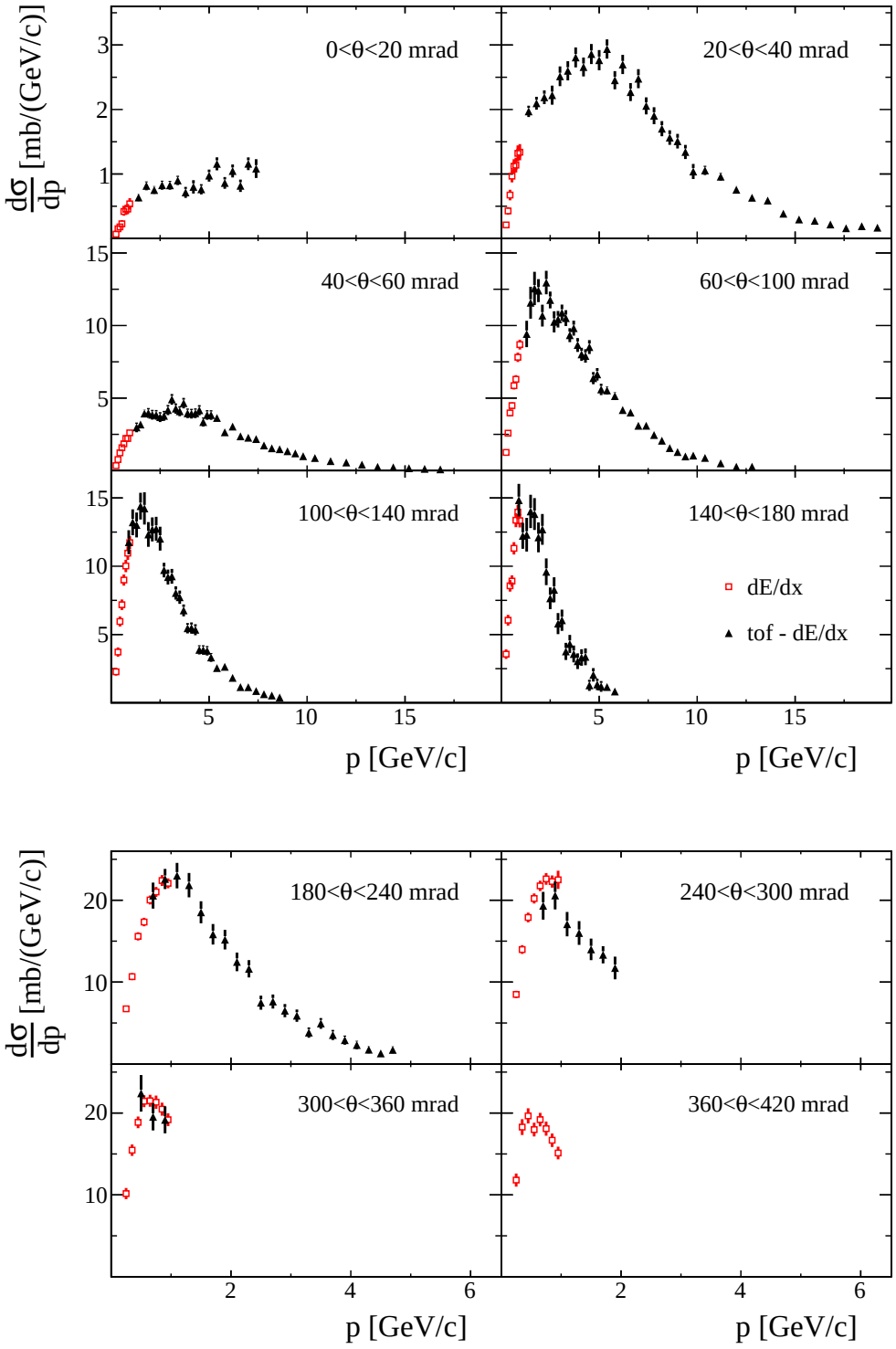

Figure 8.9: Differential cross sections for π^+ meson production in p+C interactions at 31 GeV/c . The spectra are presented as a function of laboratory momentum (p) in different intervals of polar angle (θ). Results obtained using two analysis methods are presented by different symbols: red open squares, *dE/dx* analysis, and black full triangles, *tof - dE/dx* analysis. Error bars indicate only statistical uncertainties. Figure taken from Ref. [1].

Chapter 9

Studies of systematic errors

At the beginning we should mention that statistical errors on the particle yields include contributions from the finite statistics of data and Monte Carlo (MC) simulation used to obtain the correction factors (see Chapter 7). The MC statistics was about 10 times larger than the data statistics so the total statistical errors are dominated by the statistical uncertainty of the data.

This chapter is devoted to discussion of systematic error studies. At first vital sources of systematics which are taken into consideration are introduced. Later on detailed discussion of each contributor to the systematics is presented. At the end of the chapter we show total error evaluated for both charged pion mesons and protons.

9.1 Sources of systematic uncertainties

The main contributors to the systematic uncertainties have several different sources. They are based on:

- The uncertainty of *feed-down* corrections for secondary interactions and for weak decays of strange particles, (see Sec. 7.3.4 on page 101). We assigned an uncertainty of 30% of the correction for both sources. For further information the reader is referred to review next section.
- Comparison of results obtained with different track topologies, *i.e.* RST and WST sample. All details of this studies may be found in Sec. 9.1.2.
- Methods used for particle identification described in Chapter 6. The procedure used for identification of charged pion mesons and protons was not exactly the same. These differences will result in various approach used to evaluate systematic errors for discussed particles type, see Sec. 9.1.3.

9.1.1 Feed-down from weak decays and secondary interactions

The dominant impact to the systematic error comes from the uncertainty on *feed-down* correction from weak decays and secondary interactions introduced in Sec. 7.3.4 on page 101. As a reminder, corrections on *feed-down* were calculated with formula (see Eq. (7.8)):

$$C_{fd} = \frac{1}{1+x} \tag{9.1}$$

where x is the ratio between *reconstructed* secondary and primary particles ($x = \frac{n_{rec,sec}}{n_{rec,prim}}$). We assumed that uncertainty in the ratio is known within 30% ($dx/x = 0.3$). This value is

used also for other analyses, namely *tof - dE/dx* and h^- introduced in Sec. 4.7 on page 57. Evaluation of systematic error from *feed-down* (refereed to as dC_{fd}) was calculated as follows:

$$dC_{fd} = \frac{dx}{(1+x)^2} \tag{9.2}$$

Thus the relative systematic error from *feed-down* (denoted as f) is equal to:

$$f \equiv \frac{dC_{fd}}{C_{fd}} = \frac{dx}{(1+x)} = \frac{0.3 \cdot x}{(1+x)} \tag{9.3}$$

An example plot of relative systematics coming from *feed-down* is shown in Fig. 9.1 for π^+ and π^- and protons, respectively. As we have learned in Sec. 7.3.4 on page 101 the error f is expected to have larger impact on π^+ than on its charge opponent. As seen in Fig. 9.1 the size of f is maximal for low production angle intervals for both charges and it is decreasing with polar angle and momentum. For example, if we take $\theta = [20, 40]$ mrad and $p = [0.2, 0.3]$ GeV/c calculated f is at the level of $\sim$10% for π^+, whereas for π^- its already $\sim$19%. In the same momentum bin but for the largest polar angle interval (*i.e.* $\theta = [360, 420]$ mrad) the size of the systematic uncertianity resulted from *feed-down* is only $\sim$4% for π^+, and $\sim$10% for π^-. Moreover, as the momentum is increasing the uncertainty is becoming very small and in particular is reaching only $\sim$2% for π^+ and is almost independent on θ angle. Clearly there is a similarity between *right* plot shown in Fig. 7.12 on page 104 and *right* plot in Fig. 9.1. In both figures we observe momentum dependence of a type $1/p$ (see Sec. 7.3.4 on page 101). As far as protons are concerned, very similar uncertainty in f from *feed-down* corrections is seen. Mostly we get $10 - 12\%$ value on f almost in all polar and low momentum intervals, excluding first momentum bin.

At the end one has to keep in mind that amongst all particles the π^+ mesons are of major interest for the T2K neutrino beam simulations and luckily we observe the smallest systematic uncertainties coming from *feed-down* corrections for these particles.

9.1.2 Reconstruction effect studied by comparison of RST and WST track topologies

We wanted to check how results obtained using two independent subsamples of tracks, namely RST and WST, compare. As already shown RST and WST are measured in different experimental situations. In particular WST often transverse different detectors unlike the RST (see Fig. C.1 on page 147). Therefore we assume that observed difference between them will account for uncertainties coming from track reconstruction (named as *track reconstruction*). The analysis procedure requires several consecutive steps. They are as follows.

1. Preparation of both samples of RST and WST for data and MC. This point needs selection of given track topology corresponding to their definitions, see Sec. 5.3 on page 66. Next we need to apply the same event and track selection criteria defined in Chapter 5 together with described, in Sec. 7.2.1 on page 92, ϕ - *wedge* cut.

2. Identification of RST and WST samples as π^+, π^- or protons. This procedure is performed independently for both track topologies. For this purpose we use exactly the same approach for given particle type, as explained in details in Chapter 6. Once we have identified RST and WST charged pion and proton spectra we may proceed further.

3. Evaluation of corresponding *global* MC corrections separately for RST and WST for given particle species and calculation of corrected particle spectra. We are following the approach introduced in Sec. 7.3 on page 99.

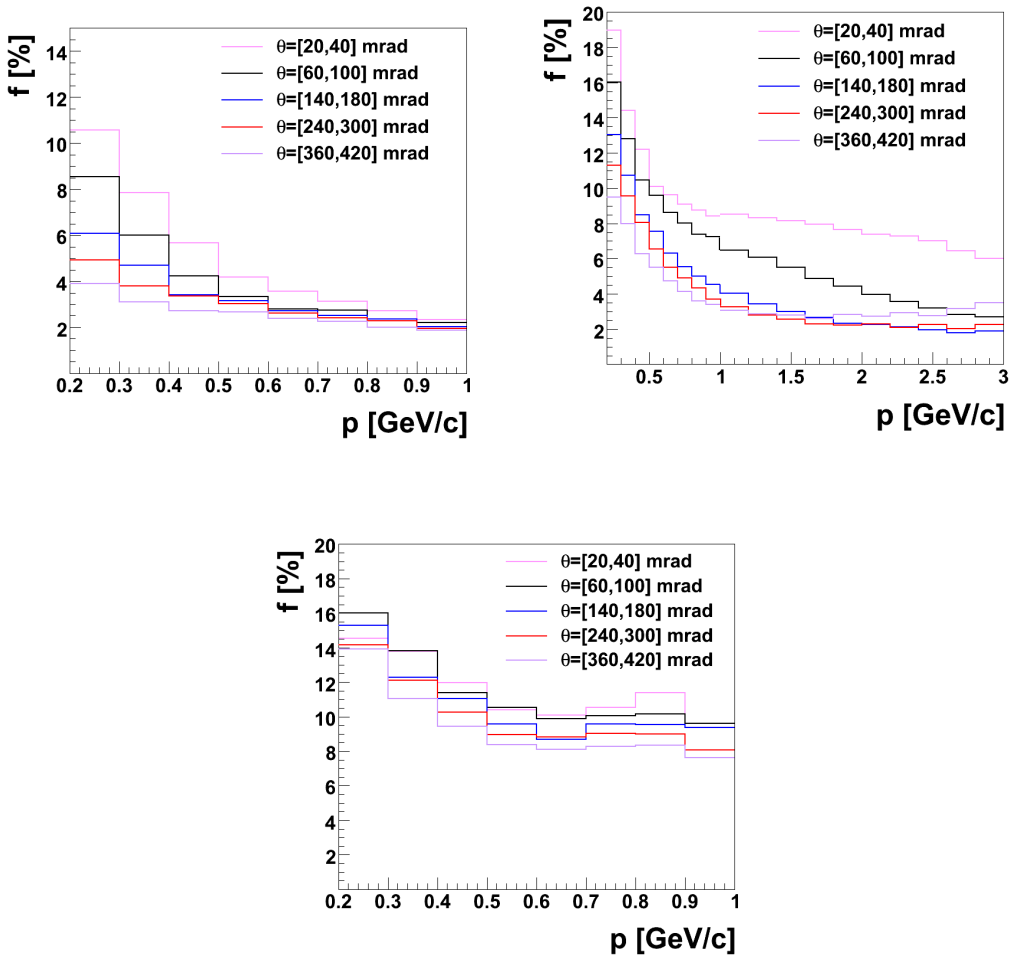

Figure 9.1: Percentage systematic error (f) coming from *feed-down* contamination evaluated for π^+ *(left)*, π^- *(right)* and protons *(lower)*. Example plots are prepared for several production angle bins starting from $\theta = [40, 60]$ mrad.

In this approach we check mainly reconstruction efficiency especially at the edges of the projection chambers that are mostly populated by WST sample. Once we have obtained corrected, normalized to inclusive cross sections spectra for given particle type and for both track topologies we check how consistent they are with each other. As an estimate of relative systematic error we define for each bin (p, θ) the ratio t as follows:

$$t \equiv \frac{|\sigma_{RST,\alpha} - \sigma_{WST,\alpha}|}{2\sigma_\alpha} \tag{9.4}$$

where $\sigma_{RST(WST),\alpha}$ stands for the cross section value corresponding to RST (WST) particle type α, whereas σ_α represents final cross section of π^+, π^- or protons obtained with total sample of tracks. Graphical example of the method is shown in Figs.[9.2 – 9.4] for π^+, π^- and protons, respectively. We decided to present several polar angle intervals starting from $\theta = [40, 60]$ mrad. The first and the third panel row in each figure illustrates the measured inclusive cross sections for given particle type for all tracks (*black*) as well as RST (*pink*) and WST (*blue*) samples. The second and the fourth panels give the corresponding percentage

ratio t. We see that statistical errors on t in momentum bins are generally larger than $|t|$ values and therefore for each angular bin we fit a constant $p0$ which gives an average percentage systematic error value coming from *track reconstruction*, separately for each bin (p, θ). The value of fitted parameter $p0$ is quoted at each plot and graphically illustrated with the red line. For both charged pion mesons we observe mostly consistent results obtained with different track topology. The comparison studies show that the contribution to total systematic error coming from *track reconstruction* is on average at the level of few %. On the other hand if we look at the comparison of spectra obtained for protons the situation is worse. Here we observe much larger discrepanicies between RST and WST which results in value of fitted parameter $p0 \simeq 19.5\%$ for the first example polar angle bin. As we increase the θ interval observed differences are getting smaller. One of the reasons of such large discrepancies is the fact that we deal with very limited statistics for the identified number of protons especially for low angle and momentum regions. If we divide the sample further into RST and WST the situation is getting worse. We decided to set a limit on number of identified protons for each sample in selected cell to be larger than 10. This is the reasons why for some points we do not observe results from RST or WST. This problem is less significant as we increase polar angle bin.

9.1.3 Uncertainties coming from particle identification

In order to estimate systematics coming from *particle identification* procedure we decided to apply approach consistent with the method used for given particle type. Thus, evaluation of the source of systematic uncertainty was performed differently for protons and both charged pion mesons. At first we will introduce impact on systematics valid for $\pi^{\pm}$. As stated in Sec. 6.6 on page 82 charged pion mesons were identified with *maximum likelihood* method. In this approach information on precise BB parametrization is crucial (see Appendix B). We decided to move BB curves and see what impact this change will have on the number of identified $\pi^{\pm}$. One has to remember that before particle identification we fit BB parametrization to the data at the very beginning of the analysis procedure, see Sec.4.4 on page 48, in order to have BB curves corresponding to the measured energy loss. Afterwords, still additional shifts of the curves may be performed. We moved BB curves for $\pm 1\%$. This value was adjusted while comparing the expected distributions of energy loss $\mathrm{dE/dx}_{theor}$ for pions with measured ones (for example see Fig. 6.10 on page 81) for which energy loss is mostly around 1 mip and is already constant in the momentum region of interest. Naturally for larger *dE/dx*, *i.e.* *dE/dx* >3-4 mip where mainly protons are seen we have larger differences that used $\pm 1\%$ but for protons we will use slightly different approach discussed further, in order to estimate systematics coming from *particle identification*.

For this study we define percentage ratio (p_{BB}):

$$p_{BB} \equiv \frac{n_{iden,BB,\pi^{\pm}}}{n_{iden,\pi^{\pm}}} \tag{9.5}$$

where $n_{iden,BB,\pi^{\pm}}$ represents number of identified $\pi^{\pm}$ while BB curves are moved by $\pm 1\%$, while $n_{iden,\pi^{\pm}}$ gives the number of identified charged pion mesons.

Clearly BB calibration uncertainty is important only for the momentum bins where BB curves for two particle hypothesis cross each other. In particular a difficult p region in [0.9-1.6] GeV/c where BB for kaons crosses that for pions. The kaon relative abundance is very low which causes additional instability in the fit. Therefore we looked for a conservative estimate of error on pions in this momentum range allowing the kaon abundance m_k to change within 0-0.5%. The limit was adjusted while studying neighbouring bins with p=[0.7-0.9] GeV/c,

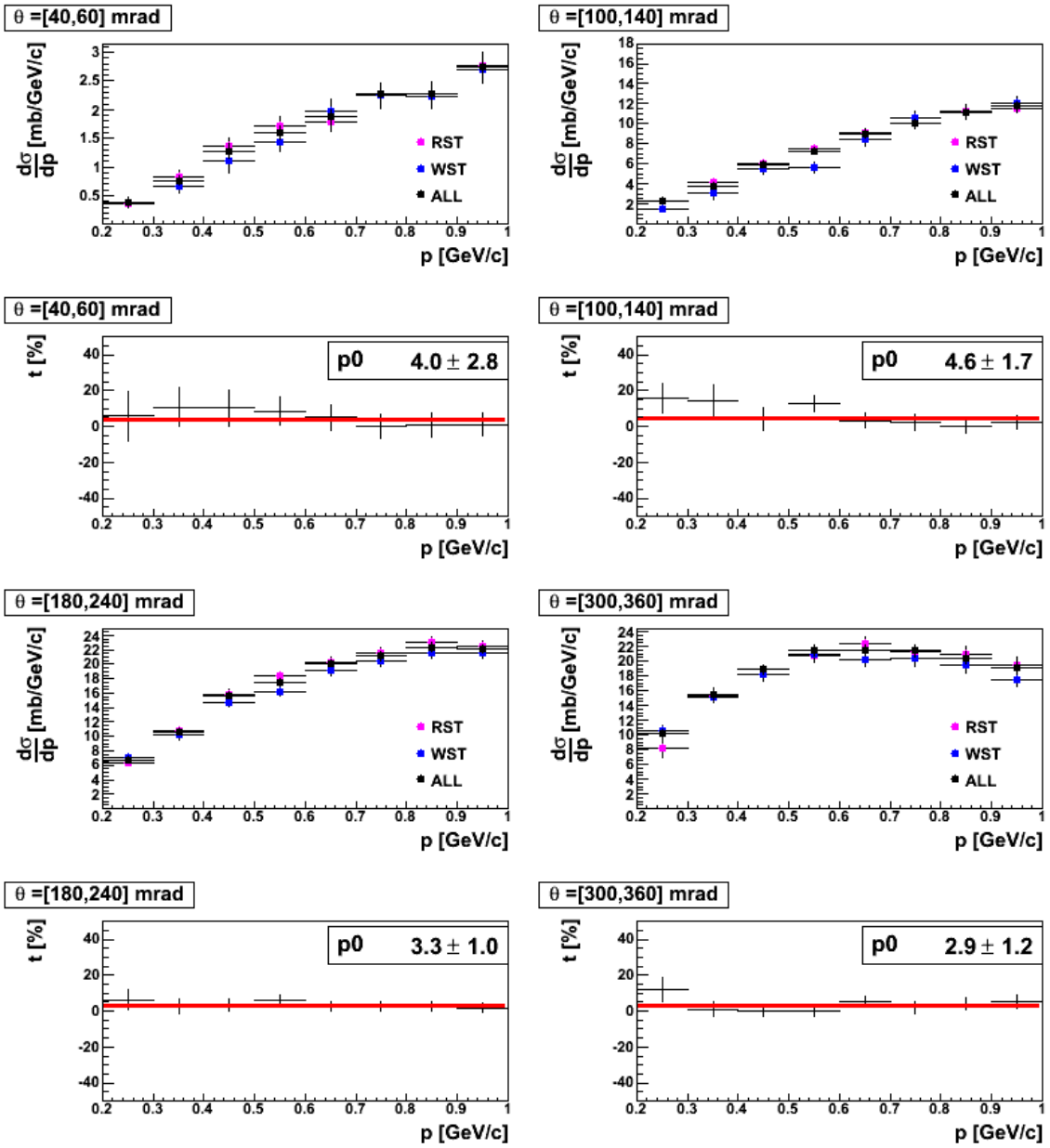

Figure 9.2: An example of percentage systematic error (t) coming from *track reconstruction* evaluated for π^+. The first and the third panel rows show cross section measurements obtained for all π^+ tracks (*black*) as well as RST (*pink*) and WST (*blue*) samples. The second and the fourth panel rows show percentage systematic error (t) for given polar angle intervals. Value of fitted parameter $p0$, which defines the average percentage systematic error in selected bin of θ, is quoted at each plot and graphically illustrated with the of red line. The example plots are prepared for several production angle bins starting from $\theta = [40, 60]$ mrad.

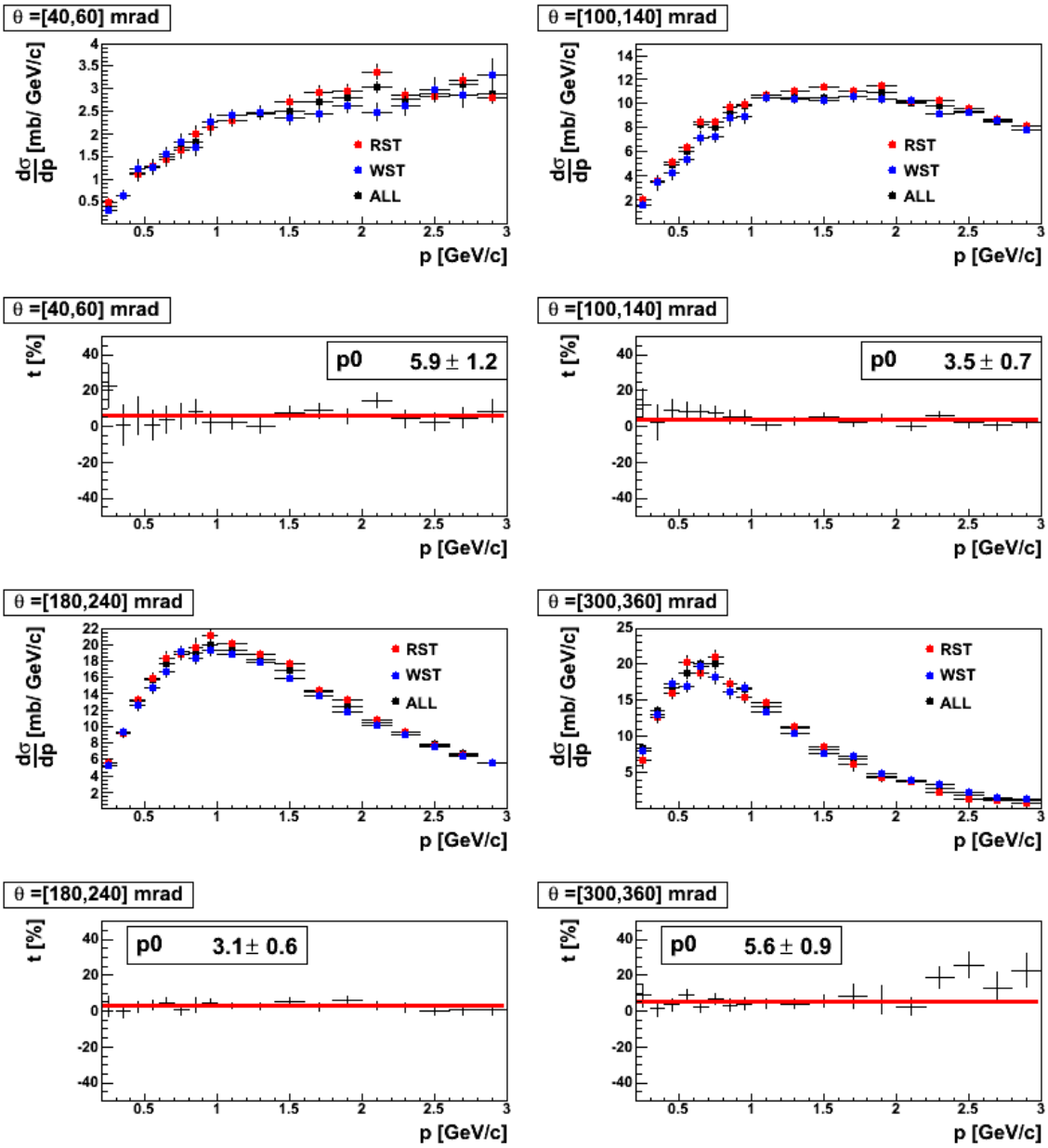

Figure 9.3: An example of percentage systematic error (t) coming from *track reconstruction* evaluated for π^-. The first and the third panel rows show cross section measurements obtained for all π^- tracks (*black*) as well as RST (*pink*) and WST (*blue*) samples. The second and the fourth panel rows show percentage systematic error (t) for given polar angle intervals. Value of fitted parameter $p0$, which defines the average percentage systematic error in selected bin of θ, is quoted at each plot and graphically illustrated with the of red line. The example plots are prepared for several production angle bins starting from $\theta = [40, 60]$ mrad.

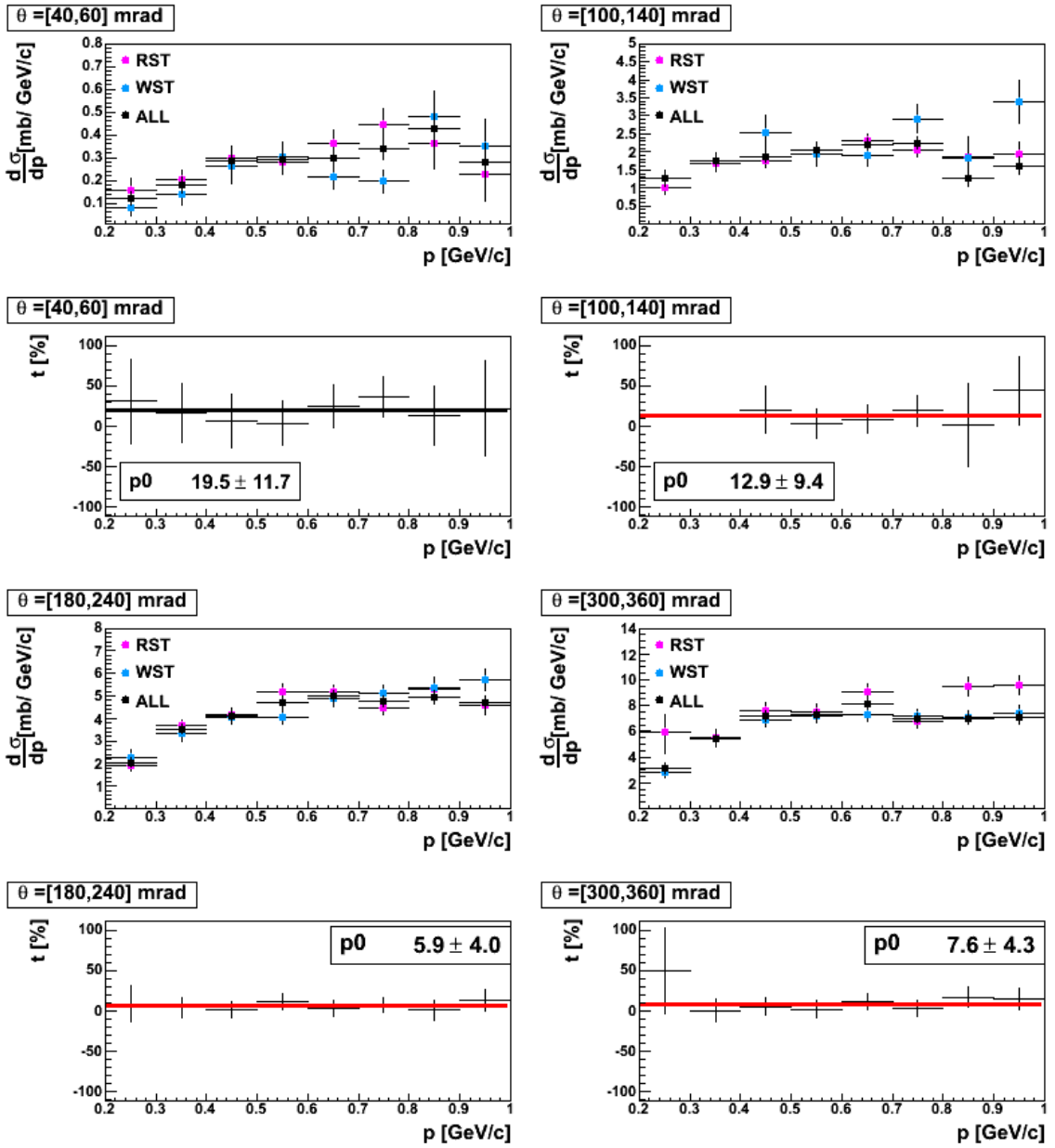

Figure 9.4: An example of percentage systematic error (t) coming from *track reconstruction* evaluated for protons. The first and the third panel rows show cross section measurements obtained for all protons tracks (*black*) as well as RST (*pink*) and WST (*blue*) samples. The second and the fourth panel rows show percentage systematic error (t) for given polar angle intervals. Value of fitted parameter $p0$, which defines the average percentage systematic error in selected bin of θ, is quoted at each plot and graphically illustrated with the of red line. The example plots are prepared for several production angle bins starting from $\theta = [40, 60]$ mrad.

where returned m_k was not larger that 0.1 %. This time ratio (p_{m_K}) is defined as:

$$p_{m_K} \equiv \frac{n_{iden,m_K,\pi^\pm}}{n_{iden,\pi^\pm}} \tag{9.6}$$

where $n_{iden,m_K,\pi^\pm}$ represents a fitted number of identified $\pi^\pm$ with 0.5% limit set on the fitted relative kaon fraction.
One has to keep in mind that both results p_{BB} and p_{m_K} are correlated. In this situation as the final value of systematic coming from identification procedure (denoted as p_f) we decided to take a result with the larger value ($p_f \equiv max[p_{BB}, p_{m_K}]$).

In Fig. 9.5 we illustrate how the final p_f looks like for π^+ and π^-, respectively. Examples are shown for selected polar angle intervals.

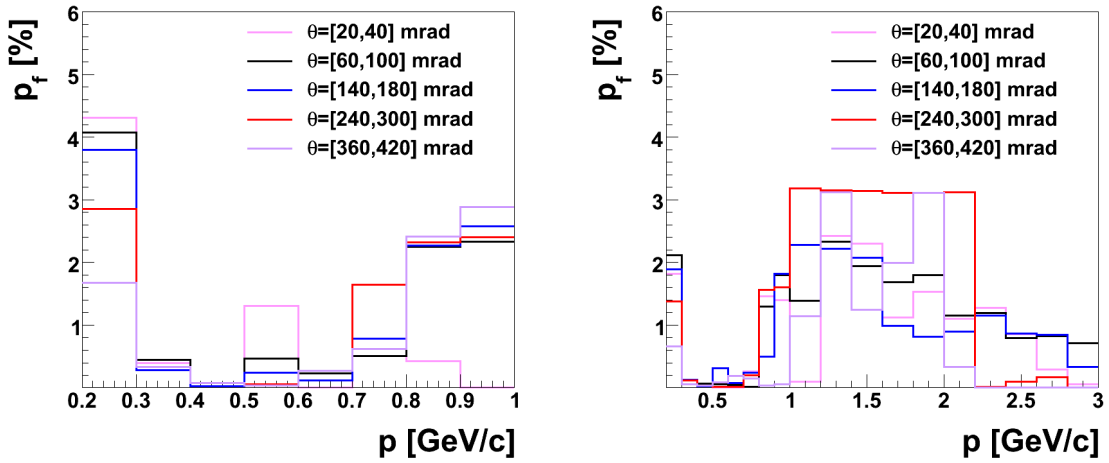

Figure 9.5: Systematic error p_f coming from *particle identification* evaluated for π^+ *(left)* and π^- *(right)*. Example plots are prepared for several production angle bins starting from $\theta = [20, 40]$ mrad.

As far as protons are concerned, we have to take into account two facts. The first is that *particle identification* for protons with $p \leq 0.7$ GeV/c is straightforward as they are well separated from competitors. Thus no systematic error coming from *particle identification* is assumed in this momentum region. The second deals with the procedure of *maximum likelihood* method. In order to correct number of identified protons we rely on the number of electrons N_{e^-} obtained from the fit performed to negatively charged particles. The studies show that number of electrons and positrons is known within ±5% (see Sec. 6.7 on page 85). We changed the number of electrons by ±5% and checked how it influences the number of identified protons. This time the ratio on *particle identification* for protons is defined as:

$$p_f \equiv \frac{n_{iden,N_{e^-}\pm 5\%}}{n_{iden,protons}} \tag{9.7}$$

where $n_{iden,N_{e^-}}$ stands for the new number of identified protons and $n_{iden,protons}$ is the final number of identified protons. The results of this study are shown in Fig. 9.6. Only for the last three momentum bins we have input from the *particle identification* method to the total systematics. On average the percentage error p_f for protons is observed to be at the level of 5-8% depending on production θ angles.

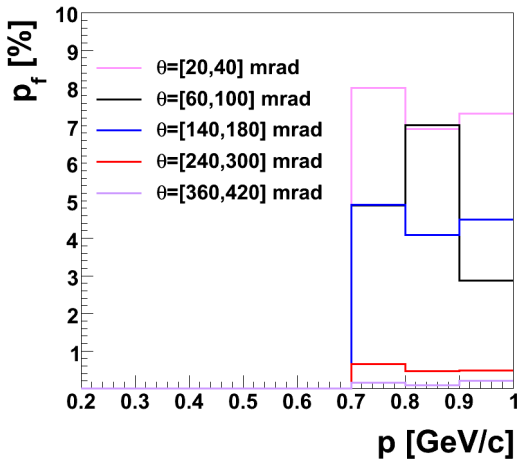

Figure 9.6: Systematic error p_f coming from *particle identification* procedure applied to protons. Example plot is prepared for several production angle bins starting from $\theta = [20, 40]$ mrad.

Detailed discussion of all sources of uncertainties and their impact on the total error is presented in the next section.

9.2 Total error calculation

The total systematic error was calculated as a sum of different contributions added in quadrature. It does not include the overall uncertainty due to the normalization procedure (see Sec. 8.2 on page 109), namely 2.5% and 2.3% for the normalization of the inclusive cross section and mean particle multiplicity in production events, respectively. Statistical and systematic uncertainties were added in quadrature in order to calculate the total error. In Figs.[9.7 – 9.9] we illustrate percentage total error (*red*) calculated for all production angle intervals for π^+, π^- and protons, respectively. In all plots the final systematic error (*yellow*) is separated into its partial ingredients: *feed-down* (*velvet*), *track reconstruction* (*blue*) and *particle identification* (*green*). Impact of statistical uncertainty (*black*) is shown as well. At first let us focus on comparison between both pion charges. Generally for small intervals of θ the statistical errors dominate. What concerns systematics particle identification appears to be the least important source of systematic uncertainty. Moreover, in all production angle bins we observe that total error is smaller for π^+ in comparison to π^-. On average it is at the level of $\simeq$5-10% while negatively charged pions have yields uncertainties by $\simeq$10-15% especially for the low production angle region, where systematic error originated from *feed-down* dominates completly. When we look at the total error evaluated for protons we come to the conclusion that it is much larger that for both meson charges. At low production angle the main contributor is the statistical error. As θ angle becomes larger we observe systematics to dominate. Here as the main source we notice *track reconstruction* as well as *feed-down*. In case of two production angles and momentum intervals we decided to modify the value of systematic error from *track reconstruction*. This is seen for $\theta = [100, 140]$ mrad and $p = [0.8, 0.9]$ GeV/c as well as $\theta = [300, 360]$ mrad and $p = [0.2, 0.3]$ GeV/c where observed differences in RST and WST samples were too large to express them by the same value used for the whole angle

bin. We excluded these points from the $p0$ parameter fit and used the observed differences as values of systematic errors coming from *track reconstruction*.

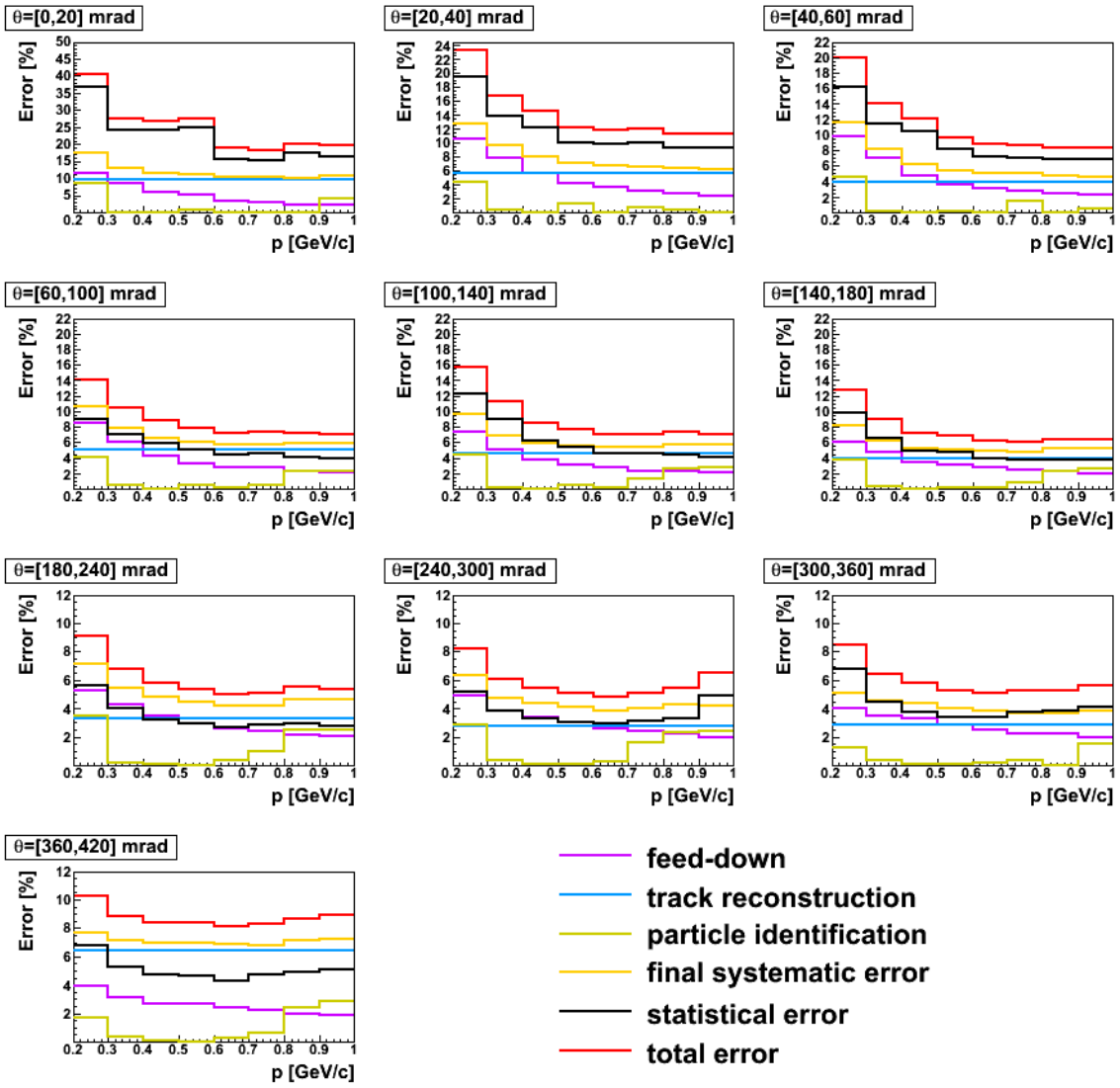

Figure 9.7: Total error (*red*) coming from final systematics (*yellow*) and statistical uncertainties (*black*) evaluated for low momentum π^+. In all plots final systematic errors are separated into their partial ingredients: *feed-down* (*velvet*), *track reconstruction* (*blue*) and *particle identification* (*green*).

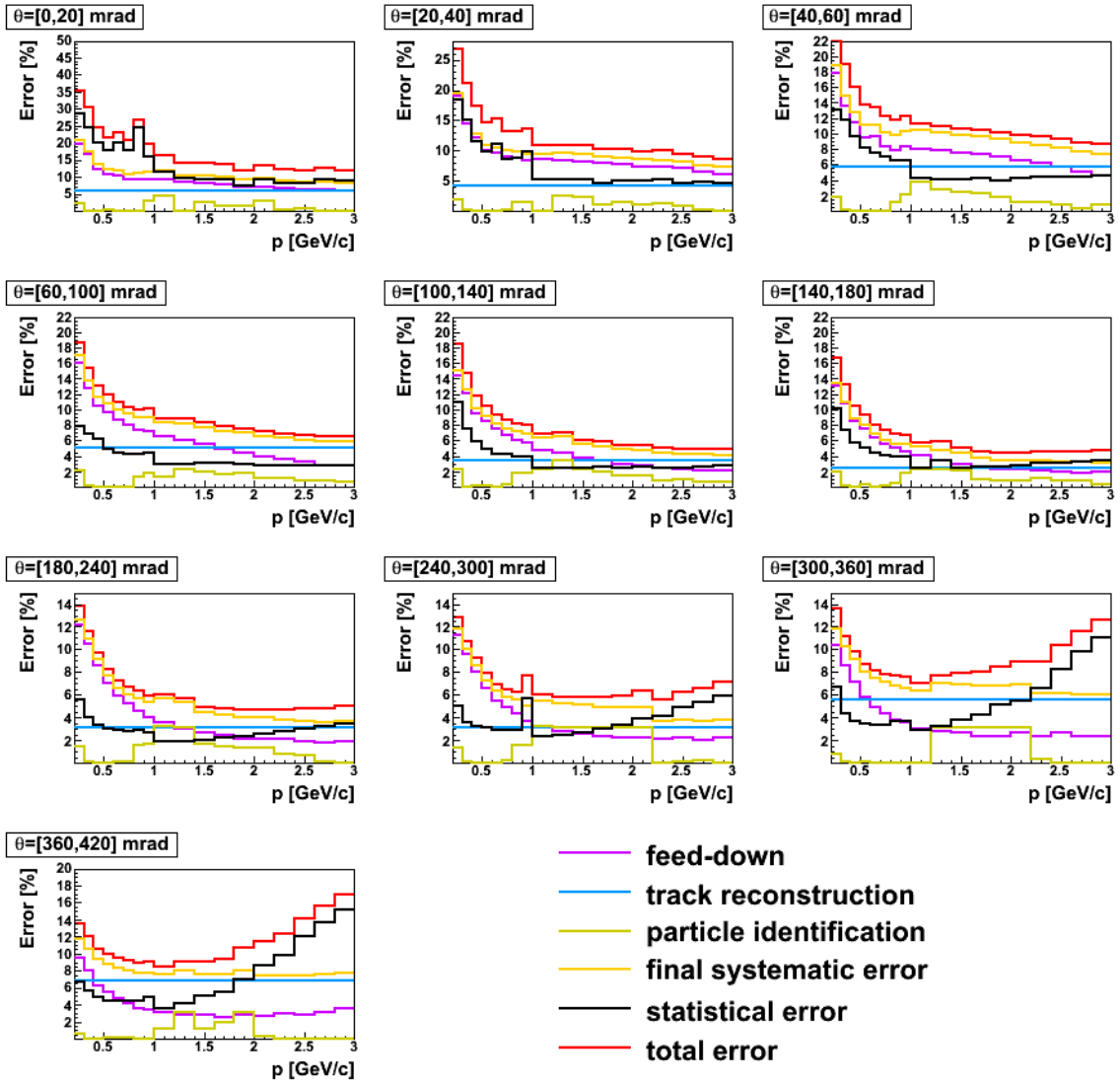

Figure 9.8: Total error (*red*) coming from final systematics (*yellow*) and statistical uncertainties (*black*) evaluated for low momentum π^-. In all plots final systematic errors are separated into their partial ingredients: *feed-down* (*velvet*), *track reconstruction* (*blue*) and *particle identification* (*green*).

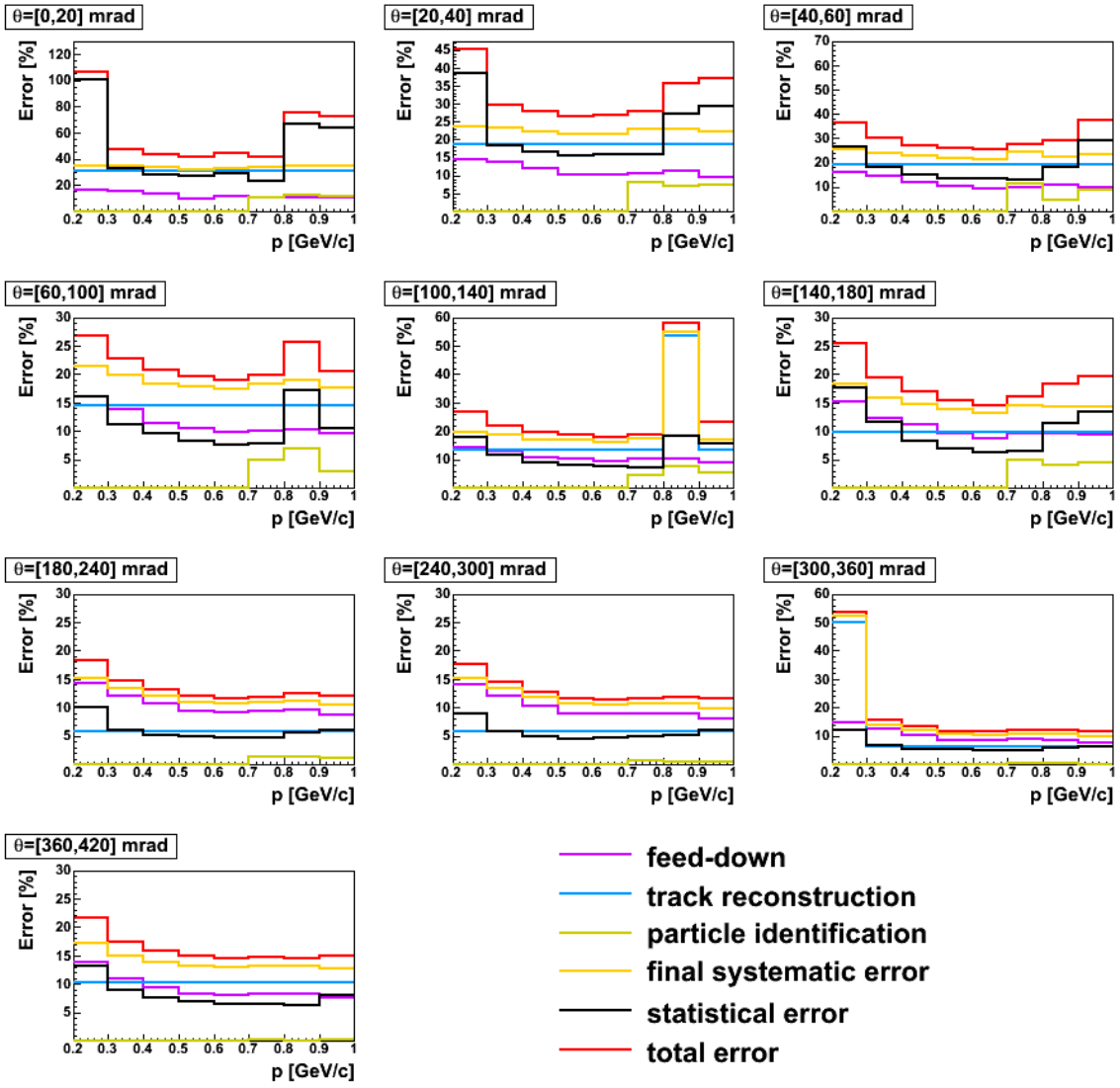

Figure 9.9: Total error (*red*) coming from final systematics (*yellow*) and statistical uncertainties (*black*) evaluated for low momentum protons. In all plots final systematic errors are separated into their partial ingredients: *feed-down* (*velvet*), *track reconstruction* (*blue*) and *particle identification* (*green*).

Chapter 10

Impact of the NA61 results on the T2K beam simulation

JNUBEAM T2K beam simulation package uses models to generate hadrons produced by the proton beam on carbon target. The neutrino flux and spectrum depends on the applied model and varies beyond the needed accuracies. Therefore at first, we present how the NA61 measurements compare with different hadron production models. The results of these studies have important influence of the JNUBEAM simulation of the T2K neutrino beam which is explained in detail in the last section of this chapter.

10.1 Comparison of NA61 results to model predictions

At the beginning we have to point out that for the purpose of a comparison of the data with model predictions the spectra were normalized to the mean $\pi^{\pm}$ or protons multiplicity in production interactions (see Sec. 8.2 on page 109). This approach allowed to avoid uncertainties due to the different treatment of quasi-elastic interactions in models as well as problems due to the absence of predictions for inclusive cross sections.

The first comparisons with the model predictions were performed as soon as the preliminary NA61 results were released, *i.e.* in 2009. At that time no detailed studies of systematic uncertainties were yet performed. We assigned 20% of systematic error value to preliminary charged pion spectra, taking into account the largest discrepancies between results obtained using three different methods: low momentum *dE/dx*, *tof* - *dE/dx* and h^- analysis. Preliminary results on mean charged pion multiplicities were compared with predictions of GCALOR [73] used in JNUBEAM (see Sec. 2.5.2 on page 26) and FLUKA2008 [113], widely used simulation package. In Fig. 10.1 we present comparison of NA61 charged pion results (*black*) with GCALOR (*blue*) and FLUKA2008 (*red*) predictions. In botton plots corresponding ratios between measured NA61 data and given model are also shown. Example plots are chosen for two production angle intervals θ=[120,180] mrad *(left)* and θ=[180,240] mrad *(right)*.

In both plots in Fig. 10.1 FLUKA2008 predictions are in better agreement with measured NA61 data than those coming from GCALOR. This statement is valid for used production angle intervals for π^+ as well as for π^- mesons. As conclusion T2K decided to incorporate FLUKA2008 hadron production model in JNUBEAM simulations of the T2K neutrino beam and use it instead of its predecessor, *i.e.* GCALOR. In the meantime, we could work on finalizing all there analyses used to obtain charged pion spectra from 2007 data taking. In particular detailed studies of systematic uncertainties were performed, which in case of low

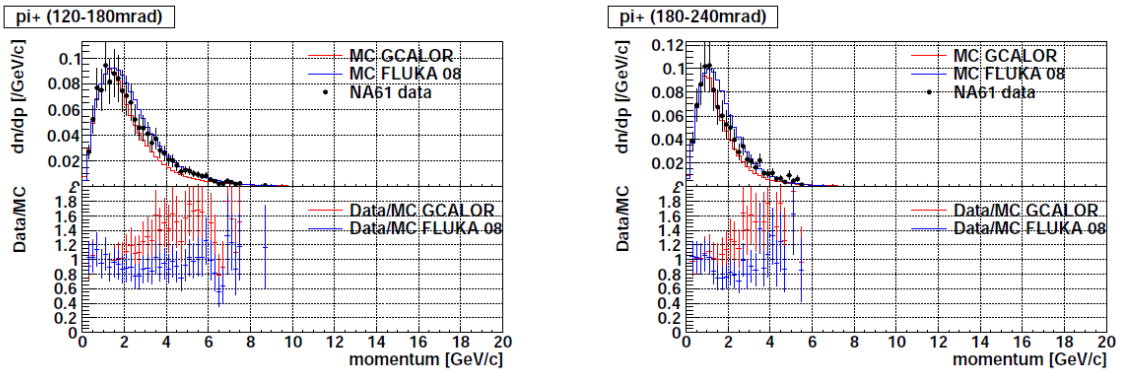

Figure 10.1: *Upper:* Comparison of preliminary results on mean π^+ multiplicity distributions with predictions of GCALOR and FLUKA2008. *Lower:* Ratio between NA61 data and GCALOR (red) as well as FLUKA2008 (blue) are also shown. The example plots are chosen for two production angle intervals θ=[120,180] mrad *(left)* and θ=[180,240] mrad *(right)*. Figure taken from Ref. [119].

momentum dE/dx analysis are the subject of Chapter 9. We were able to derive final spectra of π^+ and π^- meson with their total errors, *i.e.* errors resulted from statistical and systematic uncertainties added in quadrature. The comparison of the final spectra of charged pion meson in broad momentum range with different models may be found in Ref [1]. We focus here only on the low momentum region which was the subject for the analysis presented in this thesis. Thus, in Figs.[10.2, 10.3] we present mean multiplicities of π^+ and π^- obtained with dE/dx analysis at low momenta, respectively. Model predictions are based on: VENUS4.12 [107] - generator used in the NA61 simulation chain (see Sec. 7.1 on page 90), FLUKA2008 [113], URQMD 1.3.1 [114]. All listed models are part of the CORSIKA [115] framework for the simulation of air showers and are typically used to generate hadron-air interactions at energies below 80 GeV. There is one extra model available within CORSIKA framework, *i.e.*GHEISHA [116]. However, as already shown in [117], simulations completely fail to describe the NA61/SHINE measurements at all production angles and momenta.
While looking in Figs.[10.2, 10.3] we observe that mean charged pion multiplicities in low momentum are in good agreement with FLUKA2008 model. In case of VENUS4.12 predictions good agreement is also seen but this time for all production angle bins excluding those in $180<\theta<360$ mrad. The URQMD 1.3.1 model qualitatively disagrees with the measurements at low momenta and polar angles below about 140 mrad. In addition, we also show model predictions for low momentum mean proton multiplicities (see Fig. 10.4). None of the models describe the smaller proton yields for p <0.5 GeV/c. The best agreement is observed for the production angle range $\theta = [100, 360]$ mrad. For smaller as well as the largest polar angles, *i.e.* $\theta < 100$ mrad and $\theta > 360$ mrad we observe the predictions for all three models to be above the measured ones.

10.2 Impact of the NA61 results on the T2K beam simulation

The preliminary NA61 results of charged pion mean multiplicities measured during first pilot run in 2007 indicate the best agreement with FLUKA2008 model predictions, as shown in previous section. This conclusion was the first important input to the JNUBEAM simulation tool used by the T2K. Afterwards, FLUKA2008 became the only hadron production model

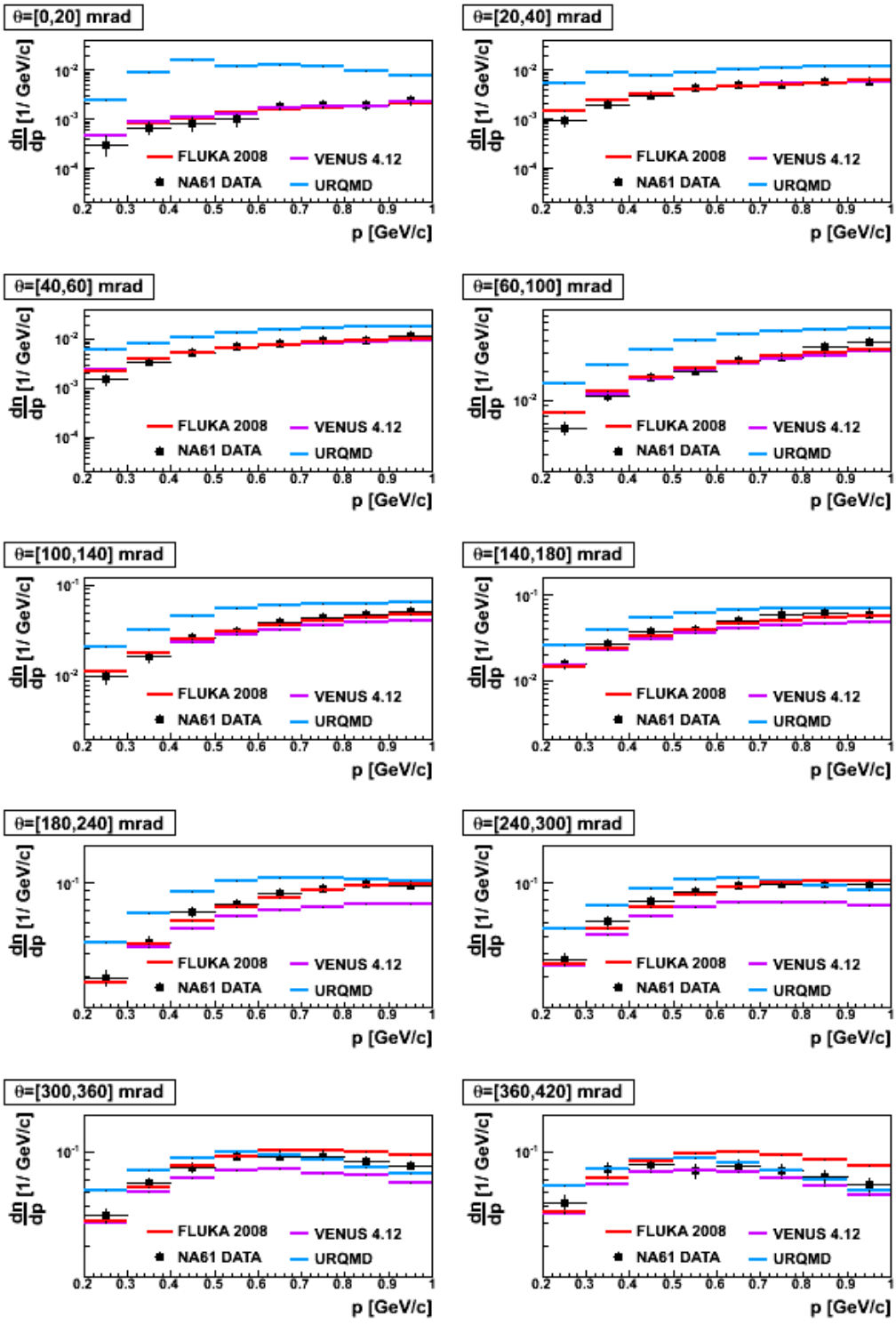

Figure 10.2: Comparison of the final low momentum mean π^+ multiplicities (*black*) with model predictions: FLUKA2008 (*red*), VENUS4.12 (*velvet*) and URQMD 1.3.1 (*blue*).

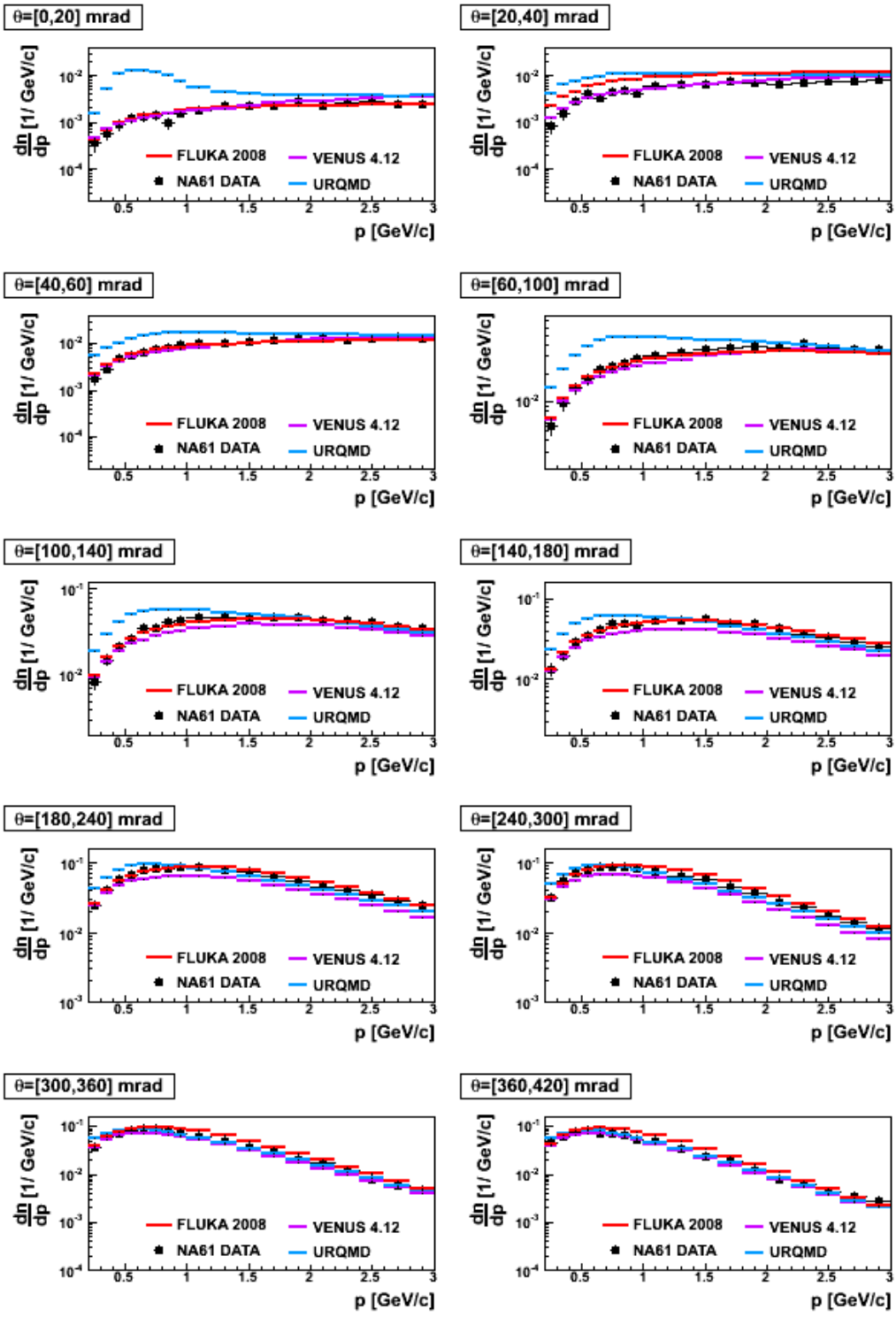

Figure 10.3: Comparison of the final low momentum mean π^- multiplicities (*black*) with model predictions: FLUKA2008 (*red*), VENUS4.12 (*velvet*) and URQMD 1.3.1 (*blue*)

.

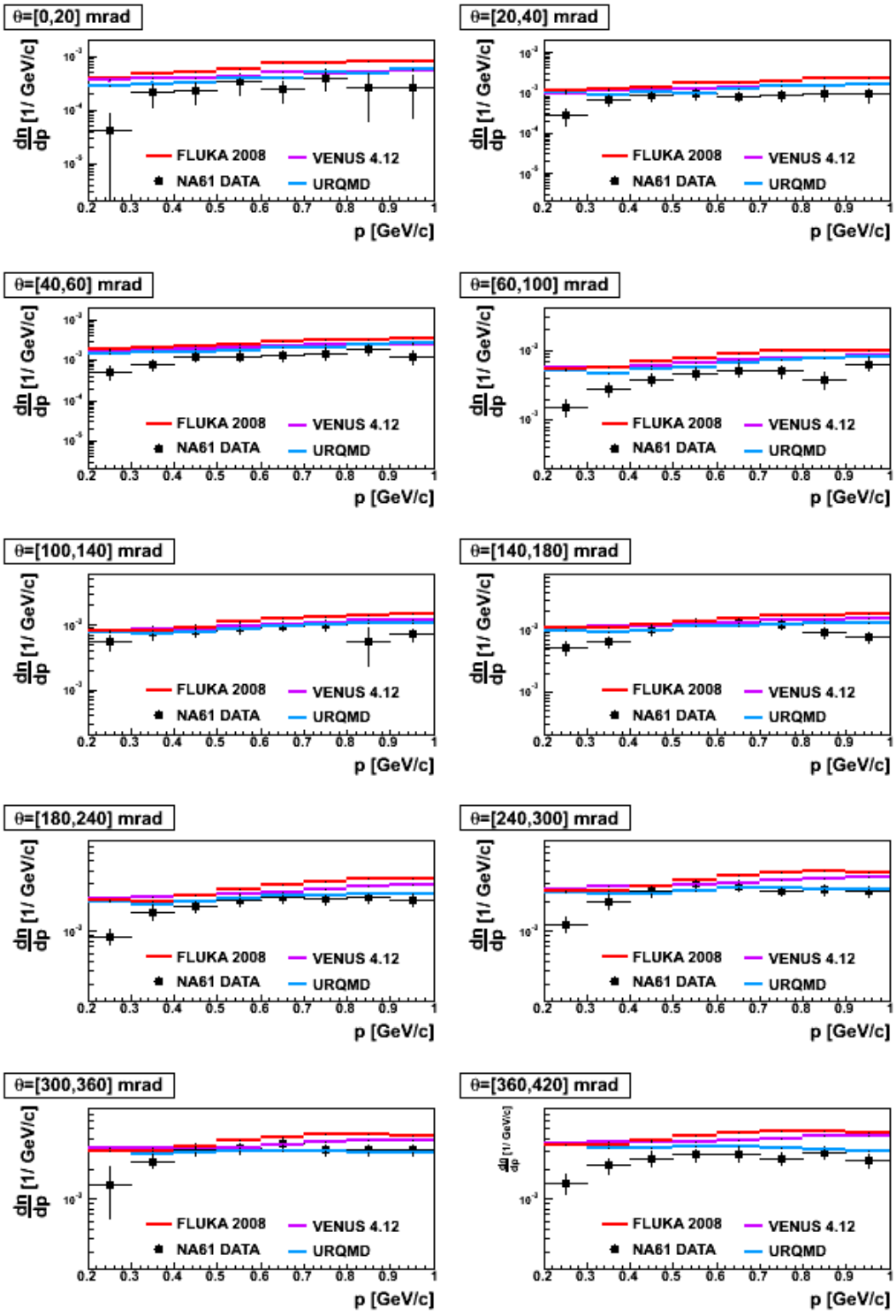

Figure 10.4: Comparison of the final low momentum mean proton multiplicities (*black*) with model predictions: FLUKA2008 (*red*), VENUS4.12 (*velvet*) and URQMD 1.3.1 (*blue*)

.

reliable enough to be used in the T2K neutrino beam simulation package. Next tuning of the results with updated JNUBEAM had to be performed with the help of the final NA61 results. The tuning was applied to distributions of simulated mean multiplicities for π^+ as well as π^- meson ($\frac{d^2n}{dpd\theta}$) by the T2K beam neutrino group (see Ref. [119, 120]). The distributions of charged pions from NA61 final measurements were compared with those simulated using JNUBEAM code updated with FLUKA2008. For each of ten polar angle intervals and many momentum bins the ratios between NA61 data and T2K neutrino beam simulations were calculated and later on used to reweight the number of secondary simulated pions produced. Thus, in each (p, θ) bin the weights ($w(p\theta)$) are defined as follows:

$$w(p,\theta) = \frac{\frac{d^2n_{NA61}}{dpd\theta}}{\frac{d^2n_{FLUKA}}{dpd\theta}} \tag{10.1}$$

In Fig. 10.5 we demonstrate the total tuning weights w, versus neutrino energy E_ν, applied for each neutrino flavor for flux predictions at the SK *(left)* and ND280 off-axis detector *(right)*. Observed differences in mean pion multiplicity between NA61 data and FLUKA2008 predictions are the largest for ν_μ flux (*black*) and are on the level of 5-8% (5-10%) for SK (ND280 off-axis) detector in the region of E_ν <4 GeV. In case of ν_e flux (*green*) we see smaller differences, *i.e.* in max around 5% for E_ν <1 GeV.

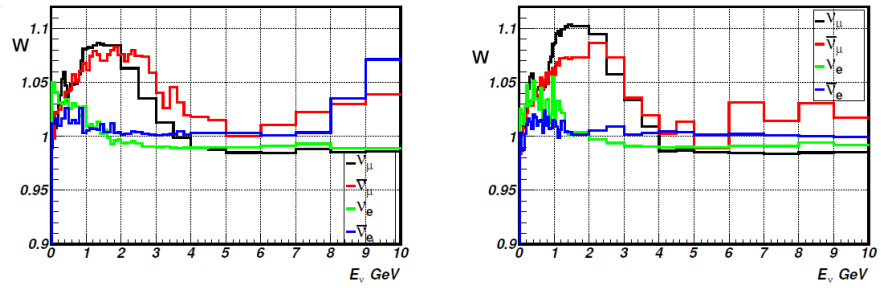

Figure 10.5: Flux tuning weights for SK *(left)* and ND280 off-axis *(right)* detectors versus neutrino energy for different neutrino and antineutrino species. Figure taken from Ref. [120, 119].

The phase space covered by NA61 measurements comprises around 95% of that needed for T2K. Thus, for pions outside the phase space covered by the NA61, the FLUKA2008 prediction is used without any correction. Note that π^+ coming from NA61 measurements have typically 5-10% uncertainties, while those pions which were produced outside experimentally measured phase space, are assigned 50% systematic uncertainty on their production [2]. In case of kaons, FLUKA2008 predicitons were used, but this time their asigned production uncertainties were varing from 10-100%, and, as stated in Ref. [2], were estimated from a comparison with the data from Ref [118].
The importance of NA61 measurements on T2K JNUBEAM simulations may be also demonstrated by comparison of flux predictions using NA61 data and FLUKA2008 with those obtained at the very beginning of JNUBEAM studies, *i.e.* with GCALOR model. This is demonstarted in Fig. 10.6 where ratios of tuned fluxes (NA61 data plus FLUKA2008 predictions) and those obtained using JNUBEAM simulations based on the GCALOR predictions are plotted for each neutrino or antineutrino species of interest. Starting from ν_μ (*upper, left* plot) we observe the differences at the level of around 10% for the oscillation peak *i.e.* $E \sim 0.6$ GeV. For $E > 2$ GeV the differences are even larger and may be even around ∼20%.

In case of ν_e flux (*lower, left* plot), the second most important ingredient of the T2K beam, we observe discrepancies larger than ∼10% for energies below 1 GeV/c.

The tuned T2K neutrino flux was used in the *appearance* analysis which resulted in observation of six ν_e candidates coming from the oscillation of ν_μ off-axis neutrino beam where 1.5±0.3(syst) were expected in case of no transition of a type $\nu_\mu \to \nu_e$ [2].

To conclude, the NA61 results allowed to improve precision of the T2K neutrino beam simulation. In the region of interest, *i.e.* $E < 1$ GeV for the ν_μ flux 10% improvement is obtained with the NA61 measurements on p+C interactions with 31 GeV/c in comparison to JNUBEAM results obtained using GCALOR model.

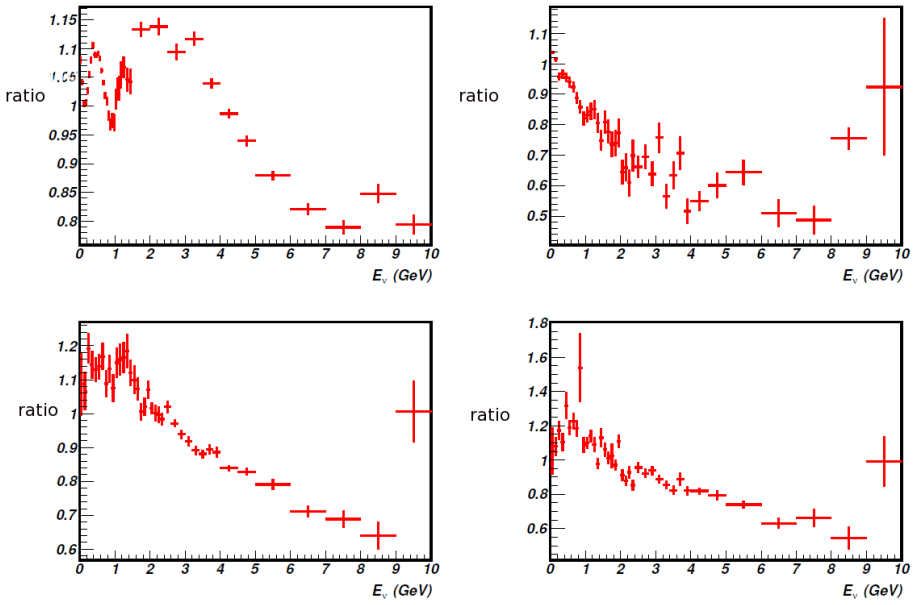

Figure 10.6: Ratios of flux obtained with FLUKA2008 predictions tuned with NA61 measurements to flux predictions derived using GCALOR model for the SK for different neutrino species. Starting from the *upper, left* plot we have ratios for ν_μ then clockwise: $\bar{\nu_\mu}$, $\bar{\nu_e}$ and ν_e fluxes. Figure taken from Ref. [119].

Chapter 11

Summary and Conclusions

The main results of the presented analysis in this thesis are low momentum differential cross sections and mean multiplicities of both charged pions and protons obtained in p+C interactions at 31 GeV/c measured within NA61/SHINE experiment. The analysis presented here is based on a set of data collected during the first NA61/SHINE run in 2007 with thin graphite target with a thickness of 4% of nuclear interaction length. A total sample of registered and reconstructed thin target events consists of around 669 thousand.

We concentrate on the low momentum region $p \leq 1$ GeV/c where information of the particle type can be obtained only with the *dE/dx* measurements. Identification of π^+ mesons and protons was not possible at momenta above 1 GeV/c where the Bethe-Bloch curves for pions, kaons and protons cross each other. On the other hand, for π^- mesons, where the contribution of K^- and antiprotons is almost negligible, the *dE/dx* analysis could be extended in momentum up to 3 GeV/c allowing consistency checks with the other analysis methods in the region of overlap.

The identification procedure, based on the maximum likelihood method, was performed in bins of particle momentum p and polar angle θ. Narrow momentum intervals of 0.1 GeV/c for $0.2 < p \leq 1$ GeV/c and 0.2 GeV/c for $1 < p \leq 3$ GeV/c were chosen to account for the strong dependence of *dE/dx* on momentum. For the final results of identified charged pion mesons and protons spectra ten polar angle intervals covering the range from 0 up to 420 mrad were chosen.

The second step of the analysis involved calculation of Monte Carlo corrections which need to be applied to the identified spectra of charged pion mesons and protons. These corrections take into account several experimental effects like: detector geometrical acceptance, reconstruction inefficiency, decays of particles, secondary interactions.

Next outcome of this thesis were the studies of different sources of systematic uncertainties. They include uncertainty in the corrections originated in secondary interactions and decays of strange particles, comparison of results obtained with different track topologies which account for the reconstruction efficiency, and finally uncertainties resulted in methods used for particle identification.

Presented in this dissertation results on π^+ mean multiplicities were complementary to those obtained with the combined *tof* - *dE/dx* analysis and were used in order to tune the existing T2K neutrino beam simulation. In addition results on π^- were also taken into account in the simulations, although they are less significant for T2K neutrino beam production. With NA61 measurements uncertainty on π^+ production from the p+C interactions at 31 GeV/c was reduced significantly in the T2K neutrino beam simulation. As a result predicted T2K muon neutrino flux was modified by 10% in maximum for the region of most interest, *i.e.* with $E_\nu < 1$ GeV where oscillation maximum at ~ 0.6 GeV is present.

The same data set, *i.e.* coming from pilot run in 2007, was used to obtain spectra of

positively charged kaons for two intervals of polar angle covering range from 20 up to 240 mrad. The adopted binning scheme was driven mainly by the limited available statistics in 2007. These results are prepared for the publication and are used by the T2K neutrino beam group to predict the electron neutrino component and the high energy tail of the T2K beam.

Currently the analysis is being performed for the data of 2009 with an order of magnitude more events recorded in comparison to first NA61/SHINE pilot run. This will improve not only results obtained for charged pion mesons but first of all significantly enrich those measurements already present for kaons.

In addition to analysis of thin target data the NA61/SHINE performed also measurements of p+C interactions at 31 GeV/c with full size replica of the T2K target, called long target (1.9 interaction length). These measurements were conducted in pilot run in 2007 as well as in 2009 and 2010 with much larger statistics. The analysis of the 2007 pilot long target data show that the T2K flux predictions may be effectively re-weighted with NA61/SHINE long target. However, the analysis of 2009 and 2010 data is still ongoing.

Appendix A

Parametrization of the Bethe-Bloch function

We use functional shape of the BB formula (see Eq. (4.11) on page 49) considering the parameters depending on composition, pressure and temperature of the detector gas mixture as free fit parameters that can be adjusted to experimental measurements:

$$\left\langle \frac{dE}{dx} \right\rangle = \frac{e^4 z^2}{8\pi m_e c^2 \epsilon_0^2} N \frac{1}{\beta^2} (K + 2\ln(\beta\gamma) - \beta^2 - \delta(\beta\gamma)) \tag{A.1}$$

with K equal to:

$$K = \ln\left(\frac{2m_e c^2 E_{cut}}{I^2}\right) \tag{A.2}$$

As parametrization of the $\delta(\beta\gamma)$ term we use a description that was introduced by Sternheimer and Peierls [103] :

$$\delta(\beta\gamma) = \begin{cases} 0 & \text{if } X < X_0 \\ 2\ln(10)(X - X_A) + a(X_1 - X)^3 & \text{if } X_0 \leq X < X_1 \\ 2\ln(10)(X - X_A) & \text{if } X \geq X_1 \end{cases} \tag{A.3}$$

where $X = \log_{10}(\beta\gamma)$. The $\delta(\beta\gamma)$ function has to fulfill the following continuity conditions:

1. $\delta(X = X_0)$=0,

2. $\frac{d\delta}{dX}(X = X_0)$=0

It is seen that we thus have 6 parameters: X_0, X_A, X_1, N, K, and a depending on the TPC material properties. The number of parameters can be reduced to four by using 2 continuity condition.

From the first continuity condition we get:

$$\delta(X_0) = 0 \tag{A.4}$$

$$2\ln(10)(X_0 - X_A) + a(X_1 - X_0)^3 = 0 \tag{A.5}$$

with

$$a = \frac{2\ln(10)(X_A - X_0)}{(X_1 - X_0)^3} \tag{A.6}$$

Second continuity condition with help of Eq. (A.6) leads us to relation of X_1 and X_0:

$$\begin{aligned} 2\ln(10) - 3a(X_1 - X_0)^2 &= 0 && \text{(A.7)} \\ 2\ln(10) - 6\ln(10)\frac{(X_A - X_0)}{(X_1 - X_0)} &= 0 && \text{(A.8)} \\ X_1 - X_0 - 3X_A + 3X_0 &= 0 && \text{(A.9)} \\ X_1 &= -2X_0 + 3X_A && \text{(A.10)} \end{aligned}$$

Thus we have two equations (A.5) and (A.10), allowing to determine X_0 and X_1: Substituting X_1 from (A.10) to (A.5) we get:

$$\begin{aligned} 2\ln(10)(X_0 - X_A) + a(-2X_0 + 3X_A - X_0)^3 &= 0 \\ X_0^2 - 2X_A X_0 + X_A^2 - \frac{2\ln(10)}{27a} &= 0 && \text{(A.11)} \end{aligned}$$

Eq. (A.11) has two solutions for X_0. Taking into account the fact that $X_0 < X_1$ and knowing relation between X_0 and X_1 from Eq. (A.10) we obtain the final solution as:

$$\begin{aligned} X_0 &= X_A - \frac{1}{3}\sqrt{\frac{2\ln(10)}{3a}} \\ X_1 &= X_A + \frac{2}{3}\sqrt{\frac{2\ln(10)}{3a}} && \text{(A.12)} \end{aligned}$$

Now we show that the energy loss (A.1) is constant with momenta when it reaches Fermi plateau. This takes place when:

(a) relativistic rise is over, *i.e.* $X \geq X_1$ and term $\delta(\beta\gamma) = 2\ln(10)(X - X_A) = 2\ln(10)[\log_{10}(\beta\gamma) - X_A]$, see Eq. (A.10),

(b) $\beta \to 1$

From (a) we have:

$$\begin{aligned} \left\langle \frac{dE}{dx} \right\rangle &= \frac{e^4 z^2}{8\pi m_e c^2 \epsilon_0^2} N \frac{1}{\beta^2}(K + 2\ln(\beta\gamma) - \beta^2 - 2\ln(10)[\log_{10}(\beta\gamma) - X_A]) \\ &= \frac{e^4 z^2}{8\pi m_e c^2 \epsilon_0^2} N \frac{1}{\beta^2}(K + 2\ln(\beta\gamma) - \beta^2 - 2\ln(\beta\gamma) + 2\ln(10)X_A) \\ &= \frac{e^4 z^2}{8\pi m_e c^2 \epsilon_0^2} N \frac{1}{\beta^2}(K + 2\ln(10)X_A - \beta^2) && \text{(A.13)} \end{aligned}$$

Now for $\beta \to 1$ we get:

$$\left\langle \frac{dE}{dx} \right\rangle (\beta \to 1) = \frac{e^4 z^2}{8\pi m_e c^2 \epsilon_0^2} N(K + 2\ln(10)X_A - 1) = \text{const} \qquad \text{(A.14)}$$

Eq. (A.14) proves that energy loss at Fermi plateau is constant. We define it as s:

$$\left\langle \frac{dE}{dx} \right\rangle = \frac{e^4 z^2}{8\pi m_e c^2 \epsilon_0^2} N(K + 2\ln(10)X_A - 1) \equiv s \qquad \text{(A.15)}$$

Instead of electron density N still present in the (A.1), it is convenient to use experimentally well defined and measured s. With auxiliary variable F equal to $F = \frac{e^4 z^2}{8\pi m_e c^2 \epsilon_0^2} N$ from Eq. (A.15) we obtain:

$$F = \frac{s}{K + 2\ln(10)X_A - 1} \qquad \text{(A.16)}$$

Finally Bethe-Bloch parametrization Eq. (A.1) may be rewritten with help of (A.12) and (A.16) in terms of four unknown parameters: X_A, a, K, and s, all dependent on properties of the absorbing material:

$$\left\langle \frac{dE}{dx} \right\rangle = \left(\frac{s}{K + 2\ln(10)X_A - 1} \right) \frac{1}{\beta^2} \left(K + 2\ln(\beta\gamma) - \beta^2 - \delta(\beta\gamma) \right) \tag{A.17}$$

with term $\delta(\beta\gamma)$ given by Eq. (A.3).

Appendix B

Maximum likelihood method for particle identification

One would like to identify particle type (π^+, e^+, K^+ and protons for positive and π^-, e^-, K^- for negative) in low momentum region, where fast change of energy loss with momentum (as well as relative particle hypotheses) is observed. The identification procedure was performed in (p, θ) bins. Narrow momentum intervals (of 0.1 GeV/c for $p < 1$ GeV/c and 0.2 GeV/c for $1 < p < 3$ GeV/c) were chosen to account for the strong dependence of dE/dx on momentum. In each (p, θ) bin the *maximum likelihood* method was used on a track-by-track basis to fit relative particle abundances assumed to be constant in this bin (the approach suggested in Ref. [106]). For each track "l" inside a bin (p, θ) one has information on its:

- energy loss measurement $\mathrm{dE/dx}_l$,
- uncertainty on energy loss measurement σ_l,
- momentum p_l,

Using BB (see App. A) parametrization one can calculate for each track its expected value of energy loss measurement $\mathrm{dE/dx}^i_{BB}(p_l)$ a different particle hypothesis "i".

Gaussian probability density function ($P_i(\mathrm{dE/dx}_l)$) is then expressed by:

$$P_i(\mathrm{dE/dx}_l) = \frac{1}{\sqrt{2\pi}\sigma_l} \exp\left(-\frac{(\mathrm{dE/dx}^i_{BB}(p_l) - \mathrm{dE/dx}_l)^2}{2\sigma_l^2}\right) \quad \text{(B.1)}$$

Taking into account all possible, alternative particle hypotheses one constrains the following function f_l:

$$f_l = m_0 \cdot P_\pi(\mathrm{dE/dx}_l) + m_1 \cdot P_K(\mathrm{dE/dx}_l) + m_2 \cdot P_e(\mathrm{dE/dx}_l) + m_3 \cdot P_p(\mathrm{dE/dx}_l) \quad \text{(B.2)}$$

where m_0, m_1, m_2 and m_3 are the relative abundances of the particles in selected bin of phase space fullfilling the condition:

$$\sum_{i=0}^{3} m_i = 1 \quad \text{(B.3)}$$

One of the parameters can be calculated from (B.3):

$$m_3 \;=\; 1 - \sum_{i=0}^{2} m_i \tag{B.4}$$

Thus we will fit three parameters: m_0, m_1 and m_2.

Minimized function L is expressed by the following formula:

$$L \;=\; -\sum_{l=1}^{N_{ent}} \ln f_l \tag{B.5}$$

where N_{ent} is the total number of tracks in selected bin.

Number of type "i" particles in the selected bin is then expressed by:

$$n_i \;=\; N_{ent} \cdot m_i \tag{B.6}$$

and its relative uncertainty:

$$\left(\frac{n_{i,err}}{n_i}\right)^2 \;=\; \left(\frac{1}{N_{ent}}\right) + \left(\frac{m_{i,err}}{m_i}\right)^2 \tag{B.7}$$

where m_i and $m_{i,err}$ we take from the fit.

Appendix C

RST and WST configurations

In order to investigate more the RST and WST population and configurations for small polar angles we decided to check what is the contribution to ϕ distributions coming from tracks reaching different detectors. For this study we selected well defined in MC particles: π^+, π^- and protons which were measured in different detectors configuration (see Tab. C.1). The results of this task are illustrated in Fig. C.1, where with different colors we show impact of discussed track topologies on the azimuthal angle distributions. Plots are prepared for $\theta = [100, 140]$ mrad *(left)* and $\theta = [140, 180]$ mrad *(right)*.

π^+, protons	π^-
VTPC1 only	VTPC1 only
VTPC1 + VTPC2	VTPC1 + VTPC2
VTPC1 + MTPC-L	VTPC1 + MTPC-R
VTPC2 + MTPC-L	VTPC2 + MTPC-R
VTPC1 + VTPC2 + MTPC-L	VTPC1 + VTPC2 + MTPC-R
VTPC1 + VTPC2 + MTPC-R	VTPC1 + VTPC2 + MTPC-L

Table C.1: Selected different detectors configuration as input to ϕ distributions for π^+, π^- and protons.

First let us focus on the comparison of RST and WST samples shown for π^+ mesons and protons. The important conclusion is that RST group is very uniform as most of particles representing this track topology are measured only in the VTPC1. This statement is no longer valid as we look at the WST. Here we observe many transition regions between different detectors. For $\phi = [160, 200]$ deg the population of tracks reaching VTPC1 is almost negligible, especially for $\theta = [100, 140]$ mrad. Instead we can notice all combinations of tracks which have part of their points measured in the MTPC-L. As we increase value of θ bin we see that situation improves. We are able to measure more WST tracks in VTPC1. However, the transition region is still present. For negative tracks we can see mirror image after reflection at $\phi = 90^0$. WST for low θ have complicated non-flat distributions and can be subject of various problems with reconstruction (we will study that considering systematical errors in Chapter 9).

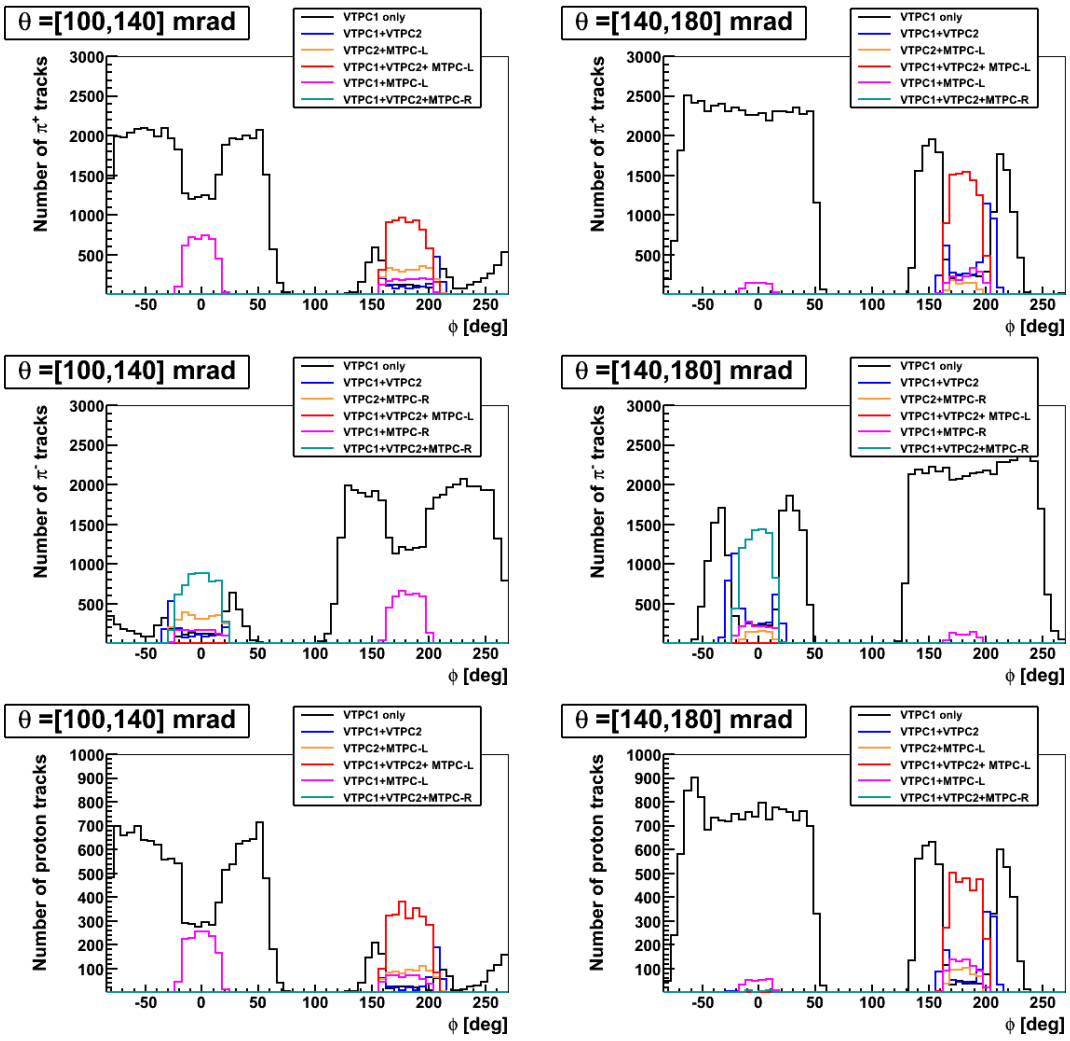

Figure C.1: Impact of different track topologies on the azimuthal angle distributions for π^+ *(upper)*, π^- *(middle)* and protons *(lower)*, respectively. Plots are prepared for MC *reconstructed* tracks with $\theta = [100, 140]$ mrad *(left)* and $\theta = [140, 180]$ mrad *(right)*.

Bibliography

[1] N. Abgrall *et al.*, [NA61/SHINE Collaboration], *Measurements of Cross Sections and Charged Pion Spectra in Proton–Carbon Interactions at 31 GeV/c*, Phys. Rev. **C84**, 034604, arXiv:1102.0983 [hep-ex], (2011).

[2] K. Abe *et al.*, [T2K Collaboration], *Indication of Electron Neutrino Appearance from an Accelerator-produced Off-axis Muon Neutrino Beam*, Phys. Rev. Lett. **107**, 041801 (2011).

[3] F. Reines, *40 Years of Neutrino Physics*, Prog. of Part. and Nucl. Phys. **32**, 1, (1994).

[4] E. Fermi, *Versuch einer Theorie der β-Strahlen.*, Z. Phys. **88**, (1934).

[5] *All Nobel Prizes in Physics*, `http://www.nobelprize.org/nobel_prizes/physics/laureates/`

[6] C. L. Cowan, F. Reines *et al.*, *Detection of the Free Neutrino: a Confirmation*, Science **124**, 103, (1956).

[7] K. Kodama *et al.*, [DONuT Collaboration], *Final tau-neutrino results from the DONuT experiment*, Phys. Rev. **D78**, 052002, (2008).

[8] T. Morii, C. S. Lim, S. N. Mukherjee, *The physics of the standard model and beyond*, World Scientific Publishing, (2004).

[9] A. Aguilar *et al.*, [LSND Collaboration], *Evidence for neutrino oscillations from the observation of anti-neutrino(electron) appearance in a anti-neutrino(muon) beam*, Phys. Rev. **D64**, 112007, (2001).

[10] A. A. Aguilar-Arevalo *et al.*, [MiniBooNe Collaboration], *A Search for muon neutrino and antineutrino disappearance in MiniBooNE*, Phys. Rev. Lett. **103**, (2009).

[11] ALEPH, DELPHI, L3, OPAL and SLD Collaborations, Phys. Reports **427**, 257, (2006).

[12] B. Pontecorvo, *Neutrino experiments and the problem of conservation of leptonic charge*, Zh. Eksp. Teor. Fiz. **53**, 1717, (1967).

[13] Z. Maki, M. Nakagawa and S. Sakata, *Remarks on the Unified Model of Elementary Particles*, Progress of Theoretical Physics **28**, 870 (1962).

[14] L. Wolfenstein, *Neutrino oscillations in matter*, Phys. Rev. **D17**, 2369 (1978).

[15] S. P. Mikheyev and A. Y. Smirnov, *Resonance enhancement of oscillations in matter and solar neutrino spectroscopy*, Yad. Fiz **42**, 1441 (1985).

[16] S. Dowson, R. Mohapatra, *Colliders and neutrinos: the window into physics beyond the standard model*, World Scientific Publishing (2007).

[17] `https://www.sns.ias.edu./~jnb/`.

[18] J. N. Bahcall, *et al.*, *Solar Models: current epoch and time dependences, neutrinos, and helioseismological properties*, Astrophys. J. **555**, 9901012, (2001).

[19] R. Davis Jr., *Solar neutrinos. II. Experimental*, Phys. Rev. Lett. **12**, 303, (1964).

[20] V. N. Gavrin, Proc. Int. Conf. on Topics in Astroparticle and Underground Physics, Seattle WA, Sept. 5-9, (2003).

[21] W. Hampel *et al.*, [GALLEX Collaboration], *GALLEX solar neutrino observations: results for GALLEX IV*, Phys. Lett. **B447**, 127, (1999).

[22] M. Altmann *et al.*,[GNO Collaboration], *GNO progress report for 2001*, LNGS annual report 2001, Phys. Lett. B **490**, 15, (2000).

[23] K. S. Hirata, *et al.*, [Kamiokande Collaboration], *Observation of ^8B solar neutrinos in the Kamiokande-II detector*, Phys. Rev. Lett. **63**, 16, (1989).

[24] S. Fukuda *et al.*, [Super-Kamiokande Collaboration], *Solar ^8B and hep Neutrino Measurements from 1258 Days of Super-Kamiokande Data*, Phys. Rev. Lett. **86**, 5651, (2001).

[25] S. Fukuda *et al.*, [Super-Kamiokande Collaboration], *Determination of Solar Neutrino Oscillation Parameters using 1496 Days of Super-Kamiokande-I Data*, Phys. Lett. **B539**, 179, (2002).

[26] K. Nakamura *et al.*, (Particle Data Group), J. Phys. **G37**, 075021 (2010).

[27] B. Aharmim *et al.*, [SNO Collaboration], *Electron energy spectra, fluxes, and day-night asymmetries of ^8B solar neutrinos from measurements with NaCl dissolved in the heavy-water detector at the Sudbury Neutrino Observatory*, Phys. Rev. **C72**, 055502, (2005).

[28] B. Aharmim *et al.*, [SNO Collaboration], *Low-energy-threshold analysis of the Phase I and Phase II data sets of the Sudbury Neutrino Observatory*, Phys. Rev. **C81**, 055504, (2010).

[29] C. Arpesella *et al.*, [Borexino Collaboration], *New results on solar neutrino fluxes from 192 days of Borexino data*, Phys.Rev.Lett. **101**, 091302, (2008).

[30] K. Eguchi *et al.*, [KamLAND Collaboration], *First results from KamLAND: Evidence for reactor anti-neutrino disappearance.* Phys. Rev. Lett. **90**, 021802, (2003).

[31] S. Abe *et al.*, [KamLAND Collaboration], *Precision Measurement of the Neutrino Oscillation Parameters with KamLAND*, Phys. Rev. Lett. **100**, 221803, (2008).

[32] F. Reines *et al.*, *Evidence for High-Energy Cosmic-Ray Neutrino Interactions*, Phys. Rev. Lett. **15**, 429, (1965).

[33] R. Becker-Szendy *et al..*, [IMB Collaboration], *Neutrino Measurements with the IMB Detector*, Phys. Rev. **D46**, 3720, (1992).

[34] Y. Fukuda *et al.*, [Super-Kamiokande Collaboration], *Evidence for oscillation of atmospheric neutrinos*, Phys. Rev. Lett. **81**, 1562, (1998).

[35] M. Aglietta *et al.*, [NUSEX Collaboration], *Experimental Study of Atmospheric Neutrino Flux in the NUSEX Experiment*, Europhys. Lett. **8**, 611, (1989).

[36] K. Daum, [Frejus Collaboration], *Determination of the atmospheric neutrino spectra with the Frejus detector*, Z. Phys. **C66**, 417, (1995).

[37] M. Ambrosio, [MACRO Collaboration], *Atmospheric neutrino oscillations from upward through going muon multiple scattering in MACRO*, Phys. Lett. **B566**, 35, (2003).

[38] M. C. Sanchez *et al.*, [Sudan-2 Collaboration], *Measurement of the L/E distribution of atmospheric neutrinos in Sudan-2 and their interpretation as neutrino oscillations*, Phys. Rev. **D68**, 113004, (2006).

[39] Y. Ashie *et al.*, [Super-Kamiokande Collaboration], *A measurement of atmospheric neutrino oscillation parameters by Super-Kamiokande I.*, Phys. Rev. **D71**, 112005, (2005.)

[40] M. Ahn *et al.*, [K2K Collaboration], *Measurement of Neutrino Oscillation by the K2K Experiment*, Phys. Rev. **D74**, 072003, (2006).

[41] D. G. Michael *et al.*, [MINOS Collaboration], *Observation of Muon Neutrino Disappearance with the MINOS Detectors in the NuMI Neutrino Beam*, Phys. Rev. Lett. **97**, 191801, (2006).

[42] N. Agafonova *et al.*, [OPERA Collaboration], *Observation of a first ν_τ candidate in the OPERA experiment in the CNGS beam*, Phys. Lett. **B691**, 138, (2010).

[43] P. Adamson *et al.*, [MINOS Collaboration], *Measurement of Neutrino Oscillations with the MINOS Detectors in the NuMI Beam*, Phys. Rev. Lett. **101**, 131802, (2008).

[44] M. Apollonio *et al.*, [CHOOZ Collaboration], *Search for neutrino oscillations on a long base-line at the CHOOZ nuclear power station*, Eur. Phys. J. **C27**, 331, (2003).

[45] F. Boehmm *et al.*, [Palo Verde Collaboration], *Search for neutrino oscillations at the Palo Verde nuclear reactors*, Phys. Rev. Lett. **84**, 3764, (2000).

[46] S. Yamamoto *et al.*, [K2K Collaboration], *Improved search for $\nu_\mu \to \nu_e$ oscillation in a long-baseline accelerator experiment*, Phys. Lett. **96**, 181801, (2006).

[47] B. Aharmim *et al.*, [SNO Collaboration], *Low Energy Threshold Analysis of the Phase I and Phase II Data Sets of the Sudbury Neutrino Observatory*, Phys. Rev. **C81**, 055504, (2010).

[48] M. Mezzetto and T. Schwetz, *θ_{13}: phenomenology, present status and prospect*, J. Phys. **G37**, 103001, (2010).

[49] X. Guo *et al.*, [Daya-Bay Collaboration], *A Precision measurement of the neutrino mixing angle theta(13) using reactor antineutrinos at Daya-Bay*, (2007).

[50] F. Suekane *et al.*, [Double Chooz Collaboration], *A High Precision Reactor Neutrino Detector for the Double Chooz Experiment.*, Nucl.Instrum.Meth. **A623**, 440, (2010).

[51] J. K. Ahn *et al.*, [Reno Collaboration], *RENO: An Experiment for Neutrino Oscillation Parameter θ_{13} Using Reactor Neutrinos at Yonggwang.*, arXiv:1003.1391 [hep-ex], (2010).

[52] D. Ayres *et al.*, [NOvA Collaboration], *The NOvA Technical Design Report.*, FERMILAB-DESIGN-2007-01, (2007).

[53] Y. Itow *et al.*, [T2K Collaboration], *The JHF-Kamioka neutrino project*, hep-ex/0106019, (2001).

[54] `http://j-parc.jp/index-e.html`

[55] J. Coulombe *et al.*, [T2K-ND280 Collaboration], *T2K ND280 Conceptual Design Report*, T2K Internal Document, (2005).

[56] T2K-ND280 Collaboration, `http://www.nd280.org/info`

[57] K. Abe *et al.*, [T2K Collaboration], *The T2K experiment*, accepted for publication in Nucl. Instrum. Methods, article in press, arXiv:1106.1238 [physics.ins-det], (2011).

[58] D. Beavis, A. Carroll, I. Chiang *et al.*, *Long Baseline Neutrino Oscillation Experiment at the AGS (Proposal E889)*, Physics Design Report, BNL 52459, (1995).

[59] Y. Fukuda *et al.*, [Super-Kamiokande Collaboration], *Evidence for Oscillation of Atmospheric Neutrinos*, Phys. Rev. Lett. **81**, 1562, (1998).

[60] Y. Fukuda *et al.*, [Super-Kamiokande Collaboration], *Measurement of the Solar Neutrino Energy Spectrum Using Neutrino Electron Scattering*, Phys. Rev. Lett. **82**, 2430, (1999).

[61] Y. Ashie *et al.*, [Super-Kamiokande Collaboration], *A Measurement of Atmospheric Neutrino Oscillation Parameters by Super-Kamiokande I*, Phys. Rev. **D71**, 112005, (2005).

[62] M. Shiozawa *et al.*, [Super-Kamiokande Collaboration], *Search for Proton Decay via* $p \to e^+ + \pi^0$ *in a Large Water Cherenkov Detector,* , Phys. Rev. Lett. **81**, 3319, (1998).

[63] Y. Hayato *et al.*, [Super-Kamiokande Collaboration], *Search for proton decay through* $p \to \bar{\nu} + K^+$ *in a large water Cherenkov detector*, Phys. Rev. Lett. **83**, 1529, (1999).

[64] H. Nishino *et al.*, [Super-Kamiokande Collaboration], *Search for Proton Decay via* $p \to e^+ + \pi^0$ *and* $p \to \mu^+ + \pi^0$ *in a Large Water Cherenkov Detector*, Phys. Rev. Lett. **102**, 141801, (2009).

[65] Y. Fukuda *et al.*, [Super-Kamiokande Collaboration], *The Super-Kamiokande detector*, Nucl. Instrum. Meth. **A501**, 418, (2003).

[66] J-PARC TDR, KEK-Report and JAERI-Tech, `http://hadron.kek.jp/~accelerator/TDA/tdr3003/index2.html`, (2003).

[67] S. van der Meer, *A directive device for charged particles and its use in an enhanced neutrino beam*, CERN-61-07, (1961).

[68] R. B. Plamer, presented at Informal Conference on Experimental Neutrino Physics, CERN-65-32, 141-146, (1961).

[69] P. Przewłocki, Ph.D. thesis, *A study of neutrino interactions constituting the background to electron neutrino appearance in T2K experiment*, Soltan Institute for Nuclear Studies, Warsaw, Poland, (2010).

[70] K. T. McDonald, *An Off-Axis Neutrino Beam*, [arXiv:hep-ex/0111033], (2001).

[71] N. Abgrall, B. Popov, J. M. Levy, *Prediction of neutrino fluxes for T2K: NA61 analysis and data taking strategy*, T2K/NA61 internal note, draft 2.1, (2009).

[72] R. Brun, F. Carminati, GEANT Detector Description and Simulation Tool, CERN Program Library Long Writeup W5013, (1993).
`http://wwwasdoc.web.cern.ch/wwwasdoc/geant/geantall.html`

[73] `http://www.staff.uni-mainz.de/zeitnitz/Gcalor/gcalor.html`

[74] N. Abgrall, *Hadroproduction measurements: The NA61-SHINE experiment at CERN*, AIP Conf. Proc. **981**, 157, (2008).

[75] C. Meurer *et al.*, [HARP Collaboration], *New p+C data in fixed target experiments and the muon component in extensive air showers*, arXiv:astro-ph/0612157v1, (2006).

[76] C. Alt *et al.*, [NA49 Collaboration], *Inclusive production of charged pions in p+C collisions at 158 GeV/c beam momentum*, Eur. Phys. J. **C49**, 897, (2007).

[77] S. Afanasev *et al.* [NA49 Collaboration], *The NA49 large acceptance hadron detector.*, Nucl. Instrum. Meth. **A430**, 210, (1999).

[78] `http://ab-dep-op-sps.web.cern.ch/ab-dep-op-sps/`

[79] N. Antoniou *et al.*, [NA49-Future Collaboration], *Study of Hadron Production in Hadron-Nucleus and Nucleus-Nucleus Collisions at the CERN SPS*, CERN-SPSC-2006-034, (2006).

[80] N. Antoniou *et al.*, [NA61 Collaboration], *Additional Information Requested in the Proposal Review Process (addendum to the proposal P330)*, CERN-SPSC-2007-004, (2007).

[81] N. Abgrall *et al.*, [NA61 Collaboration], *Further Information Requested in the Proposal Review Process*, CERN-SPSC-2007-019, (2007).

[82] N. Abgrall *et al.*, [NA61 Collaboration], *Calibration and Analysis of the 2007 Data*, CERN-SPSC-2008-018, (2008).

[83] C. Bovet *et al.*, *The Cedar Counters For Particle Identification In The Sps Secondary Beams: A Description And An Operation Manual*, CERN-YELLOW-82-13, (1982).

[84] F. Sauli, *Principles of Operation of a Multiwire Proportional and Drift Chambers*, CERN Report 77-09 (1977).

[85] W. R. Leo, *Techniques for Nuclear and Particle Physics Experiments*, Springer (1987).

[86] C. Grupen, B. Shwartz, *Particle Detectors*, Cambridge University Press, (2008).

[87] H. Appelshauser, *Optimization of the VTPC1 pad layout*, NA49 internal note (1995).

[88] M. Gaździcki and R. Renford, *Optimization of the pad geometry of VTPC2*, NA49 internal note, (1993).

[89] M. Fuchs, *Vertex TPC1 pad orientation study*, NA49 internal note, (1992).

[90] H. A. Bethe, *Theorie des Durchgangs schneller Korpuskularstrahlen durch Materie*, Annalen der Physik **5**, 325, (1930).

[91] F. Bloch, *Bremsvermogen von Atomen mit mehreren Elektronen*, Z. Physik **81**, 393, (1933).

[92] H. A. Bethe, J. Ashkin, *Passage of radiations through matter*, Experimental Nuclear Physics, 166, (1953).

[93] E. Fermi, *The Ionization Loss of Energy in Gases and in Condensed Materials*, Phys. Rev. **57**, 485, (1940).

[94] U. Fano, Ann. Rev. Nucl. Sc. **13**, 1 (1963).

[95] `http://physics.nist.gov/PhysRefData/Star/Text/ESTAR.html`

[96] `http://pdg.lbl.gov/AtomicNuclearProperties/HTML_PAGES/018.html`

[97] G. I. Veres, Ph.D. thesis, *Baryon Momentum Transfer in Hadronic and Nuclear Collisions at the CERN NA49 Experiment*, Eotvos Lorand University, Budapest, Hungary, (2001).

[98] L. D. Landau *On the energy loss of fast particles by ionization*, J. Phys. **8**, 201, (1944).

[99] J. E. Moyal, *Theory of the Ionization Fluctuations*, Phil. Mag. **46**, No 374, 263, (1955).

[100] B. Boimska, Ph.D. thesis, *Transverse Characteristics of Hadron Production in Elementary and Nuclear Collisions at the CERN SPS Energies*, Soltan Institute for Nuclear Studies, Warsaw, Poland, (2004).

[101] S. Murphy, Ph.D. thesis in preparation, University of Geneva, Geneva, Switzerland, (2012).

[102] T. Palczewski, Ph.D. thesis in preparation, National Centre for Nuclear Research, Warsaw, Poland, (2012).

[103] R. M. Sternheimer, R. F. Peierls, *General Expression for the Density Effect for the Ionization Loss of Charged Particles*, Phys. Rev. **B3**, 3681, (1971).

[104] M. Posiadała, *Measurements of hadron production for neutrino and cosmic-ray physics-program of the NA61/SHINE experiment at CERN SPS*, Non. Phen. in Comp. Syst. **12**, 4, (2009).

[105] M. Posiadała, *Measurements of hadron production for neutrino physics within NA61/SHINE experiment at CERN SPS*, Acta Phys. Pol. **B41**, 1585, (2010).

[106] M. Gaździcki, *Statistical tool for particle identification by mass measurement*, Nucl. Instrum. Meth. **A345**, 148, (1994).

[107] K. Werner, *Space-time structure and rescattering in ultrarelativistic nuclear collisions*, Nucl. Phys. **A525**, 501, (1991).

[108] N. Abgrall, Ph.D. thesis, University of Geneva, Geneva, Switzerland, (2011).

[109] C. Alt *et al.*, [NA49 Collaboration], *Inclusive production of charged pions in p+p collisions at 158 GeV/c beam momentum* Eur. Phys. J. **C45**, 343, (2006).

[110] C. Strabel, Ph.D. thesis, *Evaluation of Particle Yields in 30 GeV Proton–Carbon Interactions for Estimating the T2K Neutrino Flux*, ETH, Zurich, Switzerland, (2011).

[111] R. J. Glauber and G. Matthiae, *High-energy scattering of protons by nuclei*, Nucl. Phys. **B21**, 135, (1970).

[112] S. Agostinelli *et al.*, [GEANT4 Collaboration], *GEANT4: A simulation toolkit*, Nucl. Instrum. Meth. **A506**, 250, (2003).

[113] G. Battistoni *et al.*, *The FLUKA code: Description and benchmarking*, AIP Conf. Proc. **896**, 31, (2007).

[114] S. M. Bass *et al.*, *Microscopic models for ultrarelativistic heavy ion collisions*, Prog. Part. Nucl. Phys. **41**, 225, (1998).

[115] D. Heck *et al.*, *CORSIKA: A Monte Carlo Code to Simulate Extensive Air Showers*, Report Forschungszentrum Karlsruhe FZKA-6019, (1998).

[116] H. Fesefeldt, *GHEISHA program*, Report Aachen PITHA-85-02, (1985).

[117] M. Unger for the NA61/SHINE Collaboration, *Hadron Production at Fixed Target Energies and Extensive Air Showers*, arXiv:1012.2604 [nucl-ex], (2010).

[118] T. Eichten *et al.*, *Particle production in proton interactions in nuclei at 24 GeV/c*, Nucl. Phys. **B44**, 333, (1972).

[119] N. Abgrall *et al.*, [T2K Collaboration], *Neutrino flux prediction*, T2K internal note, T2K-TN-038, (2011).

[120] V. Galymow for the T2K Collaboration, *Predicting The Neutrino Flux at T2K*, presentation prepared for the XIIIth International Workshop on Neutrino Factories, Super beams and Beta beams, NUFACT2011, Geneva, Switzerland, (2011).